

**“MANGANESE SUBSTITUTED ZINC FERRITE
NANOSTRUCTURES FOR PHOTOCATALYTIC DYE
DEGRADATION”**

A THESIS SUBMITTED TO

**D. Y. PATIL EDUCATION SOCIETY
(DEEMED TO BE UNIVERSITY), KOLHAPUR**



FOR THE DEGREE OF

DOCTOR OF PHILOSOPHY

IN

PHYSICS

UNDER THE FACULTY OF

INTERDISCIPLINARY STUDIES

BY

Miss. Ketaki Vasantao Kadam

M.Sc.

UNDER THE SUPERVISION OF

Dr. Vishwajeet M. Khot

M.Sc., Ph.D.

DEPARTMENT OF MEDICAL PHYSICS,

CENTRE FOR INTERDISCIPLINARY RESEARCH,

D. Y. PATIL EDUCATION SOCIETY (DEEMED TO BE UNIVERSITY),

KOLHAPUR- 416 006, MAHARASHTRA, (INDIA)


2024

DECLARATION

I hereby declare that the thesis entitled "*MANGANESE SUBSTITUTED ZINC FERRITE NANOSTRUCTURES FOR PHOTOCATALYTIC DYE DEGRADATION*" submitted for the degree of *Doctor of Philosophy (Ph.D.)* in *Physics* at Department of Medical Physics, *Centre for Interdisciplinary Research, D. Y. Patil Education Society (Deemed to be University), Kolhapur* is completed and written by *Miss. Ketaki Vaishali Vasantrao Kadam*, under the supervision of *Dr. Vishwajeet M. Khot*, has not before made the basis for the award of any degree/diploma/other related heading of this or any other university in India/any other country/examining body to the best of my knowledge. Further, I assert that, I have not dishonored any of the requirements under copyright and piracy/cyber/IPR act amended by UGC from time to time.

Place: Kolhapur

Date: 21 / 11 /2024


Miss. Ketaki V. Kadam
(Research Student)

D. Y. Patil Education Society
(Deemed to be University), Kolhapur
Centre for Interdisciplinary Research



Certificate

This is to certify that the thesis entitled "**MANGANESE SUBSTITUTED ZINC FERRITE NANOSTRUCTURES FOR PHOTOCATALYTIC DYE DEGRADATION**" which is being submitted herewith for the award of the Degree of **Doctor of Philosophy (Ph.D.)** in **Physics** at Department of Medical Physics, CIR, **D. Y. Patil Education Society (Deemed to be University), Kolhapur**, is the result of the original research work completed by **Miss. Ketaki Vasantrao Kadam** under my supervision and guidance and to the best of my knowledge and belief the work embodied in this thesis has not formed earlier the basis for the award of any Degree or similar title of this or any other University or examining body.

Place: **Kolhapur**

Date: **21 / 11 / 2024**

Forwarded through,
Prof. C. D. Lokhande
Dean and Research Director,
Centre for Interdisciplinary Research
Research Director
D. Y. Patil Education Society
(Institution Deemed to be University)

Research Guide
Dr. Vishwajeet M. Khot
Associate Professor
Department of Medical Physics

Dr. Vishwajeet M. Khot
Associate Professor
Department of Medical Physics,
Centre for Interdisciplinary Research,
D.Y.Patil Education Society, Kolhapur.
(Institution Deemed to be University)
Kolhapur-416 006. (India)

KOLHAPUR JR-416006



ACKNOWLEDGEMENT

A journey is easier when you travel together. Interdependence is certainly more valuable than independence. This thesis is the result of work where I have been accompanied and supported by many people.

*At the completion of my Ph.D. thesis, I would like to express my sincere gratitude towards my advisor, **Dr. Vishwajeet M. Khot** Associate Professor, Department of Medical Physics, Centre for Interdisciplinary Research (CIR), D. Y. Patil Education Society (Deemed to be University), Kolhapur for the continuous support during my Ph.D. study and related research, for his motivation, and immense knowledge. I thank him not only for the guidance he rendered in the field of research but also for enlightening the path of my life with a deep love for science. With his support, I could overcome my personal and scientific problems in writing scientific papers including this Ph.D. thesis and this work could not have been completed without his inspiring guidance and constant encouragement during the course of my research tenure.*

*I sincerely acknowledge the whole hearted help, valuable discussions, guidelines, and suggestions by **Prof. C. D. Lokhande**, Research Director and Dean, Centre for Interdisciplinary Research (CIR). He provided a very fruitful discussion and helpful guidance for time management regarding my Ph.D. progress.*

*I would like to express my sincere thanks to Vice-Chancellor **Prof. R. K. Mudgal**, Registrar **Dr. V. V. Bhosale** for the inspiration and support. I also thank **Dr. Satish Jadhav**, **Dr. Dhanaji Malavekar** and **Dr. Vinayak Parale** for providing me very important sample characterization data, during the entire research work.*

*I would like to thank my colleagues at the Centre for Interdisciplinary Research, **Vikas Magdum**, **Yogesh Chitare**, **Shraddha Bhosale**, **Sambhaji Kumbhar**, **Sambhaji Khot**, **Ranjit Nikam**, **Satish Phalake**, and **Manohar Lad** for their support, Scientific discussions and valuable suggestions during research work.*

*I am also thankful **Mr. Ramdas** and **Mrs. Namarata** and non-teaching staff of the CIR Department for their kind co-operation during my research work.*

*In addition, I acknowledge the funding support from **Chhatrapati Shahu Maharaj Research Training and Human Development Institute (SARTHI)**, Pune of the **Government of Maharashtra State** for **Chhatrapati Shahu Maharaj National***

Research Fellowship (CSMNRF) sanctioned to me. And I also thankful to D. Y. Patil Education Society, Kolhapur-416006 (India), for financial support through research project sanction No. **DYPES/DU/R&D/2021/276**.

*I hereby express my deepest appreciation and regards to my beloved parents **Aai and Baba**, brother **Shreyas**, all of family members who in spite of their hard times and sufferings, continuously supported and encouraged me throughout my academic journey. Their belief in me has been my greatest strength and inspiration. I would like to confess that even though I try my best, it is not possible for me to acknowledge and thank all those known and unknown faces individually for their direct and indirect contribution for the successful completion of this work. I am grateful to all of you for your kind cooperation.*

-Ketaki Kadam

SUMMARY OF RESEARCH WORK

A) Papers Published / Submitted at International Journals: (03)

- 1) **Kadam KV**, Phalake SS, Lad MS, Parale VG, Gunjekar JL, Khot VM. Low temperature glycine nitrate combustion synthesis of nanostructured zinc ferrites for enhanced visible light-driven methylene blue degradation. Emergent Materials. 2024 Mar 18:1-3. (I.F. – 4.01).
- 2) Phalake SS, Lad MS, **Kadam KV**, Tofail SA, Thorat ND, Khot VM. Application of $Mn_xFe_{1-x}Fe_2O_4$ ($x= 0-1$) nanoparticles in magnetic fluid hyperthermia: correlation with cation distribution and magnetocrystalline properties. ACS omega. 2022 Nov 22;7(48):44187-98. (I.F-4.1).
- 3) **Kadam KV**, Malavekar DB, Jadhav SB, Magdum VV, Chitare YM, Gunjekar JL, Kim JH, Khot VM, Recyclable Manganese Substituted Zinc Ferrite Nanoparticles for Efficient Photocatalytic Degradation of Organic Dyes, Journal of material science (Revision Submitted)

B) Published (Indian) Patents: (01)

- 1) Dr. V. M. Khot, **Ms. K. V. Kadam**, Dr. A. B. Salunkhe, Radiosensitizer based on iron oxide nanoparticles, (2023), Application No.- 202321038527.

C) Papers / Poster Presented at National/International Conferences:(03)

- 1) **Ms. K. V. Kadam**, Photocatalytic Studies of Combustion Method Synthesized $ZnFe_2O_4$ Nanoparticles, in International Conference on “Nanotechnology Addressing the Convergence of Materials Science, Biotechnology and Medical Science (IC-NACMBM-2024)” dated 12th to 14th February 2024, D. Y. Patil Education Society (Deemed to be University, Kolhapur.
- 2) **Ms. K. V. Kadam**, Zinc Ferrite Nanostructures for Photocatalytic MB dye degradation, in National Conference on “Physics of Materials and Materials based Fabrication” dated 25th and 26th November, 2023, Shivaji University, Kolhapur.
- 3) **Ms. K. V. Kadam**, Induction Heating Studies Combustion Synthesized $ZnFe_2O_4$ Nanoparticles for Hyperthermia Application, in International Conference on “Emerging Trends in Material Science” dated 9th and 10th November, 2022, D. P. Bhosale College, Koregaon, Satara. (First prize)

D) Attended National / International Conferences / Seminar: (07)

- 1) Attended a guest lecture of Dr. Savita D. Mali on the subject of Use of Biofertilizer for Sustainable Environment held on 22nd August 2024 in Centre for Interdisciplinary Research D. Y. Patil Education Society, Deemed to be University, Kolhapur.
- 2) Attended a guest lecture of Dr. Rupesh S. Devan, Associate Professor, IIT, Indore on “X-ray Photoelectron Spectroscopy (XPS) for Chemical Analysis of Nanomaterials” held on 6th June 2023 in Centre for Interdisciplinary Research D. Y. Patil Education Society, Deemed to be University, Kolhapur.

- 3) Attended a guest lecture of Dr. Akshay Joshi on “Necessity and Easiness of English Language” held on 19th May 2023 in Centre for Interdisciplinary Research D. Y. Patil Education Society, Deemed to be University, Kolhapur.
- 4) One day International Conference on “Recent Trends in Fabrication of Nanomaterials and Their Applications (ICRTFNA-2023)” held on 15th Mar 2023 in Rajarshri Chhatrapati Shahu College, Kolhapur.
- 5) Attended a guest lecture of Prof. J. H. Kim on the subject of Materials for Hydrogen Production held on 17th Jan 2023 D. Y. Patil Education Society, Deemed to be University, Kolhapur.
- 6) Attended a guest lecture of Dr. B. R. Sankapal on the subject of Development of colourful dye sensitized, Q-dot sensitized and nanowire based solar cells held on 7th Jan 2022 in Centre for Interdisciplinary Research D. Y. Patil Education Society, Deemed to be University, Kolhapur.
- 7) Participated International seminar series on Nanotechnology on Environment and Sustainability, organized by D. Y. Patil Education Society, deemed to be University, Kolhapur held on 12 & 13 Jan. 2021.

E) Workshops Attended:(05)

- 1) Selected for Hands-on Training Program on Advanced Research Characterization Techniques (17-23 Dec., 2022) organized by Banasthali Vidyapith, Rajasthan under the scheme Synergistic Training program Utilizing the scientific and Technological Infrastructure (STUTI).
- 2) Attended workshop on Concepts of Radiation in Medical Physics, Organized by Medical Physics, Centre for Interdisciplinary Research, D. Y. Patil Education Society, (Deemed to be University), Kolhapur, held on 28th Jan 2022.
- 3) Completed course work in Introduction to the basics of Medical coding and application Phase-I organized by Biocyte Lab (Institution of Research and Development).
- 4) Participated in the Workshop & Hands-On Training on XRD Organized by SAIF-CFC, Shivaji University, Kolhapur held during 11-12 Nov 2021 under the STRIDE (Scheme for Trans-disciplinary Research for India’s Developing Economy) programme.
- 5) Volunteer in the three “IN-YAS Science Camp-2021, 2022 & 2024” organised by CIR, D. Y. Patil Education Society, (Deemed to be University), Kolhapur, Indian National Young Academy of Science (IN-YAS), Indian National Science Academy (INSA), held at the Halkarni, Tal. Gadhinglaj during 18th Dec. 2021, D. Y. Patil Knowledge Campus Salokhenagar, during 16th & 17th Dec, 2022, and CIR, D. Y. Patil Education Society, (Deemed to be University), Kolhapur during 4th & 5th October 2024.

Index

Chapter I: Introduction and literature review		
Sr. No.	Details	Page No.
1.1	Introduction	1
1.2	Need of wastewater treatment	1-2
1.3	Different techniques for wastewater purification	2-6
1.4	Types of photocatalysis	7-8
1.5	Ferrite nanoparticles	8-11
1.6	Nanoparticles for photocatalysis	11-13
1.7	Statement of problem	14
1.8	Challenges for catalysis and scope of thesis	14-16
1.9	Aim and Objectives of research	16
1.10	References	17-22

Chapter II: Experimental and Characterization Techniques			
2.1	Introduction		25-28
2.2	Combustion Synthesis		28-30
2.3	Experimental Process		31-32
2.4	Characterization techniques		
	2.4.1	Field emission -scanning electron microscopy (FE-SEM)	32-34
	2.4.2	Energy dispersive X-ray spectroscopy (EDS)	34-36
	2.4.3	X-ray diffraction (XRD)	36-38
	2.4.4	Transmission electron microscopy (TEM)	39-40
	2.4.5	X-ray photoelectron spectroscopy (XPS)	40-41
	2.4.6	Brunauer-Emmett-Teller (BET)	41-43
	2.4.7	UV-visible Spectroscopy	44-45
	2.4.8	Fourier transforms infrared Spectroscopy	45-46
2.5	References		47-49

Chapter III: Synthesis and characterization of zinc ferrite nanoparticles		
3.1	Introduction	51-53
3.2	Experimental process	
	3.2.1	Preparation of ZNPs
	3.2.2	Thermodynamic Analysis:
3.3	Results and discussion:	
	3.3.1	X-ray diffraction analysis
	3.3.2	FTIR analysis
	3.3.3	SEM analysis
	3.3.4	TEM analysis
	3.3.5	XPS analysis
	3.3.6	BET analysis
	3.3.7	UV-DRS analysis
3.4	Conclusions	69
3.5	References	70-72

Chapter IV: Synthesis and characterization of manganese substituted zinc ferrite nanoparticles		
4.1	Introduction	75-76
4.2	Experimental process of MZNPs	76
4.3	Results and discussion	
	4.3.1	XRD analysis
	4.3.2	FT-IR analysis
	4.3.3	Raman analysis
	4.3.4	SEM analysis
	4.3.5	Elemental composition analysis
	4.3.6	XPS analysis
	4.3.7	BET analysis
	4.3.8	UV-DRS analysis
4.4	Conclusions	88
4.5	References	89-92

Chapter V: Photocatalytic degradation of MB, RhB, and ChT dyes by zinc ferrite nanoparticles		
5.1	Introduction	95-96
5.2	Photocatalytic dye degradation study Experimental Setup	96-98
5.3	Photocatalytic degradation of MB, RhB, and ChT dyes	98-103
	5.3.1 Catalyst dosage for MB RhB and ChT dyes	104-108
	5.3.2 Scavenger studies of MB, RhB, ChT dyes	108-111
	5.3.3 Investigation of the reusability and chemical stability	111-114
5.4	Plausible dye degradation mechanism	115-116
5.5	Conclusions	116
5.6	References	117-118

Chapter VI: Photocatalytic degradation of MB, RhB, and ChT dyes by manganese substituted zinc ferrite nanoparticles		
6.1	Introduction	121-122
6.2	Photocatalytic dye degradation study Experimental Setup	123
6.3	Photocatalytic degradation of MB, RhB, and ChT dyes	124-131
	6.3.1 Catalyst dosage for MB RhB and ChT dyes	131-135
	6.3.2 Scavenger studies of MB, RhB, ChT dyes	135-136
	6.3.3 Investigation of the reusability and chemical stability	136-138
6.4	Plausible dye degradation mechanism	138-139
6.5	Conclusions	139
6.6	References	140-141

Chapter VII: Summary and conclusions	143-149
Chapter VIII: 80- Recommendations	151-153

List of Figures

Chapter 1	Introduction and literature review	
Figure 1.1	Conventional methods for waste water treatment.	03
Figure 1.2	Schematic reactions occurring via photocatalysis to produce $\cdot\text{OH}$ to react with contaminants.	06
Figure 1.3	Schematic representation of recycling magnetic NPs	10
Figure 1.4	Spinel structure of ferrites	12
Figure 1.5	Advantages of ferrites for water and wastewater treatment	13
Chapter 2	Experimental and characterization techniques	
Figure 2.1	Synthesis of ZnFe_2O_4 nanoparticles using the proposed combustion method	32
Figure 2.2	Block diagram of SEM instrument	34
Figure 2.3	The ray diagram of emission X-ray spectrum in EDS	35
Figure 2.4	Schematic of X-ray diffractometer	37
Figure 2.5	The block diagram of TEM	39
Figure 2.6	XPS instrument analysis	41
Figure 2.7	Schematic diagram of BET isotherm	43
Figure 2.8	Schematic representation of UV-visible spectrophotometer	45
Figure 2.9	Schematic representation of the working principle of FTIR	46
Chapter 3	Synthesis and characterization of zinc ferrite nanoparticles.	
Figure 3.1	(a) XRD patterns of samples using different G/N ratio: 0.48 (Z1), 0.74 (Z2), 1.48 (Z3), 2.22 (Z4) and 2.96 (Z5). (b) Enlarged version of (311) peak in XRD pattern	56
Figure 3.2	FT-IR spectra of Z1, Z2, Z3, Z4 and Z5 samples at different G/N ratios: 0.48, 0.74, 1.48, 2.22 and 2.96 respectively	57
Figure 3.3	SEM images of different G/N ratios, (a) 0.48 (Z1), (b) 1.48 (Z3) and (c) 2.96 (Z5)	59
Figure 3.4	(a) TEM images, and (b) SAED pattern, and (c) Histogram for optimized Z1 sample (0.48)	60
Figure 3.5	Survey spectra of Z1, Z2, Z3, Z4, and Z5	62
Figure 3.6	XPS spectra of stoichiometric sample Z1: (a) survey spectrum of Z1 sample ZnFe_2O_4 (0.48), (b) high-energy resolution Zn 2p core-level spectrum, (c) high-energy resolution Fe 2p core-level spectrum, (d) high-energy resolution O 1s core-level spectrum, (e) high-energy resolution C 1s core-level spectrum.	63
Figure 3.7	XPS spectra of stoichiometric sample Z2: (a) survey spectrum of Z2 sample ZnFe_2O_4 (0.74), (b) high-energy resolution Zn 2p core-level spectrum, (c) high-energy resolution Fe 2p core-level spectrum, (d) high-energy resolution O 1s core-level spectrum, (e) high-energy resolution C 1s core-level spectrum	64
Figure 3.8	XPS spectra of stoichiometric sample Z3: (a) survey spectra of Z3 sample ZnFe_2O_4 (1.48), (b) high-energy resolution Zn 2p core-level spectrum, (c) high-energy resolution Fe 2p core-level spectrum, (d) high-energy resolution O 1s core-level spectrum, (e) high-energy resolution C 1s core-level spectrum	65
Figure 3.9	XPS spectra of stoichiometric sample Z4: (a) survey spectrum of Z4 sample ZnFe_2O_4 (2.22), (b) high-energy resolution Zn 2p core-level spectrum, (c) high-energy resolution Fe 2p core-level spectrum, (d) high-energy resolution O 1s core-level spectrum, (e) high-energy resolution C 1s core-level spectrum	65
Figure 3.10	XPS spectra of stoichiometric sample Z5: (a) survey spectrum of Z5 sample	66

	ZnFe ₂ O ₄ (2.96), (b) high-energy resolution Zn 2p core-level spectrum, (c) high-energy resolution Fe 2p core-level spectrum, (d) high-energy resolution O 1s core-level spectrum, (e) high-energy resolution C 1s core-level spectrum	
Figure 3.11	BET adsorption-desorption isotherm graph of different G/N ratios, (a) Z1, (b) Z2, (c) Z3, (d) Z4, and (e) Z5	67
Figure 3.12	UV-vis spectra of different G/N ratios, (a) Z1, (b) Z2, (c) Z3, (d) Z4, and (e) Z5	68
Chapter 4	Synthesis and characterization of manganese substituted zinc ferrite nanoparticles.	
Figure 4.1	(a) XRD patterns (b) enlarged version of (311) peak in XRD patterns, (c) FT-IR spectra, and (d) Raman spectra of Z1, MZ1, MZ2, MZ3, MZ4, and M1	77
Figure 4.2	SEM images of (a) Z1, (b) MZ1, (c) MZ2, (d) MZ3, (e) MZ4, and (f) M1. And (g, h) TEM image, (i) SAED pattern for MZ4 sample	80
Figure 4.3	EDS images of the (a) MZ1 (b) MZ2 (c) MZ3 (d) MZ4 (e) M1	81
Figure 4.4	XPS spectra of MZ4: (a) survey spectrum of MZ4, high resolution core spectrum of (b) Zn 2p, (c) Mn 2p, (d) Fe 2p, and (e) O 1s	84
Figure 4.5	XPS spectra of M1: (a) Mn 2p, (b) Fe 2p, and (c) O 1s	85
Figure 4.6	BET adsorption-desorption isotherm graph of different Mn substitution (a) MZ1, (b) MZ2, (c) MZ3, (d) MZ4, and (e) M1	87
Figure 4.7	UV-DRS spectrum of different Mn substitution (a) MZ1, (b) MZ2, (c) MZ3, (d) MZ4, and (e) M1.	88
Chapter 5	Photocatalytic degradation of MB, RhB, and ChT dyes by zinc ferrite nanoparticles.	
Figure 5.1	Assembly of photocatalytic dye degradation experiment	97
Figure 5.2	(a) Control experiment (without light) for MB (black) and RhB (blue) dyes and ChT (red). (b) Control experiment (without catalyst) for MB (black) and RhB (red) dyes and ChT (blue).	98
Figure 5.3	Photocatalytic dye degradation of MB by using different G/N ratios, (a) Z1, (b) Z2, (c) Z3, (d) Z4, and (e) Z5	100
Figure 5.4	Photocatalytic dye degradation of RhB by using different G/N ratios, (a) Z1, (b) Z2, (c) Z3, (d) Z4, and (e) Z5	102
Figure 5.5	Photocatalytic dye degradation of ChT by using different G/N ratios, (a) Z1, (b) Z2, (c) Z3, (d) Z4, and (e) Z5	103
Figure 5.6	Photocatalytic dye degradation of MB by using G/N=0.48 (Z1) Effect of catalyst loading (a) 15 mg (b) 30 mg (c) 45 mg (d) 60 mg	105
Figure 5.7	Photocatalytic dye degradation of RhB by using G/N=0.48 (Z1) Effect of catalyst loading (a) 15 mg (b) 30 mg (c) 45 mg (d) 60 mg	106
Figure 5.8	Photocatalytic dye degradation of ChT by using G/N=0.48 (Z1) Effect of catalyst loading (a) 15 mg (b) 30 mg (c) 45 mg (d) 60 mg	107
Figure 5.9	Pseudo first-order kinetics for (a) MB, (b) RhB, (c) ChT dyes of Z1	108
Figure 5.10	Scavenger study of Z1 photocatalyst for MB dye	109
Figure 5.11	Scavenger study of Z1 photocatalyst for RhB dye	110
Figure 5.12	Scavenger study of Z1 photocatalyst for ChT dye	111
Figure 5.13	Recyclability study of Z1 photocatalyst for MB dye	112
Figure 5.14	Recyclability study of Z1 photocatalyst for RhB dye	113
Figure 5.15	Recyclability study of Z1 photocatalyst for ChT dye	114
Figure 5.16	Stability study of Z1 before and after irradiation using an XRD	114

Chapter 6	Photocatalytic degradation of MB, RhB, and ChT dyes by manganese substituted zinc ferrite nanoparticles	
Figure 6.1	(a) Control experiment (without light) for MB (black) and RhB (red) dyes and ChT (Blue). (b) Control experiment (without catalyst) for MB (black) and RhB (red) dyes and ChT (green)	123
Figure 6.2	Photocatalytic dye degradation of RhB using (a) Z1, (b) MZ1, (c) MZ2, (d) MZ3, (e) MZ4, and (f) M1	125
Figure 6.3	Photocatalytic dye degradation of MB using (a) Z1, (b) MZ1, (c) MZ2, (d) MZ3, (e) MZ4, and (f) M1	126
Figure 6.4	Photocatalytic dye degradation of ChT using (a) Z1, (b) MZ1, (c) MZ2, (d) MZ3, (e) MZ4, and (f) M1	127
Figure 6.5	Pseudo first-order kinetics for (a) MB, (b) RhB, (c) ChT dyes of MZ4	130
Figure 6.6	Photocatalytic dye degradation of RhB using MZ4 catalyst loading (a) 15 mg, (b) 30 mg, (c) 45 mg, and (d) 60 mg, respectively	132
Figure 6.7	Photocatalytic dye degradation of MB by using MZ4 Effect of catalyst loading (a) 15 mg, (b) 30 mg, (c) 45 mg, and (d) 60 mg, respectively	133
Figure 6.8	Photocatalytic dye degradation of ChT by using MZ4 Effect of catalyst loading (a) 15 mg, (b) 30 mg, (c) 45 mg, and (d) 60 mg, respectively	134
Figure 6.9	Scavenger study of MZ4 photocatalyst for MB, RhB and ChT dyes	135
Figure 6.10	Recyclability study of MZ4 photocatalyst	137
Figure 6.11	Stability study of MZ4 before and after irradiation using an XRD	138

List of Tables and Charts

Table 3.1	Adiabatic flame temperature measurement needs thermodynamic information	54
Table 3.2	Variations in the quantity of heat absorbed by the product (Q), the adiabatic flame temperature (T_{ad}), and the number of moles of gases generated during combustion at various G/N ratios	55
Table 3.3	The effect of G/N ratio on $ZnFe_2O_4$ crystallite size (D), lattice parameter (a) Lattice Strain	56
Table 3.4	The broad range peaks property of zinc ferrite (Z1 to Z5) nanoparticles determined from XPS data	61
Table 3.5	The effect of G/N ratio on crystal size and band gap	68
Table 4.1	Structural parameters obtained from XRD pattern analysis of all the samples	79
Table 4.2	The element atomic percentage by energy dispersive X-ray (EDS) analysis	82
Table 5.1	Comparison with the reported literature	101
Table 5.2	Kinetic parameters of Z1 for MB, RhB, and ChT dyes	108
Table 6.1	Degradation percentages of all the samples for MB, RhB, and ChT dyes	129
Table 6.2	Kinetic parameters of MZ4 for MB, RhB, and ChT dyes	131
Table 7.1	Photocatalytic Degradation of MB, RhB, ChT dyes using Various G/N Ratios for Different Pollutants	149
Table 7.2	Photocatalytic Degradation of MB, RhB, ChT dyes using Manganese Substituted Zinc Ferrite	149

List of Abbreviations

AOPs - Advanced oxidation processes

BET - Brunauer–Emmett–Teller

BJH - Barrett-Joyner-Halenda

CB - Conduction band

ChT - Chloramine T

CO₂ - Carbon dioxide

EDS - Energy-Dispersive X-Ray Spectroscopy

FE-SEM - Field Emission Scanning Electron Microscopy

FTIR - Fourier Transform Infrared Spectroscopy

F/O - Fuel-to-oxidizer ratio

HOMO - Highest occupied molecular orbital

HR-TEM - High-Resolution Transmission Electron Microscopy

LUMO - Lowest unoccupied molecular orbital

MB - Methylene blue

MNPs - Magnetic nanosized photocatalysts

MZF - Manganese-Zinc Ferrite

NPs - Nanoparticles

RhB - Rhodamine B

SAED - Selected Area Electron Diffraction

SCS - Solution combustion synthesis

TiO₂ - Titanium dioxide

UV-DRS - UV-vis diffuse reflectance spectroscopy

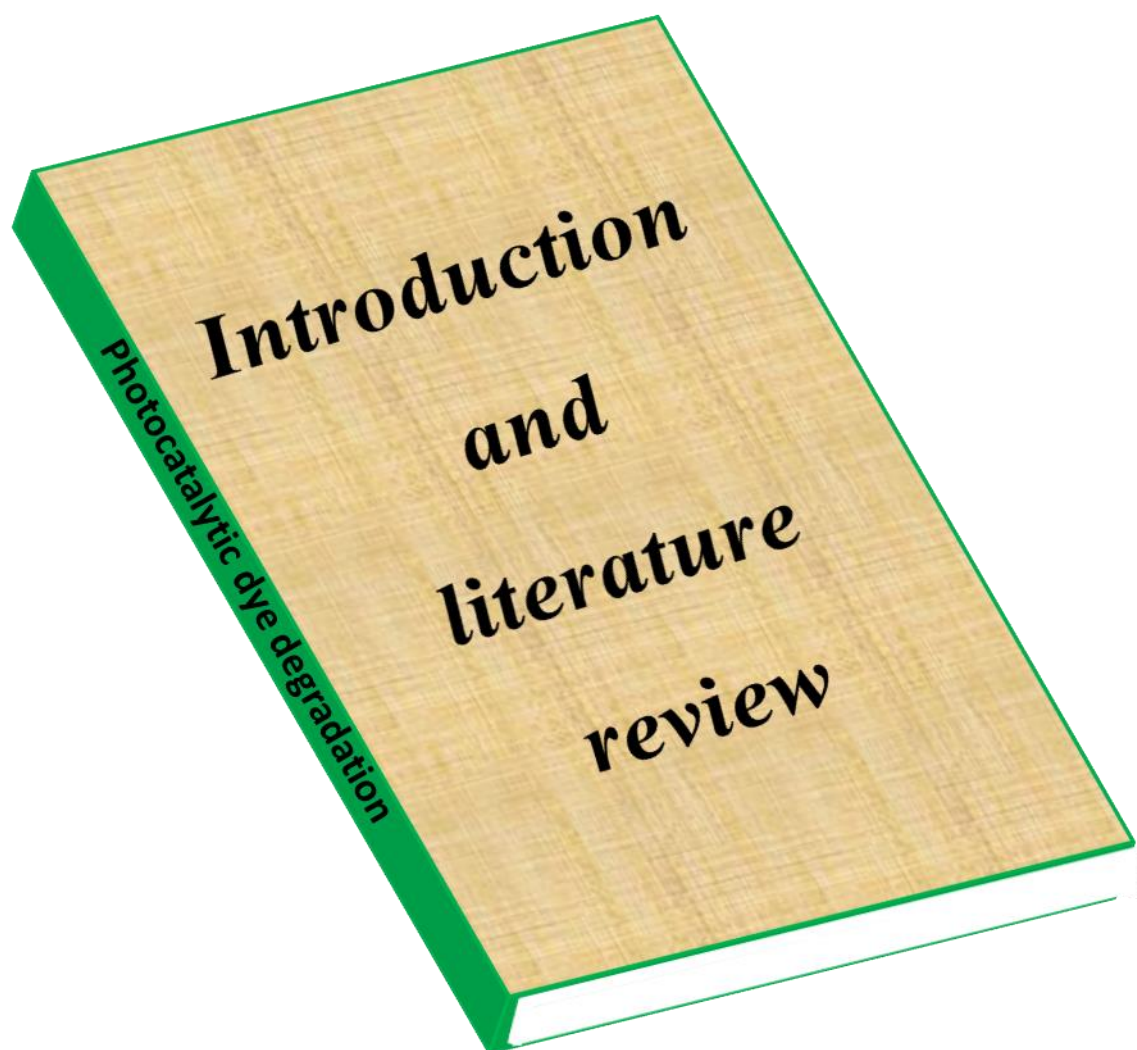
UV-VIS - UV-visible Spectroscopy

VB - Valence band

XPS - X-ray Photoelectron Spectroscopy

XRD - X-ray Diffraction

CHAPTER I



1.1. Introduction:

Water plays a crucial role in the environment and exists in three forms: solid, liquid, and gas, under conditions of relatively low temperature and pressure. The Earth holds approximately 1.39 billion cubic kilometers of water, with about 96.5% residing in the global oceans and 4% found in rivers, lakes, streams, and groundwater [1]. The growing human population, along with industrialization and the presence of living organisms, has led to the contamination of groundwater resources, creating an urgent demand for clean water worldwide. As a result, water can no longer be considered an unlimited resource for scientific advancement. The industrial revolution brought both benefits and drawbacks for humans and the environment. Numerous water-related issues have arisen, particularly the contamination of rivers, wells, ponds, and lakes, which are vital sources of fresh water. The growing demand for fresh water, driven by suburbanization and overpopulation, has led to a decline in groundwater levels [2]. Water contamination is a significant issue caused by the discharge of wastewater from urban and industrial sectors, which contains a variety of harmful chemicals, including pharmaceutical compounds, dyes, and metal ions. These pollutants in drinking water can lead to numerous health problems in humans and pose a threat to the environment [3]. To address these challenges and improve water quality, various effective treatment methods have been developed and implemented.

1.2. Need of wastewater treatment:

The continuous discharge of dyes and other pollutants has increasingly harmed aquatic ecosystems over time. These contaminants pose additional risks due to their toxic effects on the environment and their resistance to biodegradation. They can disrupt the endocrine system, leading to various harmful effects, including both chronic and acute toxicity, as well as the development of antibiotic-resistant genes [4-5].

Currently, water purification methods have gained significant global attention due to the growing concerns over environmental pollution and industrial progress. Industrial activities generate a variety of pollutants, including dyes and heavy metals, which contaminate both surface water and groundwater, thereby damaging the

environment. As a result, a wide range of water treatment techniques, such as ion exchange, coagulation, membrane filtration, flocculation, adsorption, and other chemical processes, have been employed to treat wastewater [6-7].

1.3 Different techniques for wastewater purification:

Conventional wastewater treatment methods primarily consist of three main types: physical separation, chemical decomposition, and biodegradation (**Fig. 1.1**). Physical separation is a straightforward technique used to remove insoluble suspended contaminants. However, it has the drawback of being less efficient, with a slower purification rate, making it challenging to achieve large-scale emission reductions. Physical purification methods include sedimentation, filtration (both membrane and depth filtration), and adsorption. While all these methods are applicable for treating textile wastewater, sedimentation is particularly effective in purifying contaminated water. Membrane filtration is a highly efficient and cost-effective approach, but it faces challenges such as membrane fouling caused by foreign molecules present in the water [5-8].

The removal or reduction of pollutants from polluted environments and contaminated water is of critical importance. Typically, physical, chemical, and biodegradation methods are effective for eliminating organic contaminants from wastewater [9-10]. These methods can be quite costly when used for large-scale water purification. Given the lack of affordable purification options, there is a strong need to develop efficient, cost-effective, and environmentally friendly water treatment techniques that ensure both human health and environmental safety.

Several Advanced Oxidation Processes (AOPs), including O_3 -UV (ozone-ultraviolet), O_3 - H_2O_2 (ozone-hydrogen peroxide), Fenton, UV- TiO_2 (ultraviolet-titanium dioxide), and UV- H_2O_2 (ultraviolet-hydrogen peroxide), are used for wastewater treatment. Among these, UV- TiO_2 has demonstrated the highest efficiency due to the photocatalytic activity of TiO_2 , which generates hydroxyl ($\cdot OH$) radicals. These radicals play a crucial role in various experimental processes. Typically, the process occurs under standard conditions, utilizing atmospheric oxygen as an oxidant

to mineralize organic compounds into carbon dioxide (CO_2). In recent years, the photocatalytic properties of TiO_2 have attracted significant interest [11-12].

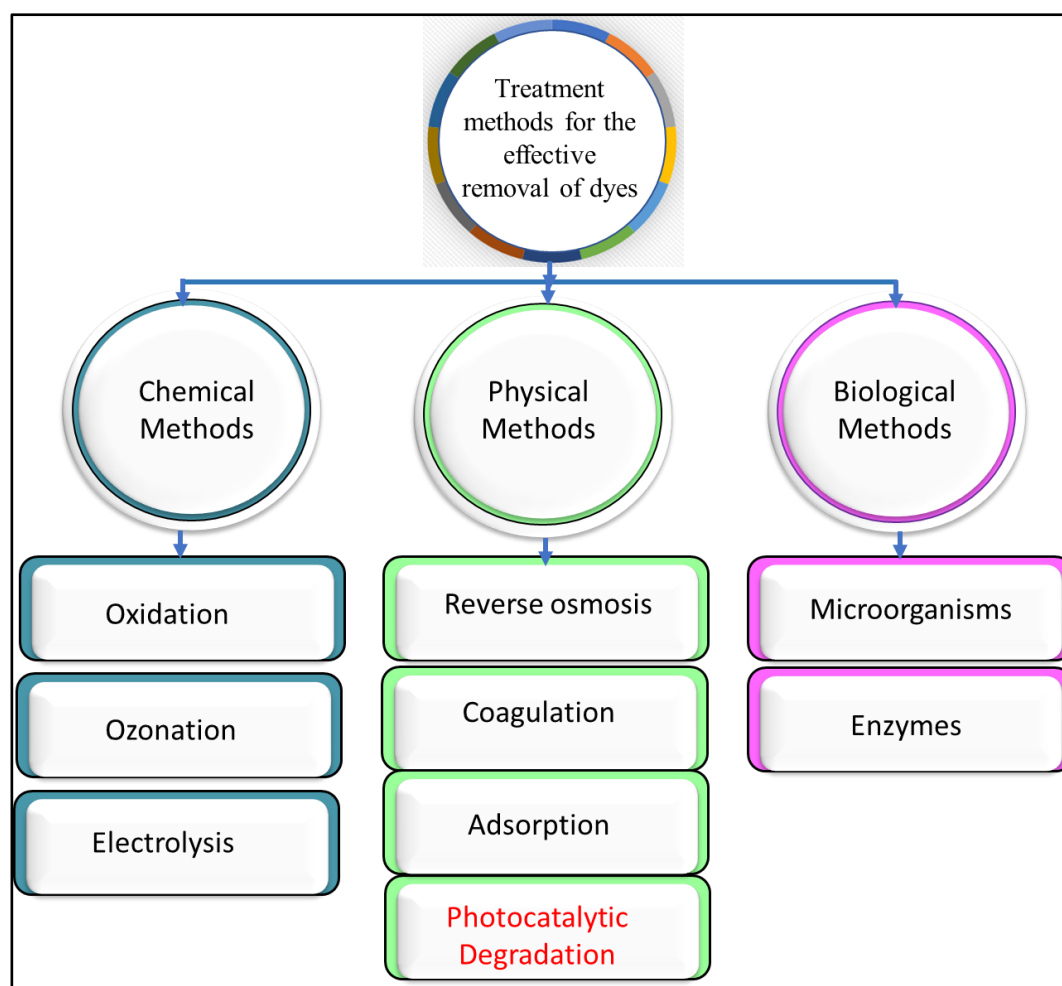


Fig. 1.1: Conventional methods for waste water treatment.

1.3.1 AOPs: a promising photocatalysis technique:

Advantageous AOPs are commonly employed in the degradation of organic pollutants due to their high efficiency, simplicity, good reproducibility, and ease of use [11]. Photocatalysis is an efficient and cost-effective method for decomposing organic pollutants, capable of mineralizing them into completely harmless products using only atmospheric oxygen. This approach is nontoxic, energy-efficient, and environmentally friendly, making it an ideal solution for removing hazardous pollutants [12].

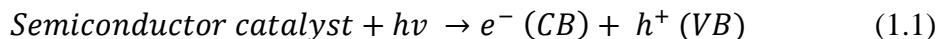
AOPs are environmentally friendly, benefiting both biological and chemical processes as they avoid the production of large quantities of toxic chemicals and prevent the transfer of contaminants from one phase to another, unlike some chemical methods. Nearly all organic pollutants can be converted into non-toxic substances by AOPs, which generate reactive $\bullet\text{OH}$ radicals with a redox potential of 2.8 eV. These initially formed $\bullet\text{OH}$ radicals react with organic contaminants, leading to mineralized products such as CO_2 and water (H_2O) through a series of oxidation reactions [13]. These characteristics of AOPs have spurred extensive research into their applications for water purification systems. While AOPs play an important role in photocatalytic processes, certain types of water pollutants remain challenging to treat with currently available AOP methods [14].

AOPs offer numerous potential methods for treating polluted water, increasing their utility and enabling more tailored treatment approaches. Photocatalysis and AOPs provide significant advantages, as they are highly efficient, straightforward, easy to handle, reproducible, and widely used for wastewater remediation [15]. The photocatalytic method has proven to be an effective and economically favorable approach for decomposing contaminants, with the ability to mineralize organic pollutants into safe, non-toxic compounds under natural conditions. As a result, it is an eco-friendly, energy-saving, and safe method for treating highly toxic contaminants [16].

Photocatalysts are central to the photocatalysis process, with semiconductor photocatalysts being the most commonly used. Among these, the TiO_2 photocatalyst demonstrates outstanding activity and has attracted significant interest due to its crucial role under UV irradiation. However, semiconductor photocatalysts also have certain limitations: (1) their technical efficiency and versatility are restricted by low visible light absorption, (2) quantum yield is reduced due to the rapid recombination of holes (h^+) and electrons (e^-), and (3) the decomposition rate of organic contaminants is hindered by the low surface coverage of the photocatalysts [17-18].

1.3.2: Basics of photocatalysis mechanism:

Photocatalytic degradation consists of multiple stages, including the generation of e^-/h^+ pairs, adsorption-desorption processes, chemical reactions, and e^-/h^+ pair recombination. When the semiconducting photocatalyst is exposed to photons with energy equal to or greater than its band gap, valence electrons are excited to the conduction band (CB), leaving holes in the valence band (VB):



Here, $h\nu$ represents the energy required to move electrons from the valence band (VB) to the conduction band (CB). The electrons generated through irradiation can be readily captured by dissolved O_2 or O_2 adsorbed on the catalyst surface, leading to the formation of $O_2^{\bullet -}$ species;



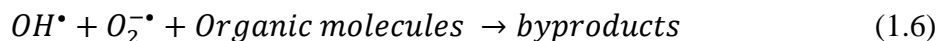
As a result, $O_2^{\bullet -}$ have reacted with H_2O molecules to generate hydroperoxyl radicals (HOO^{\bullet}) and OH^{\bullet} species, these are strong oxidizing agents which are involved in the decomposition of the organic molecule.



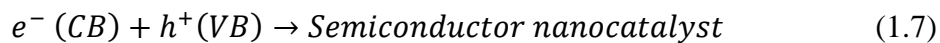
Meanwhile, in the VB the photogenerated h^+ are trapped by hydroxyl groups on the surface of the catalyst to generate high per active species such as OH^{\bullet} species:



At the end, the organic molecules get oxidized by strong oxidizing agents, and the $O_2^{\bullet -}$, HOO^{\bullet} , OH^{\bullet} and h^+ species to produce byproducts such as; CO_2 , H_2O , etc.



In the interim, the recombination of photoinduced h^+ and e^- could take place which reduce the photocatalytic activity of photocatalyst:



as described in **Fig. 1.2**.

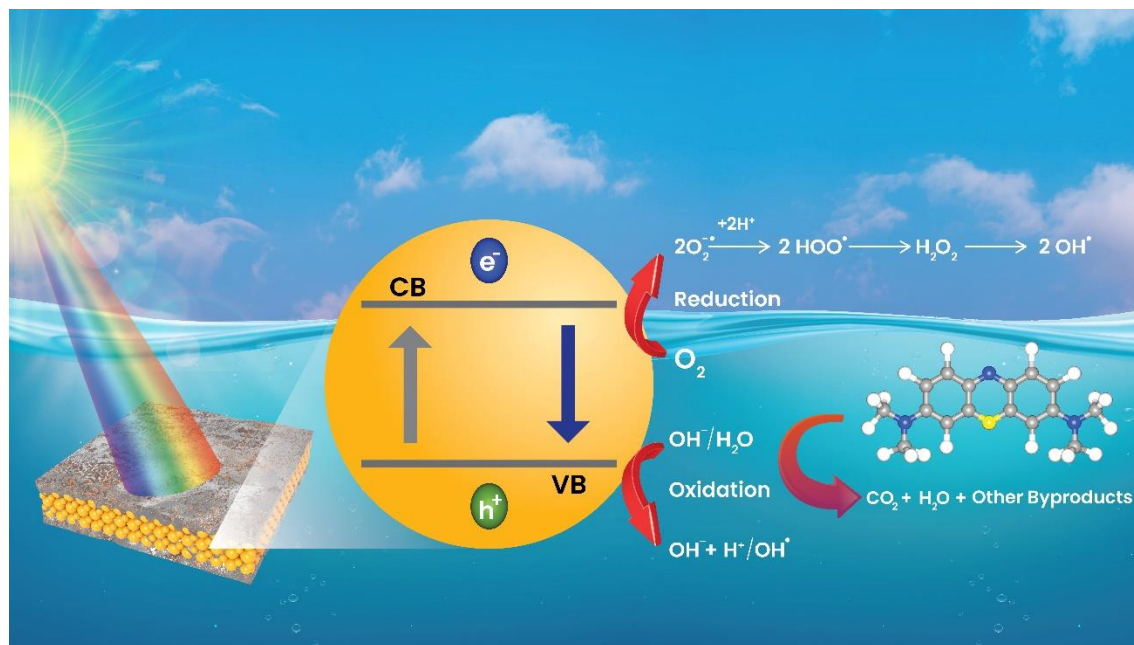


Fig. 1.2: Schematic reactions occurring via photocatalysis to produce $\cdot\text{OH}$ to react with contaminants.

The photocatalytic method has become one of the most promising and valuable technologies; however, it currently lacks widespread application, limiting its impact on advancing sustainable green chemistry. Studies on photocatalysis demonstrate its effectiveness in dye decomposition, generating oxygen and hydrogen from water splitting, and reducing pollutants [19-21].

Zinc oxide (ZnO) and TiO_2 are among the most widely used semiconductor photocatalysts for decomposing organic pollutants. However, these photocatalysts face limitations due to their high band gap energies, approximately 3.2 eV for both ZnO and anatase TiO_2 , and slightly lower for rutile TiO_2 . As a result, only photons from the near-UV region can excite electrons in these semiconductors [22-23].

1.4. Types of photocatalysis:

Recently, semiconductors have been advanced and their applications have gained significant attention in research and industry, particularly in the medical, chemical, and environmental sectors. Nanotechnology has enabled these semiconductors to demonstrate promising effectiveness in removing toxic pollutants from water. Their efficient role in water treatment has been widely reported [24-27].

Iron serves as a potent reducing agent, contributing to the breakdown of various organic and inorganic contaminants in polluted water, particularly chlorinated solvents, and transforming them into less harmful substances [28-29]. Numerous studies have highlighted the role of highly reactive nano-sized zero-valent iron in the breakdown of specific pollutants, such as pesticides and polycyclic aromatic hydrocarbons, present in contaminated water.

Nano-sized zero-valent iron and iron oxides (Fe_3O_4 and Fe_2O_3) are among the most commonly used magnetic semiconductors. Their ability to retain unique physicochemical properties, due to the variation in iron's oxidation states, enables them to effectively remove contaminants from polluted water [30]. The most extensively studied iron oxide is Fe_3O_4 (magnetite), a ferromagnetic black-colored compound that contains both Fe(III) and Fe(II) oxidation states. The presence of Fe^{2+} allows magnetite to donate electrons, enhancing its reactivity. Crystals exhibiting paramagnetism have randomly oriented magnetic moments, resulting in a small but positive net magnetization. When exposed to an external magnetic field, the paramagnetic material aligns with the field, producing a slight net crystal magnetization. In contrast, antiferromagnetic and ferromagnetic materials have randomly arranged individual moments even in the presence of an external magnetic field. The majority of applications for magnetic nanomaterials depend on external magnetic fields, utilizing the field gradient and the magnetic moment of the particles [31-32].

However, bare magnetic semiconductors have limitations in practical applications. The van der Waals forces, high surface energy, and dipole-dipole

interactions between magnetic particles often lead to aggregation of the uncoated magnetic semiconductor. This aggregation is driven by the hydrophobic nature of certain magnetic semiconductor surfaces and the reduction in Gibbs free energy. Additionally, the presence of an external magnetic field can further promote aggregation. Furthermore, uncoated magnetic semiconductors are more susceptible to acid/base corrosion, oxidation, and the release of metal ions [32].

1.5. Ferrite nanoparticles:

Magnetic nanosized photocatalysts (MNPs) have garnered significant attention due to their unique properties, especially when compared to their bulk counterparts. Among the most widely studied MNPs, spinel ferrites have been extensively evaluated for their remarkable characteristics, including chemical, optical, magnetic, and electrical properties [34-36].

Many semiconducting materials face intrinsic limitations due to their optical band gap being greater than 3.5 eV, which makes them active only under UV light. The sun emits only about 4% of its light as UV radiation, while it provides 45% as visible light. Therefore, catalysts with a lower band gap are more suitable for utilizing a broader spectrum of sunlight [38]. Improving the efficiency of catalysts under visible light for environmental pollution control has become a key area of focus in photocatalysis. Although there has been progress in achieving moderately effective photocatalytic reactions, challenges related to catalyst separation and recycling continue to be significant. These issues hinder the practical use of such catalysts in wastewater treatment, limiting their overall effectiveness for large-scale environmental remediation. Incorporating the magnetic properties into the catalyst during the photocatalytic reaction process is a widely recognized method for magnetic separation, as illustrated in **Fig 1.3** [39]. When magnetic nanoparticles are used, separation can be easily achieved through the application of external magnetic fields, enabling the efficient recycling of the nanocatalyst. This process contributes to more effective, cost-efficient, and environmentally friendly wastewater treatment [40].

Moreover, the use of ferrite nanoparticles as antibacterial and antimicrobial agents is gaining significant attention because they can be easily manipulated using an external magnetic field. These nanoparticles have been tested for various medical applications, including magnetic hyperthermia, targeted drug delivery, and as bactericides.

Among the various structures of ferrites, spinel ferrites possess unique physical and magnetic properties, which contribute to their widespread use in the medical field. In antibacterial applications, reactive oxygen species are generated on the surface of nanoparticles. Superoxide anions damage nucleic acids, DNA, and lipids, as they are unable to penetrate the cell membrane directly.

H₂O₂ and [•]OH species are strong oxidizing agents that directly interact with the bacterial cell membrane, causing damage and inhibiting cell growth. The term "ferrite" is derived from the Latin word "Ferrum," meaning iron. For decades, ferrites have been of great interest as magnetic nanoparticles with a wide range of applications. These are mixed metal oxides, with iron oxide being the primary component. The properties of these nanoparticles are determined by their particle size, chemical composition, and interactions with the surrounding environment [41]. The properties of ferrite nanoparticles of the same type can vary significantly, as they can be adjusted by altering their structural properties, size, and composition. Due to their deepened magnetic, electric, and optical properties, these ferrites have been applied for tremendous applications including microwave devices [42], sensors [43-44], magnetic recording [45], biomedical materials [43], batteries [46], MRI contrast agents [47], etc.

However, there are fewer reports on their photocatalytic applications. Ferrites play a crucial role as catalysts in visible light-driven catalysis due to their efficient utilization of solar light. These ferrites benefit from having suitable optical absorption for low-energy photons ($h\nu \sim 2.2$ eV) and possess an electronic structure that is well-suited for photocatalytic applications [48-49]. The band gap of ferrites can be reduced by substituting transition and inner transition metal ions into their tetrahedral or octahedral sites. These materials possess a high surface area, and the presence of

unstable forces at the surface is crucial for adsorption. Ferrites are involved in the combined adsorption and degradation of organic molecules.

Ferrites are electrically non-conductive and ferrimagnetic, meaning they can be easily magnetized or attracted to a magnet. Recently, researchers have shown significant interest in developing photocatalytic materials that can harness clean and sustainable solar energy for both energy production and environmental remediation. Generally, there are two main approaches in which photocatalysts can exclusively utilize visible light for photocatalytic degradation [50].

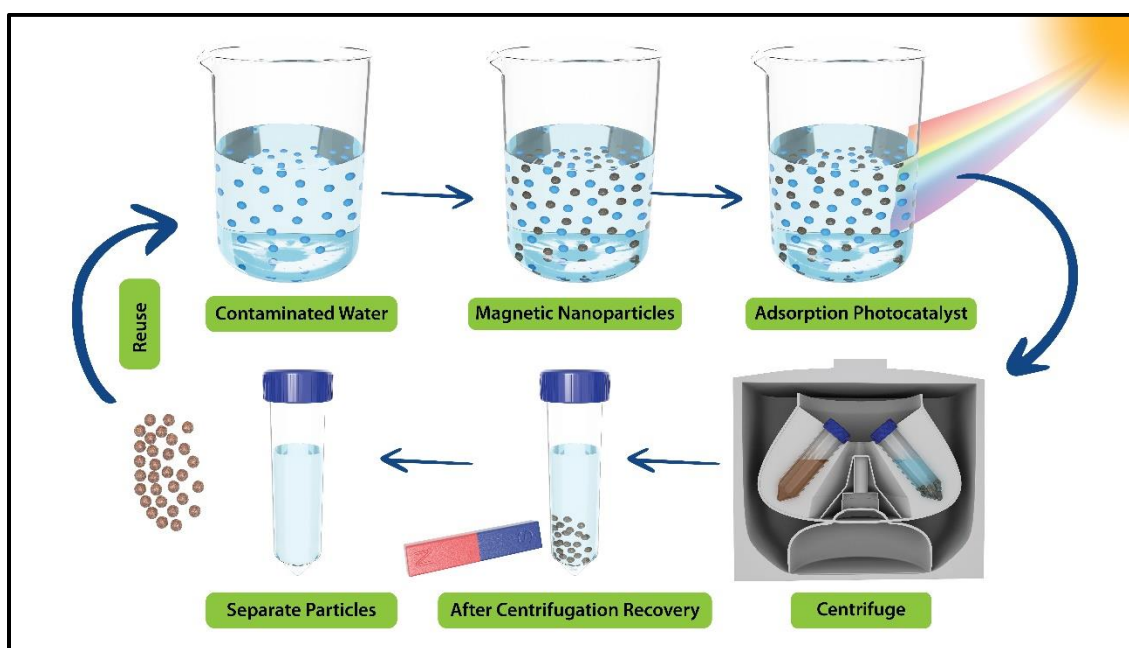


Fig. 1.3: Schematic representation of recycling of magnetic NPs

The first approach involves doping UV-active materials with an element that enables them to become active under visible light [51-53]. For example, the use of dopants in UV-light active TiO_2 photocatalyst decreases its bandgap energy and makes it visible light active. The use of common dopants is nitrogen [54-57] carbon [58], sulphur [59] etc. Some heavy metals like Cobalt [60], silver [61], gold [62] and platinum [63]. etc were also used as dopants in TiO_2 to make it visible light active. The second approach is to develop materials having narrow bandgap energy that are suitable for the absorption of visible light to carry out the photocatalytic reaction [64-

70]. The selected photocatalyst i.e. CaFe_2O_4 [71], MgFe_2O_4 [72], CdS , and WO_3 [73] effectively utilize visible light due to narrow bandgap energy.

Spinel ferrites, with the general chemical formula MFe_2O_4 (where $\text{M} = \text{Zn}, \text{Ca}, \text{Mg}, \text{or Ni}$), are chemically and thermally stable magnetic materials that have found a wide range of applications [74]. They are utilized in magnetic resonance imaging (MRI), electronic devices, drug delivery, and also in photocatalysis [75-76]. Ferrites possess many important photocatalytic properties for industrial processes such as oxidative dehydrogenation of hydrocarbon [77], alcohol and water decomposition, phenol hydroxylation [78], CO oxidation [79], and methane combustion [80]. Additionally, the incorporation of different metals into the lattice structure can alter the redox properties of the ferrites and enhance their stability by preserving the spinel structure. The incorporation of divalent metal cations such as Mg^{2+} [81] and Zn^{2+} [82] improves the stability of the ferrites. When substitution takes place by transition metals such as Ni^{2+} , Cu^{2+} [83], Mn^{2+} [84] and Co^{2+} [85] into the spinel ferrite, it can strongly modify the redox properties of the ferrites.

1.6. Nanoparticles for photocatalysis:

In recent times, the magnetic properties of nanoparticles have attracted considerable attention due to their high adsorption capabilities, unique superparamagnetic characteristics, and large surface area-to-volume ratio. Specifically, spinel structures made from transition metal oxides, commonly known as ferrite nanoparticles, are among the most significant types of magnetic nanoparticles. Ferrites are categorized based on their crystal structure and magnetic properties into spinel (MFe_2O_4 , where M represents transition metals), orthoferrite (MFeO_3 , where M refers to rare earth metals), hexaferrite ($\text{SrFe}_{12}\text{O}_{19}$ and $\text{BaFe}_{12}\text{O}_{19}$), and garnet ($\text{M}_3\text{Fe}_5\text{O}_{12}$, where M is rare earth metals). Among these, spinel and orthoferrite ferrites attract particular attention due to their simple chemical composition, exceptional magnetic properties, and wide-ranging applications in fields such as wastewater treatment, catalysis, biomedical applications, and electronic devices.

The spinel ferrite structure, depicted in **Fig. 1.4**, consists of a close-packed arrangement of oxygen ions forming a face-centered cubic structure. Within this arrangement, a unit cell is made up of 32 oxygen ions. Each unit cell contains eight formula units of MFe_2O_4 , with a total of 32 octahedral sites (each one-quarter occupied) and 64 tetrahedral sites (each one-eighth occupied) by metal cations. During the synthesis of ferrites, if the ratio of metal ions to oxygen ions is too low, some octahedral sites may remain unfilled, creating vacancies in the structure. If the ratio of metal ions to oxygen ions is too low during the preparation process, some of the octahedral sites may remain vacant. These sites are then stated as vacancies. Spinel ferrites are divided into three types; normal, inverse, and mixed ferrites, depending upon occupancy of tetrahedral sites (A) and octahedral sites (B). Normal spinel: A site is completely occupied by 8 M^{2+} ions and B site by 16 Fe^{3+} ions. Example: ZnFe_2O_4 , MgFe_2O_4 . Inverse spinel: If 8 M^{2+} ions have a preference for the B site, they will displace 8 Fe^{3+} ions to the A site. Example: CoFe_2O_4 , MnFe_2O_4 , NiFe_2O_4 . Mixed spinel: When Fe^{3+} and M^{2+} ions occupy both A and B sites, then ferrite is categorized as mixed spinel. Example: $\text{Ni-ZnFe}_2\text{O}_4$. The placement of cations in the tetrahedral and octahedral sites is determined by factors such as their electronic configurations, electrostatic energy, and ionic radii within the spinel lattice [86].

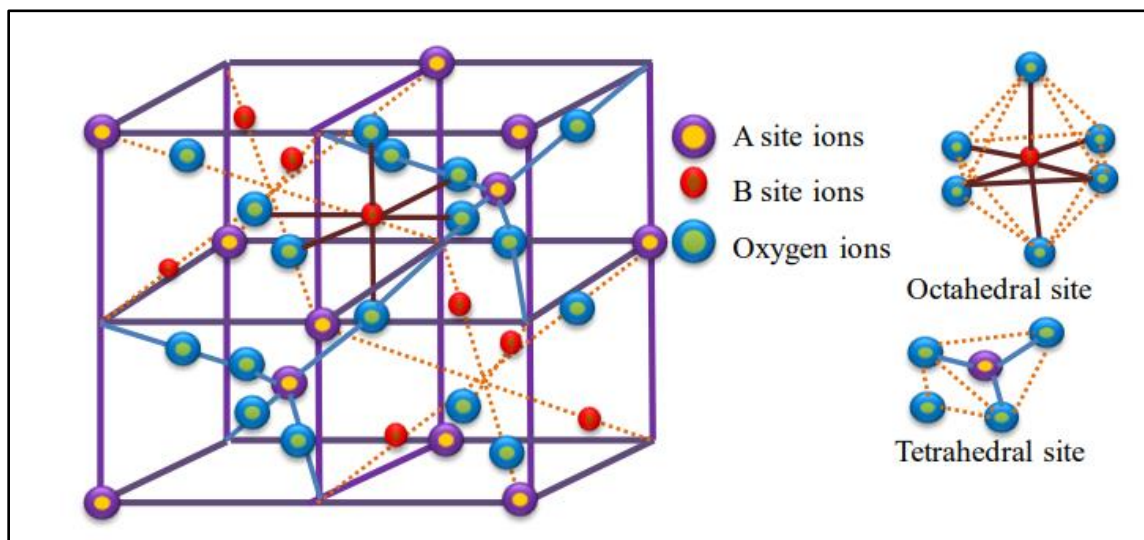


Fig. 1.4: Spinel structure of ferrites.

Zinc ferrite and other metal ferrites have garnered significant attention in photocatalysis for the degradation of organic and inorganic pollutants. These materials are capable of absorbing visible light to generate photoexcited electron-hole pairs, which play a crucial role in breaking down contaminants. With a bandgap energy between 1.7 and 2 eV, they are considered visible-light active photocatalysts. However, the recombination of photogenerated electrons and holes can reduce their efficiency and lower photocatalytic performance. Due to their narrow bandgap energy and unique anisotropic layered structure, these materials exhibit a strong photoresponse in the visible light region, enhancing their photocatalytic activity. Despite their potential, the photocatalytic activity of metal ferrites is often limited by factors such as instability under strong reducing agents, poor conductivity, and high electron-hole recombination rates. To address these challenges, various modifications have been explored, such as forming composites with metal oxides (e.g., TiO_2 , ZnO , ZnTiO_3), metal salts (e.g., AgI , CdCl_2 , AuCl), noble metals (e.g., Pt , Ag , Au), and carbon-based materials (e.g., graphene, MWCNT). These modifications enhance the separation of photogenerated excitons and reduce electron-hole recombination, leading to improved photocatalytic performance. This unique approach to modifying metal ferrites helps to enhance their ability to degrade environmental pollutants and boosts their overall photocatalytic activity (see Fig. 1.5).

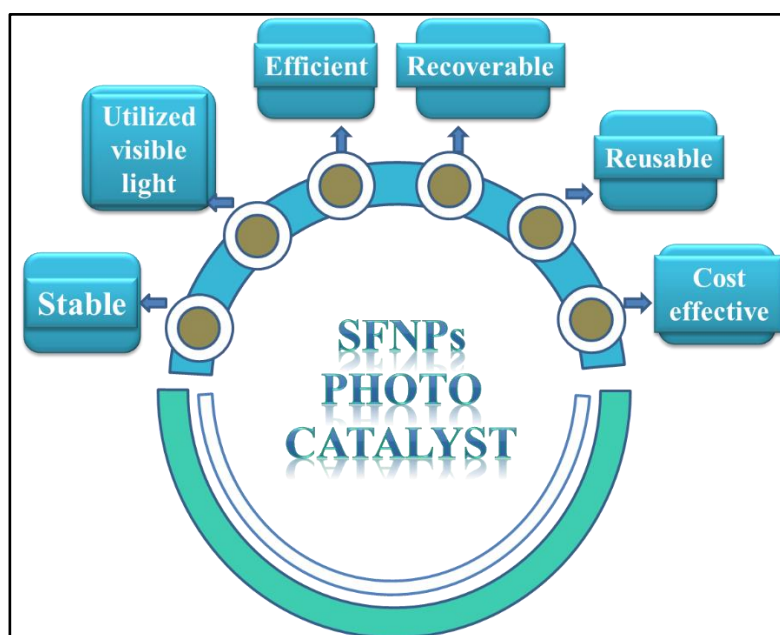


Fig. 1.5: Advantages of ferrites for water and wastewater treatment

1.7 Statement of problem:

Contamination of drinking water sources is becoming increasingly problematic in the modern world. In recent years photocatalysis has received much attention as a potential method of removing/degrading highly toxic organic and inorganic compounds from contaminated water [87]. Photocatalytic degradation of organic pollutants by using high-performance nanostructured semiconductor photocatalysts has been recognized as one of the most promising strategies to create a clean and comfortable aquatic environment for human beings in modern society [88]. In order to treat pollutants, efforts have been made towards the development of advanced oxidation processes, such as photocatalysis, which can achieve efficient degradation of recalcitrant molecules. The two types of reaction mechanisms are involved in the photocatalytic degradation of toxic dyes. Schemes 1.2 illustrates the schematic representation of reaction mechanisms for direct and indirect photocatalytic dye degradation.

Among many nanocrystalline oxides, nanostructured titanium oxide and potassium hexaniobate have been considered as stable materials for photocatalysis. Bulk TiO_2 based composite materials are investigated for photocatalytic applications. However, their optimum performance is restricted by the difficulty in controlling crystallite size and limited electronic coupling due to the large crystallites. On the other hand, manganese-substituted zinc ferrite nanostructures provide an intermediate energy level, increase the lifetime of excitons, and enhance photocatalytic activity with high efficiency, high photostability, and cover a wide solar spectrum. In addition, the magnetic nature of this material allows the reusability of the manganese-substituted zinc ferrite NPs which again increases the efficiency of the material. Therefore, the photocatalytic performance of Mn-Zn ferrite nanoparticles in the presence of methylene blue, chloramine T, and rhodamine B dye will be studied.

1.8 Challenges for catalysis and scope of thesis:

So far, a number of semiconductors have been identified as photocatalysts. The main disadvantage of using these photocatalysts is uncontrolled charge recombination,

which decreases the number of active species. Many researchers have reported in the literature that this can be overcome by using spinel ferrite structures as photocatalysts. These materials have the following unique properties that aid in displaying or enhancing catalytic activity. They are as follows:

- 1) Charge transport is simple due to corner-sharing octahedral and tetrahedral structures.
- 2) Special dispersion of cations at tetrahedral and octahedral sites.
- 3) Oxygen-deficient structures can be made by doping elements with different valence and ionic radii.
- 4) Because photo-generated charges are anisotropic, recombination can be avoided.

In view of the above discussion, the present study leads to the synthesis and characterization of zinc ferrite (ZnFe_2O_4) nanoparticles using the combustion method, which presents challenges in achieving uniform particle size and phase purity due to the rapid and exothermic nature of combustion reactions. The scope includes optimizing reaction conditions, selecting appropriate precursors, and conducting comprehensive characterizations using XRD, SEM/TEM, EDS, FTIR, and BET to evaluate phase purity, crystallite size, morphology, and surface area, comparing these with literature values to validate the synthesis method.

Secondly, evaluating the effect of manganese substitution on the optical, and structural, properties of zinc ferrite [$\text{Mn}_x\text{Zn}_{1-x}\text{Fe}_2\text{O}_4$ ($x=0$ to 1)] nanoparticles, which involves challenges in controlling the substitution level and understanding its impact on material properties. The scope encompasses synthesizing nanoparticles with varying manganese content, employing characterization techniques such as XRD for phase and lattice parameter analysis, SEM/TEM for morphology, UV-Vis spectroscopy for band gap determination, analyzing the changes and correlations between structural, and optical properties understanding the implications of manganese substitution. Lastly, assessing the visible-light mediated photocatalytic dye degradation efficiency of manganese-substituted zinc ferrite nanoparticles in the

presence of methylene blue, chloramine T, and rhodamine B, which presents challenges in achieving high photocatalytic efficiency and understanding the degradation mechanism. The scope includes setting up photocatalytic experiments, monitoring dye degradation using UV-Vis spectroscopy, calculating degradation efficiency and rate constants, discussing the influence of structural and optical properties on photocatalytic activity, elucidating the degradation mechanism involving electron-hole pair generation and reactive species formation, and summarizing findings to highlight the role of manganese substitution in enhancing photocatalytic performance and suggesting future research directions.

1.9 Aim and Objectives of research:

Manganese substituted zinc ferrite synthesized by a chemical method such as combustion will exhibit enhanced photocatalytic activity towards the degradation of methylene Blue, chloramine-T, and rhodamine B dyes due to its modified band gap which provides visible light absorption capability, well-matched band positions which can help to improve electron transfer as well as suppress the recombination of electron-hole pairs. In view of the above discussion the present study leads to the following aim and objectives:

Aim: Manganese substituted zinc ferrite nanostructures for photocatalytic dye degradation

Objectives:

1. To synthesis and characterize of zinc ferrite (ZnFe_2O_4) NPs by chemical method such as combustion
2. To evaluate the effect of manganese substitution on optical, and structural, properties of zinc ferrite $[\text{Mn}_x\text{Zn}_{1-x}\text{Fe}_2\text{O}_4$ ($x=0$ to 1)] NPs
3. To evaluate visible-light mediated photocatalytic dye degradation efficiency of manganese substituted zinc ferrite $[\text{Mn}_x\text{Zn}_{1-x}\text{Fe}_2\text{O}_4$ ($x=0$ to 1)] NPs in the presence of methylene blue, chloramine T, rhodamine B dye

1.10 References:

1. Shiklomanov I. In Proceedings of the international symposium to commemorate., 25, (1991), 93-126.
2. Sikder M, Kihara Y, Yasuda M, Yustiawati, Mihara Y, Tanaka S, Odgerel D, Mijiddorj B, Syawal S, Hosokawa T, Saito T. CLEAN–Soil, Air, Water., 41, (2013), 60-68.
3. Sikder M, Tanaka S, Saito T, Hosokawa T, Gumiri S, Ardianor A, Uddin M, Tareq S, Shammi M, Kamal A, Kurasaki M. Pollution., 1, (2015), 333-346.
4. Wang F, Wang C, Yu Z, Xu K, Li X, Fu Y. Polyhedron., 105, (2016), 49-55.
5. Schweitzer L, Noblet J. InGreen chemistry., (2018), 261-290.
6. Suryavanshi R, Rajpure K. Journal of Photochemistry and Photobiology A: Chemistry., 357, (2018), 72-80.
7. Singh P, Shandilya P, Raizada P, Sudhaik A, Rahmani-Sani A, Hosseini-Bandegharai A. Arabian Journal of Chemistry., 13, (2020), 3498-3520.
8. Gusain R, Gupta K, Joshi P, Khatri O. Advances in Colloid and Interface Science., 272, (2019) 102009 (1-81).
9. Boelee E, Geerling G, van der Zaan B, Blauw A, Vethaak A. Acta tropica., 193, (2019), 217-226.
10. Sharma K, Dutta V, Sharma S, Raizada P, Hosseini-Bandegharai A, Thakur P, Singh P. Journal of Industrial and Engineering Chemistry., 78, (2019), 1-20.
11. Sudhaik A, Raizada P, Shandilya P, Jeong D, Lim J, Singh P. Journal of Industrial and Engineering Chemistry. 67, (2018), 28-51.
12. Sharma S, Dutta V, Singh P, Raizada P, Rahmani-Sani A, Hosseini-Bandegharai A, Thakur V. Journal of Cleaner Production., 228, (2019), 755-769.
13. Brillas E, Martínez-Huitle C. Applied Catalysis B: Environmental., 166, (2015), 603-643.
14. Oturan M, Aaron J. Critical Reviews in Environmental Science and Technology., 44, (2014), 2577-2641.
15. Chong S, Zhang G, Wei Z, Zhang N, Huang T, Liu Y. Ultrasonics Sonochemistry., 34, (2017), 418-425.

16. Garcia-Segura S, Brillas E. *Journal of Photochemistry and Photobiology C: Photochemistry Reviews.*, 31, (2017), 1-35.
17. Matos J, Miralles-Cuevas S, Ruíz-Delgado A, Oller I, Malato S. *Carbon.*, 122, (2017), 361-373.
18. Tang X, Wang Z, Wang Y. *Chemical Physics Letters.*, 691, (2018), 408-414.
19. Ohtani B. *Catalysts.*, 3, (2013), 942-953.
20. Shi N, Li X, Fan T, Zhou H, Zhang D, Zhu H. *International journal of hydrogen energy.*, 39, (2014), 5617-5624.
21. Kondarides D, Daskalaki V, Patsoura A, Verykios X. *Catalysis Letters.*, 122, (2008), 26-32.
22. Clarizia L, Spasiano D, Di Somma I, Marotta R, Andreozzi R, Dionysiou D. *International Journal of Hydrogen Energy.*, 39, (2014), 16812-16831.
23. Dincer I, Acar C. *International Journal of Hydrogen Energy.*, 40, (2015), 11094-11111.
24. Gawande M, Rathi A, Nogueira I, Varma R, Branco P. *Green Chemistry.*, 15, (2013), 1895-1899.
25. Amiri M, Eskandari K, Salavati-Niasari M. *Advances in Colloid and Interface Science.* 271, (2019), 101982 (1-44).
26. White R, Luque R, Budarin V, Clark J, Macquarrie D. *Chemical Society Reviews.*, 38, (2009), 481-494.
27. Tong J, Cai X, Wang H, Xia C. *Journal of SolGel Science and Technology.*, 66, (2013), 452-459.
28. Zheng Y, Stevens P, Gao Y. *The Journal of Organic Chemistry.*, 71, (2006), 537-542.
29. Eskandari K, Khodabakhshi S. *Letters in Organic Chemistry.*, 15, (2018), 463-471.
30. Wang Z, Xiao P, Shen B, He N. *Colloids and Surfaces A: Physicochemical and Engineering Aspects.*, 276, (2006), 16-21.
31. Yavari S, Mohammad N, Shahmoradi B, Gharibi F, Maleki A. *Journal of Health.*, 7, (2016), 343-355.

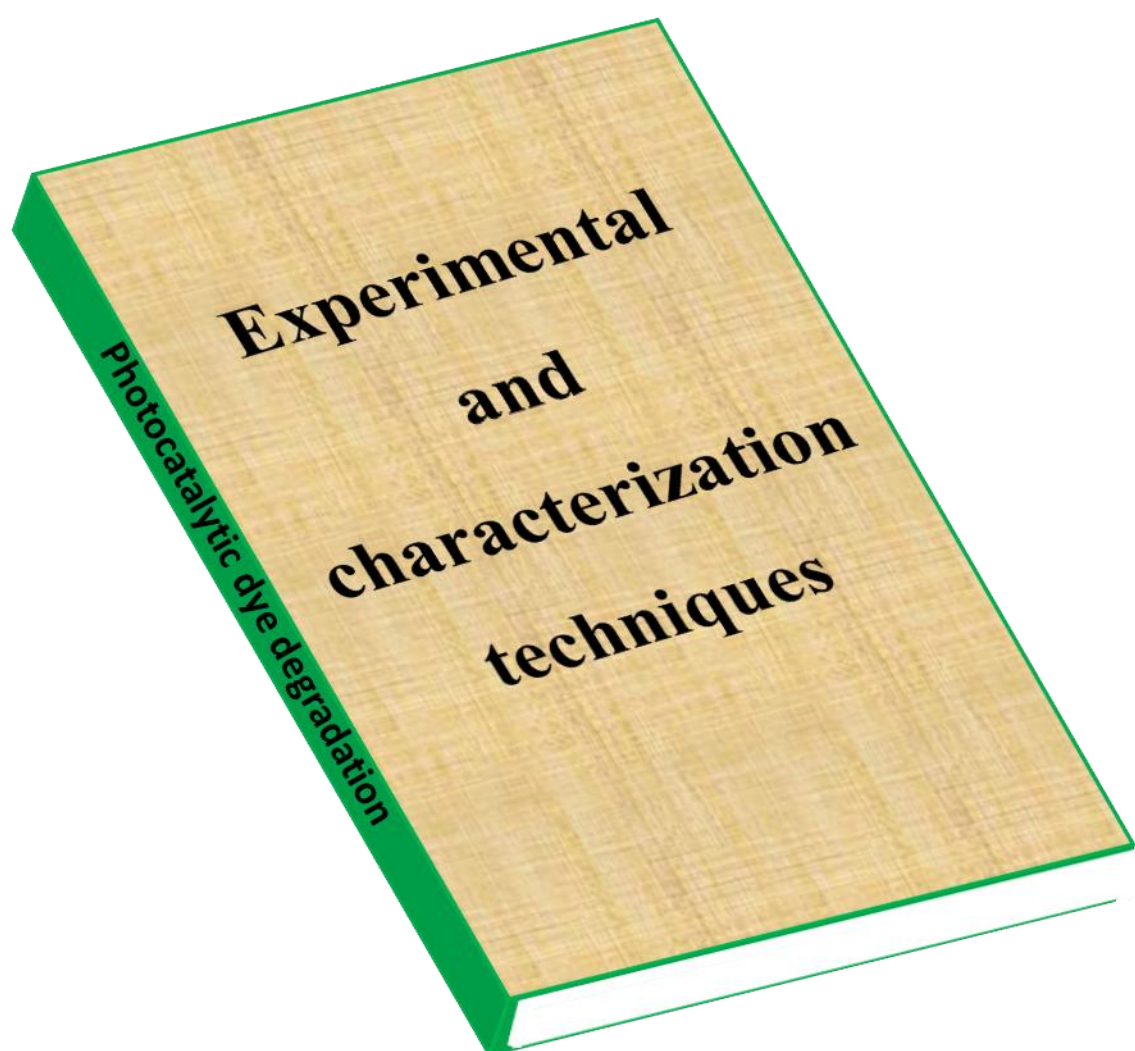
-
32. Amiri M, Eskandari K, Salavati-Niasari M. *Advances in Colloid and Interface Science.*, 271, (2019), 101982 (1-44).
 33. Zhao Q, Yan Z, Chen C, Chen J. *Chemical Reviews.*, 117, (2017), 10121-10211.
 34. Bogacz B, Gargula R, Kurzydło P, Pędziwiatr A, Tatarchuk T, Paliychuk ND. *Acta Physica Polonica. A.*, 134, (2018), (1-5).
 35. Kane S, Raghuvanshi S, Satalkar M, Reddy V, Deshpande U, Tatarchuk T, Mazaleyrat F. In *AIP Conference Proceedings* 1953, (2018), 030089 (1-4).
 36. Jauhar S, Kaur J, Goyal A, Singhal S. *RSC advances.*, 6, (2016), 97694-719.
 37. Casbeer E, Sharma V, Li X. *Separation and Purification Technology.*, 6, (2012), 1-4.
 38. Sun L, Shao R, Tang L, Chen Z. *Journal of Alloys and Compounds.*, 564, (2013), 55-62.
 39. Saha M, Mukherjee S, Kumar S, Dey S, Gayen A. *RSC advances.*, 6, (2016), 58125-58136.
 40. Costa R, Lelis M, Oliveira L, Fabris J, Ardisson J, Rios R, Silva C, Lago R. *Catalysis Communications.*, 4, (2003), 525-529.
 41. Linley S, Leshuk T, Gu F. *Clean–Soil, Air, Water.*, 41, (2013), 1152-1156.
 42. Ayyappan S, Paneerselvam G, Antony M, Philip J. *Materials Chemistry and Physics.*, 128, (2011), 400-404.
 43. Kim D, Nikles D, Johnson D, Brazel C. *Journal of Magnetism and Magnetic Materials.*, 320, (2008), 2390-2396.
 44. Gadkari A, Shinde T, Vasambekar P. *Sensors and Actuators B: Chemical.*, 178, (2013), 34-39.
 45. Frey N, Peng S, Cheng K, Sun S. *Chemical Society Reviews.*, 38, (2009), 2532-2542.
 46. Bhukal S, Dhiman M, Bansal S, Tripathi M, Singhal S. *SC advances.*, 6, (2016), 1360-1375.
 47. Lee J, Huh Y, Jun Y, Seo J, Jang J, Song H, Kim S, Cho E, Yoon H, Suh J, Cheon J. *Nature medicine.*, 13, (2007), 95-99.
 48. Wang T, Jiang Z, An T, Li G, Zhao H, Wong P. *Environmental Science & Technology.*, 52, (2018), 4774-4784.
-

49. Jaafarzadeh N, Ghanbari F, Ahmadi M. Chemical Engineering Journal., 320, (2017), 436-447.
50. Tang J, Zou Z, Ye J. Angewandte Chemie International Edition., 43, (2004), 4463-4466.
51. Martyanov I, Uma S, Rodrigues S, Klabunde K. Chemical Communications., (2004), 2476-2477.
52. Yang J, Chen C, Ji H, Ma W, Zhao J. The Journal of Physical Chemistry B., 109, (2005), 21900-21907.
53. Anpo M, Takeuchi M. Journal of catalysis., 216, (2003), 505-516.
54. Fu H, Zhang L, Zhang S, Zhu Y, Zhao J. The Journal of Physical Chemistry B., 110, (2006), 3061-3065.
55. Hsu H, Chen S, Chen Y. Separation and Purification Technology., 80, (2011), 663-669.
56. Park S, Heo J. Separation and Purification Technology., 58, (2007), 200-205.
57. Li G, Jimmy C, Zhang D, Hu X, Lau W. Separation and Purification Technology., 67, (2009), 152-157.
58. Irie H, Watanabe Y, Hashimoto K. Chemistry Letters., 32, (2003), 772-773.
59. Zhang X, Lei L, Zhang J, Chen Q, Bao J, Fang B. Separation and Purification Technology., 66, (2009), 417-421.
60. Hsieh C, Fan W, Chen W, Lin J. Separation and Purification Technology., 67, (2009), 312-318.
61. Zielińska A, Kowalska E, Sobczak J, Łacka I, Gazda M, Ohtani B, Hupka J, Zaleska A. Separation and Purification Technology., 72, (2010), 309-318.
62. Luo S, Xiao Y, Yang L, Liu C, Su F, Li Y, Cai Q, Zeng G. Separation and Purification Technology., 79, (2011), 85-91.
63. Li D, Chen Z, Chen Y, Li W, Huang H, He Y, Fu X. Environmental Science & Technology., 42, (2008), 2130-2135.
64. Fu H, Zhang S, Xu T, Zhu Y, Chen J. Environmental Science & Technology., 42, (2008), 2085-2091.
65. Dillert R, Taffa D, Wark M, Bredow T, Bahnemann D. APL Materials., 3, (2015), 1-16.

66. Sun A, Xiong Z, Xu Y. *Journal of Hazardous Materials.*, 152, (2008), 191-195.
67. Zhu S, Xu T, Fu H, Zhao J, Zhu Y. *Environmental Science & Technology.*, 41, (2007), 6234-6239.
68. Chen C, Wang Q, Lei P, Song W, Ma W, Zhao J. *Environmental Science & Technology.*, 40, (2006), 3965-3970.
69. Zhang Y, Du Z, Li K, Zhang M. *Separation and Purification Technology.*, 81, (2011), 101-107.
70. Zhou B, Zhao X, Liu H, Qu J, Huang C. *Separation and Purification Technology.*, 77, (2011), 275-282.
71. Ida S, Yamada K, Matsunaga T, Hagiwara H, Matsumoto Y, Ishihara T. *Journal of the American Chemical Society.*, 132, (2010), 17343-17345.
72. Dom R, Subasri R, Radha K, Borse P. *Solid State Communications.*, 151, (2011), 470-473.
73. Kitano M, Hara M. *Journal of Materials Chemistry.*, 20, (2010), 627-641.
74. Guin D, Baruwati B, Manorama S. *Journal of Molecular Catalysis A: Chemical.*, 242, (2005), 26-31.
75. Mendonca M, Godinho M, Catarino M, da Silva Pereira M, Costa F. *Solid state sciences.*, 4, (2002), 175-182.
76. Gota S, Gautier-Soyer M, Douillard L, Duraud J, Le Fèvre P. *Le Journal de Physique IV.*, 7, (1997), C2-675.
77. Gibson M, Hightower J. *Journal of Catalysis.*, 41, (1976), 420-430.
78. Manova E, Tsoncheva T, Paneva D, Mitov I, Tenchev K, Petrov L. *Applied Catalysis A: General.*, 277, (2004), 119-127.
79. PalDey S, Gedevanishvili S, Zhang W, Rasouli F. *Applied Catalysis B: Environmental.*, 56, (2005), 241-250.
80. Spretz R, Marchetti S, Ulla M, Lombardo E. *Journal of Catalysis.*, 194, (2000), 167-174.
81. Fabris J, Mussel W, Coey J, de Jesus Filho M, Goulart A. *Hyperfine Interactions.*, 110, (1997), 33-40.
82. Šimša Z. *physica status solidi (b).*, 96, (1979), 581-587.

83. Ramankutty C, Sugunan S, Thomas B. Journal of Molecular Catalysis A: Chemical., 187, (2002), 105-117.
84. Lahiri P, Sengupta S. Journal of the Chemical Society, Faraday Transactions., 91, (1995), 3489-3494.
85. Persoons R, De Grave E, De Bakker P, Vandenberghe R. Physical Review B., 47 (1993), 5894-5905.
86. Valenzuela R. Physics Research International., 2012, (2012), 591839 (1-9).
87. Sharma S, Bhattacharya A. Applied water science., 7, (2017), 1043-1067.
88. Raza N, Kim K, Agbe H, Kailasa S, Szulejko J, Brown R. sian Journal of Atmospheric Environment., 11, (2017), 217-234.

CHAPTER II



2.1. Introduction:

Metal oxide nanostructures have undergone extensive study over recent decades due to their prospective applications in various fields including optics, magnetism, electronics, photocatalysis, environmental remediation, gas sensing, solar cells, photodetectors, and photoanodes for water splitting and CO₂ conversion. The adjustable bandgap of metal oxides renders them promising for photocatalytic applications, leading to changes in the light absorption and band edge positions. However, the choice of synthesis and fabrication methods significantly influences the physical and chemical properties of metal oxide semiconductors, thereby impacting their photocatalytic efficacy.

Various techniques have been explored for synthesizing nanostructured metal oxides, broadly categorized as top-down and bottom-up approaches. The top-down strategy begins with macro or micro-sized particles that are then scaled down to the nano regime. However, such methods often suffer from drawbacks such as limited control over the size, morphology, and other structural properties of the fabricated particles. In contrast, bottom-up techniques initiate at the molecular level, offering significant control over the shape, size, and morphology of the resulting particles. Consequently, bottom-up approaches are more favored and widely utilized due to their ability to finely tune the structural parameters of the derived products. In bottom-up strategies, the growth process of nanostructures can be meticulously controlled using various reagents, including growth inhibitors, ligands, and surfactants. Among the numerous bottom-up techniques, wet chemical methods are particularly prevalent, with the solution combustion synthesis (SCS) technique standing out as a widely adopted method, [1-7] Other notable bottom-up techniques include solution-based hydrothermal and solvothermal methods, as well as polyol synthesis methods. However, scaling up the production of metal oxide nanostructures using these methods faces challenges, such as controlling the properties of the bulk materials and, in some instances, the use of chemicals that are not environmentally friendly. Moreover, the necessity for high-temperature conditions in the synthesis of metal oxides increases the cost of these processes at an industrial level. Consequently, finding an efficient method for large-scale synthesis of metal oxides remains critically important.

The solution combustion synthesis (SCS) technique represents a relatively novel approach to materials manufacturing, distinguished by a robust high-temperature and self-sustained exothermic reaction, rendering it highly energy-efficient. Herein, we deployed the SCS technique for the synthesis of magnetic materials. This method involves the use of a homogeneous aqueous mixture of precursors, which undergoes condensation to form a hydrogel containing a uniform metal cation network. Subsequently, combustion occurs between an inorganic reagent, typically nitrates, and a fuel during calcination. Commonly utilized fuels include ammonium nitrate, sucrose, citric acid (CA), tetraformyl triazine (TFTA), glycine, urea, triethylamine hydrochloride, and sorbitol [8-9]. The SCS technique proves especially for crafting multi-component and hybrid nanostructures, allowing for the attainment of desired structural parameters. Moreover, the properties of resultant products can be tailored to specific applications by fine-tuning process parameters of the SCS reaction [10-11]. Notably, this method offers a rapid pathway to synthesizing nanostructures characterized by high surface area [6,12]. Furthermore, its suitability for bulk production of nanostructured metal oxides is underscored by the ability to rapidly synthesize large quantities of products via the SCS technique.

Solution combustion synthesis (SCS) derives its name from the integration of a reactive fuel and oxidizer solution that combusts [13]. Characterized by a violent exothermic reaction, SCS generates a significant release of gases. Crucially, the energy needed for the synthesis of metal oxides is supplied by the redox reactions that occur once the ignition temperature is reached. This process leads to the evolution of NO_x and CO_x gases, facilitating a self-sustained and self-propagating combustion reaction among intermediate phases during the synthesis [14]. This vigorous gas evolution results in the production of voluminous, loosely aggregated, and finely divided nanopowders. Combustion occurs once the reaction temperature surpasses the autoignition point of the redox (oxidizer and fuel) solution. The emphasis is particularly on the improved photocatalytic activity and the versatility of the SCS method for fabricating complex and multicomponent photocatalysts. Moreover, the discussion extends to the correlation between the parameters of the SCS process and the resultant photocatalytic activity.

Photocatalysis has garnered substantial interest as a green technology for environmental clean-up, air and water purification, and the production of clean energy. Initial studies in photocatalysis focused on wide bandgap semiconductors like TiO₂ and

ZnO. It has been recognized that the efficacy of a photocatalyst is greatly influenced by its structural and optical properties. These characteristics indicate the material's ability to absorb light, generate charge carriers, and facilitate charge transfer.

This chapter outlines the principles, innovations, and applications of the SCS in crafting advanced photocatalysts. It offers a comprehensive view by discussing the chemistry involved in SCS, identifying potential challenges, and exploring ways to circumvent environmental constraints. Additionally, the chapter delves into the photocatalytic uses of nanomaterials produced via SCS, analyzing how SCS conditions influence photocatalytic efficiency. The goal is to propose strategies for designing sophisticated photocatalysts through the adjustment of physical attributes like structural parameters and enhancing their activity in the visible spectrum. The discussion also covers how modifications to the semiconductor's properties can be made during the initial stages of the SCS process to optimize performance.

Spinel ferrite nanoparticles have garnered substantial interest in recent years due to their exceptional optical and magnetic characteristics, which have significant practical applications, particularly in wastewater remediation [15]. Zinc ferrite (ZnFe_2O_4) stands out among spinel ferrites for its notable high saturation magnetization, significant coercivity, and exceptional chemical stability. The physical and chemical properties of ferrites, including ZnFe_2O_4 , are profoundly influenced by particle size, shape, composition, and microstructure. These characteristics are highly dependent on the specific synthesis methods and the parameters employed during the preparation process [16-17]. In recent years, researchers have focused on synthesizing ferrite nanoparticles with specific size and magnetic properties.

Various synthesis methods have been explored, including forced hydrolysis [18], co-precipitation [19], polyol [20], combustion reaction [21], and sonochemical [22] methods, for preparing nanocrystalline ZnFe_2O_4 . Among these techniques, the combustion method emerges as a notable alternative, offering promising results for ferrite synthesis [23]. While co-precipitation is effective for producing fine zinc ferrite nanoparticles, this method necessitates precise control over several parameters such as pH, concentration, and temperature. In contrast, the combustion synthesis method offers simpler control over stoichiometry and crystallite size, both of which significantly impact the magnetic properties of the ferrite. Combustion synthesis is known for its low-temperature process, employing a highly exothermic redox reaction to produce oxide

materials. The characteristics of the resulting powder such as crystallite size, surface area, particle size distribution, and degree of agglomeration are largely influenced by the combustion's enthalpy or flame temperature. The temperature is influenced by the type of fuel and the fuel-to-oxidizer ratio. In combustion synthesis, selecting the appropriate fuel is essential for determining the morphology, phase, and particle characteristics of the final product.

Several studies have highlighted the role of different fuels in the combustion synthesis of ZnFe_2O_4 nanoparticles [21, 24-28]. Research has shown that glycine is the preferred fuel for initiating the combustion reaction, as it has a higher negative combustion heat (-3.24 kcal/g) compared to urea (-2.98 kcal/g) and citric acid (-2.76 kcal/g) [29]. It is crucial to produce particles that are highly pure and uniform for maximizing material performance while minimizing preparation costs. Therefore, this study uses a simple auto-combustion method with glycine as the fuel to synthesize ZnFe_2O_4 nanoparticles. This method offers the advantage of not requiring sophisticated instruments or high sintering temperatures. While the literature has reported the combustion synthesis of nanosized ZnFe_2O_4 , there is limited information on how the composition of the reactants affects the properties of the final product. This study aims to explore how the composition of reactants, reaction dynamics, and characteristics of the products are influenced by the fuel-to-oxidizer ratio.

2.2. Combustion Synthesis:

Combustion synthesis (CS) is a low-temperature synthesis technique that relies on a highly exothermic redox reaction to produce oxides. Unlike traditional methods that require high-temperature furnaces and prolonged annealing procedures, the combustion reaction serves as its energy source. These characteristics make CS an appealing method for producing technologically significant materials at lower costs compared to conventional ceramic processes. Some other advantages of CS are:

- i. Use of relatively simple equipment
- ii. Formation of high-purity products
- iii. Stabilization of metastable phases and
- iv. Formation of virtually any size and shape of products
- v. Control on Composition, structure, homogeneity and stoichiometry

In combustion synthesis (CS), the energy generated from the exothermic redox (reduction-oxidation) reactions is harnessed to manufacture a diverse array of materials, including advanced ceramics, catalysts, composites, alloys, intermetallic, and nanomaterials. The characteristics and efficiency of the combustion process can be significantly influenced by several key processing parameters such as C/H ratio (type of fuel), the fuel-to-oxidizer ratio (F/O), the water content of the precursor mixture, and the ignition temperature.

Different concepts defined by propellant chemistry used to understand the exothermicity of combustion reaction. A solid propellant consists of oxidizer and fuel which finally fired and gives final product in the form of power/ash. Constitution of fuel-oxidizer mixture is usually expressed in terms of parameters such as mixture ratio, equivalence ratio, elemental stoichiometric coefficient, and so on [24]. The equivalence ratio of an oxidizer and fuel mixture is expressed in terms of the elemental stoichiometric coefficient.

$$\phi_e = \frac{\sum(\text{Coefficient of oxidizing element in specific formula}) \times \text{Valency}}{(-1) \sum(\text{Coefficient of reducing elements in specific formula}) \times \text{Valency}} \quad (2.1)$$

When $\phi_e = 1$, a mixture is said to be stoichiometric, $\phi_e < 1$ be fuel lean and $\phi_e > 1$ be fuel rich. Stoichiometric mixtures produce maximum energy.

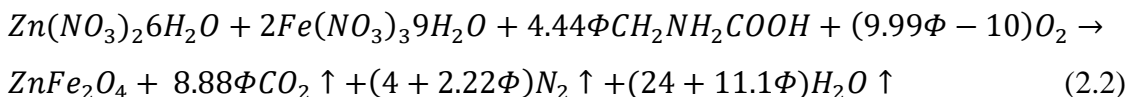
In the calculation of the equivalent ratio for CS, Oxidizing elements (like oxygen) are considered negative because they accept electrons during the combustion process. Reducing elements (like carbon, hydrogen, and metal cations) are considered positive because they donate electrons during combustion. Nitrogen is typically considered neutral since it doesn't significantly participate in the oxidation-reduction reactions during combustion. The equivalence ratio (ϕ) is determined by comparing the actual oxidizer-to-fuel ratio to the stoichiometric oxidizer-to-fuel ratio. By summing the total oxidizing and reducing valences in the oxidizer compounds and dividing by the sum of the total reducing valences in the fuel compounds, you can calculate the equivalence ratio. For a stoichiometric mixture, the F/O ratio is calculated based on the stoichiometry of the combustion reaction. This ratio ensures that all reactants are consumed in the ideal proportions for complete combustion, resulting in the formation of desired products without excess fuel or oxidizer. By summing the total oxidizing and reducing valencies in the oxidizer compounds, you can determine the molar ratio of oxidizer to fuel needed for stoichiometric combustion.

Fuels serve as complexing agents in solution, binding with metal ions. This complexation helps in achieving a more homogeneous distribution of the metal ions throughout the precursor solution, which is crucial for the uniformity of the final product. During the combustion process, fuels decompose and release energy. The energy provided is essential for reaching the temperatures necessary for the synthesis reactions to occur, leading to the formation of ceramic or metallic materials. Decomposition of the fuel also generates gases such as NH_3 (ammonia), HNCO (isocyanic acid), CO_2 (carbon dioxide), and others. These gases aid in foaming the material, creating porosity in the synthesized product. The gases also help to disperse heat uniformly throughout the material, enhancing the reaction kinetics and product homogeneity. Nitrogen-rich fuels generally produce a large volume of gas upon combustion, contributing to the foaming and porosity of the material. This is crucial in creating lightweight, porous materials with specific structural properties. N-N bond cleavage is typically highly exothermic. The release of a significant amount of energy upon decomposition not only ensures that the necessary reaction temperatures are reached quickly but also that they are sustained long enough for the synthesis to complete. The reactive nitrogen species generated from N-N bond decomposition can participate in additional chemical reactions during synthesis, potentially facilitating the formation of nitrides or other nitrogen-containing compounds in the final product. The choice of fuel in combustion synthesis is critical and depends on the desired material characteristics as well as the metal ions involved in the reaction. The effectiveness of N-N bond-containing fuels makes them particularly suitable for producing advanced ceramics and composite materials where high porosity, specific surface area, and unique microstructures are desired. An ideal fuel should possess several features: it should have a low ignition temperature, not lead to an explosion in contact with metal nitrates, be water-soluble, evolve low molecular weight, harmless gases in large amounts, yield no residual mass, be easily available, and be easy to handle.

The decomposition temperature of metal nitrates is lowered by the addition of fuel. So, the choice of fuel is critical in deciding the exothermicity of the redox reaction between the metal nitrate and the fuel. Depending upon the nature of reactants: elements or compounds (solid, liquid, or gas); and the exothermicity (adiabatic temperature, T_{ad}), CS is described as Self-propagating high-temperature synthesis (SHS); low-temperature combustion synthesis (LCS); solution combustion synthesis, sol-gel combustion, emulsion combustion, volume combustion (thermal explosion), etc.

2.3. Experimental Process:

Zinc ferrite nanoparticles were synthesized using the combustion method. Analytical grade zinc nitrate $[\text{Zn}(\text{NO}_3)_2 \cdot 6\text{H}_2\text{O}]$ (99.8%) and ferric nitrate $[\text{Fe}(\text{NO}_3)_3 \cdot 9\text{H}_2\text{O}]$ (99%) served as oxidants, while glycine $[\text{CH}_2\text{NH}_2\text{COOH}]$ (98%) acted as the fuel to facilitate the combustion reaction. In propellant chemistry, the oxidizing and reducing valences for the relevant elements are $\text{C}=4$, $\text{H}=1$, $\text{O}=-2$, $\text{N}=0$, with M values of 2 or 3, depending on the metal. For ferrites, the oxidizing valence of a divalent metal nitrate $\text{M}(\text{NO}_3)_2$ is typically -10, and for a trivalent metal nitrate $\text{M}(\text{NO}_3)_3$, it is -15. These must be counterbalanced by the total reducing valence of the fuel, glycine, which is +9. To achieve maximum energy release, the stoichiometric redox mixture requires a ratio of $-40 + 9m = 0$, where m equals 4.44 mol of glycine [29, 30]. Consequently, for the preparation of ZnFe_2O_4 , the reactants should be combined in a molar ratio of 1:2:4.44 for $\text{Zn}(\text{NO}_3)_2 \cdot 6\text{H}_2\text{O}$, $\text{Fe}(\text{NO}_3)_3 \cdot 9\text{H}_2\text{O}$, and $\text{CH}_2\text{NH}_2\text{COOH}$, respectively. At equilibrium, the combustion reaction can be represented as follows:



Here, the multiplication factor, ϕ , is used to determine different combustion conditions: fuel-lean ($\phi < 1$), stoichiometric ($\phi = 1$), and fuel-rich ($\phi > 1$). In this case, $\phi = 1$ corresponds to a glycine-to-nitrate (G/N) molar ratio of $4.44/3 = 1.48$, which represents the stoichiometric condition. This is the ratio at which the oxygen content of the oxidizer is sufficient to completely react with the fuel without requiring any heat exchange for the reaction to be fully completed.

In a typical procedure, stoichiometric amounts of zinc nitrate, ferric nitrate, and glycine ($\text{G/N} = 1.48$) were combined in a glass beaker. After mixing for 30 minutes, the hygroscopic nature of the metal nitrates resulted in the formation of a slurry. The beaker was then placed on a preheated hot plate at 350 °C. The entire combustion process was completed in less than 15 minutes, during which ignition occurred. During combustion, significant foaming was observed, and a spark that began in one corner of the mixture quickly spread, producing a voluminous and fluffy product in the beaker. The typical synthesis process is illustrated in **Fig. 2.1**.

In this study, the glycine-to-nitrate (G/N) molar ratio was varied as 0.74, 1.48, and 2.22 to achieve fuel-lean, stoichiometric, and fuel-rich conditions, respectively. Notably, no additional heat treatment was applied following the combustion synthesis.

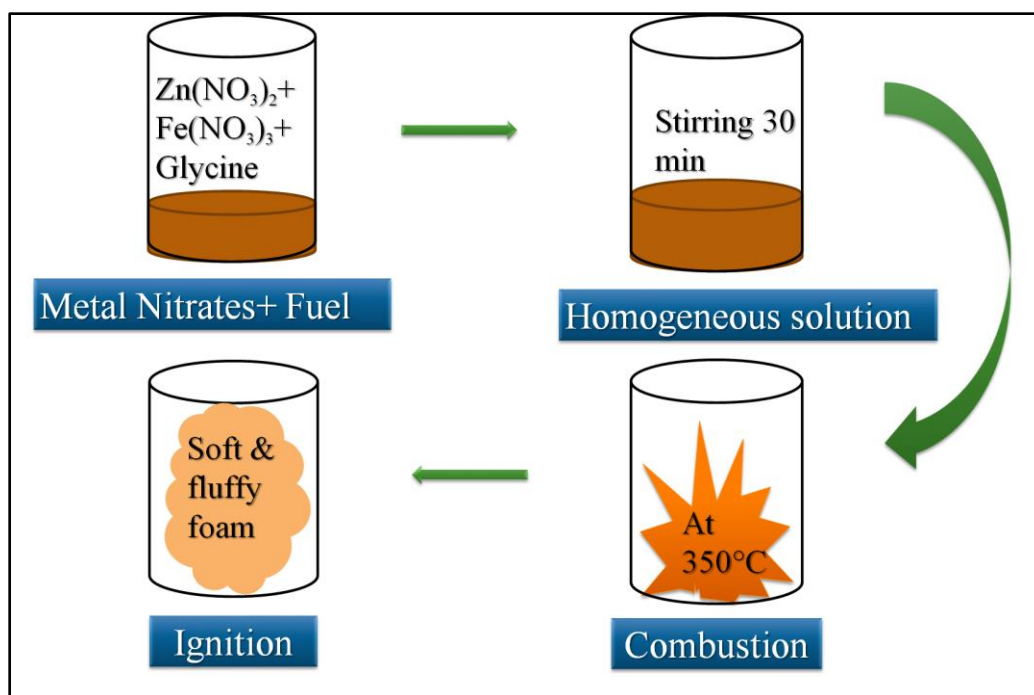


Fig.2.1: Synthesis of ZnFe₂O₄ nanoparticles using the proposed combustion method.

2.4. Characterization techniques:

Characterization techniques play a crucial role in analyzing the morphology, topography, chemical composition, and various other surface-related properties of materials. These techniques can provide detailed insight into how surface characteristics influence material performance. Here's a brief overview of some common characterization methods that are used in this work are:

2.4.1 Field emission -scanning electron microscopy (FE-SEM):

SEM images were obtained from Hitachi, Analytical make (model S-3000H), Japan. SEM is indeed a remarkable tool for visualizing three-dimensional objects, even for observers without prior knowledge of the instrument's inner workings. Its unique imaging process, which differs from our everyday experience with light-based images, allows for clear and detailed visualization of surface morphology and features. The electron column consists of an electron gun and electromagnetic lenses operating within a vacuum to generate and focus the electron beam. The scanning system controls the

movement of the focused electron beam across the specimen's surface. Detectors collect signals emitted by the specimen upon interaction with the electron beam, such as secondary and backscattered electrons. Display converts the detected signals into images visible on a TV screen or computer monitor. The vacuum system maintains the vacuum necessary for electron beam operation and sample stability. Electronic controls regulate various parameters of the SEM, such as beam intensity and scanning speed. The electron gun generates free electrons and accelerates them to energies typically ranging from 1 to 40 keV. Electromagnetic lenses focus the electron beam to a small spot size, typically less than 10 nm in diameter, allowing for high-resolution imaging. The focused electron beam is scanned across the specimen's surface using scanning coils, systematically covering the entire area of interest. When the electron beam strikes the specimen, it induces the emission of various signals, such as secondary electrons (SE) and backscattered electrons (BSE), which carry information about the specimen's surface morphology and composition (in **Fig 2.2**). Detectors collect and amplify these emitted signals, converting them into images displayed on a screen. The resulting images provide detailed topographic information about the specimen's surface. SEM images are generally intuitive and easy to interpret, especially for topographic imaging at low magnifications. SEM reveals surface features, textures, and structures with high clarity and detail, aiding in the understanding of material properties and behaviors. SEM requires minimal sample preparation compared to other techniques, making it accessible and efficient for routine analysis. Various imaging modes and techniques can enhance contrast and highlight specific features, facilitating interpretation.

The electron beam in SEM interacts with the specimen to a depth of approximately 1 μm . This interaction depth determines the volume of material from which signals are emitted and collected. Understanding this interaction depth helps in interpreting images by considering the three-dimensional structure of the specimen and the depth from which the emitted signals originate. Reliable interpretation of SEM images, particularly at high magnifications, requires a deep understanding of the image formation process. In specialized situations, such as imaging nanoscale structures or studying complex material properties, detailed knowledge of SEM operation is essential. High-magnification images may reveal subtle features or phenomena that require careful interpretation based on an understanding of electron beam behavior and specimen interactions.

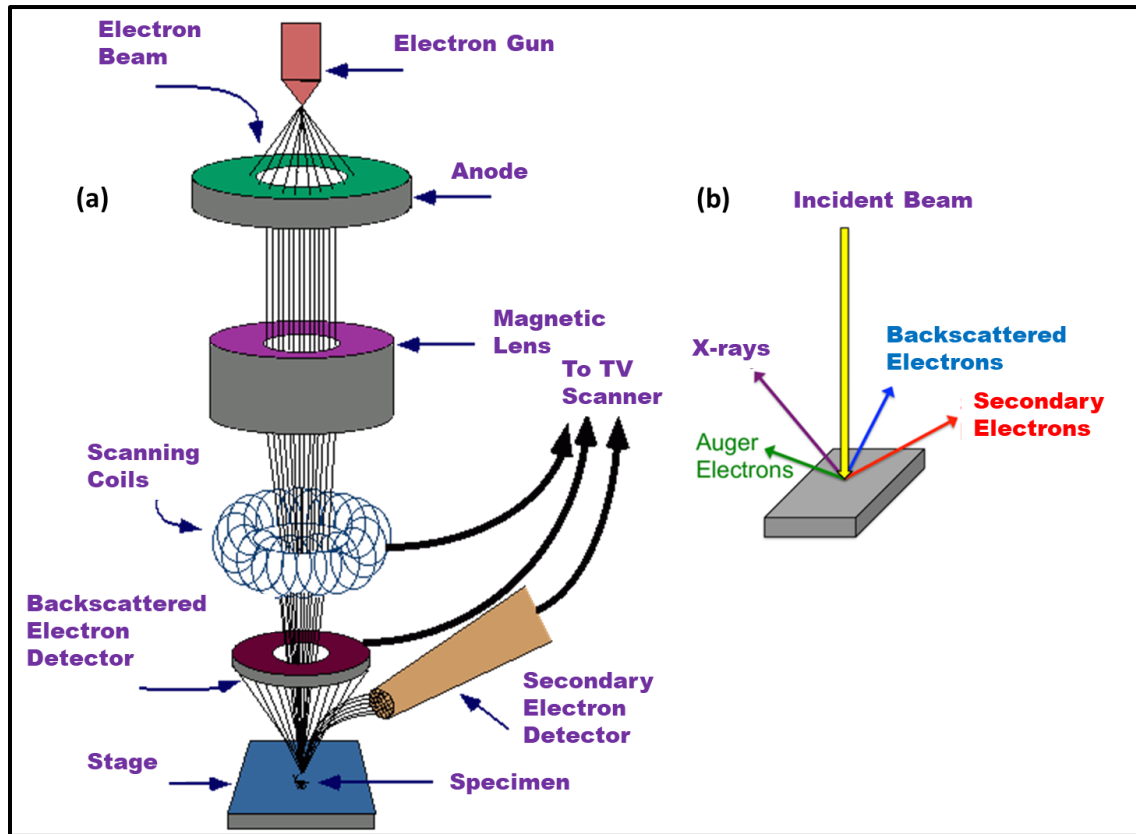


Fig. 2.2: Block diagram of SEM instrument [31].

2.4.2 Energy Dispersive X-ray Spectroscopy (EDS):

Energy-Dispersive X-ray Spectroscopy (EDS) is a powerful analytical technique used in conjunction with scanning electron microscopy (SEM) to provide elemental analysis or chemical characterization of a sample. EDS operates on the principle that each element has a unique atomic structure, which in turn emits a characteristic set of X-ray energies when excited. This unique signature allows for the identification and quantification of the elements present in the sample. A charged particle beam (usually electrons from the SEM) or a high-energy X-ray beam is focused on the specimen. This beam interacts with the atoms in the sample.

The energy from the beam excites or ejects electrons from the inner shells of the atoms in the sample. When an electron is ejected, it leaves behind a vacancy, creating what is known as a hole. Electrons from higher energy levels (outer shells) then fall into the lower energy vacant spot (hole). The transition of an electron from a higher to a lower energy level releases energy in the form of characteristic X-rays (shown ray diagram in **Fig. 2.3**). The energy dispersive spectrometer attached to the SEM detects these X-rays.

The spectrometer is capable of measuring the energies and intensities of the emitted X-rays. The energies of these characteristic X-rays are indicative of the atomic structure and energy differences between the electron shells of different elements. By analyzing these energies, the elemental composition of the specimen can be determined [32]. The following components are embedded in the EDS equipment;

1. The excitation source (X-ray beam or electron beam).
2. The X-ray detector.
3. The pulse processor.
4. The analyzer.

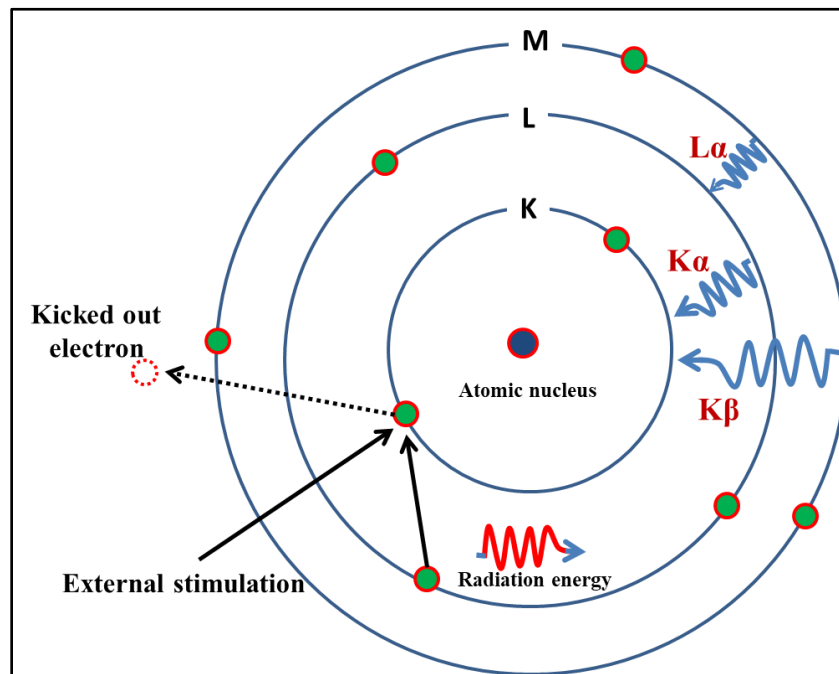


Fig. 2.3: The ray diagram of emission X-ray spectrum in EDS [32].

After the X-rays are emitted from the specimen due to electron excitation, they strike the detector. When an X-ray strikes the detector, it generates a burst of electrical charge known as a charged pulse. The amplitude of the pulse is proportional to the energy of the incident X-ray. The charged pulses are then converted into voltage signals by an amplifier. The amplifier increases the amplitude of the electrical signal to a measurable level, enhancing the signal-to-noise ratio. The voltage signals are further processed by a pulse processor. The pulse processor measures the signals and prepares them for analysis, typically by digitizing them for further processing. The processed signals, representing the energy and intensity of the detected X-rays, are sent to the analyzer. The analyzer analyzes the X-ray spectrum, plotting the number of counts (or intensity) against the X-

ray energy. Each peak in the spectrum corresponds to a specific X-ray energy characteristic of an element present in the specimen. By analyzing the X-ray spectrum, the elemental composition of the specimen can be determined. Peaks in the spectrum represent the presence of elements in the sample, with the position of each peak corresponding to the characteristic X-ray energy of a specific element. The intensity of the peaks provides information about the relative abundance of each element.

2.4.3 X-Ray Diffractometer (XRD):

The X-ray diffraction (XRD) process is a fundamental analytical technique used for characterizing the crystallographic structure, composition, and physical properties of materials. The Rigaku Miniflex-600 uses a copper anode to produce $\text{CuK}\alpha$ radiation, which has a wavelength (λ) of 1.5406 Å. The X-ray diffraction (XRD) technique is used to identify the crystal structure and confirm the phases of a material. It is a non-destructive method that provides insights into the crystalline nature of materials. Through this method, valuable information regarding the material's structure, phase composition, preferred crystal orientation, and structural properties such as lattice parameters, crystallite size, strain, and defects can be obtained. X-ray diffraction occurs when the wavelength of the incident X-rays is comparable to the spacing between the scattering centers in the crystal lattice. This diffraction phenomenon is governed by Bragg's law [33], which is expressed as:

$$2d\sin\theta = n\lambda \quad (2.3)$$

In this context, d represents the interplanar spacing, θ denotes the diffraction angle, λ signifies the wavelength of X-rays, and n indicates the order of diffraction.

In this method, the material under investigation is pulverized into a fine powder. This powder is then evenly distributed across a rectangular section of a glass slide. The sample is typically affixed to the glass using adhesive substances such as collodion grease or wax.

Various types of sample holders, including glass slides, circular discs, or thin capillaries, are employed to accommodate different instrument designs. A range of X-ray sources is available, though sealed X-ray tube sources are most commonly utilized in standard laboratory diffractometers. X-rays are generated in a sealed X-ray tube, which is

fundamentally constructed similarly to a Coolidge tube. X-rays are generated through the bombardment of high-speed electrons onto a metal target. When X-ray beams strike the sample, they scatter off the material. These scattered rays then constructively interfere according to Bragg's law, resulting in a diffracted beam. The diffracted beams are systematically scanned by moving the detector across various angles. At each angle, the detector measures either the count or count rate of X-ray photons. The obtained data is typically represented as a graph that displays the intensity of diffracted X-rays (in counts) versus the diffraction angle (2θ). When X-rays interact with a crystalline material, they generate a diffraction pattern that can be used to examine various structural properties. A schematic diagram of the X-ray diffractometer is illustrated in **Fig. 2.4**. Each crystalline material produces a unique diffraction pattern, which serves as a distinct identifier, much like a fingerprint. In a mixture, each phase generates its own individual pattern, making XRD a dependable tool for identifying different substances.

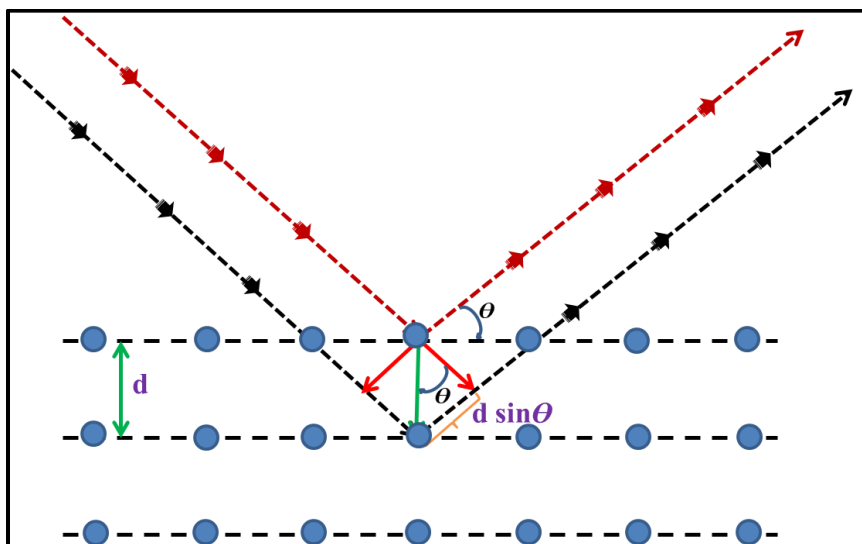


Figure 2.4: Schematic of X-ray diffractometer [34].

The powder XRD technique is highly valuable for qualitative phase analysis since each crystalline material produces a unique powder pattern, often referred to as a "powder fingerprint." This pattern is primarily influenced by two factors: (a) the size and shape of the unit cell and (b) the arrangement and atomic properties of the atoms within the unit cell. As a result, even materials with identical crystal structures can have distinct powder patterns due to variations in these factors. The powder pattern is characterized by two key features: the d-spacing of the diffraction lines and their intensity. Among these, the d-spacing is particularly significant and can be accurately measured. The d-spacing is

typically consistent across different samples unless impurities, solid solutions, stress, disorder, or metastable conditions affect the material. Quantitatively measuring the intensities of the lines in the powder pattern can be challenging and tends to vary between samples. As a result, these intensities are typically measured semi-quantitatively and may exhibit some degree of variation.

The PDF-2 2021 database comprises over 316,800 unique powder diffraction datasets, encompassing a wide range of organic, organo-metallic, inorganic, and mineral samples. These datasets are compiled into the Joint Committee on Powder Diffraction Standards (JCPDS) database. Phase identification is achieved by comparing the diffraction pattern of a sample with the standard JCPDS cards in the database.

X-ray diffraction (XRD) stands as one of the most prevalent and non-destructive characterization techniques utilized for analyzing a diverse range of materials, including fluids, powders, and crystals. Its application spans from research to production and engineering endeavors. Particularly crucial for structural materials characterization, XRD employs the Debye-Scherrer method to extract valuable structural information. This technique employs X-ray diffraction on powder or microcrystalline samples, aiming for an even representation of all possible crystalline orientations. This uniform orientation distribution effectively condenses the three-dimensional reciprocal space, commonly explored in single crystal diffraction, down to a single dimension. Typically represented by reciprocal axes x^* , y^* , and z^* or in spherical coordinates as q , ϕ^* , and χ^* , the Debye-Scherrer method simplifies this further by averaging over ϕ^* and χ^* , leaving q as the primary measurable parameter. This approach allows for the examination of the structure in a more generalized, yet comprehensive manner.

The diffracted intensity is displayed either as a function of the scattering angle 2θ or the scattering vector q , which detaches it from the dependence on the X-ray wavelength used. This diffractogram serves as a distinctive 'fingerprint' for materials, providing laboratories with a rapid method to analyze and characterize unknown substances across various fields such as metallurgy, mineralogy, forensic science, archaeology, and the biological and pharmaceutical sciences. Identification is accomplished by comparing the obtained diffractogram with established standards or by consulting international databases.

2.4.4 Transmission electron microscope (TEM):

Transmission Electron Microscopy (TEM) is the foremost technique for investigating material structures at the nanometer scale. Similar to an optical microscope but using an electron beam instead of light, TEM offers detailed insights into the morphology and size characteristics of materials, providing a deeper understanding of their structural intricacies. Schematic of TEM is shown in **Fig. 2.5**.

In TEM, an electron gun produces a beam of monochromatic electrons, which is focused into a thin, coherent beam by coherent lenses 1 and 2. When this electron beam interacts with the specimen, some electrons are transmitted through it. These transmitted electrons are subsequently focused by the objective lens to create an image. For successful TEM analysis, it is crucial that the sample is thin enough to allow electron transmission. The minimum thickness required for TEM analysis is approximately 0.5 μm .

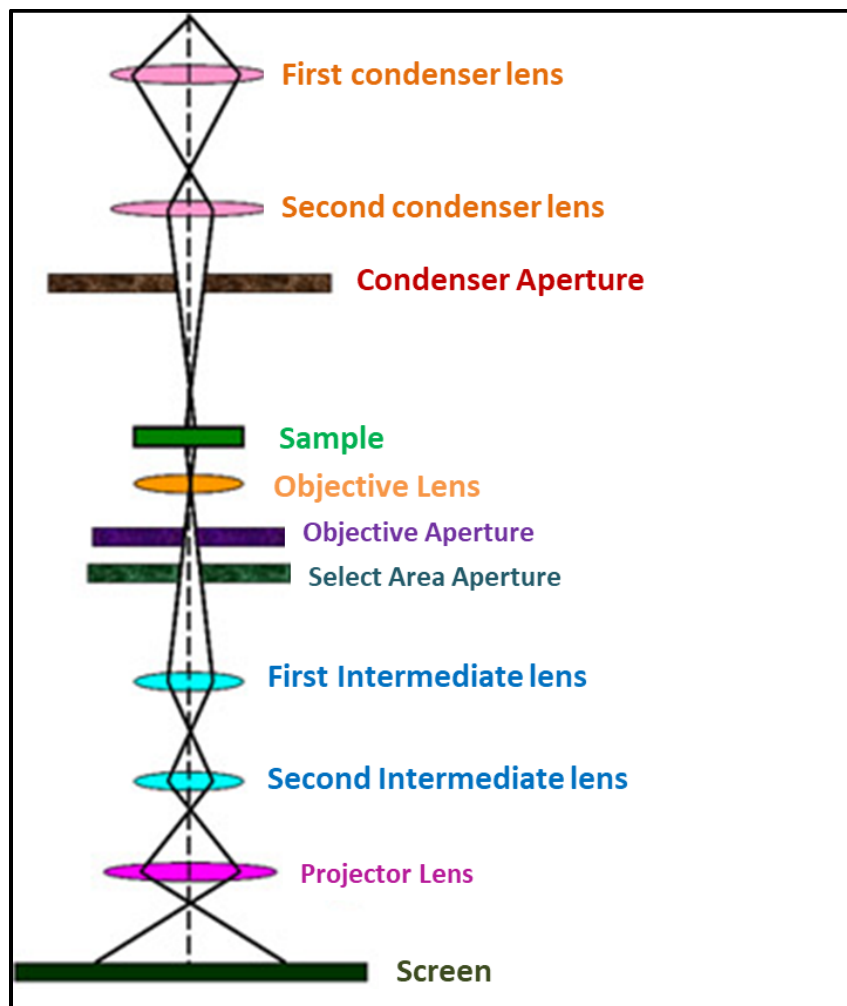


Fig. 2.5: The block diagram of TEM [35].

When examining powder samples, they are first dispersed in a dispersing medium to create a colloidal solution. A small drop of this solution is then deposited on a conducting grid, usually made of copper or silver, and allowed to dry. This grid acts as the specimen for TEM analysis, with a typical square size of about 1 μm .

2.4.5 X-Ray Photoelectron Spectroscopy (XPS):

X-ray photoelectron spectroscopy (XPS), also known as electron spectroscopy for chemical analysis (ESCA), is employed to identify the surface properties of materials or thin films. This technique utilizes the photoelectric effect, with X-rays serving as the photon source. When an X-ray beam hits the material surface, it ejects electrons, known as photoelectrons. Elemental identification can be accomplished directly by examining the kinetic energies of the emitted photoelectrons. Furthermore, the intensities of these photoelectrons offer insights into the relative composition of the elements present in the material. The kinetic energy of the ejected electrons is determined by the following relationship:[36],

$$\text{K.E.} = h\nu - \text{B.E.} - \phi_s \quad (2.4)$$

In this formula, K.E. represents the kinetic energy of the ejected photoelectrons, $h\nu$ is the energy of the X-ray photons, B.E. stands for the binding energy of the electrons in their atomic orbitals, and ϕ_s denotes the work function of the spectrometer. These parameters are used to calculate the specific energies involved in the ejection of electrons from the material's surface upon exposure to X-ray photons.

In X-ray photoelectron spectroscopy (XPS), the ionization of inner-shell electrons is triggered by the absorption of photons. This leads to the emission of electrons characteristic of each element due to the unique binding energies associated with their core-level atomic orbitals. Initially, a survey scan is conducted in XPS to record all potential energy levels, thereby confirming the elements present in the sample. An energy spectrum is created by graphing the binding or kinetic energies of the emitted electrons. This plot displays the amount of each element in the sample, with peaks at specific energies corresponding to individual elements. These peaks are directly tied to the elements' electronic configurations. Furthermore, this technique is valuable for determining the oxidation states of elements. A ray diagram of the XPS technique is shown in **Fig. 2.6**. XPS does not offer a comprehensive chemical analysis because it is

primarily a surface phenomenon. The signals used for analysis typically come from just a few atomic layers at the surface, with only minimal contribution from the deeper regions of the material.

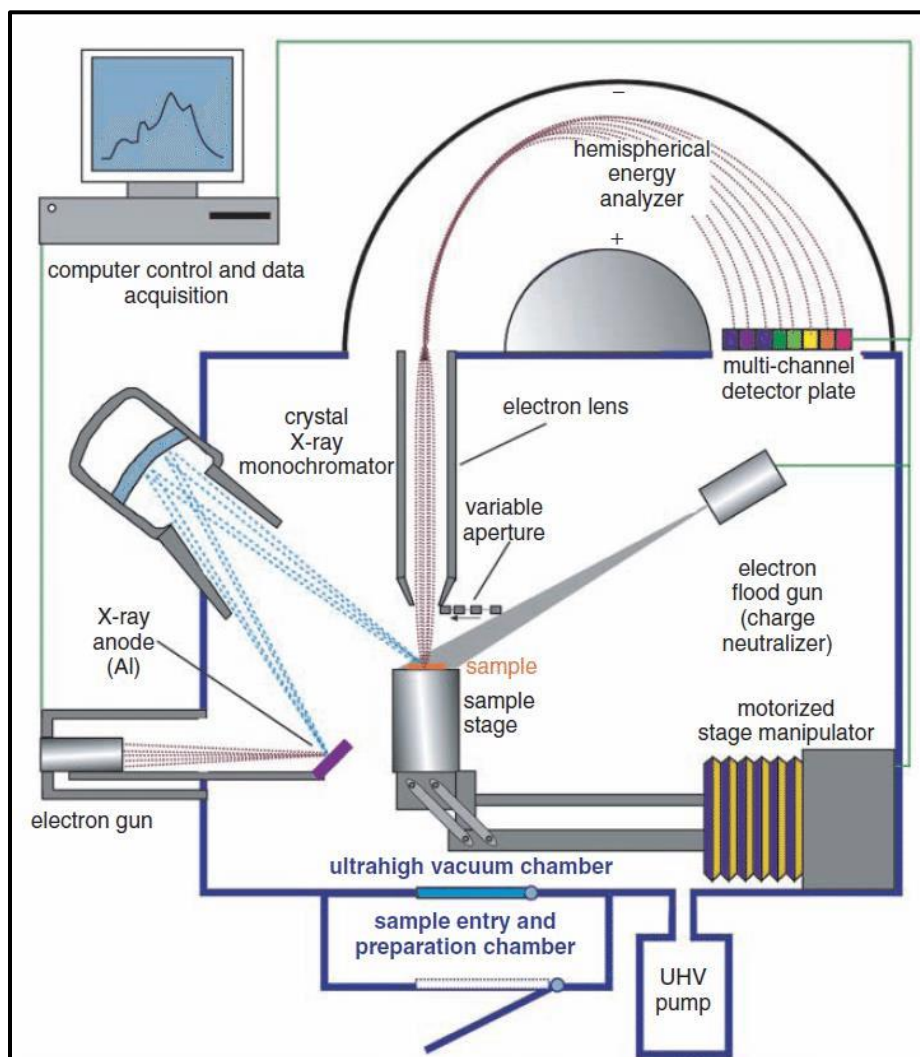


Fig. 2.6: XPS instrument analysis [37].

2.4.6 Brunauer-Emmett-Teller (BET):

The BET (Brunauer-Emmett-Teller) theory is a critical method for measuring the physisorption of gas molecules on solid surfaces and is a fundamental technique for determining specific surface area and pore volume. Measurements of specific surface area are typically conducted using the Freundlich, Langmuir, and BET isotherm models. Three isotherms are utilized for measuring specific surface area, which are briefly explained below.

Freundlich adsorption isotherm:

In 1909, the German scientist Freundlich proposed an empirical relationship that describes the amount of gas adsorbed per unit mass of solid as a function of pressure at a specific temperature. It is expressed using the following eqn.

$$\frac{x}{m} = k \cdot p^{1/n} \quad (2.5)$$

In the Freundlich adsorption isotherm equation, x represents the amount of adsorbate adsorbed, m represents the amount of adsorbent, p represents the pressure of the adsorbate, and k and n are constants.

Limitation of Freundlich isotherm:

The Freundlich isotherm approximately describes adsorption behavior, with the value of $1/n$ ranging from 0 to 1. Thus, this equation is most accurate within a limited pressure range.

1. When $1/n = 0$, X/m is constant the adsorption is independent of pressure.
2. When $1/n = 1$, $X/m = k \cdot p$ i.e $X/m \propto p$

The experimental results confirm both conditions mentioned above. At high pressures, the experimental isotherms invariably tend toward a saturation point.

The Freundlich isotherm does not account for this observation and thus is ineffective at high pressures. Following this model, two other isotherms were developed: the Langmuir and BET adsorption isotherms. The Langmuir isotherm assumes adsorption occurs in a single monolayer, whereas the BET isotherm considers adsorption as a multilayer process.

Langmuir isotherm:

Langmuir introduced this model in 1916; it applies to monolayer adsorption. It estimates the adsorption capacity of the adsorbent as follows:

$$a = \frac{K_1 p}{K_2 p + 1} \quad (\text{a gives } x/m \text{ in Freundlich}) \quad (2.6)$$

Where a is the amount of adsorbate adsorbed per gram of adsorbent, p is the equilibrium pressure, and k_1 and k_2 are constants. The BET isotherm, proposed by

Brunauer, Emmett, and Teller in 1938, is designed for measuring multilayer adsorption of an adsorbate per gram of adsorbent. This isotherm is used to describe the surface area and pore volume of solid materials using the BET formula.

$$\frac{1}{W \left(\frac{P}{P_0} \right) - 1} = \frac{1}{W_m C} + \frac{C-1}{W_m C} \left(\frac{P}{P_0} \right) \quad (2.7)$$

In the BET isotherm equation, W represents the weight of gas adsorbed, P/P_0 stands for the relative pressure, W_m denotes the weight of adsorbate adsorbed as a monolayer, and C is the BET constant. The concept of the BET isotherm is utilized for multilayer adsorption, incorporating various hypotheses.

- a) Adsorbate is physically adsorbed on solid surface
- b) No interaction occurs between each adsorption isotherm
- c) Also, Langmuir theory is used for each layer

The number of active sites is influenced by factors such as particle size, particle morphology, surface texture, and porosity. These characteristics collectively determine the accessibility and availability of sites for adsorption on the material's surface. The ray diagram of BET isotherm is shown in **Fig. 2.7**.

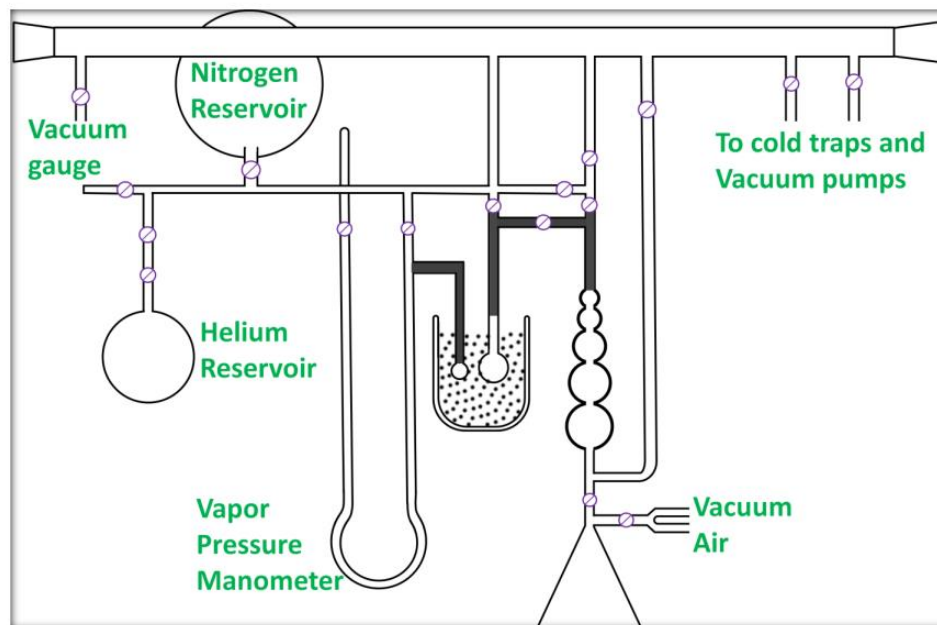


Fig. 2.7: Schematic diagram of BET isotherm [38].

2.4.7. UV-visible Spectroscopy:

UV-visible spectroscopy encompasses both absorption and reflectance spectroscopy within the UV-visible spectrum. When light interacts with matter, it may be absorbed, reflected, or transmitted. Molecules with π -electrons or non-bonding electrons (n-electrons) absorb ultraviolet or visible light, leading to the excitation of electrons from their ground state to higher anti-bonding molecular orbitals. The wavelength of light absorbed by electrons is determined by the energy gap between the highest occupied molecular orbital (HOMO) and the lowest unoccupied molecular orbital (LUMO). This wavelength is associated with the types of bonds present in the molecule, offering information about its functional groups. [39].

UV-visible spectroscopy, unlike IR spectroscopy, involves electronic transitions in the ultraviolet or visible regions, while IR spectroscopy focuses on vibrational transitions. UV-visible spectroscopy assesses analyte interactions by measuring the change in intensity of incident light within the UV (10-400 nm) and visible (400-800 nm) ranges as a function of wavelength. This is accomplished by comparing the intensity of light passing through a sample with that passing through a reference or blank. UV-visible spectroscopy provides quantitative data on the concentration of known solutes and offers valuable insights into solid-state samples.

A UV-visible spectrophotometer is composed of a light source, monochromator, sample compartment, detector, and recorder. To cover the full UV-visible range, it uses two light sources: a deuterium lamp and a tungsten lamp. Light from the lamps passes through a diffraction grating monochromator, where a half mirror splits it into two monochromatic beams of equal intensity. One beam travels through the sample solution, while the other passes through the reference solution.

A detector measures the intensity of both transmitted beams, determining the sample concentration by comparing the transmitted light through the sample (I) with the incident light (I_0) and then sending this information to the recorder. Quartz cuvettes are used as sample holders because they do not interfere in the UV or visible regions. Detectors in a spectrophotometer can include a barrier layer cell, photomultiplier tube, or photocell. The schematic of a UV-visible spectrophotometer is shown in **Fig. 2.8**.

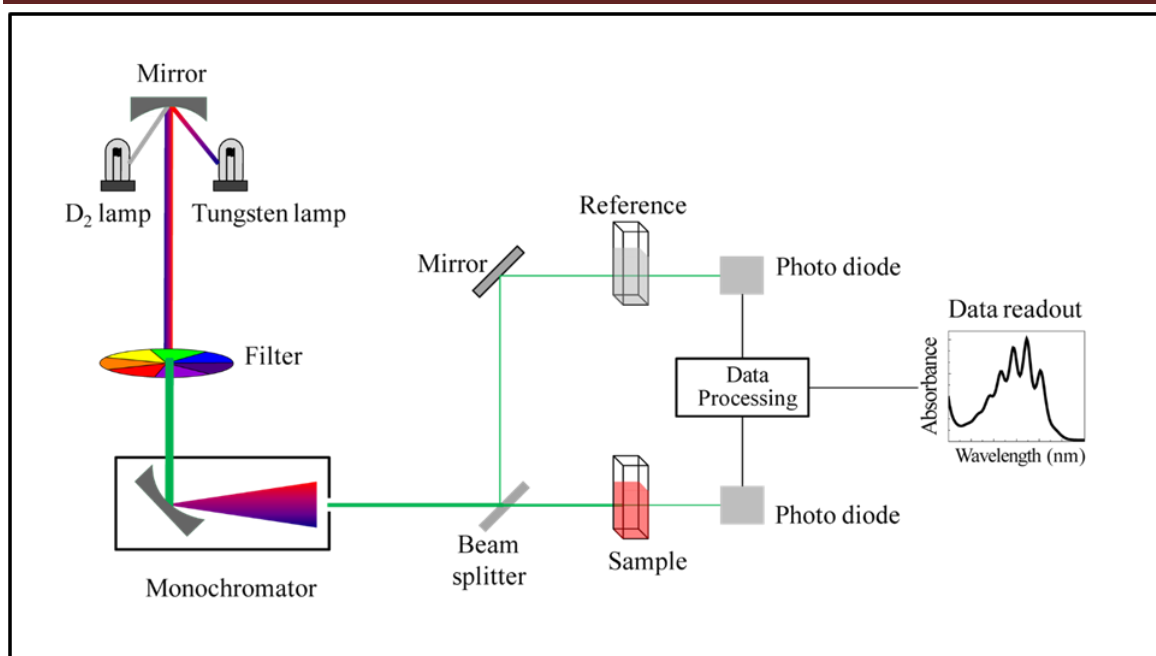


Fig. 2.8: Schematic representation of UV-visible spectrophotometer [40].

UV-visible DRS spectroscopy is employed to analyze solid samples, primarily for calculating the band gap energy values of these materials. Light cannot penetrate solid samples; instead, it reflects off their surfaces. When incident light reflects symmetrically with respect to the normal line, it is called specular reflection, whereas light scattered in various directions is termed diffuse reflection. When light is directed at a 0° angle, the specularly reflected light exits the integrating sphere and is not detected. Consequently, only the diffusely reflected light is collected by two large hemispherical mirrors positioned above the sample, which is then analyzed by the detector.

2.4.8. Fourier transforms infrared Spectroscopy:

Infrared (IR) spectroscopy is an analytical technique that examines the interaction between infrared light and matter. Infrared light occupies the electromagnetic spectrum between visible light and microwaves, with wavelengths from 780 nm to 1 mm. Fourier Transform Infrared (FTIR) spectroscopy specifically operates within the IR portion of the spectrum. This region is divided into three sub-regions based on the radiation sources, optical systems, and detectors required for each. An IR spectrophotometer uses a grating or prism-grating to cover the range of 400 to 4000 cm^{-1} , allowing for high resolution and precision in measurements.

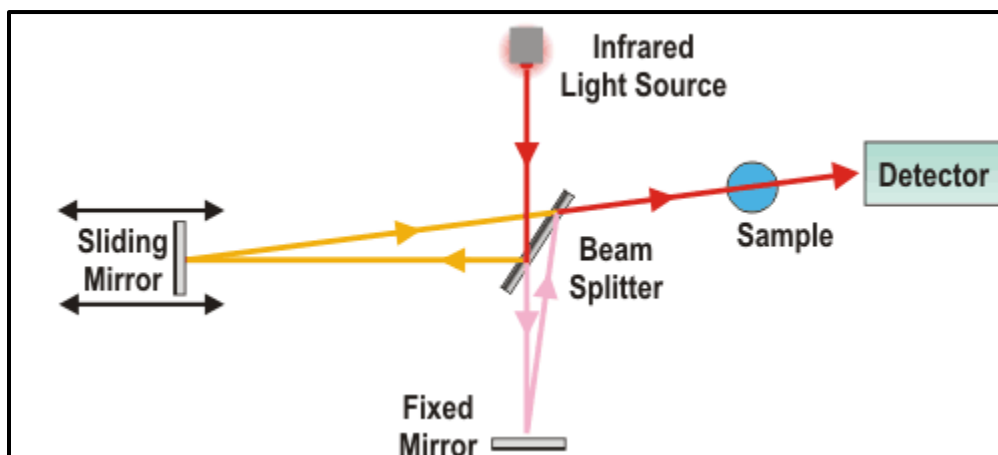


Fig. 2.9: Schematic representation of the working principle of FTIR [41]

FTIR spectroscopy operates on the principle that interference between two radiation beams produces an interferogram. This signal is generated based on the path length difference between the two beams, which are reflected from mirrors located in the interferometer block. The distance and frequency domains are interconvertible through Fourier transformation, giving rise to the name Fourier Transform Infrared (FTIR) spectroscopy.

The primary distinction between an FTIR spectrometer and a dispersive IR spectrometer lies in the use of the Michelson interferometer. This interferometer is central to FTIR spectrometers, splitting a single light beam into two separate paths. It then recombines these beams and directs them to the detector, where the intensity differences between the beams are measured based on the path difference. The operating principle of the FTIR is illustrated in **Fig. 2.9**.

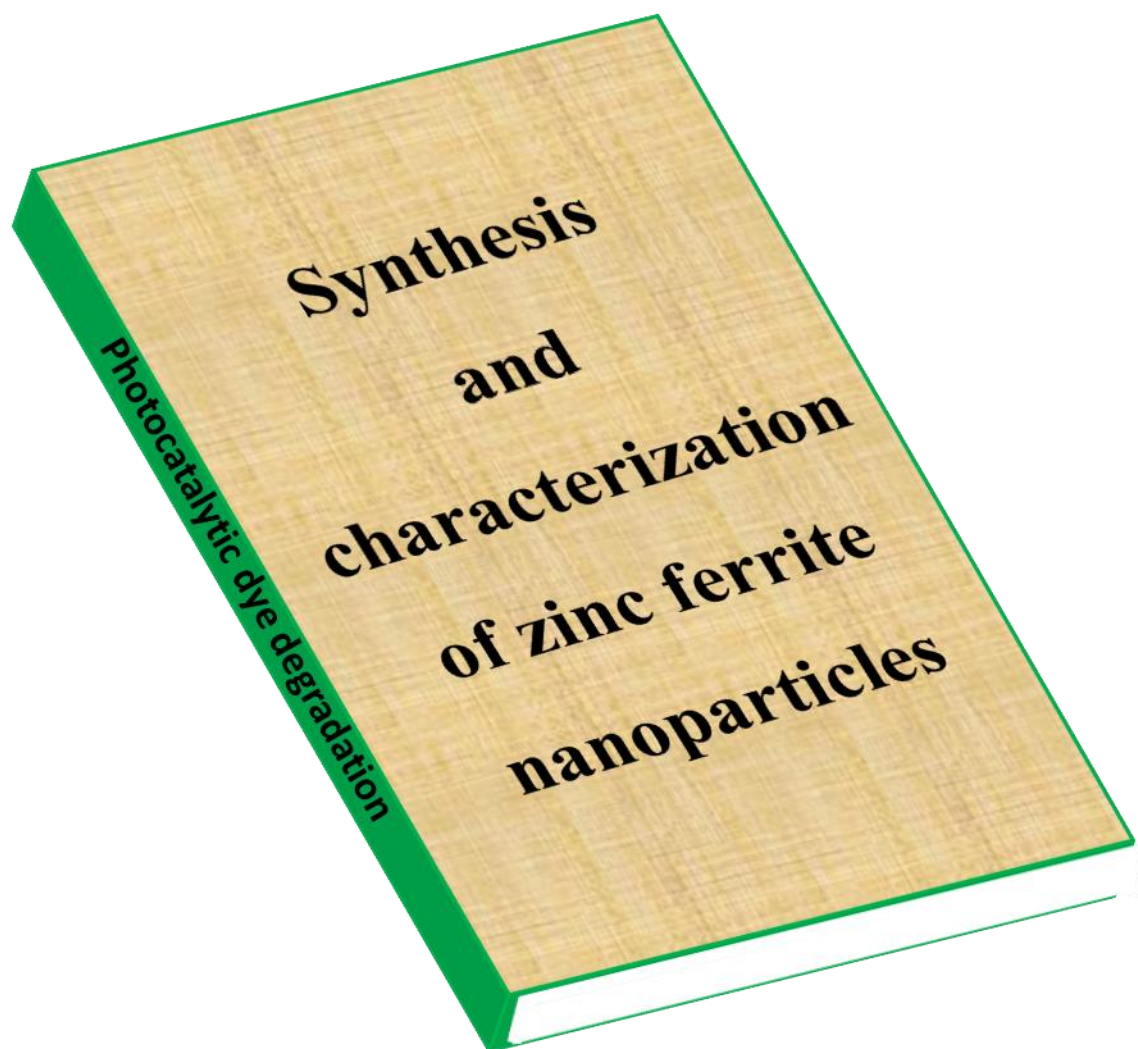
2.5 References:

1. Siddique F, Mirzaei A, Gonzalez-Cortes S, Slocombe D, Al-Megren H, Xiao T, Rafiq M, Edwards P. *Chemosphere.*, 287, (2022), 132035.
2. Balakrishnan G, Velavan R, Batoo K, Raslan E. *Results in Physics.*, 16, (2020), 103013 (1-17).
3. Piumetti M, Fino D, Russo N. *Applied Catalysis B: Environmental.*, 163, (2015), 277-287.
4. Guo H, Zhang Z, Jiang Z, Chen M, Einaga H, Shangguan W. *Journal of Environmental Sciences.*, 98, (2020), 196-204.
5. Bakkiyaraj R, Bharath G, Ramsait K, Abdel-Wahab A, Alsharaeh E, Chen S, Balakrishnan M. *RSC advances.*, 6, (2016), 51238-51245.
6. Kang W, Ozgur D, Varma A. *ACS Applied Nano Materials.*, 1, (2018), 675-685.
7. Patil S, Dasari H. *Materials Science for Energy Technologies.*, 2, (2019), 485-489.
8. Kovacheva D, Gadjov H, Petrov K, Mandal S, Lazarraga M, Pascual L, Amarilla J, Rojas R, Herrero P, Rojo J. *Journal of Materials Chemistry.*, 12, (2002), 1184-1188.
9. Li F, Zhao Y, Liu Y, Hao Y, Liu R, Zhao D. *Chemical Engineering Journal.*, 173, (2011), 750-759.
10. Xu B, Xiao T, Yan Z, Sun X, Sloan J, González-Cortés S, Alshahrani F, Green M. *Microporous and Mesoporous Materials.*, 91, (2006), 293-295.
11. González-Cortés S, Xiao T, Costa P, Fontal B, Green M. *Applied Catalysis A: General.*, 270, (2004), 209-222.
12. Essawy A, Alsohaimi I, Alhumaimess M, Hassan H, Kamel M. *Journal of Environmental Management.*, 271, (2020), 110961 (1-13).
13. Mukasyan A, Dinka P. *International Journal of Self-Propagating High-Temperature Synthesis.*, 16, (2007), 23-35.
14. Erri P, Pranda P, Varma A. *Industrial & Engineering Chemistry Research.*, 43, (2004), 3092-3096.
15. Kefeni K, Mamba B, Msagati T. *Separation and Purification Technology.*, 188, (2017), 399-422.
16. Mooney K, Nelson J, Wagner M. *Chemistry of Materials.*, 16, (2004), 3155-3161.
17. Cornejo D, Medina-Boudri A, Bertorello H, Matutes-Aquino J. *Journal of Magnetism and Magnetic Materials.*, 242, (2002), 194-196.

18. Duong G, Hanh N, Linh D, Grössinger R, Weinberger P, Schafner E, Zehetbauer M. *Journal of Magnetism and Magnetic Materials.*, 311, (2007), 46-50.
19. Millot N, Le Gallet S, Aymes D, Bernard F, Grin Y. *Journal of the European Ceramic Society.*, 27, (2007), 921-926.
20. Baldi G, Bonacchi D, Innocenti C, Lorenzi G, Sangregorio C. *Journal of Magnetism and Magnetic Materials.*, 311, (2007), 10-16.
21. Junior A, de Oliveira Lima E, Novak M, Wells Jr P. *Journal of Magnetism and Magnetic Materials.*, 308, (2007), 198-202.
22. Park S, Kim J, Kim C, Kim C. *Current Applied Physics.*, 8, (2008), 784-786.
23. Costa A, Tortella E, Morelli M, Kaufman M, Kiminami R. *Journal of Materials Science.*, 37, (2002), 3569-3572.
24. Deraz N. *Journal of Analytical and Applied Pyrolysis.*, 88, (2010), 103-109.
25. Ai L, Jiang J. *Current Applied Physics.*, 10, (2010), 284-288.
26. De Biasi R, Figueiredo A, Fernandes A, Larica C. *Solid State Communications.*, 144, (2007), 15-17.
27. Yan C, Xu Z, Cheng F, Wang Z, Sun L, Liao C, Jia J. *Solid State Communications.*, 111, (1999), 287-291.
28. Xiao S, Jiang W, Li L, Li X. *Materials Chemistry and Physics.*, 106, (2007) 82-87.
29. Franco A, Pereira Alves T, de Oliveira Lima E, da Silva Nunes E, Zapf V. *Applied Physics A.*, 94, (2009), 131-137.
30. Jain S, Adiga K, Verneker V. *Combustion and Flame.*, 40, (1981), 71-79.
31. https://icme.hpc.msstate.edu/mediawiki/index.php/Scanning_Electron_Microscopes.html.
32. http://www.wikiwand.com/en/Energy-dispersive_X-ray_spectroscopy.
33. Cullity B, Smoluchowski R. *Physics Today.*, 10, (1957), 50-50.
34. http://chemwiki.ucdavis.edu/Analytical_Chemistry/Instrumental_Analysis/Diffraction/Powder_X-ray_Diffraction.
35. <https://www.mtm.kuleuven.be/equipment/TEM-CM-200/TEM-CM-200>.
36. Kerber S, Barr T, Mann G, Brantley W, Papazoglou E, Mitchell J, *Journal of Materials Engineering and Performance.* 7, (1998), 329-333.
37. <http://ywcmatsci.yale.edu/sites/default/files/resize/images/XPS-1-500x294.JPG>.
38. http://www.pharmacopeia.cn/v29240/usp29nf24s0_c846.html.
39. Akash M, Rehman K. Singapore: Springer., (2020).

40. [https://upload.wikimedia.org/wikipedia/commons/9/95/Schematic of UV visible spectrophotometer.png](https://upload.wikimedia.org/wikipedia/commons/9/95/Schematic_of_UV_visible_spectrophotometer.png).
41. <https://www.slri.or.th/bdd/th/22-%E0B9%8C/66-ftir-micro-spectrometer.html>.

CHAPTER III



3.1 Introduction:

Water pollution is a critical environmental issue primarily caused by the release of harmful substances, including organic dyes and heavy metals, in industrial wastewater [1]. These pollutants pose a serious threat to humans, animals, plants, and aquatic ecosystems [2]. Various types of dyes, such as synthetic, azo, acidic, basic, reactive, diazo, and anthraquinone, further contribute to water pollution [3]. Cationic dyes like methylene blue (MB) are challenging to remove from wastewater due to their harmful effects, and they are commonly used in industries for applications like coloring paper, clothing dye, photosensitizers, and redox indicators [4-6]. Several wastewater treatment methods exist, including physical-chemical processes like coagulation, irradiation, ozonation, chemical oxidation, ion exchange, adsorption, and reverse osmosis [7]. Photocatalysis, particularly visible light-driven photocatalysis, has emerged as a promising technology for wastewater cleanup, effectively breaking down dyes by absorbing a broad spectrum of light and promoting the formation of hydroxyl groups [8]. Nanoparticles responding to visible light, such as zinc ferrite (ZnFe_2O_4), have shown effectiveness in photocatalytic degradation of MB and other dyes, making them promising for wastewater treatment [9 -13]. Their choice is driven by affordability, non-toxicity, and magnetic properties, especially under visible light exposure [14,15].

In photocatalysis, the role of surface area is crucial in influencing the efficiency of the process. A larger surface area provides more active sites for photocatalytic reactions, enhancing the contact between the catalyst and the target pollutants [16-17]. Improving surface area in materials, particularly for catalytic applications, often involves using template-based and template-free methods. Template-free methods are often simpler, cost-effective, and do not require the use of complex templates. While template-based methods offer valuable control over the final material's structure, researchers often weigh these advantages and consider alternative approaches, such as template-free methods or innovative modifications to increase efficiency.

The ZnFe_2O_4 spinel structure has emerged as a promising solution for dye removal, demonstrating photocatalytic activity under visible light irradiation [18,19,21]. Makofane et al. [20] reported remarkable results that 99.8% removal of MB achieved at

pH 12 within 45 minutes, with an optimal ZnFe_2O_4 dosage of 25 mg. Ullah et al. [9] reported the degradation (99.9%) of remazol brilliant violet 5R under specific conditions at pH 10, and 0.1 g of ZnFe_2O_4 , with 6 mM of H_2O_2 within 30 minutes.

In this context, the combustion synthesis, specifically the glycine nitrate process, provides a promising alternative for the fabrication of zinc ferrite nanoparticles. This method offers distinct advantages, including the rapid and self-sustaining nature of the fuel-oxidant combustion reaction. The resultant high-surface-area, compositionally homogeneous powder, characterized by low levels of residual carbon, further enhances its potential for applications in photocatalysis. These properties can be fine-tuned by varying the preparative parameters such as fuel to oxidizer ratio.

One critical factor influencing the properties of the synthesized nanoparticles is the adiabatic flame temperature, a parameter dependent on the nature of the fuel and the fuel-to-oxidant ratio (F/O). The crystallization and formation of the desired compound phase are significantly influenced by the adiabatic flame temperature. Notably, very little prior work has systematically investigated the impact of the F/O ratio on product characteristics, particularly concerning thermodynamic considerations, including adiabatic flame temperature and heat absorbed during the reaction. [22,23]

To address this gap, the present study explores the effect of the glycine-to-nitrate (G/N) ratio on the powder characteristics of ZnFe_2O_4 , focusing on the thermodynamic aspects of the combustion reactions. The chosen fuel, glycine ($\text{NH}_2\text{CH}_2\text{COOH}$), proves to be a cost-effective alternative to traditional options such as urea and citric acid. Its selection is justified not only by economic considerations but also by its relatively negative heat of combustion ($-3.24 \text{ kcal g}^{-1}$), surpassing that of urea ($-2.98 \text{ kcal g}^{-1}$) and citric acid ($-2.76 \text{ kcal g}^{-1}$) [24].

This study aims to provide a comprehensive understanding of the combustion synthesis process, shedding light on its potential for optimizing nanoparticle characteristics for enhanced photocatalytic applications. The systematic variation of the glycine-to-nitrate (G/N) molar ratio has a notable impact on the characteristics of the resulting product, specifically influencing changes in nanoparticle porosity and surface area.

The systematic evaluation of variation in morphology, porosity, surface area of nanoparticles correlating with varying composition of fuel has been carried out. This contribution underscores the potential application of our synthesized nanoparticles in the efficient photocatalytic degradation of dyes, addressing environmental concerns related to water pollution.

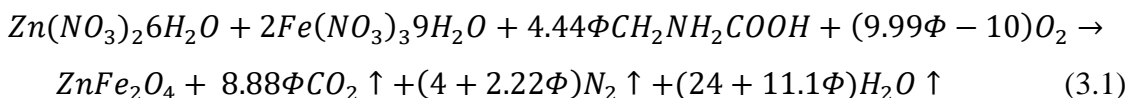
3.2 Experimental:

3.2.1 Preparation of Zinc Ferrite Nanoparticles:

In a synthesis 0.2M of zinc nitrate, 0.4M of ferric nitrate and glycine were mixed in a beaker. The metal nitrates (Zn and Fe) were employed as an oxidizer while glycine as a complexing and reducing agent. The mixed solution was kept on a hot plate at 350°C for 45 min to ignite the solution during the combustion process. Then the fluffy $ZnFe_2O_4$ powder was formed. As the amount of glycine (fuel) is significant the glycine to nitrate ratio (G/N) was modified as 0.48, 0.74, 1.48, 2.22, and 2.96. Thus, three alternative combustion systems are produced i.e., fuel lean, fuel efficient, and fuel rich, with the stoichiometric combustion ratio being $G/N = 1.48$. The samples were indexed as Z1, Z2, Z3, Z4, and Z5 for G/N ratios 0.48, 0.74, 1.48, 2.22, and 2.96, respectively.

3.2.2 Thermodynamic Analysis:

The evolution of favourable gases such as H_2O , CO_2 , and N_2 during the combustion reaction is due to the stoichiometric addition of fuel into nitrate solution. The reaction mechanism of nitrates and glycine in combustion reaction is described as follows:



where Φ is the multiplier to get fuel lean ($\Phi < 1$), fuel stoichiometric ($\Phi = 1$), and fuel rich condition ($\Phi > 1$). In above reaction, $\Phi = 1$ illustrates $G/N = 4.44/3 = 1.48$ [25,26]. As a result, the various values of Φ in the preceding equation indicate various G/N ratios. Theoretical calculations using thermodynamic factors like reaction and flame temperatures enthalpy aid in predicting the ignition stage and initiating the combustion reaction. The heat of creation of products and reactants determines the enthalpy of a process.

The enthalpy of reaction is calculated using the equation below:

$$\Delta H^\circ = (\sum n \Delta H_f^\circ)_{products} - (\sum n \Delta H_f^\circ)_{reactants} \quad (3.2)$$

Where, ‘n’ denotes the number of moles, ‘ ΔH_f° ’ denotes the heat of formation, and ‘ ΔH° ’ denotes the reaction enthalpy [27]. Thermodynamic information for different reactants and products used in combustion is presented in **Table 3.1** and is accessible in the literature.

Table 3.1. Adiabatic flame temperature measurement needs thermodynamic information.

Compound	Heat of formation ΔH_f° (kcal mol ⁻¹)	Heat capacities C_p (cal mol ⁻¹ K)
$Zn(NO_3)_2 \cdot 6H_2O$	-550.92	0.0722
$Fe(NO_3)_3 \cdot 9H_2O$	-785.2	-
CH_2NH_2COOH	-79.71	-
O_2	0	$5.92 + 0.00367 T$
CO_2	-94.051	$10.34 + 0.00274 T$
N_2	0	$6.5 + 0.001 T$
H_2O	-57.79	$7.2 + 0.0036 T$
$ZnFe_2O_4$	-281.81	-

Using thermodynamic data (**Table 3.1**) and the enthalpy of reaction as a function of may be derived in Eq. (1) as follows: [28].

$$\Delta H^\circ = 464.23 + \Phi(-1122.72) \quad (25^\circ C, kcal) \quad (3.3)$$

Theoretically, this formula can be used to determine how much heat the product received during the combustion reaction:

$$Q = -\Delta H^\circ = \int_{298}^{T_{ad}} (\sum n c_p)_{products} dT \quad (3.4)$$

To compute adiabatic flame temperature (T_{ad}), modify Eq. (4) as follows,

$$T_{ad} = \frac{Q}{c_p} \quad (3.5)$$

Where, T is the reference temperature ($T = 298\text{ K}$), C_p is a heat capacity at constant pressure, Q is the adiabatic heat absorbed by the products, and T is the reference temperature. For different G/N ratios, the heat absorbed by the products and the adiabatic flame temperatures were estimated and summarized in **Table 3.2** using data from **Table 3.1** and Eq^{ns}. (3), (4), and (5). When predicted, as the amount of glycine in the product increases, so does the theoretically estimated T_{ad} and the heat absorb by the product. The reaction temperature and T_{ad} rise as the G/N ratio rises. However, increasing the G/N ratio beyond the optimal temperature value causes a fall in reaction temperature owing to the number of gases emitted during the reaction, which might cause heat loss. As a result, the reaction temperature is lower than the theoretically expected T_{ad} .

Table 3.2. Variations in the quantity of heat absorbed by the product (Q), the adiabatic flame temperature (T_{ad}), and the number of moles of gases generated during combustion at various G/N ratios.

Sample	G/N	Q (kcal mol ⁻¹)	T_{ad} (K)	Number of moles of gases evolved
Z1	0.48	85.053	298.289	35.32
Z2	0.74	-105.808	619.8	39.1
Z3	1.48	-667.16	1843.1	50.2
Z4	2.22	-1228.5	2595.1	61.3
Z5	2.96	-1789.8	3104.2	72.4

3.3. Results and discussion:

3.3.1 X-ray diffraction analysis:

X-ray diffraction (XRD) technique was employed to identify the crystallography of $ZnFe_2O_4$. The cubic spinel structure was confirmed by XRD pattern of $ZnFe_2O_4$ material as shown in **Fig. 3.1a**. The diffraction peaks corresponding to crystallographic planes (220), (311), (222), (400), (422), (511), and (440) aligned well which enabled to confirmation of cubic spinel structure of $ZnFe_2O_4$ and additionally supported by the $Fd3m$ space group. The XRD pattern well matched with standard ICDD card no. 22-1012

[29]. The sharp intensity of Bragg peaks confirms the stoichiometric prepared samples are crystalline. The enlarged high intense peak is ascribed to the defects in the crystallite size as shown in **Fig. 3.1b**. From **Table 3.3**, the effect of variation of G/N ratio observed due to the corresponding shift towards lower angles as the lattice parameter changed. Also, lattice strain decreases as G/N increases, indicating a correlation between G/N ratios and lattice parameter variations. Therefore, it concluded that the synthesized ZnFe_2O_4 material exhibited insignificant changes in crystallite size, lattice parameters, and lattice strain due to the variation of G/N ratio [30].

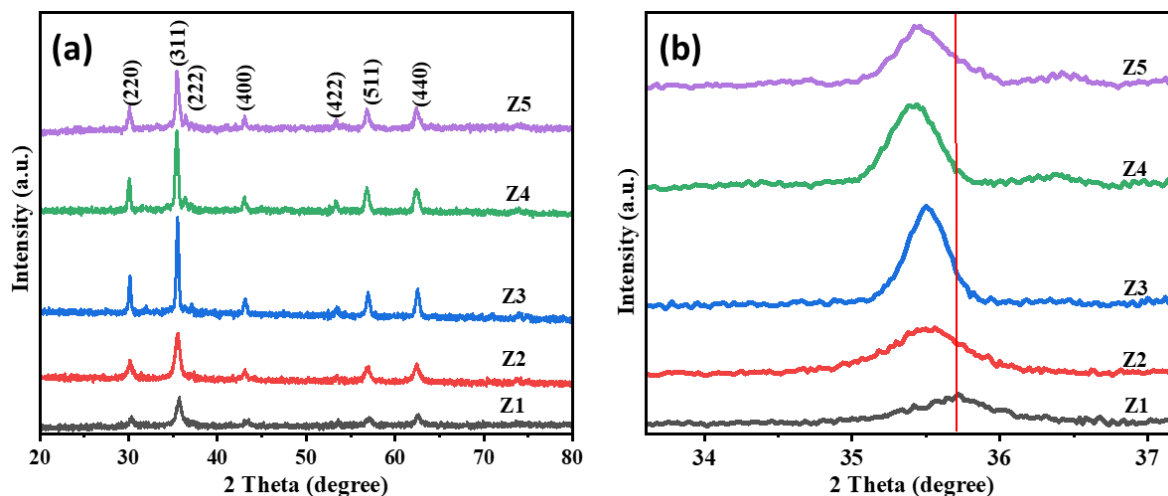


Fig. 3.1: (a) XRD patterns of samples using different G/N ratio: 0.48 (Z1), 0.74 (Z2), 1.48 (Z3), 2.22 (Z4) and 2.96 (Z5). (b) Enlarged version of (311) peak in XRD pattern.

Table 3.3. The effect of G/N ratio on ZnFe_2O_4 crystallite size (D), lattice parameter (a) Lattice Strain.

Sample ID	G/N ratio	D ₍₃₁₁₎ (nm)	a ₍₃₁₁₎ (nm)	Lattice Strain ₍₃₁₁₎ %
Z1	0.48	9.74	8.32	0.747
Z2	0.74	10.36	8.35	0.643
Z3	1.48	22.85	8.35	0.484
Z4	2.22	20.07	8.39	0.376
Z5	2.96	16.83	8.39	0.322

4.3.2 FTIR analysis:

The FT-IR spectra of ZnFe_2O_4 samples with varied G/N ratios displayed in **Fig. 3.2** show broad absorption spectra recorded from wavenumber 400 to 2000 cm^{-1} . The absorption bands corresponding to metal-oxygen bond stretching at octahedral (ν_2) and tetrahedral (ν_1) sites are identified at $\sim 432 \text{ cm}^{-1}$ and $\sim 545 \text{ cm}^{-1}$, respectively. Additionally, the N-O stretching band intensity was observed at 1353 cm^{-1} owing to the variation of G/N ratio. Symmetrical vibration bands at 1600 cm^{-1} correspond to the water molecules represent vibrations associated with water molecules. The variation in terms of decrease/increase in the intensity of tetrahedral and octahedral bands is susceptible to migration of metal ions among A- and B- sites. The variation in glycine may result into redistribution of cations namely Zn^{2+} and Fe^{3+} among these sites. This change indicates the decrease in the $\text{Fe}^{3+}-\text{O}^{2-}$ and $\text{Zn}^{2+}-\text{O}^{2-}$ distances, providing evidence for the formation of ZnFe_2O_4 with a spinel phase cation distribution. The vibrational stretching absorption bands at 545 cm^{-1} and 432 cm^{-1} are specifically attributed to the formation of the spinel cubic structure [31]. The change in adsorption band position confirmed by the variation of G/N ratio and is supportive to the XRD study.

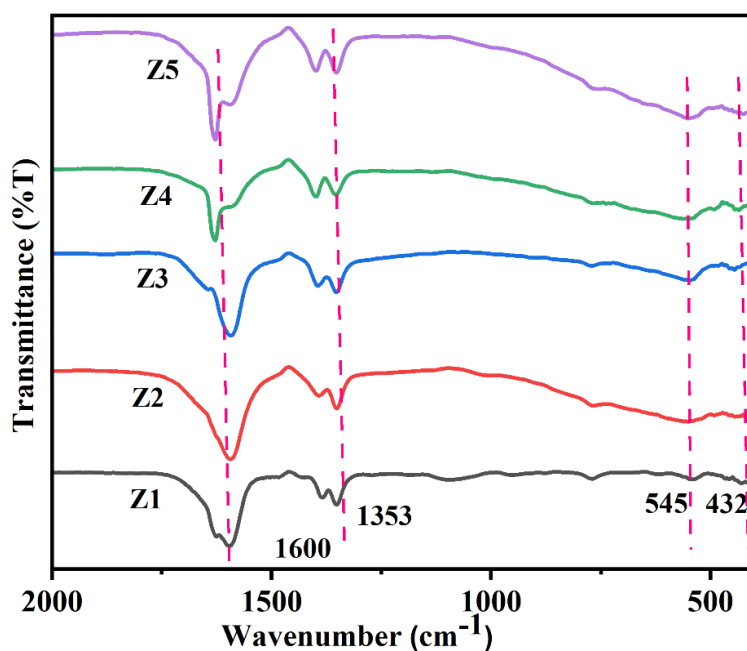


Fig. 3.2: FT-IR spectra of Z1, Z2, Z3, Z4 and Z5 samples at different G/N ratios: 0.48, 0.74, 1.48, 2.22, and 2.96, respectively.

It can be seen in the **Fig 3.2** that the intensity of bands increases as the G/N ratio increases. The octahedral site frequencies increased from 545 to 551 cm^{-1} for Z1 to Z5 samples. The tetrahedral site frequencies also varies in the range 432 to 448 cm^{-1} with varying G/N ratio.

4.3.3 SEM analysis:

SEM gives information about surface morphology, microstructures and agglomeration among materials synthesized. As these parameters have direct impact in terms of availability of active sites in photocatalytic dye degradation activity. Therefore, it is important to analyze these parameters as a function of varied G/N ratio.

Fig. 3.3 shows SEM images of different G/N ratios, **(a)** 0.48 (Z1), **(b)** 1.48 (Z3), and **(c)** 2.96 (Z5), respectively. The morphological structure of ZnFe_2O_4 nanoparticles (samples Z1, Z3, and Z5) was observed using SEM images. The nanocrystalline grains exhibit a spherical morphology with some agglomeration. In **Fig. 3.3a** (sample Z1), a low G/N ratio was assisted for the highly porous structure formation which is observed in the BET study. This effect can be attributed to the substantial volume of gas released during the combustion process, contributing to the formation of a spherical and porous structure. By increasing the G/N ratio, the dominance of tiny spherical porous structure changes was observed as depicted in **Fig. 3.3b** (sample Z3). Also, at higher G/N ratios, large voids with a wide dispersion of phased aggregate particles were observed as shown in **Fig. 3.3c** (sample Z5).

It concluded that the lower G/N ratios promoted to development of multigrain agglomerates, dense nanostructure, tiny particles, and spongy structure formation. The differences observed in microstructures for Z1, Z3 and Z5 may be attributed to competition between number of moles of gases released during combustion and adiabatic flame temperature.

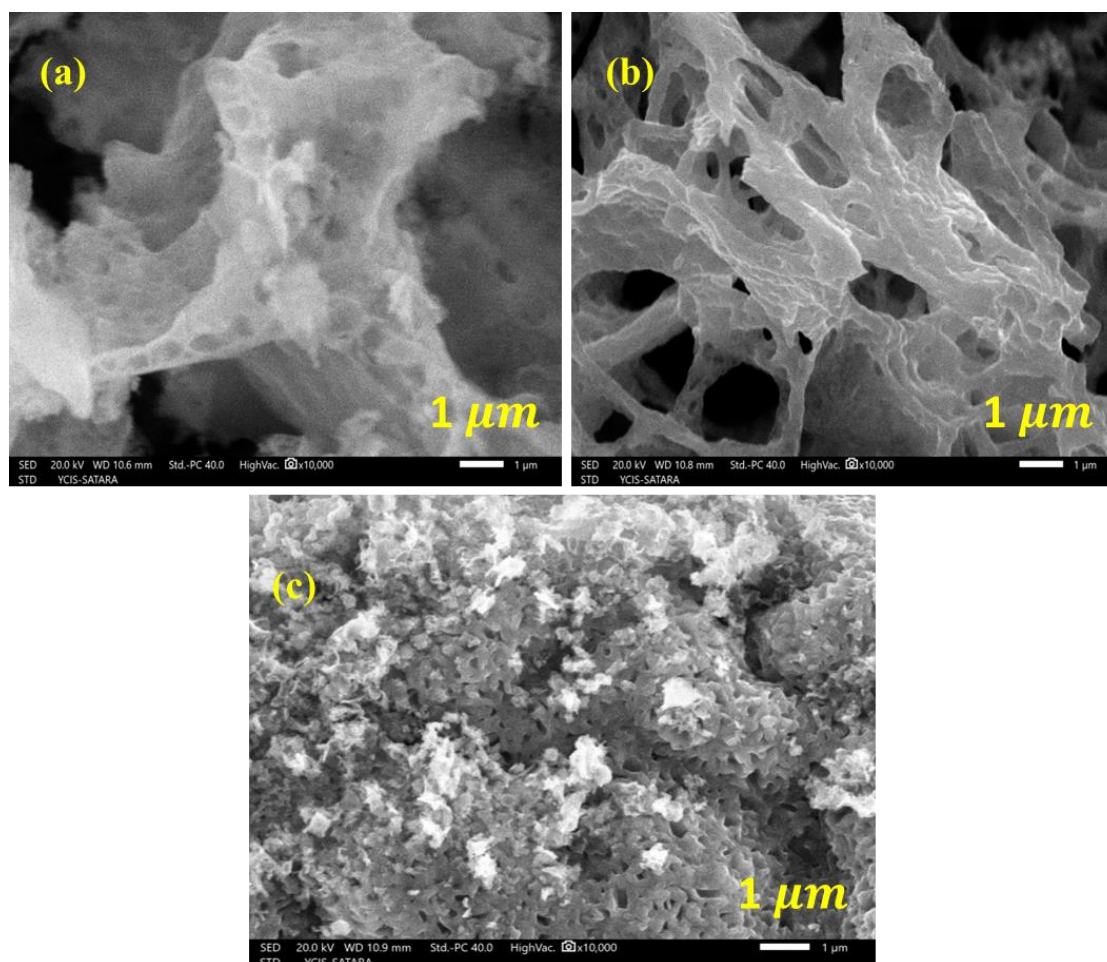


Fig. 3.3: SEM images of different G/N ratios, (a) 0.48 (Z1), (b) 1.48 (Z3), and (c) 2.96 (Z5).

4.3.4 TEM analysis:

The transmission electron microscopic study was evaluated for particle size and crystallographic structure analysis. The particle size of ZnFe_2O_4 is found to be $12.86 \text{ nm} \pm 3.42 \text{ nm}$ (**Fig. 3.4a**). It suggests that the particles exhibit broad size distribution, within the range of approximately 9.08 nm to 16.28 nm with nearly spherulitic shape. The size of nm is calculated using imagej software and histogram has presented in the following figure.

The SAED pattern (**Fig. 3.4b**) shows a ring pattern, which is mentioned to be consistent with the XRD pattern. This indicates that the crystalline structure of ZnFe_2O_4 is confirmed by both SAED and XRD. The SAED pattern showed a polycrystalline

nature, with diffraction rings corresponding to (220), (311), (400), (511), and (440) planes. The consistency between the SAED pattern and XRD pattern suggests that the crystalline phases identified in XRD are well represented in the TEM analysis. This consistency indicates well crystallographic structure of the material and the presence of nanometer sized particles. Histogram is plotted using the imagej software and calculated average particle size about $12.86 \text{ nm} \pm 3.42 \text{ nm}$ (see **Fig. 3.4c**).

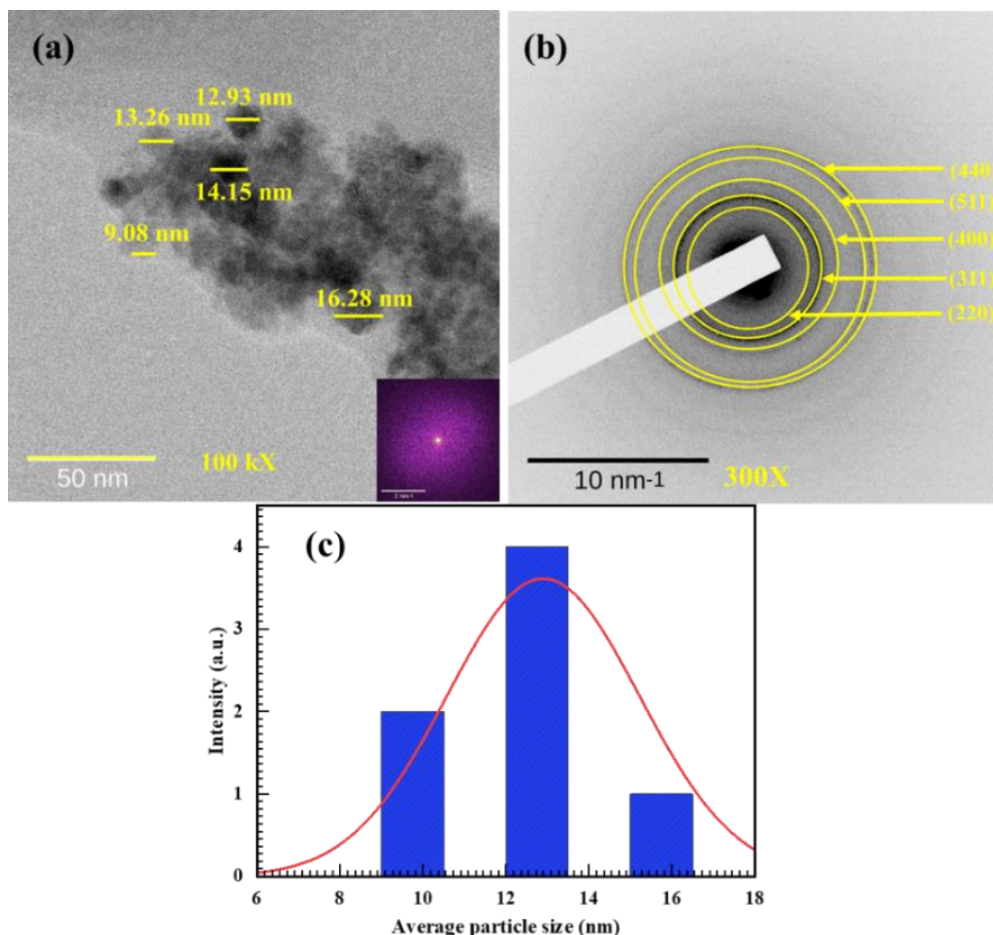


Fig. 3.4: (a) TEM images, and (b) SAED pattern, and (c) Histogram for optimized Z1 sample (0.48).

4.3.5 XPS analysis:

To examine the surface analysis and chemical states of the all sample, the XPS technique was utilized. **Fig 3.5** shows the survey spectra of all the samples Z1 to Z5. All the samples reveals photoelectron peaks for Zn 2p, Fe 2p, and O 1s, as well as C 1s. **Fig.**

3.5 demonstrates that variation of the G/N ratio, there is no observable difference in the survey spectra or atomic ratios. This consistency indicates the successful synthesis of pure zinc ferrite, maintaining the expected Zn:Fe atomic ratio of 1:2.

Table 3.4. The broad range peaks property of zinc ferrite (Z1 to Z5) nanoparticles determined from XPS data.

Sample ID	Name	Position (eV)	FWHM (eV)	At%
Z1	Zn 2p	1020.35	1.87	8.98
	Fe 2p	709.93	3.77	12.72
	O 1s	529	1.77	46.13
	C 1s	283.78	1.6	32.17
Z2	Zn 2p	1020.5	1.65	6.55
	Fe 2p	710.21	3.79	15.56
	O 1s	529.1	1.39	44.51
	C 1s	283.82	1.47	33.37
Z3	Zn 2p	1020.5	1.74	6.91
	Fe 2p	709.83	3.8	13.8
	O 1s	528.94	1.42	43.11
	C 1s	283.77	1.74	36.17
Z4	Zn 2p	1020.39	1.73	9.65
	Fe 2p	709.8	3.92	13.18
	O 1s	528.87	1.48	43.5
	C 1s	283.73	1.5	33.66
Z5	Zn 2p	1020.42	1.7	8.26
	Fe 2p	709.9	3.91	15.98
	O 1s	528.94	1.53	43.28
	C 1s	283.79	1.51	32.48

Fig. 3.6a depicts the XPS broad spectrum of the ZnFe_2O_4 (Z1) sample and reveals photoelectron peaks for Zn 2p, Fe 2p, and O 1s, as well as C 1s. The C 1s peak in this sample is caused by carbon generated during the combustion process of the synthesis of ZnFe_2O_4 . The atomic ratio details for all ZnFe_2O_4 (Z1 to Z5) nanoparticles are provided in **Table 3.4**. According to this data, the Zn, Fe, and O ion ratio is approximately similar to 1:2:4 respectively, which corresponds to the probable chemical bonding of ZnFe_2O_4 nanoparticles. For a detailed analysis of this wide spectrum, Shirley type of background was removed from the individual peak spectra of Zn 2p, Fe 2p, O1s, and C1s using XPS PEAK-41 software.

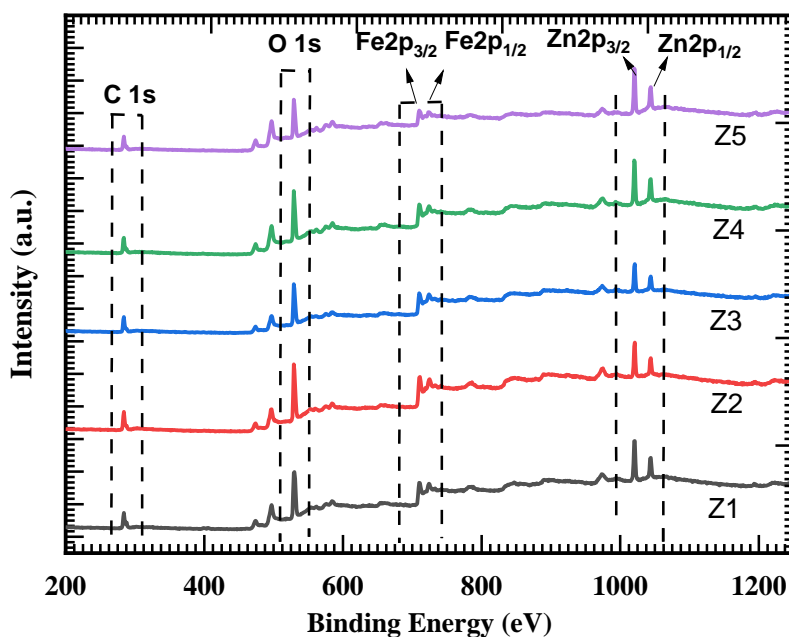


Fig. 3.5: Survey spectra of Z1, Z2, Z3, Z4, and Z5.

Deconvolution spectra of ZnFe_2O_4 nanoparticles Zn 2p peak are shown in **Fig. 3.6b**. These spectra contained two main peaks of Zn $2p_{3/2}$ and Zn $2p_{1/2}$, with binding energies of 1020.35 eV and 1043.44 eV, respectively. It has two sub-peaks. The existence of Zn^{2+} ion in ZnFe_2O_4 nanoparticles is shown by peaks at 1020.20 eV and 1020.94 eV for Zn $2p_{3/2}$ and for Zn $2p_{1/2}$ has two sub-peaks 1043.18 eV and 1043.93 eV [32].

The Fe 2p core-shell XPS spectra of ZnFe_2O_4 are shown in **Fig. 3.6c**. It comprises two characteristics of binding energy values observed at 709.93 eV for Fe $2p_{3/2}$ and 724.51 eV for Fe $2p_{1/2}$, with a satellite peak at 718.17 eV in between. This finding is

consistent with prior research on the Fe^{3+} ion in ferrite materials. Significantly, the Fe 2p deconvolution spectra in **Fig. 3.6c** can be fitted into three distinct peaks at 709.84 eV, 711.90 eV, and 724.51 eV. The binding energies of $\text{Fe } 2p_{3/2}\text{-Fe}^{2+}$, $\text{Fe } 2p_{3/2}\text{-Fe}^{3+}$, and $\text{Fe } 2p_{1/2}\text{-Fe}^{2+}$ are shown by these peaks. As a result, the oxidation states of Fe in the formed nanoparticles must contain both Fe^{3+} and Fe^{2+} ions. According to Chen's research, [33] in the spinel system (AB_2O_4), Fe^{2+} occupies B sites with a binding energy of 709.5 eV, A and B sites are occupied by Fe^{3+} , which have binding energies of 710.6 and 711.3 eV, respectively.

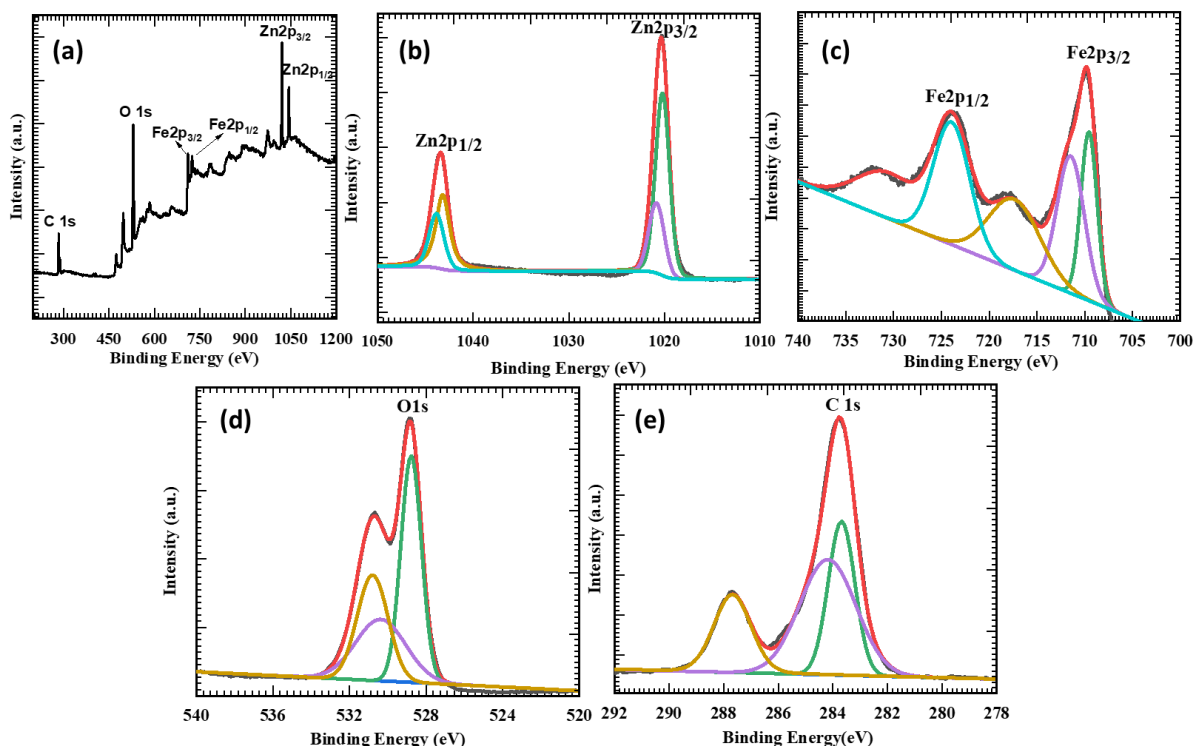


Fig. 3.6: XPS spectra of stoichiometric sample Z1: (a) survey spectrum of Z1 sample ZnFe_2O_4 (0.48), (b) high-energy resolution Zn 2p core-level spectrum, (c) high-energy resolution Fe 2p core-level spectrum, (d) high-energy resolution O 1s core-level spectrum, (e) high-energy resolution C 1s core-level spectrum.

The O 1s spectrum in **Fig. 3.6d** shows that oxygen is present in three distinct states. Lattice-oxygen is responsible for the 528.81 eV and 530.36 eV binding energy peaks as well as the chemical binding of Fe-O and Zn-O. However, the peak at 530.86 eV was caused by oxygen ions in adsorbed OH- groups on sample surfaces [34]. **Fig. 3.6e**

shows the C 1s core-level XPS spectra. It contains two components with energies of 283.69 eV and 287.68 eV. The C-H bond is responsible for the peak at 284.21 eV [35].

Fig. 3.7-3.10 depicts the XPS broad spectrum of the ZnFe_2O_4 (Z2, Z3, Z4, Z5) sample and reveals photoelectron peaks for Zn 2p, Fe 2p, and O 1s, as well as C 1s. The C 1s peak in this sample is caused by carbon generated during the combustion process of the synthesis of ZnFe_2O_4 . All Binding energy of the for all samples are same. According to this data, the Zn, Fe, and O ion ratio is approximately similar to 1:2:4 respectively, which corresponds to the probable chemical bonding of ZnFe_2O_4 nanoparticles. For a detailed analysis of this wide spectrum, Shirley type of background was removed from the individual peak spectra of Zn 2p, Fe 2p, O1s, and C1s using XPS PEAK-41 software.

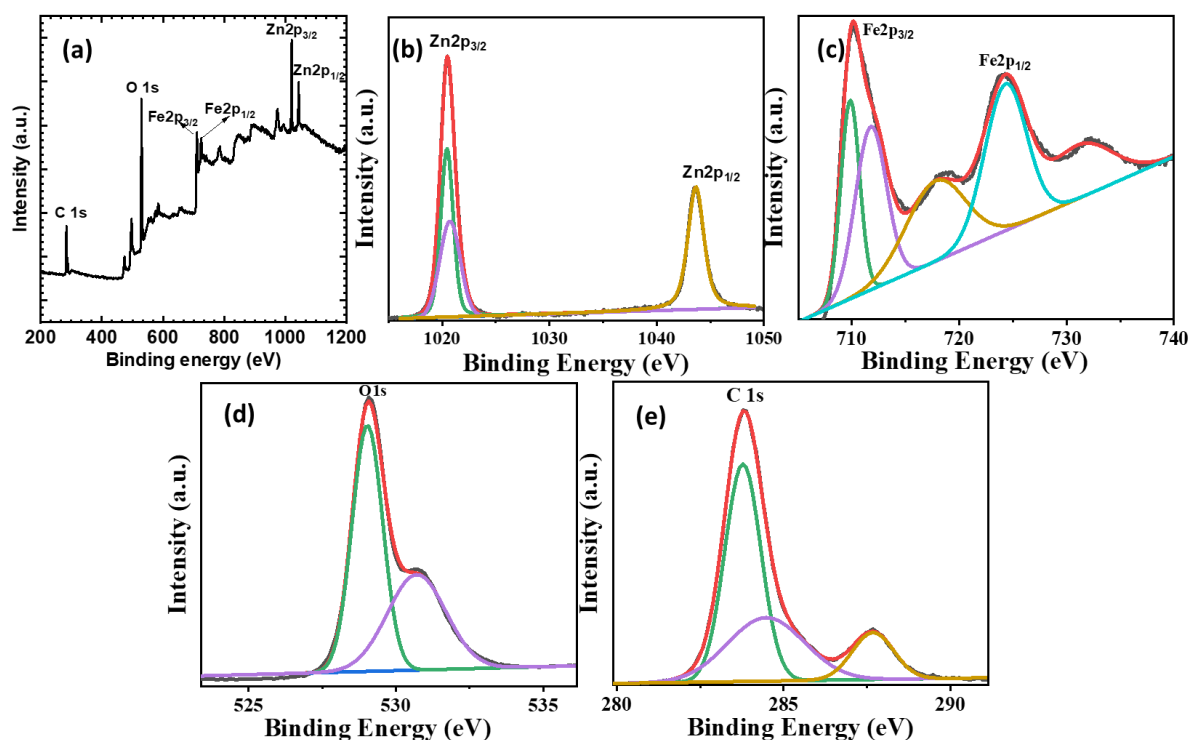


Fig. 3.7: XPS spectra of stoichiometric sample Z2: (a) survey spectrum of Z2 sample ZnFe_2O_4 (0.74), (b) high-energy resolution Zn 2p core-level spectrum, (c) high-energy resolution Fe 2p core-level spectrum, (d) high-energy resolution O 1s core-level spectrum, (e) high-energy resolution C 1s core-level spectrum.

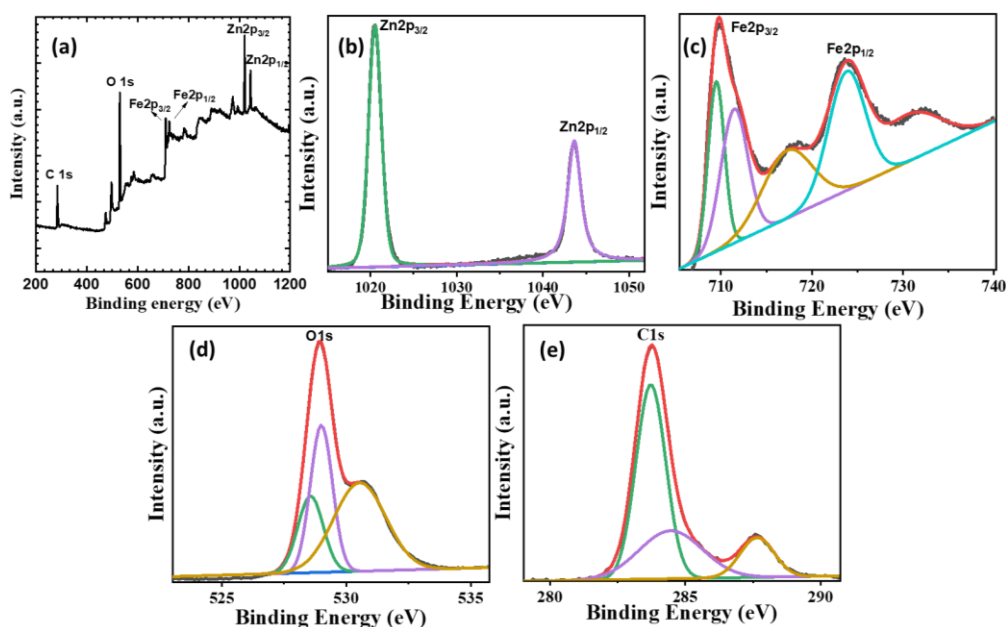


Fig. 3.8: XPS spectra of stoichiometric sample Z3: (a) survey spectrum of Z3 sample ZnFe_2O_4 (1.48), (b) high-energy resolution Zn 2p core-level spectrum, (c) high-energy resolution Fe 2p core-level spectrum, (d) high-energy resolution O 1s core-level spectrum, (e) high-energy resolution C 1s core-level spectrum.

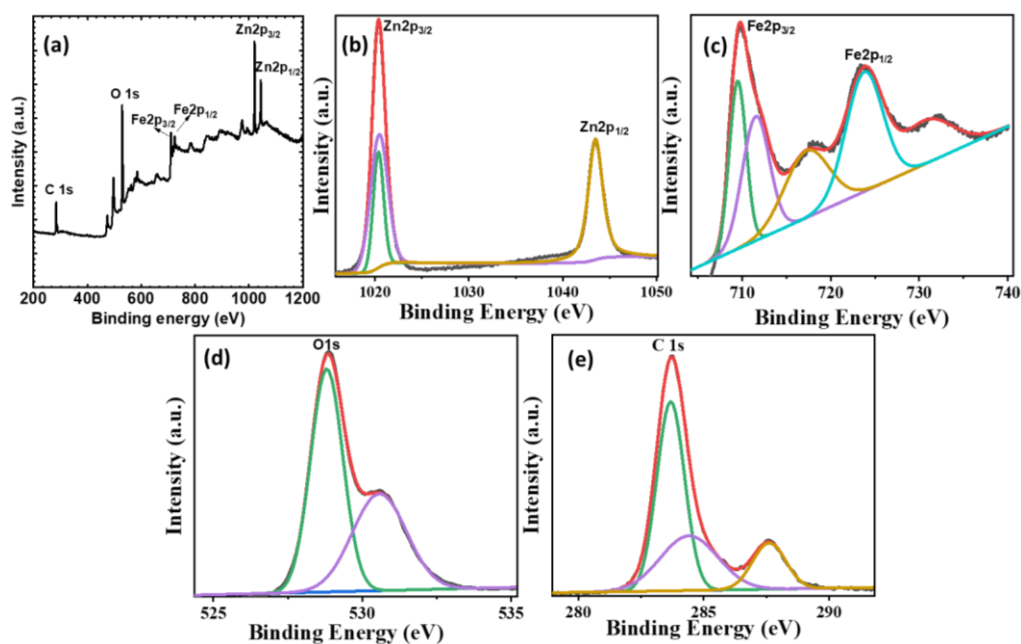


Fig. 3.9: XPS spectra of stoichiometric sample Z4: (a) survey spectrum of Z4 sample ZnFe_2O_4 (2.22), (b) high-energy resolution Zn 2p core-level spectrum, (c) high-energy resolution Fe 2p core-level spectrum, (d) high-energy resolution O 1s core-level spectrum, (e) high-energy resolution C 1s core-level spectrum.

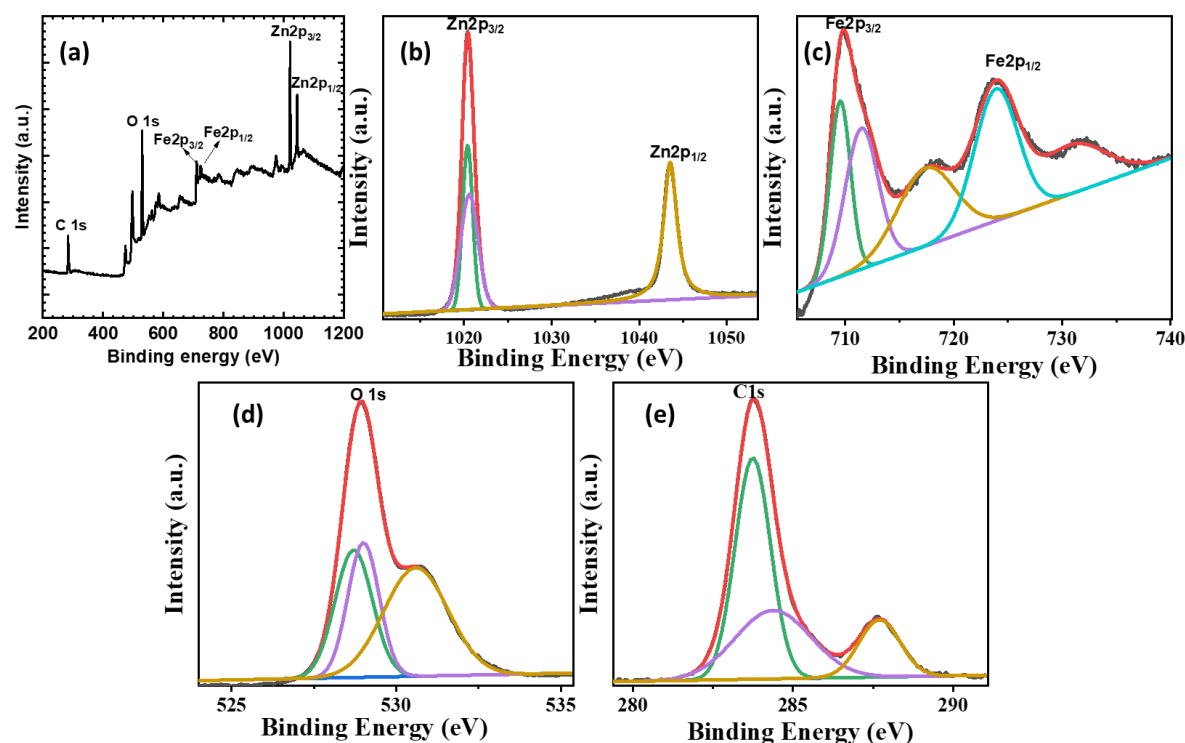


Fig. 3.10: XPS spectra of stoichiometric sample Z5: (a) survey spectrum of Z5 sample ZnFe_2O_4 (2.96), (b) high-energy resolution Zn 2p core-level spectrum, (c) high-energy resolution Fe 2p core-level spectrum, (d) high-energy resolution O 1s core-level spectrum, (e) high-energy resolution C 1s core-level spectrum.

4.3.6 BET analysis:

The N_2 adsorption-desorption isotherms were obtained by using the Brunauer-Emmett-Teller (BET) study for the analysis of specific surface area and pore size distribution. The BET study was investigated for Z1, Z2, Z3, Z4, and Z5 samples as depicted in **Fig. 3.11(a-e)**. The detected isotherms are identified as type V, indicating the presence of mesopores material and diameters typically between 2 and 50 nm. A typical H3 type hysteresis in the desorption step and a sharp step in the adsorption are observed which are characteristics of mesoporous materials. The BET study was correlated with degradation application in that the active surface area and pores enabled catalysis. Accordingly, the BET surface area of Z1, Z2, Z3, Z4, and Z5 samples were calculated to be 41, 21, 17, 8, and 7 m^2/g , respectively. The BET results reveal that the surface area decreased by the increasing G/N ratio due to the changes in porous structure. The more active site can assist in enhancing the surface area that supports for catalysis. The highest

surface area of 41.86 m²/g was observed for the Z1 sample which is noted to be more significant than reported in earlier literature [36]. A higher BET surface area was observed due to more active sites and sufficient pore size for gas adsorption. Furthermore, it is observed that the decrease in surface area with increasing G/N ratio might be attributed to the impact of G/N on the porosity of the zinc ferrite nanoparticles. It is concluded that the G/N ratio has shown an effect on surface area and pore size distribution.

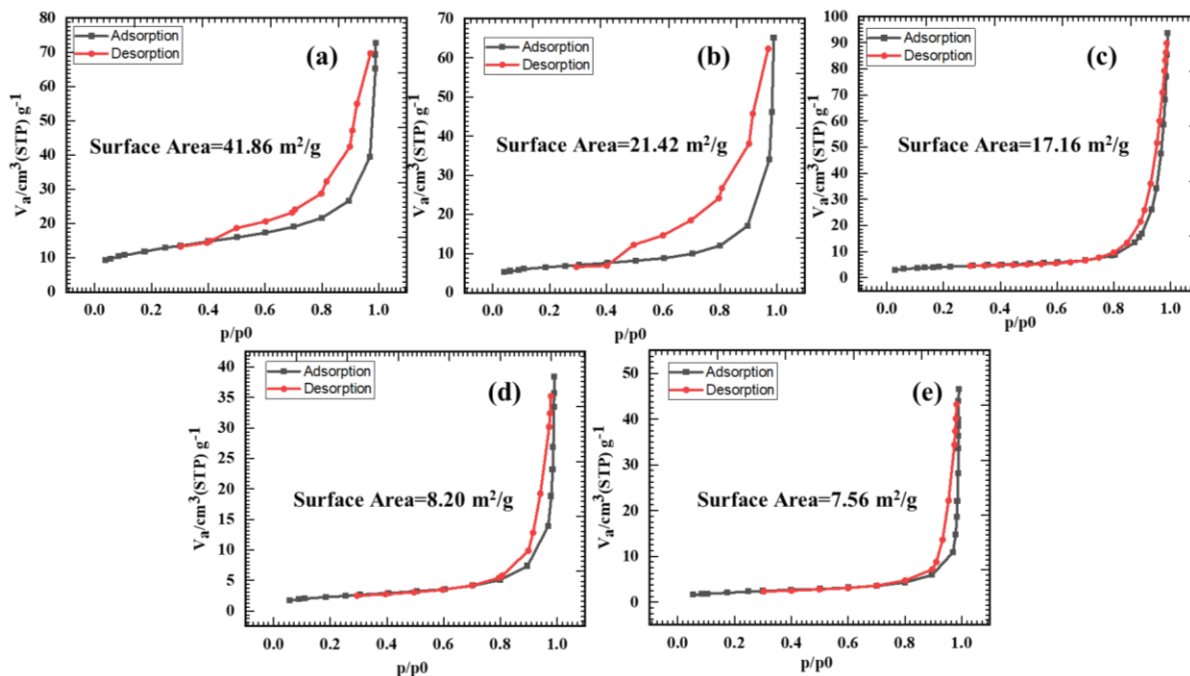


Fig.3.11: BET adsorption-desorption isotherm graphs of different G/N ratios, (a) Z1, (b) Z2, (c) Z3, (d) Z4, and (e) Z5.

4.3.7 UV-DRS analysis:

The measured UV-vis diffuse reflectance spectroscopy (UV-DRS) of ZnFe₂O₄ samples (Z1, Z2, Z3, Z4, and Z5) are shown in **Fig. 3.12(a-e)**. It can be seen that ZnFe₂O₄ nanoparticles absorb an excessive amount of visible light. These values decrease from Z1 to stoichiometric sample Z3 and again increased. These are comparable to previously obtained ZnFe₂O₄ band gap values [37]. The synthesised ZnFe₂O₄ nanoparticles may have the capacity to degrade various contaminants in the visible-light spectrum. It is concluded that the optical band gap energy decreases with increasing the crystallite size of the materials (**Table 3.5**) which was observed in degradation study. As

a result, there are more molecular orbitals, both bonding and antibonding, and this will result in a smaller band gap. Here, As fuel increases to the stoichiometric ratio, the crystallite size grows, reducing the band gap due to diminished quantum confinement. In fuel-rich samples, rapid combustion leads to smaller crystallites and increased surface defects, causing the band gap to increase again. This reflects how fuel levels control crystallite size and band gap through growth rate and defect formation.

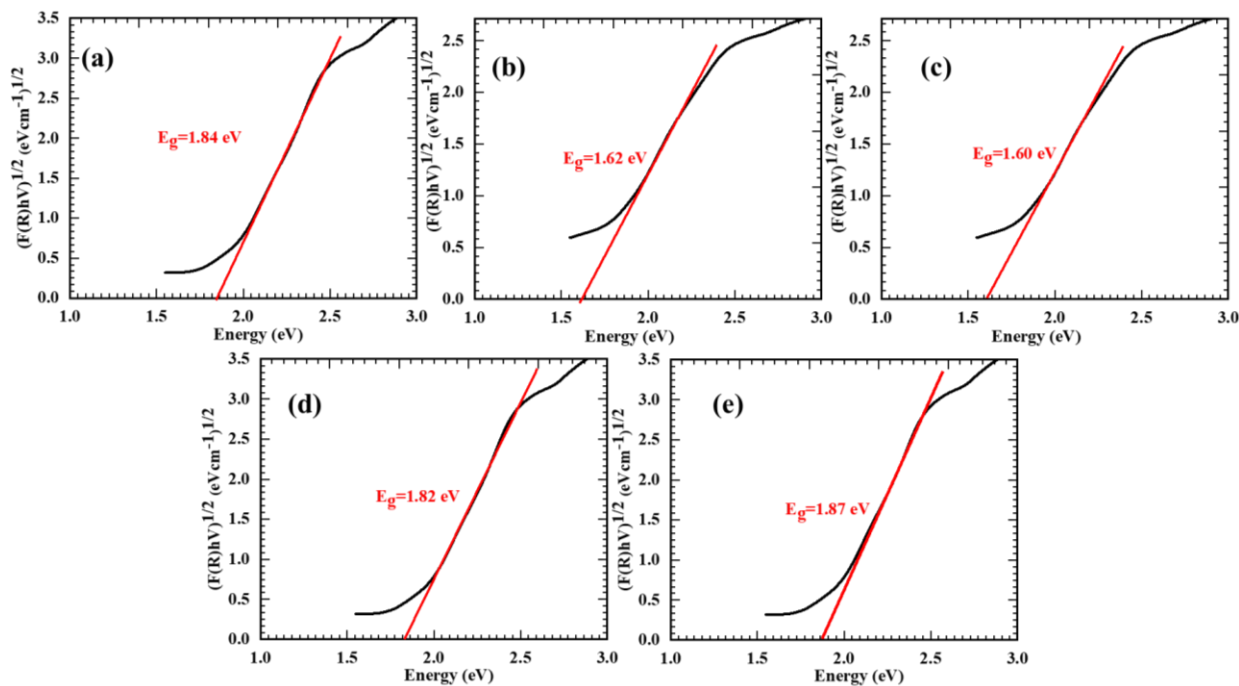


Fig. 3.12: UV–DRS spectrum of different G/N ratios, (a) Z1, (b) Z2, (c) Z3, (d) Z4, and (e) Z5.

Table 3.5. The effect of G/N ratio on crystal size and band gap.

Sample	D_{XRD} (nm)	Optical Band Gap (eV)
Z1	9.74	1.84
Z2	10.36	1.62
Z3	22.85	1.6
Z4	20.07	1.82
Z5	16.83	1.87

3.4. Conclusions:

The structural, morphological, and optical properties of ZnFe_2O_4 nanoparticles synthesized with varying glycine-to-nitrate (G/N) ratios are analyzed. The thermodynamic study reveals that increasing G/N ratio elevates the reaction and adiabatic flame temperatures, influencing the nanoparticle formation process. Structural characterization through XRD confirms the cubic spinel structure of ZnFe_2O_4 , with shifts in lattice parameters indicating changes in lattice strain. FT-IR spectroscopy supports the formation of the spinel structure and highlights variations in cation distribution. The SEM analyses show that G/N ratio affects the porosity, agglomeration of the nanoparticles. The TEM analysis observed that average particle size about $12.86 \text{ nm} \pm 3.42 \text{ nm}$. The XPS analysis identifies the oxidation states of Zn, Fe, and O ions, while BET studies indicate a decrease in surface area from 41 to $7 \text{ m}^2/\text{g}$ with increasing G/N ratios. DRS analysis demonstrates that ZnFe_2O_4 nanoparticles absorb visible light and that their band gap energy decreases with increasing crystallite size, suggesting their potential for photocatalytic applications. Overall, this chapter elucidates the significant impact of G/N ratio variations on the properties of ZnFe_2O_4 nanoparticles, providing valuable insights for optimizing their performance in photocatalytic dye removal and environmental remediation.

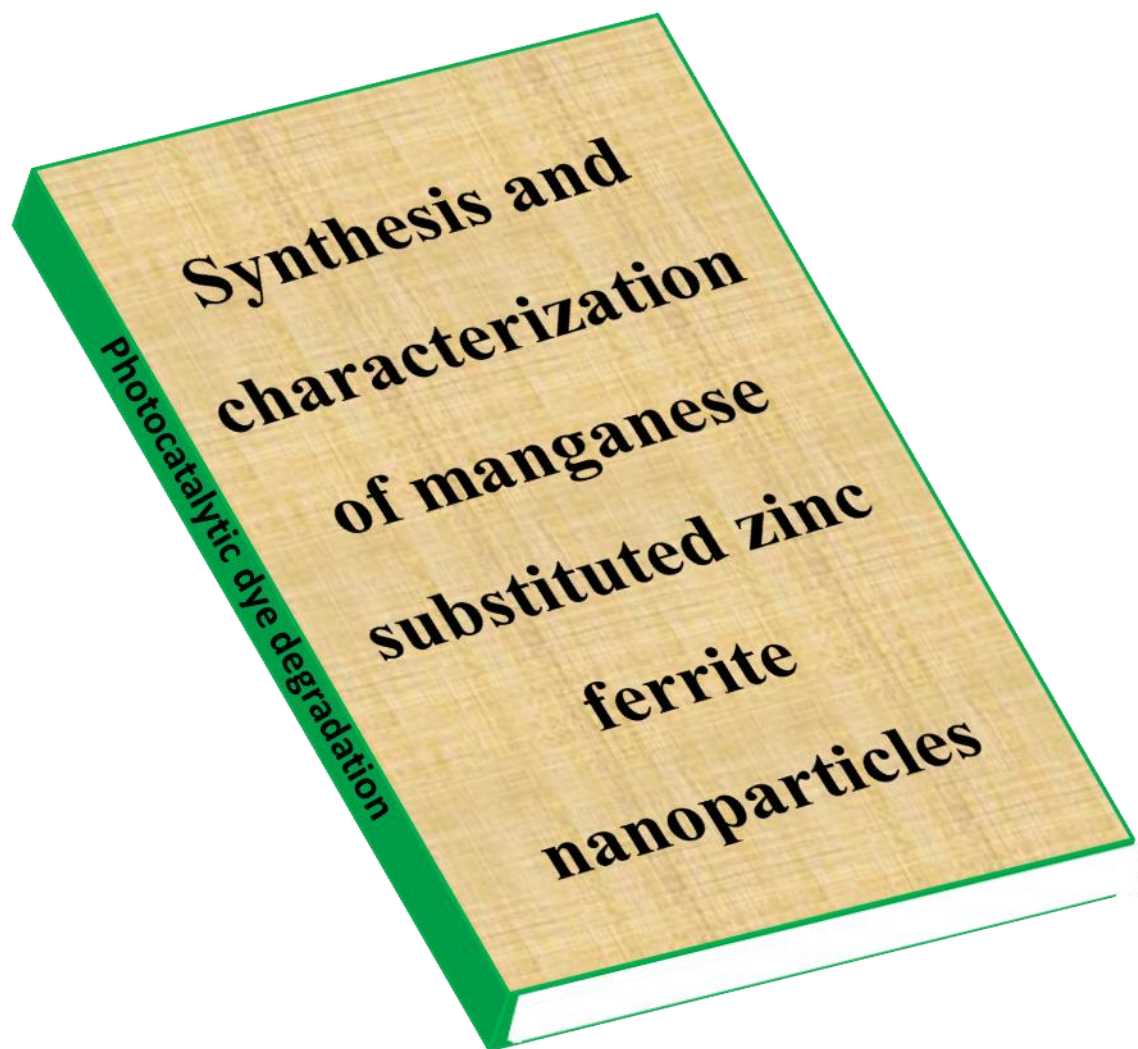
3.5. References:

1. Bessy T, Bindhu M, Johnson J, Chen S, Chen T, Almaary K. Environmental Research., 204, (2022), 111917 (1-12).
2. Sharma G, ALOthman Z, Kumar A, Sharma S, Ponnusamy S, Naushad M. Nanotechnology for Environmental Engineering., 2, (2017), 1-7.
3. Al-Tohamy R, Ali S, Li F, Okasha K, Mahmoud Y, Elsamahy T, Jiao H, Fu Y, Sun J. Ecotoxicology and Environmental Safety., 231, (2022), 113160 (1-17).
4. Dissanayake N, Pathirana M, Wanasekara N, Mahltig B, Nandasiri G. Nanomaterials., 13, (2023), 1350 (1-22).
5. Ghorai S, Sarkar A, Raoufi M, Panda A, Schönherr H, Pal S. ACS Applied Materials & Interfaces., 6, (2014), 4766-4777.
6. Ashraf M, Yang Y, Fakhri A. Ceramics International., 46, (2020), 8379-8384.
7. Mohan H, Ramasamy M, Ramalingam V, Natesan K, Duraisamy M, Venkatachalam J, Shin T, Seralathan K. Journal of Hazardous Materials., 412, (2021), 125330 (1-10).
8. Sathishkumar K, AlSalhi M, Sanganyado E, Devanesan S, Arulprakash A, Rajasekar A. Journal of Photochemistry and Photobiology B: Biology., 200, (2019), 111655 (1-7).
9. Ullah R, Khitab F, Gul H, Khattak R, Ihsan J, Khan M, Khan A, Vincevica-Gaile Z, Aouissi H. Catalysts., 13, (2023), 1061 (1-19).
10. Kasinathan K, Kennedy J, Elayaperumal M, Henini M, Malik M. Scientific reports., 6, (2016), 38064 (1-12).
11. Naseri M, Saion E, Hashim M, Shaari A, Ahangar H. Solid State Communications., 151, (2011), 1031-1035.
12. Yadav N, Chaudhary L, Sakhare P, Dongale T, Patil P, Sheikh A. Journal of Colloid and Interface Science., 527, (2018), 289-297.

13. Preethi G, Ninan A, Kumar K, Balan R, Nagaswarupa H. *Materials Today: Proceedings.*, 4, (2017), 11816-11819.
14. Idris M, Hafeez H, Mohammed J, Suleiman A, Ndikilar C. *Applied Surface Science Advances.*, 18, (2023), 100468 (1-13).
15. Bayat R, Derakhshi P, Rahimi R, Safekordi A, Rabbani M. *Solid State Sciences.*, 89, (2019), 167-171.
16. Liu S, Yu J, Jaroniec M. *Journal of the American Chemical Society.*, 132, (2010), 11914-11916.
17. Chen X, Mao S. *Chemical Reviews.*, 107, (2007), 2891-2959.
18. Ajormal F, Moradnia F, Taghavi Fardood S, Ramazani A. *Journal of Chemical Reviews.*, 2, (2020), 90-102.
19. Mahmoodi N. *Materials Research Bulletin.*, 48, (2013), 4255-4260.
20. Makofane A, Motaung D, Hintsho-Mbita N. *Ceramics International.*, 47, (2021), 22615-22626.
21. Makofane A, Motaung D, Hintsho-Mbita N. *Photoreactors in advanced oxidation processes: the future of wastewater treatment.*, (2023), 109-150.
22. Ai L, Jiang J. *Current Applied Physics.*, 10, (2010), 284-288.
23. Sharma S, Pitale S, Malik M, Dubey R, Qureshi M, Ojha S. *Physica B: Condensed Matter.*, 405, (2010), 866-874.
24. Sutka A, Mezinskis G. *Frontiers of Materials Science.*, 6, (2012), 128-141.
25. Salunkhe A, Khot V, Phadatare M, Pawar S. *Journal of Alloys and Compounds.*, 514, (2012), 91-96.
26. Zec S, Dukić J, Puševac M, Bošković S, Petrović R. *Materials and Manufacturing Processes.*, 24, (2009), 1104-1108.
27. Naderi F, Nayebzadeh H. *Industrial Crops and Products.*, 141, (2019), 111814 (1-9).

28. Khot V, Salunkhe A, Phadatare M, Pawar S. *Materials Chemistry and Physics.*, 132, (2012), 782-787.
29. Grecu I, Samoila P, Pascariu P, Cojocaru C, Ignat M, Dascalu I, Harabagiu V. *Catalysts.*, 13, (2023), 266 (1-18).
30. Nikam D, Jadhav S, Khot V, Phadatare M, Pawar S. *Journal of Magnetism and Magnetic Materials.*, 349, (2014), 208-213.
31. Borade R, Somvanshi S, Kale S, Pawar R, Jadhav K. *Materials Research Express.*, 7, (2020), 016116 (1-22).
32. Karamat S, Rawat R, Lee P, Tan T, Ramanujan R. *Progress in Natural Science: Materials International.*, 24, (2014), 142-149.
33. Chen M, Wang X, Yu Y, Pei Z, Bai X, Sun C, Huang R, Wen L. *Applied Surface Science.*, 158, (2000), 134-140.
34. Pan F, Guo Y, Cheng F, Fa T, Yao S. *Chinese Physics B.*, 20, (2011), 127501 (1-6).
35. Hou Y, Li X, Zhao Q, Quan X, Chen G. *Advanced Functional Materials.*, 20, (2010), 2165-2174.
36. Behera A, Kandi D, Majhi S, Martha S, Parida K. *Beilstein Journal of Nanotechnology.*, 9, (2018), 436-446.
37. Mohan H, Ramalingam V, Adithan A, Natesan K, Seralathan K, Shin T. *Journal of Hazardous Materials.*, 416, (2021), 126209 (1-12).

CHAPTER IV



4.1 Introduction:

The emergence of nanotechnology a transformative approach to reduce water pollution, primarily through the disposal of nanomaterials designed for the efficient diminish of contaminants [1-3]. Notably, dyes such as methylene blue (MB), rhodamine B (RhB), and chloramine T (ChT), predominantly discharged by the textile industry, have been identified as significant pollutants owing to their harmful impacts on both environmental matrices and human health [4-6]. The array of technologies earlier employed in wastewater treatment surrounds diverse techniques including coagulation, ozonation, microbial degradation, electrochemical processes, precipitation, adsorption, and photocatalytic degradation [7-9]. The recent, an example of advanced oxidation processes, is distinguished by its effectiveness and cost-efficiency, predicated on the generation of reactive species proficient at organic pollutants degradation.

The realm of photocatalysis is enhance by nano-sized semiconductors such as TiO_2 , ZnO , Fe_2O_3 , CdS , CdO , and ZnS , noted for their eco-compatibility, facilitating the oxidative degradation of organic dyes in aqueous environments [10-13]. A pivotal determinant of photocatalytic efficiency is the catalyst's light-absorption capability, provide materials that are active under visible light especially valuable due to the predominance of this spectrum in solar radiation. In this context, semiconducting materials, inclusive of ferrites and their transition metal-doped equivalents, are lauded for their proficient absorption of visible light. These materials exhibit relatively narrow band gaps (<2.2 eV), conducive to the absorption of visible solar radiation, with doping serving to augment their photocatalytic efficacy by introducing surface defects and reducing electron-hole pair recombination [14-16].

Despite the widespread use of TiO_2 and ZnO as photocatalysts, their utility is somewhat inhibited by their substantial band gaps, which hinder effective sunlight absorption [17-19]. To avoid this limitation, scholarly inquiries have delved into the photocatalytic potentials of nickel and zinc-doped cobalt ferrites, along with a spectrum of spinel ferrite nanocrystals [20, 21]. The magnetic attributes of ferrites, moreover, simplify the recovery of these materials post-photocatalytic application, thus underscoring their efficiency in contaminant removal [22, 23].

The investigation for ferrite nanoparticles characterized by uniform size distribution, elevated surface area, and pronounced porosity remains a formidable challenge, although

crucial for the amplification of photocatalytic performance. The combustion synthesis method stands out for its proficiency in fabricating nanoparticles that meet these criteria, using its inherent advantages of homogeneity control, operational simplicity, cost efficiency, and time effectiveness, utilizing readily available precursors [24-29]. This investigation introduces the utilization of the combustion method for the fabrication of manganese-doped zinc ferrite nanoparticles (MZNPs), with a focus on illustrating the influence of Mn ion concentration on the photocatalytic degradation efficiencies against RhB, MB, and ChT dyes. By spotlighting the combustion synthesis approach, this study endeavors to reveal novel insights into optimizing spinel ferrites for environmental remediation, elucidating the contribution of a wider array of reactive species in photocatalysis, including but not limited to hydroxyl radicals (OH^\bullet), superoxide anions ($\text{O}_2^{\bullet-}$), and singlet oxygen (O_2), which are instrumental in the photocatalytic degradation mechanism [30, 31].

4.2 Experimental Process of MZNPs:

The MZNPs were synthesized by a simple and cost-effective combustion method. $\text{Mn}(\text{NO}_3)_2 \cdot 6\text{H}_2\text{O}$, $\text{Fe}(\text{NO}_3)_3 \cdot 9\text{H}_2\text{O}$, and $\text{Zn}(\text{NO}_3)_2 \cdot 6\text{H}_2\text{O}$ were used as oxidants and $\text{NH}_2\text{-CH}_2\text{-COOH}$ as fuel. The careful consideration of oxidation valences from metal nitrates and their balancing with the reduction valences of glycine ensured an fuel lean ratio that optimized the energy released during the combustion reaction. This meticulous balancing act was essential to achieve the desired efficiency in the initiation and progression of the reaction, paving the way for successful synthesis. The Mn concentration was varied in $\text{Mn}_x\text{Zn}_{1-x}\text{Fe}_2\text{O}_4$ as $X=0, 0.2, 0.4, 0.6, 0.8$, and 1 for Mn substituted ZnFe_2O_4 nanocomposites and denoted by Z1, MZ1, MZ2, MZ3, MZ4, and M1, respectively.

4.3. Results and discussion:

4.3.1 XRD analysis:

The XRD patterns in **Fig. 4.1a** provide insight into the crystallographic characteristics of MZNPs. The diffraction peaks corresponding to various crystallographic planes, such as (220), (311), (222), (400), (422), (511), and (440), are observed for all samples [31, 32].

X-ray diffraction patterns of pure zinc ferrite are well matched with the ICDD card 22-1012, indicating structural conformity. For pure manganese ferrite, a good agreement is

observed with the ICDD card 01-073-1964. In **Fig 4.1b**, the enlarged peak (311) suggests a shift towards lower angles as manganese substitutes in zinc ferrite. The lattice parameter exhibits an increasing trend with rising Mn^{2+} ion concentration (8.44-8.51 Å), attributed to the larger ionic radius of Mn^{2+} (0.82 Å) compared to Zn^{2+} (0.65 Å). This larger radius leads to bond length stretching and an overall augmentation of the lattice parameter, influencing unit cell volume [33]. The shift in the main peak (311) towards lower 2θ angle supports the successful incorporation of Mn^{2+} into ZnFe_2O_4 lattice. [detailed in **Table 4.1**]. These alterations in lattice parameters and peak positions offer insightful information about the crystallographic characteristics of the synthesized materials. Crystallite size is calculated from characteristic peak (311) by scherrers formula is found to be between 21.54 to 28.14 nm for mn substituted zinc ferrite.

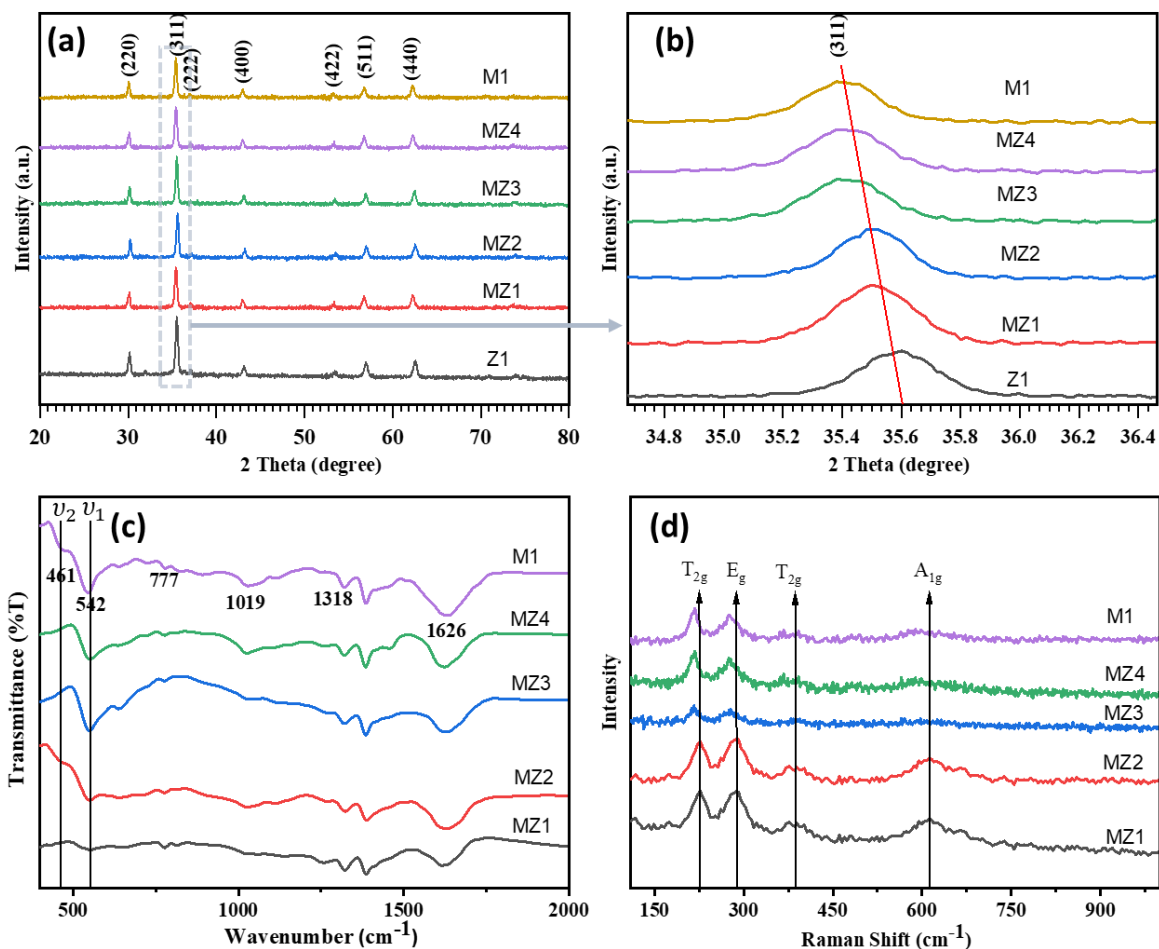


Fig. 4.1: (a) XRD patterns (b) enlarged version of (311) peak in XRD patterns, (c) FT-IR spectra, and (d) Raman spectra of Z1, MZ1, MZ2, MZ3, MZ4, and M1.

4.3.2 FT-IR analysis:

The confirmation of spinel $\text{Mn}_x\text{Zn}_{1-x}\text{Fe}_2\text{O}_4$ structure in nanocrystalline form is supported by the FT-IR spectra, as depicted in **Fig. 4.1c**. In the spectrum for ZnFe_2O_4 ($x=0$) nanoparticles, the absorption band ν_1 appears near 542 cm^{-1} , and the second absorption band ν_2 appears near 461 cm^{-1} . These bands are associated with the bending vibration of Fe-O and stretching vibration in the octahedral and tetrahedral complexes, respectively [34, 35].

Notably, with the addition of Mn, the ν_1 and ν_2 bands exhibit a linear shift to lower frequencies. The difference in intensities between ν_1 and ν_2 is attributed to changes in bond lengths (Fe-O) within octahedral and tetrahedral sites, suggesting alterations in the molecular structure induced by the introduction of Mn ions. The observed variations in intensity (I_{ν_1} and I_{ν_2}) indicate changes in cation redistribution, possibly influenced by the combustion synthesis process. The positions and intensities of ν_1 and ν_2 slightly vary due to the differences in the Fe-O distances for the tetrahedral and octahedral complexes. The replacement of Zn^{2+} ions with Mn^{2+} ions, having a larger ionic radius and higher atomic weight, at the tetrahedral site in the ferrite lattice affects the stretching vibrations of Fe-O. Overall, the FT-IR analysis provides supportive information about the molecular structure changes in the ferrite due to the introduction of Mn ions, contributing to a comprehensive understanding of the synthesized nanomaterials [36]. The absorption band at 777 cm^{-1} is related to C-C stretching vibration and the band observed at 1019 cm^{-1} is about C-O cm^{-1} vibration. Additionally, the N-O stretching band intensity was observed at 1318 cm^{-1} . Band observed at 1626 cm^{-1} corresponds to OH bending vibration.

4.3.3 Raman analysis:

Further, Raman spectroscopy was employed to investigate the microscopic vibrations associated with slight structural distortions in MZ1, MZ2, MZ3, MZ4, and M1 nanoparticles. The Raman spectra for all samples were recorded and the results reveals distinct vibrational modes as shown in **Fig. 4.1d**. The Raman spectrum exhibited six first-order Raman modes, including T_{2g} , E_g , and A_{1g} , with corresponding frequencies. The Raman spectra of Mn-doped ZnFe_2O_4 samples at room temperature indicated a normal spinel structure, allowing the occurrence of five active Raman modes ($A_{1g} + E_g + 3T_{2g}$) [37]. The observed variations in frequency bands are attributed to changes in the tetrahedral and octahedral environments. It is

evident that the spinel ferrite structure, with the molecular formula $M^{2+}Fe^{3+}_2O^{2-}_4$ involves divalent and trivalent metal cations occupying tetrahedral and octahedral local symmetry within the lattice of O^{2-} ions. Depending on the arrangement of these cations, the spinel structure is classified as normal, inverse, or mixed spinel. In present case, the shift toward higher wave numbers, as Zn is substituted by Mn, suggests that Mn-substituted Zn ferrites possess a spinel structure lying between normal and inverse [38]. The absence of broadening in the Raman peaks in the current study confirms an increase in unit cell size due to substituting smaller Zn ions with larger Mn ions as confirmed from XRD results. Overall, the Raman spectroscopy results affirm the spinel structure of $Mn_xZn_{1-x}Fe_2O_4$ nanoparticles, providing valuable insights into the composition and arrangement of cations within the ferrite lattice.

Table 4.1: Structural parameters obtained from XRD analysis of all the samples.

Sample ID	X	Lattice Parameter (Å)	Density (g/cm ³)	Volume cell (10 ⁶ pm ³)	D ₃₁₁ (nm)
Z1	0	8.44	5.32	601	21.54
MZ1	0.2	8.46	5.24	605	25.31
MZ2	0.4	8.47	5.16	609	23.23
MZ3	0.6	8.49	5.08	613	28.14
MZ4	0.8	8.51	5.01	617	25.31
M1	1	8.51	4.96	617	27.09

4.3.4 SEM analysis:

The SEM analysis was carried out to examine the surface morphology of the synthesized samples. In **Fig. 4.2 (a-f)**, micrographs show soft agglomeration in all samples. This agglomeration could be due to attractive forces between particles during the synthesis process. SEM images demonstrate the presence of voids and pores in the samples. These voids and pores are likely a result of the release of large amounts of gas during the combustion process. The spongy structure observed in the samples suggest the formation of multigrain agglomerations consisting of very fine crystallites [39]. The SEM analysis clearly shows that as the concentration of Mn ions increases, the porosity of the samples also increases. The porous morphology observed in the images contribute to the enhancement of surface area. This increase in surface area is significant for photocatalytic applications, as it provides more active

sites for catalytic reactions. Consequently, the material becomes more effective in degrading dyes through photocatalysis.

The TEM analysis provided valuable insights into the morphology and size distribution of the MZ4 nanoparticles. The TEM images in **Fig. 4.2(g) and (h)** reveal well-dispersed nanoparticles that confirmed the successful formation of nanoparticles with size of 54.32 nm, ± 22.49 nm through the combustion method.

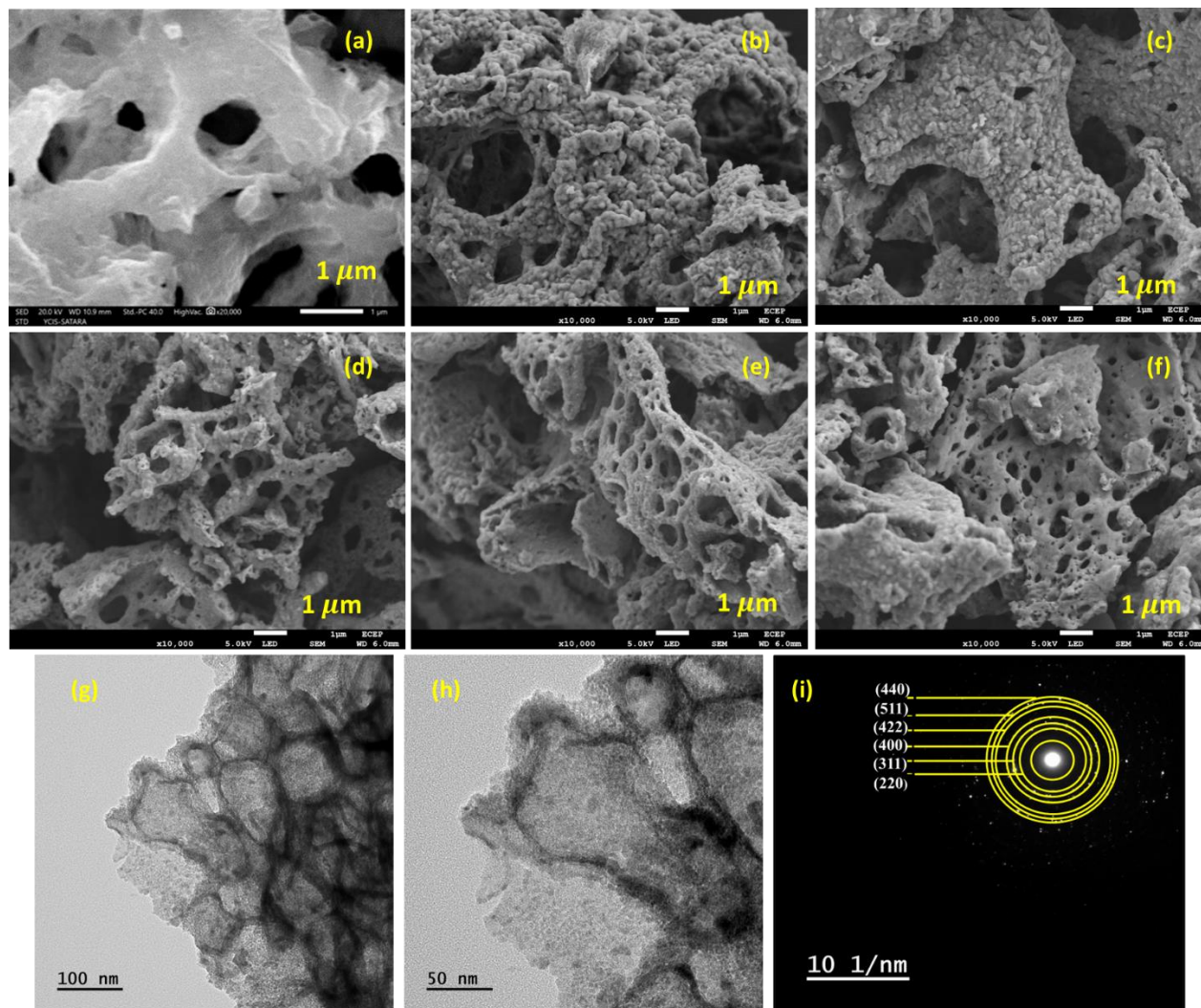


Fig. 4.2: SEM images of (a) Z1, (b) MZ1, (c) MZ2, (d) MZ3, (e) MZ4, and (f) M1. And (g, h) TEM image, (i) SAED pattern for MZ4 sample.

Selected Area Electron Diffraction (SAED) in TEM is a technique that provides diffraction patterns from a specific, localized region within a sample. This method enables the

analysis of crystal structures, phase identification in nanoscale materials. By examining the resulting diffraction spots or rings, information on lattice spacing, crystal symmetry, and degree of crystallinity can be deduced. The SAED pattern is presented in **Fig. 4.2(i)**, exhibited a characteristic ring pattern that is associated with the XRD pattern. The presence of diffraction rings indicated the crystalline nature of the nanoparticles, further confirming the spinel structure as identified by XRD. The congruence between SAED and XRD patterns provided additional confirmation of the crystalline nature of the MZ4 sample. In summary, the TEM analysis demonstrated that the MZ4 sample was well-formed, uniform in size, and exhibited a crystalline structure.

4.3.5 Elemental composition analysis:

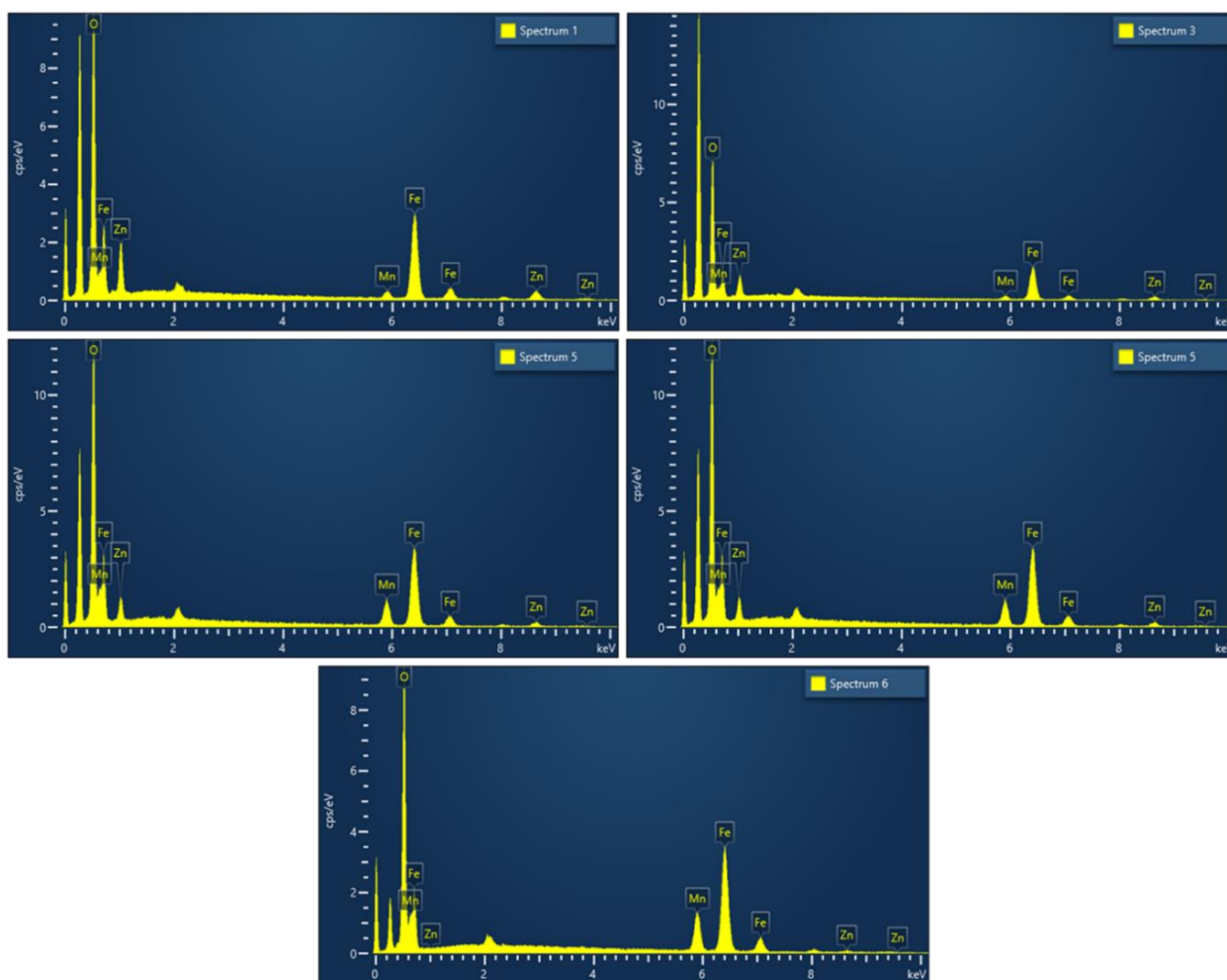


Fig.4.3: EDS images of the (a) MZ1, (b) MZ2, (c) MZ3, (d) MZ4, and (e) M1.

The EDS analysis confirms the elemental composition of the $\text{Mn}_x\text{Zn}_{1-x}\text{Fe}_2\text{O}_4$ samples. Strong peaks related to Mn, Zn, and Fe are observed in the spectrum with distinguishable intensities [40]. **Fig. 4.3** shows EDS patterns of (a) MZ1 (b) MZ2 (c) MZ3, (d) MZ4, and (e) M1, highlighting the elemental composition. Elemental analysis of Z1 sample is already confirmed and verified using XPS in previous chapter (please refer **Fig. 3.6** for details). The patterns exhibit clear and distinct peaks corresponding to Mn, Zn, and Fe, emphasizing the effectiveness of substitution and the presence of these elements in the product.

The EDS pattern reflects the compositional stoichiometry of the Mn-substituted ZnFe_2O_4 . The presence of Mn^{2+} , Fe^{3+} , Zn^{2+} , and O^{2-} ions in proper proportions suggest that the expected stoichiometry is maintained in the prepared samples as shown in supporting **Table 4.2**. This is crucial for the consistent and targeted properties of the nanocomposites. The EDS results indicate that the precursors have fully undergone the chemical reaction to form single-phase Mn-substituted ZnFe_2O_4 nanocomposites. Thus, the EDS analysis demonstrates the elemental composition, stoichiometry, and homogeneity of the Mn-substituted ZnFe_2O_4 nanocomposites.

Table 4.2: The element atomic percentage by energy dispersive X-ray (EDS) analysis.

Mn²⁺ Conc.	Element	Atomic percentage (%)
0.2	Mn	2.24
	Zn	8.94
	Fe	31.38
	O	57.44
0.4	Mn	2.36
	Zn	7.53
	Fe	27.13
	O	62.98
0.6	Mn	7.55
	Zn	2.63
	Fe	44.09
	O	45.73
0.8	Mn	8.11
	Zn	4.50
	Fe	30.52
	O	56.87
1	Mn	11.73
	Zn	0
	Fe	37.20
	O	51.07

4.3.6 XPS analysis:

To determine the oxidation states and presence of elements, such as Fe, Mn, Zn, and O, the XPS was performed and results for the MZ4 sample are presented in **Fig. 4.4a**. Given that the binding energy varies for different elements, the binding energy values are used to find out the elements present in the samples. **Fig. 4.4b** shows the deconvoluted spectra of photoelectron Zn2p in nanoparticles, where Zn2p_{3/2} splits into two peaks centered at 1021.3 and 1023.2 eV. The peak at 1021.3 eV is attributed to Zn2p cations occupying tetrahedral sites, while the peak at 1023.2 eV is assigned to Zn2p cations occupying octahedral sites [41]. The unique splitting of the Zn2p_{3/2} peak in this study may be related to an improved ordering degree of Zn²⁺. The high-resolution Mn 2p spectra are shown in **Fig. 4.4c**. The XPS spectra that correspond to Mn2p show two major peaks at 641.21 eV (Mn 2p_{3/2}) and 653.09 eV (Mn 2p_{1/2}). This result reveals that the Mn2p peak detected at the surface of the sample is considered as divalent Mn ions, in agreement with other reports [42]. Hwang et al. [43] previously reported for Ga_{1-x}Mn_xN thin films that Mn ions incorporate into the tetrahedral sites of the wurtzite structure as substitutional impurities and that their valence is divalent. The Fe2p peaks in **Fig. 4.4d** consist of Fe2p_{3/2} and Fe2p_{1/2} with binding energies at 710.5 and 723.8 eV, respectively. Two small peaks at about 718.8 and 731 eV are identified as satellite peaks of Fe2p_{3/2} and Fe2p_{1/2}, indicating the presence of Fe³⁺ on the nanoparticle surface/near-surface. The Fe2p_{3/2} peak shows contributions at about 709.8, 711, and 712.3 eV, suggesting different circumstances of Fe³⁺ ions. The peaks at 709.8 and 711 eV correspond to Fe³⁺ in different coordination environments (tetrahedral or octahedral), while the higher binding energy at about 712.3 eV is associated with Fe³⁺ bonded with hydroxyl groups. **Fig. 4.4e** shows the high-resolution spectrum for O1s displays three distinct oxygen peaks at 529.7, 530, and 531.5 eV. At 529.7 eV, the peak signifies oxygen bonded to metal atoms such as Zn, Mn, and Fe. Oxygen deficiency permits the adsorption of functional groups like -OH, commonly referred to as surface oxygen, indicated by the peak at 530 eV. Oxygen absorbed from moisture is characterized as loosely bonded oxygen, as indicated by the peak at 531.5 eV [41, 44]. The presence of these elements and their respective oxidation states provides conclusive evidence for the formation of the Mn-ZnFe₂O₄ composite.

The XPS data collectively indicates that the surface of the sample MZ4 has a composition containing Mn²⁺, Zn²⁺, Fe³⁺, and O²⁻. Notably, a portion of Zn²⁺ is identified as

occupying octahedral sites on the particle surface, representing Mn^{2+} substitution in ZnFe_2O_4 . The unique features in the XPS spectra, such as the splitting of $\text{Zn}2p_{3/2}$ peaks, provide insights into the specific coordination environments and ordering of elements in the samples. The presence of Fe^{3+} and Zn^{2+} in different coordination environments suggests a complex and well-defined chemical structure at the surface of the nanoparticles.

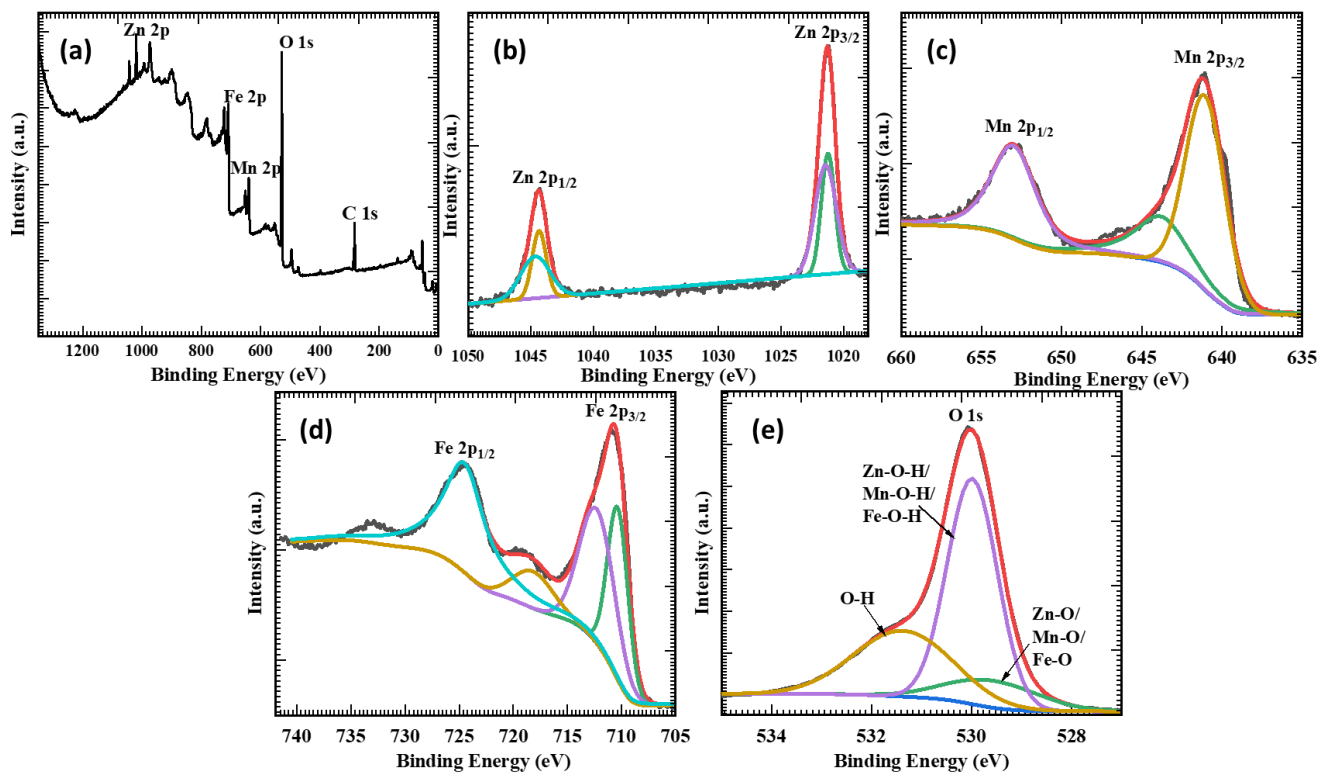


Fig. 4.4: XPS spectra of MZ4: (a) survey spectrum of MZ4, high resolution core spectrum of (b) Zn 2p, (c) Mn 2p, (d) Fe 2p, and (e) O 1s.

Fig 4.5 shows XPS spectra of M1. The high-resolution Mn 2p spectra are shown in **Fig. 4.5a**. The XPS spectra that correspond to Mn2p show major peak at 641.62 eV (Mn 2p_{3/2}). This result reveals that the Mn2p peak detected at the surface of the sample is considered as divalent Mn ions. The Fe2p peaks in **Fig. 4.5b** consist of Fe2p_{3/2} and Fe2p_{1/2} with binding energies at 711.30 and 725.02 eV, respectively. Significantly, the Fe 2p deconvolution spectra can be fitted into two distinct peaks at 711.12 eV, and 713.89 eV. The binding energies of Fe 2p_{3/2}-Fe²⁺, Fe 2p_{3/2}-Fe³⁺, and Fe 2p_{1/2}-Fe²⁺ are shown by these peaks. As a result, the oxidation states of Fe in the formed nanoparticles must contain both Fe³⁺ and Fe²⁺ ions. The O 1s

spectrum in **Fig. 4.5c** shows that oxygen is present in three distinct states. Lattice-oxygen is responsible for the 531.55 eV binding energy peaks. The deconvolution spectra can be fitted into two distinct peaks at 530.92 eV and 532.46 eV as the chemical binding of Fe-O and Zn-O. (for XPS of Z1 sample please see **Fig. 3.6** for detail information in chapter III)

In conclusion, it is observed that all tested samples stoichiometry in terms of elemental composition which is in good agreement with that calculated from EDS.

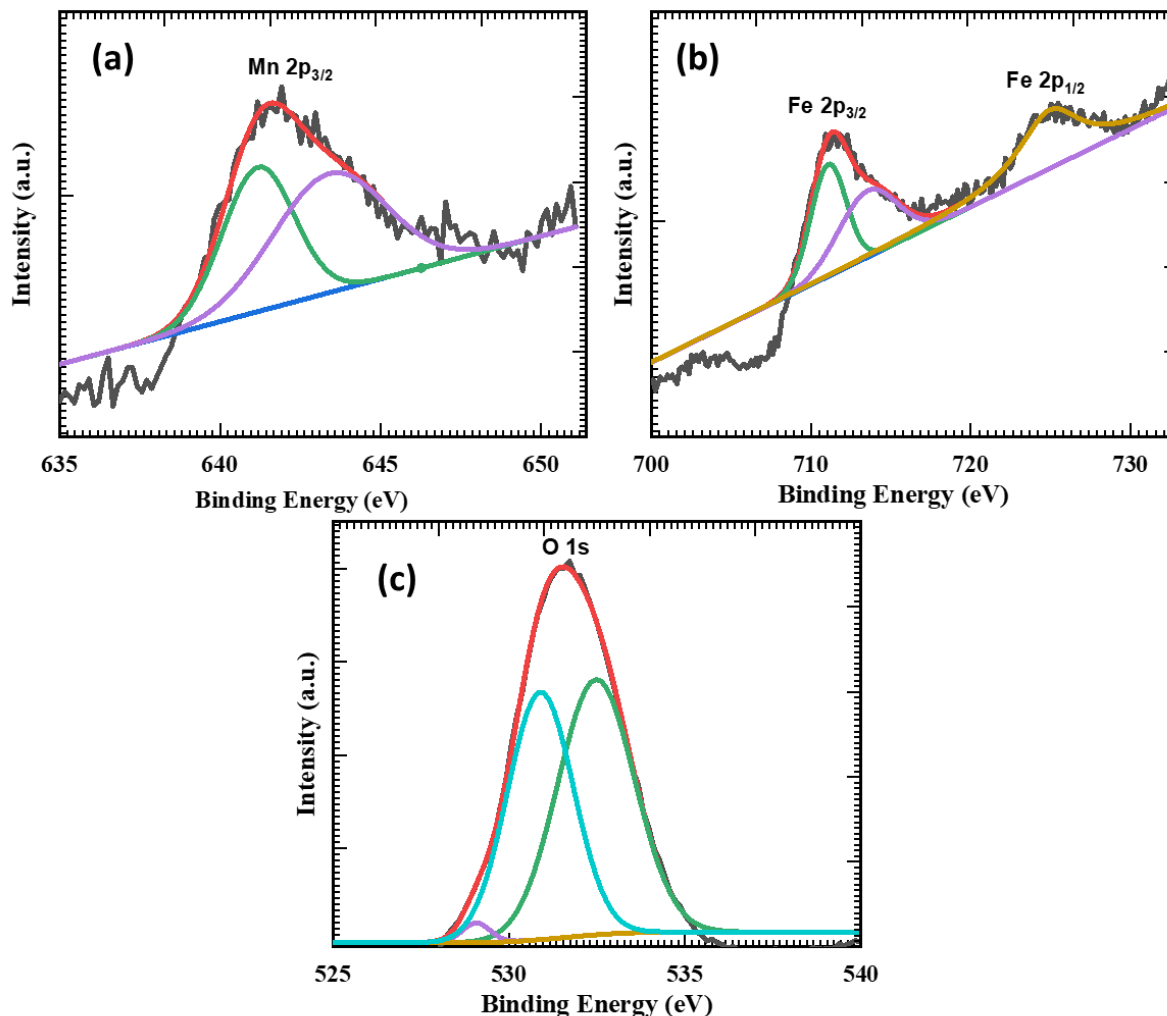


Fig. 4.5: XPS spectra of M1: (a) Mn 2p, (b) Fe 2p, and (c) O 1s.

4.3.7 BET analysis:

The low-temperature nitrogen (N_2) adsorption and desorption isotherms were utilized to examine the surface area and porous nature of the synthesized ferrite nanoparticles as shown in **Fig. 4.6**. A type-VI isotherm with a narrow hysteresis loop at a relatively high-pressure range was observed. This characteristic indicates the presence of typical mesoporous solids [45], suggesting that the as-prepared ferrites possess mesoporous structures. The specific surface area of these nanoparticles was quantified using the BET equation, and the pore size distributions were determined from the desorption branch using the BJH method. The BET surface areas for MZ1, MZ2, MZ3, MZ4, and M1 were measured to be 3.41, 4.19, 5.77, 6.07, and 4.68 m^2/g , respectively. These values provide insights into the extent of surface exposure and the potential for various applications based on surface interactions. The BJH plot illustrated in **Fig. 4.6** (Inset), indicates the mesoporous nature of the synthesized ferrites with pore size lies in 14 to 17 nm. Substitution of Mn ions in $ZnFe_2O_4$ can introduce defects and vacancies in the crystal lattice. These defects can create additional sites on the surface, contributing to an increase in surface area. The increased surface area provides more active sites for the adsorption of dye molecules and the subsequent photocatalytic degradation. This can lead to a more efficient degradation process, as there are more opportunities for the interaction between the dye molecules and the catalyst [46].

The porous morphology observed in the SEM images contributes to the enhancement of surface area. The increase in surface area observed in the BET analysis aligns with the SEM analysis showing an increase in porosity, especially with the higher concentration of Mn ions. In summary, the data indicates a positive correlation between the porosity observed in SEM analysis and the surface area measured through BET analysis.

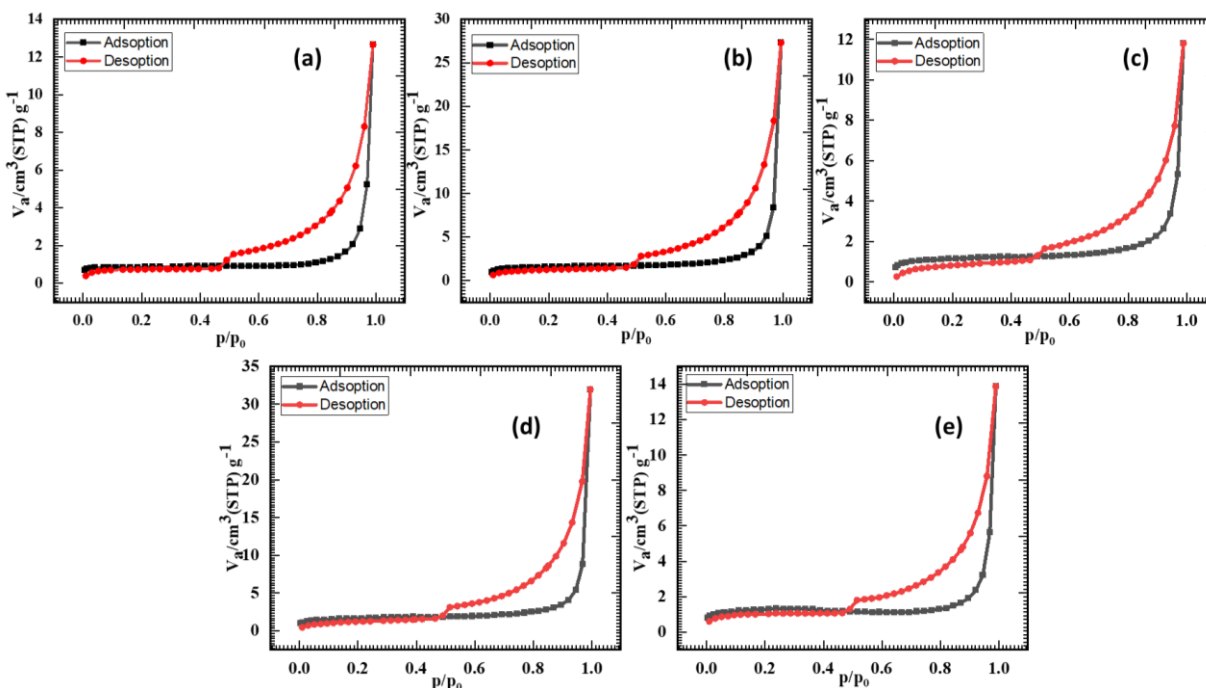


Fig. 4.6: BET adsorption-desorption isotherm graph of different Mn substitution (a) MZ1, (b) MZ2, (c) MZ3, (d) MZ4, and (e) M1.

4.3.8 UV-DRS analysis:

The UV-DRS analysis was conducted to assess the optical properties of various samples, namely Z1, MZ1, MZ2, MZ3, MZ4, and M1. The results, as depicted in **Fig. 4.7**, reveals a noteworthy trend in the band gap variations corresponding to different Mn concentrations in ZnFe_2O_4 NPs. Mn substitution in ZnFe_2O_4 NPs can influence the electronic structure and alter the band gap. The specific impact on the band gap depends on several factors, such as the concentration, electronic configuration of Mn ions, and the crystal field effects. The band gap is a crucial parameter in understanding optical behavior, and in this case, the band gap was observed to decrease systematically with substitution of Mn concentration in ZnFe_2O_4 NPs. The specific band gap values observed for each sample were as follows: For ZnFe_2O_4 NPs (Z1), the band gap was measured to be 1.8 eV. With the addition of Mn concentration in ZnFe_2O_4 NPs, the band gap exhibited a decreasing order as the MZ1, MZ2, MZ3, MZ4, and M1 samples showed band gap of 1.56, 1.54, 1.47, 1.46, and 1.43 eV, respectively. This reduction could be attributed to the creation of additional energy levels within the band structure, making it easier for electrons to move from the valence band to the

conduction band. A decreased band gap allows the material to absorb a broader range of wavelengths, especially in the visible light region. This expanded absorption range can enhance the efficiency of the photocatalytic process, as visible light is more abundant in sunlight.

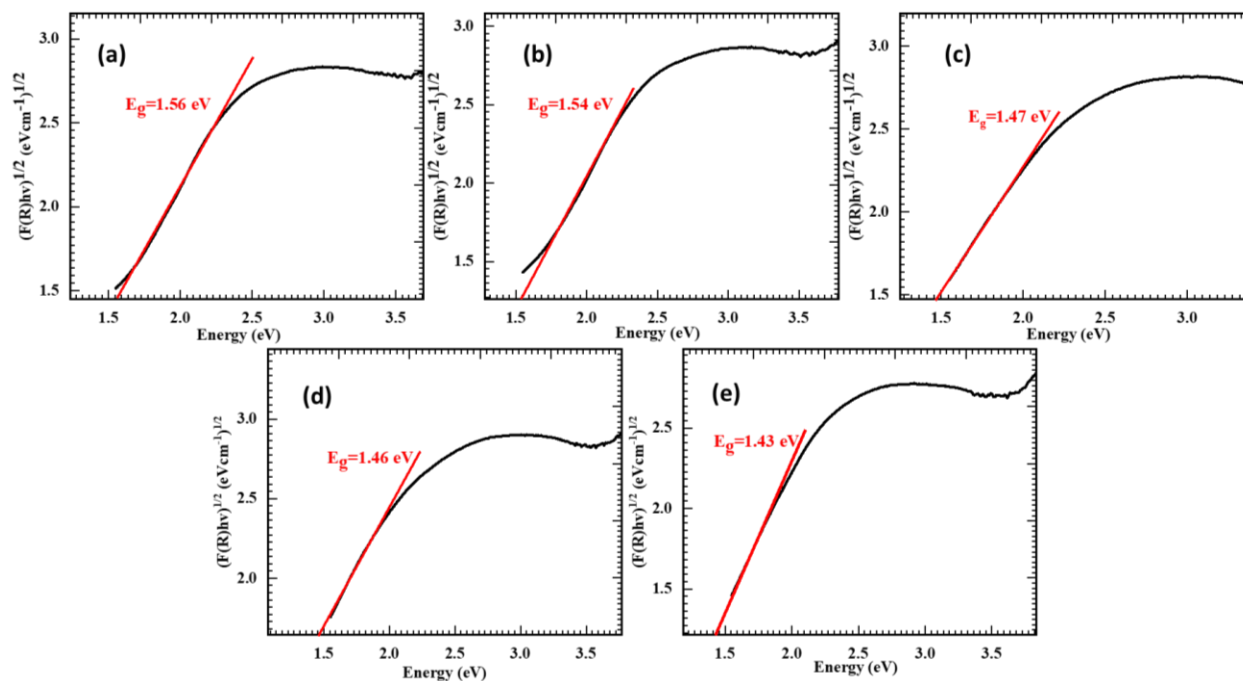


Fig. 4.7: UV-DRS spectrum of different Mn substitution (a) MZ1, (b) MZ2, (c) MZ3, (d) MZ4, and (e) M1.

4.4. Conclusions:

The successful synthesis of manganese-substituted zinc ferrite nanoparticles (MZNPs) via a combustion method, has achieved which demonstrating varying manganese concentration influencing structural, morphological, and optical properties. The spinel structure was confirmed by XRD. The increase in lattice parameters due to Mn^{2+} substitution has been observed for Mn-Zn ferrite. FT-IR and Raman spectroscopy indicated molecular changes and spinel phase. The SEM and TEM analyses showed formation nanoparticles, with size $54.32 \text{ nm} \pm 22.49 \text{ nm}$ and EDS confirms the elemental composition. The XPS confirmed the oxidation states of the constituent elements. BET analysis revealed mesoporous structures with increased surface area. UV-DRS studies showed a decreased band gap with higher Mn^{2+} concentration from 1.56 to 1.43 eV, enhancing visible light absorption. These tailored properties make MZNPs are highly effective for photocatalytic dye degradation and environmental remediation which are studied in subsequent chapters.

4.5. References:

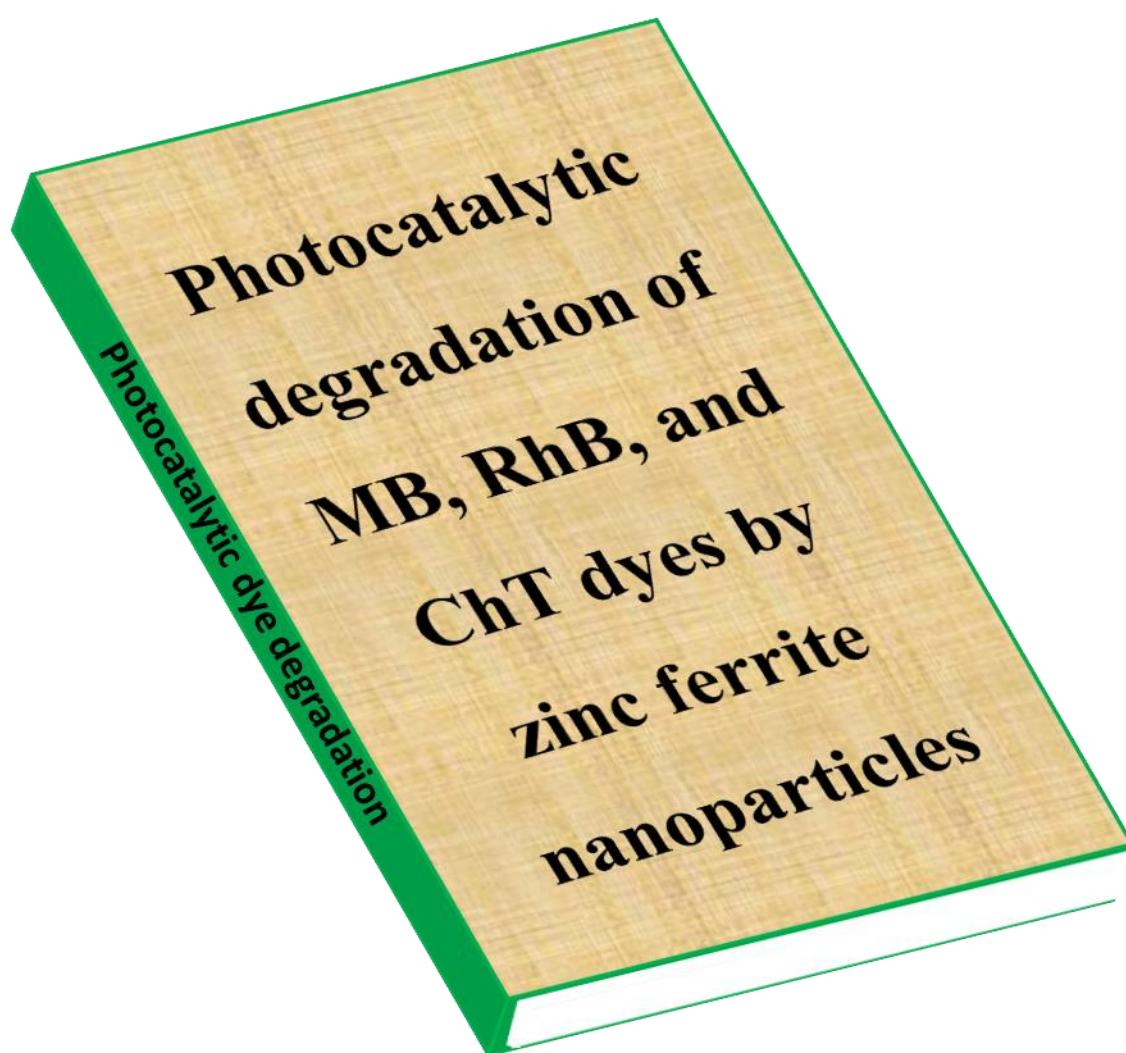
1. Hu P, Long M. *Applied Catalysis B: Environmental.*, 181, (2016), 103-117.
2. Gomez-Pastora J, Dominguez S, Bringas E, Rivero M, Ortiz I, Dionysiou D. *Chemical Engineering Journal.*, 310, (2017), 407-427.
3. Casbeer E, Sharma V, Li X. *Separation and Purification Technology.*, 87, (2012), 1-4.
4. Padhi B. *International Journal of Environmental Sciences.*, 3, (2012), 940-955.
5. Demirbas A. *Journal of Hazardous Materials.*, 167, (2009), 1-9.
6. Gupta V, Pathania D, Agarwal S, Singh P. *Journal of Hazardous Materials.*, 243, (2012), 179-186.
7. Körbahti B, Artut K, Geçgel C, Özer A. *Chemical Engineering Journal.*, 173, (2011), 677-688.
8. Cardoso N, Lima E, Pinto I, Amavisca C, Royer B, Pinto R, Alencar W, Pereira S. *Journal of Environmental Management.*, 92, (2011), 1237-1247.
9. El Nemr A, Abdelwahab O, El-Sikaily A, Khaled A. *Journal of Hazardous Materials.*, 161, (2009), 102-110.
10. Mora E, Barojas E, Rojas E, González R. *Solar Energy Materials and Solar Cells.*, 91, (2007), 1412-1415.
11. Kazemi M, Mohammadizadeh M. *Chemical Engineering Research and Design.*, 90, (2012), 1473-1479.
12. Nwanya A, Deshmukh P, Osuji R, Maaza M, Lokhande C, Ezema F. *Sensors and Actuators B: Chemical.*, 206, (2015), 671-678.
13. Chang Y. *Journal of Alloys and Compounds.*, 637, (2015), 112-118.
14. Guo X, Zhu H, Li Q. *Applied Catalysis B: Environmental.*, 160, (2014), 408-414.
15. Liu X, Gao W. *Materials and Manufacturing Processes.*, 27, (2012), 905-909.
16. Jadhav S, Hankare P, Patil R, Sasikala R. *Materials letters.*, 65, (2011), 371-373.

17. Cheng X, Leng W, Liu D, Zhang J, Cao C. *Chemosphere.*, 68, (2007), 1976-1984.
18. Su N, Lv P, Li M, Zhang X, Li M, Niu J. *Materials Letters.*, 122, (2014), 201-204.
19. Castro T, Da Silva S, Nakagomi F, Moura N, Franco Jr A, Morais P. *Journal of Magnetism and Magnetic Materials.*, 389, (2015), 27-33.
20. Singh C, Jauhar S, Kumar V, Singh J, Singhal S. *Materials Chemistry and Physics.*, 156, (2015), 188-197.
21. He Z, Sun C, Yang S, Ding Y, He H, Wang Z. *Journal of Hazardous Materials.*, 162, (2009), 1477-1486.
22. Zhang Z, Kong J. *Journal of Hazardous Materials.*, 193, (2011), 325-329.
23. Wang L, Li J, Wang Y, Zhao L, Jiang Q. *Chemical Engineering Journal.*, 181, (2012), 72-79.
24. Janani B, Syed A, Sruthi L, Sivaranjani P, Elgorban A, Bahkali A, Zaghloul N, Badawy M, Das A, Khan S. *Colloids and Surfaces A: Physicochemical and Engineering Aspects.*, 628, (2021), 127307 (1-11).
25. Yao H, Fan M, Wang Y, Luo G, Fei W. *Journal of Materials Chemistry A.*, 3, (2015), 17511-17524.
26. Tahir M, Nabi G, Khalid N. *Materials Science in Semiconductor Processing.*, 84, (2018), 36-41.
27. Tahir M, Kiran H, Iqbal T. *Environmental Science and Pollution Research.*, 26, (2019), 10515-10528.
28. Prakash T, Kumar E, Gnanamoorthi K, Munshi A, Almehmadi S, Mersal G, El Metwaly N. *Solid State Communications.*, 336, (2021), 114388 (1-6).
29. Munawar T, Mukhtar F, Nadeem M, Asghar M, Mahmood K, Hussain A, Arshad M, un Nabi M, Iqbal F. *Ceramics International.*, 46, (2020), 22345-22366.
30. Chahar D, Taneja S, Bisht S, Kesarwani S, Thakur P, Thakur A, Sharma P. *Journal of Alloys and Compounds.*, 851, (2021), 156878 (1-9).

-
31. Nekvapil F, Bortnic R, Leoştean C, Barbu-Tudoran L, Bunge A. *Analytical Letters.*, 56, (2022), 42-52.
 32. Mahmood A, Maqsood A, Abdi A. *Physica Scripta.*, 97, (2022), 065707 (1-17).
 33. Phalake S, Lad M, Kadam K, Tofail S, Thorat N, Khot V. *ACS omega.*, 7, (2022), 44187-44198.
 34. Zhou B, Zhang Y, Liao C, Yan C, Chen L, Wang S. *Journal of Magnetism and Magnetic Materials.*, 280, (2004), 327-333.
 35. Zaki H, Dawoud H. *Physica B: Condensed Matter.*, 405, (2010), 4476-4479.
 36. Salunkhe A, Khot V, Phadatare M, Thorat N, Joshi R, Yadav H, Pawar S. *Journal of Magnetism and Magnetic Materials.*, 352, (2014), 91-98.
 37. White W, DeAngelis B. *Spectrochimica Acta Part A: Molecular Spectroscopy.*, 23, (1967), 985-995.
 38. Murugesan C, Chandrasekaran G. *Journal of Superconductivity and Novel Magnetism.*, 29, (2016), 2887-2897.
 39. Khot V, Salunkhe A, Phadatare M, Pawar S. *Materials Chemistry and Physics.*, 132, (2012), 782-787.
 40. Ahmadi F, Saeedi M, Akbari J, Seyedabadi M, Ebrahimnejad P, Morteza-Semnani K, Ghasemi S, Moalem-Banhangi M, Babaei A, Hashemi SM, Asare-Addo K. *AAPS PharmSciTech.*, 24, (2023), 222 (1-13).
 41. Li M, Fang H, Li H, Zhao Y, Li T, Pang H, Tang J, Liu X. *Journal of Superconductivity and Novel Magnetism.*, 30, (2017), 2275-2281.
 42. Guzmán G, Escudero R, Silva R, Herrera M. *Journal of Applied Physics.*, 123 (2018), 161578 (1-10).
 43. Hwang J, Ishida Y, Kobayashi M, Hirata H, Takubo K, Mizokawa T, Fujimori A, Okamoto J, Mamiya K, Saito Y, Muramatsu Y. *Physical Review B.*, 72, (2005), 085216 (1-6).

44. Joshi B, Samuel E, Park C, Kim Y, Lee H, Yoon S. *Applied Surface Science.*, 559, (2021), 149951 (1-10).
45. Kooti M, Sedeh A. *Scientia Iranica.*, 19, (2012), 930-933.
46. Molinari R, Lavorato C, Argurio P. *Catalysis Today.*, 281, (2017), 144-164.

CHAPTER V



5.1. Introduction:

Photocatalytic degradation is a promising approach for the removal of organic pollutants from wastewater, utilizing catalysts that can be activated by light to break down contaminants [1]. Zinc ferrite (ZnFe_2O_4) has emerged as an effective photocatalyst due to its favourable properties such as high stability, non-toxicity, and efficient light absorption [2]. The synthesis of ZnFe_2O_4 can be optimized by adjusting the fuel-to-oxidizer ratio, which impacts the material's photocatalytic performance by influencing particle size, surface area, and the number of active sites. This study focuses on the degradation of three dyes: Methylene Blue (MB), Rhodamine B (RhB), and Chloramine T (ChT) by ZnFe_2O_4 NPs. These dyes were selected due to their widespread use in various industries, their environmental persistence, and their distinct chemical structures, which provide a comprehensive assessment of ZnFe_2O_4 as a photocatalytic capability.

MB is a commonly used dye in the textile industry, known for its recalcitrance in the environment. Its molecular structure includes aromatic rings and sulfur atoms, which contribute to its stability and resistance to degradation [3]. RhB is extensively used in biological staining and dye lasers, presenting a different structural challenge for degradation [4]. RhB has a complex aromatic structure with amino groups that contribute to its stability and vivid color, making it a persistent pollutant [5]. ChT, a chlorinated aromatic compound, is used in organic synthesis and as a disinfectant, posing a significant threat due to its stability and potential toxicity. The chlorine atoms in ChT add to its resistance to biodegradation and its toxicity to aquatic life [6].

The selection of these dyes allows for a thorough evaluation of ZnFe_2O_4 efficiency in degrading diverse pollutants. Photocatalytic degradation efficiency is closely related to the positions of the highest occupied molecular orbital (HOMO) and the lowest unoccupied molecular orbital (LUMO) of the dyes [7]. The HOMO-LUMO gap determines the dye's stability and reactivity. ZnFe_2O_4 , with its suitable band gap, can absorb visible light and generate electron-hole pairs. The photo-generated electrons in the conduction band (CB) and holes in the valence band (VB) can migrate to the surface and participate in redox reactions [2].

MB, with a relatively higher HOMO energy level, can easily donate electrons to the photo-generated holes in ZnFe_2O_4 , facilitating its degradation. RhB, on the other hand, has a lower LUMO level, making it an efficient acceptor of electrons from the CB of ZnFe_2O_4 . This electron transfer can enhance the breakdown of RhB molecules [8-9]. ChT, with its chlorinated aromatic structure, presents a challenge due to its lower reactivity, but the electron-hole pairs generated in ZnFe_2O_4 can still effectively initiate the degradation process.

By varying the fuel-oxidizer (F/O) ratio during combustion synthesis of ZnFe_2O_4 , the study aims to determine the optimal conditions for maximizing photocatalytic degradation efficiency across these different types of dyes. Adjusting (F/O) ratio impacts the material's crystallinity, surface area, and defect density, which in turn affects the generation and separation of electron-hole pairs, and thus the overall photocatalytic activity. These findings will provide insights into the design of efficient photocatalysts for environmental cleanup applications, particularly in degrading diverse and persistent organic pollutants like MB, RhB, and ChT.

5.2. Photocatalytic dye degradation study experimental setup:

Synthesis of ZnFe_2O_4 at different F/O ratio as mention in Chapter 3 and labeled as Z1, Z2, Z3, Z4, Z5. In this study, the photocatalytic degradation capability of ZNPs for MB, RhB, and ChT dyes under visible light irradiation was systematically investigated using a Xenon lamp (35 W) as the light source. To ensure selective visible light irradiation, an infrared, AM 1.5 G, and a 400 nm cut-off filters were employed (see **Fig. 5.1**).

The experiments were conducted with a controlled light intensity of 100 mW cm^{-2} , measured using a solar power meter. Batch experiments were carried out, tracking the decrease in the concentration of the dye solution over time by performing UV–Visible absorption measurements at regular time intervals. Initially, 30 mL solution containing 10 ppm of dye was prepared, and a predetermined amount of the ZNPs catalyst was introduced into the photoreactor. The system was left in the dark for 30 minutes to establish adsorption–desorption equilibrium between the dye and the catalyst. Subsequently, 2 mL of the effluent was extracted from the photoreactor, filtered using a syringe filter (PTFE

0.45 micron), and the UV–Vis absorption spectrum was recorded. This procedure was repeated at 30-minute intervals to monitor the decrease in the absorption intensity. The collected data, consisting of UV–Vis absorption spectra recorded over time, allows the assessment of the catalyst's effectiveness in degrading dye under visible light irradiation. The analysis of absorption intensity variations provides insights into the kinetics and efficiency of the photocatalytic degradation process, offering a comprehensive understanding of the material's photocatalytic performance in water treatment applications.

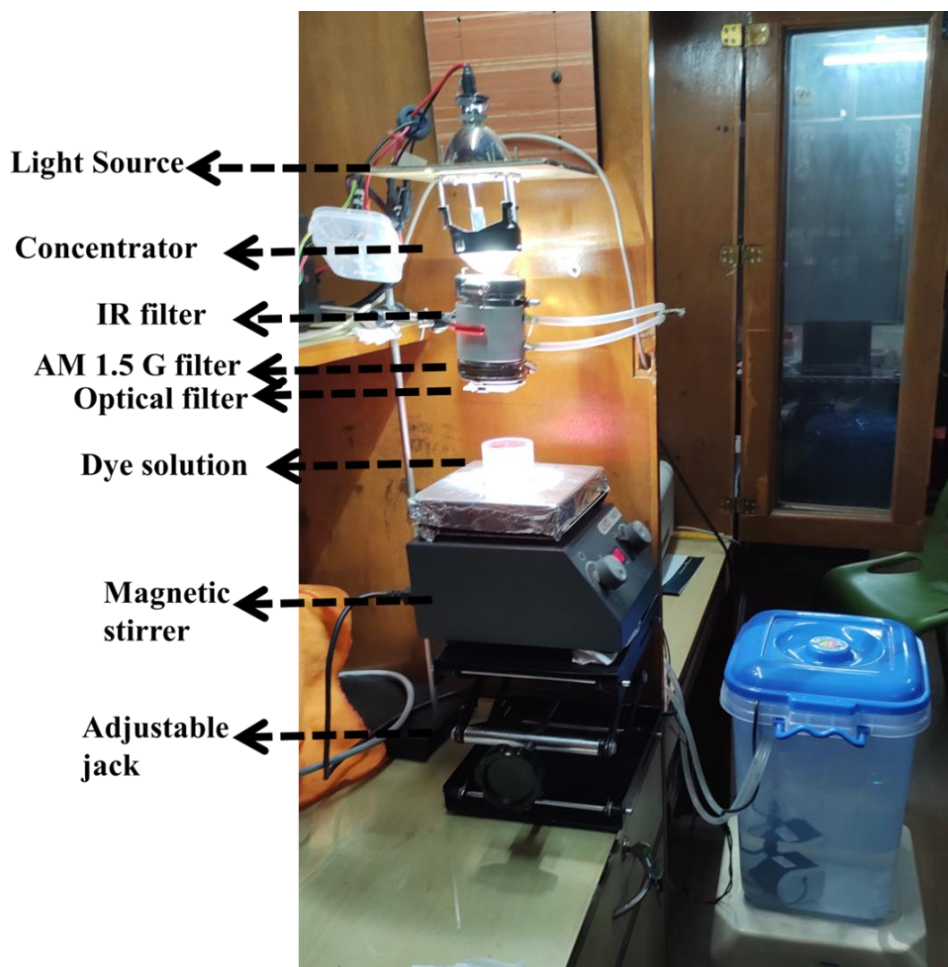


Fig. 5.1: Assembly of photocatalytic dye degradation experiment

The % dye degradation was calculated by the following equation,

$$\% \text{ dye degradation} = \frac{C_0 - C_t}{C_0} \times 100, \quad (5.1)$$

where C_0 and C_t represent the absorption intensity at initial and at time t , respectively.

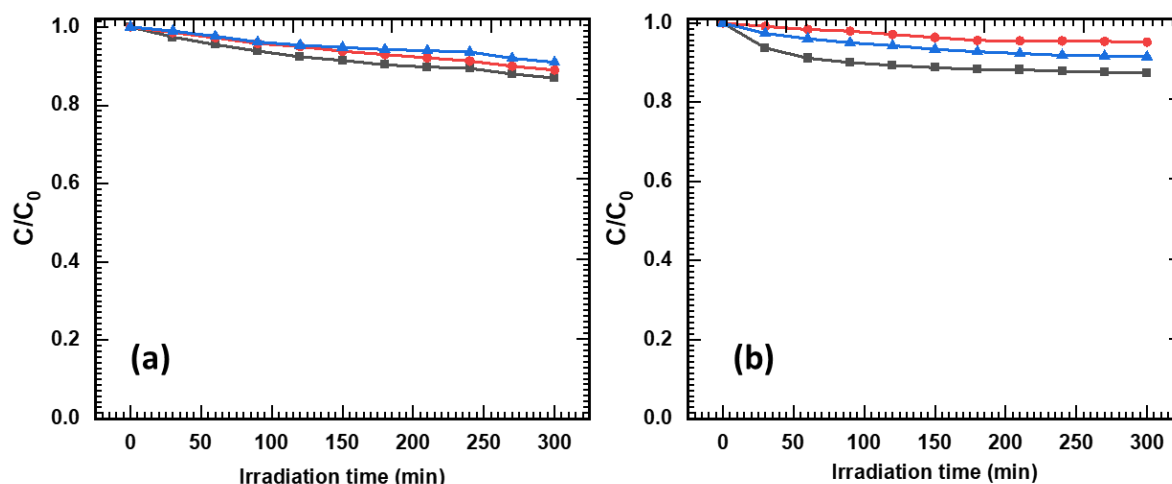


Fig. 5.2: (a) Control experiment (without light) for MB (black) and RhB (blue) dyes and ChT (red). (b) Control experiment (without catalyst) for MB (black) and RhB (red) dyes and ChT (blue).

Further, to verify that the degradation is not taking place by photolysis, blank experiments were performed in presence of light for MB, RhB and ChT dyes without using a catalyst. As shown in **Fig. 5.2a** and **b**, the photolysis of MB, RhB and ChT is very less as compared to the degradation performance in the presence of a catalyst. In addition, the photoactivity of Z1 was checked in the absence of light for all three dyes. The results show a significant difference in the degradation performance of Z1 in the presence and absence of light confirming the excellent visible light activity of Z1 material.

5.3. Photocatalytic Degradation of MB, RhB, and ChT Dyes:

The percentage of MB dye removal was examined as a function of Z1 to Z5 catalysts. We investigated the removal of MB dye over ZnFe_2O_4 under the influence of visible light and observed that it was 90.65% in 5h. Yadav et al. [10] synthesized ZnFe_2O_4 by co-precipitation technique. Prepared nano-ferrites used for photocatalytic studies and the depletion of MB dye over a radiation time of 5 h to 50 minutes was observed. It showed an initial concentration of 10 mgL^{-1} contaminants and about 74% efficiency for 50 mg nanophotocatalysts. In the current study, the photocatalytic degradation performance of MB, RhB, and ChT dyes was systematically studied using ZnFe_2O_4 Nps synthesized through different fuel-oxidizer ratios.

Fig 5.3 shows Photocatalytic dye degradation of MB by using different G/N ratios Z1 to Z5 upto 300 min. The Z1 sample demonstrate the highest activity against all three dyes under visible light irradiation, showcasing its superior photocatalytic properties. For MB dye, the Z1 sample achieves a remarkable 90.65% degradation efficiency within 5 hours, significantly higher compared to other samples such as Z2 (85.10%), Z3 (81.95%), Z4 (83.58%), and Z5 (65.64%) as shown in **Fig. 5.3**. This performance can be attributed to the optimal glycine-to-nitrate ratio in Z1, which facilitated the formation of active sites and enhanced photocatalytic activity. In contrast, increasing the glycine and nitrate content in other samples resulted in decreased degradation efficiency due to lower specific surface areas and fewer active sites.

Similarly, for RhB dye, Z1 exhibits the highest degradation percentage at 88.40%, while samples Z2 to Z5 showed a gradual decline in performance, with degradation percentages ranging from 87.94% to 83.44% as shown in **Fig. 5.4**. The fuel-lean Z1 sample contributed to a more reduced state of metal ions and increased defect sites, which are crucial for photocatalytic activity. Conversely, higher oxidizer ratios in other samples produced more stable but less reactive materials, reducing the number of catalytically active sites.

For ChT dye, the Z1 sample again demonstrates superior photocatalytic activity with an 81.92% degradation efficiency. Samples Z2 to Z5 showed decreased performance, with degradation percentages from 77.5% to 72.28% as shown in **Fig. 5.5**. This decline indicates that deviations from the optimal fuel-oxidizer ratio in Z1 resulted in less effective photocatalytic properties, such as larger particle sizes and reduced surface areas.

Overall, the study highlights that the specific synthesis conditions, particularly the fuel-to-oxidizer ratio, have a significant impact on the photocatalytic efficiency of ZnFe_2O_4 . The optimal conditions achieved in the Z1 sample facilitated maximum degradation of MB, RhB, and ChT dyes, emphasizing the importance of precise control over synthesis parameters for environmental cleanup applications.

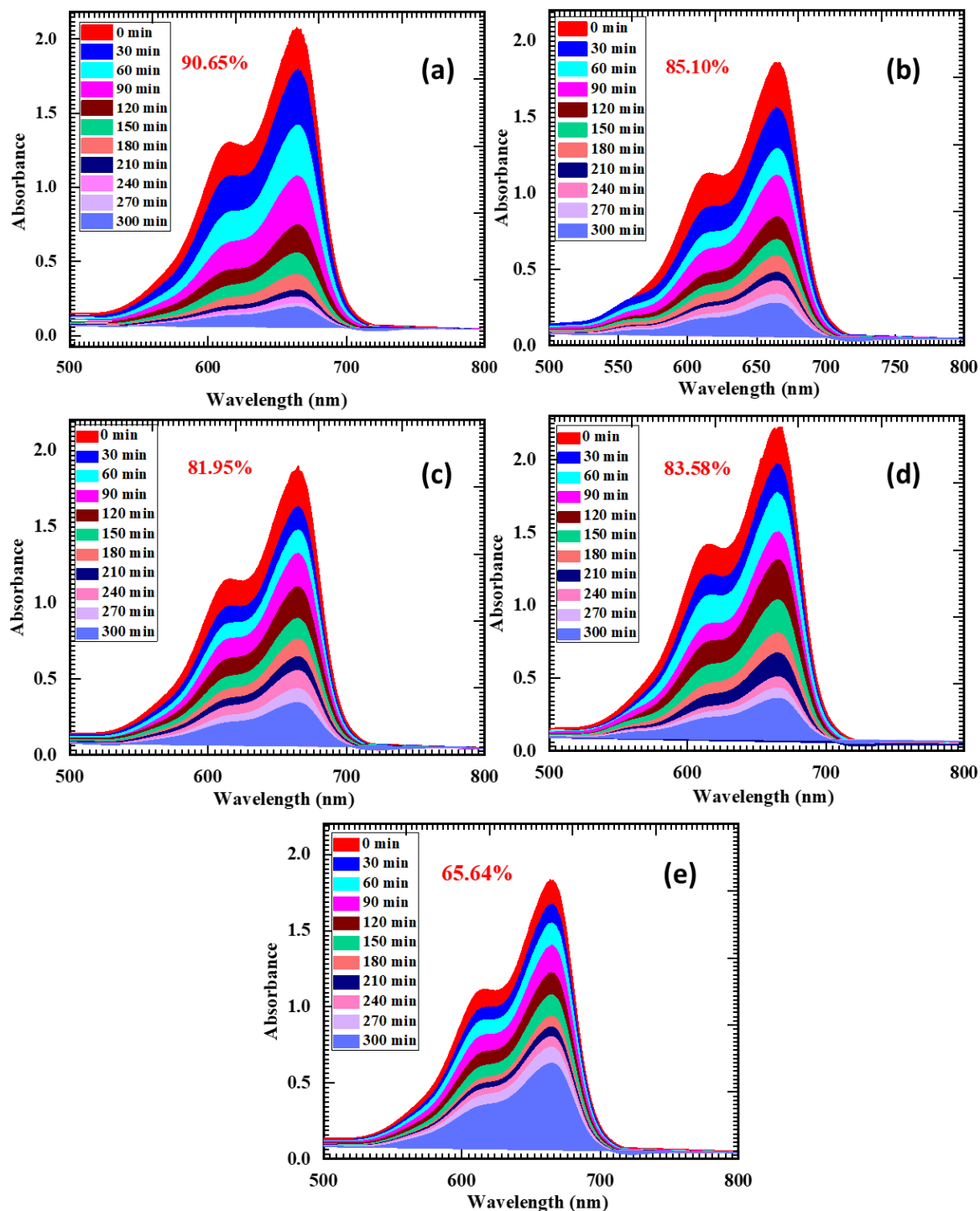


Fig. 5.3: Photocatalytic dye degradation of MB by using different G/N ratios, (a) Z1, (b) Z2, (c) Z3, (d) Z4, and (e) Z5.

Z1 shows the best photocatalytic performance due to its smaller crystallite size 9.74 nm, which provides a larger surface-to-volume ratio, increasing the number of active sites

for the reaction. Its porous structure, observed in SEM, further enhances dye adsorption. Z1 also has an optimal band gap of 1.84 eV, suitable for absorbing visible light, promoting efficient electron-hole pair generation. Additionally, its high surface area 41.86 m²/g allows for better interaction with dye molecules, resulting in superior degradation efficiency 90.65%. However, as the content of glycine and nitrate increases, degradation activity decreases due to the formation of larger particles and excess carbon residues, reducing active surface sites and overall efficiency.

The ZnFe₂O₄ prepared by combustion method displays excellent photocatalytic performance compared with the available literature (given in **Table 5.1**) [11-14].

Table 5.1. Comparison with the reported literature.

Catalyst	Time (min)	Light Source	Degradation (%)	References
ZnFe ₂ O ₄ (Z1)	300	Visible Light ($\lambda \geq 400$ nm)	90.65	Present work
ZnFe ₂ O ₄	60	Visible Light	65	11
ZnFe ₂ O ₄	160	Visible Light	66.4	12
ZnFe ₂ O ₄	90	sunlight	89	13
ZnFe ₂ O ₄	40	Visible Light + H ₂ O ₂	100	14

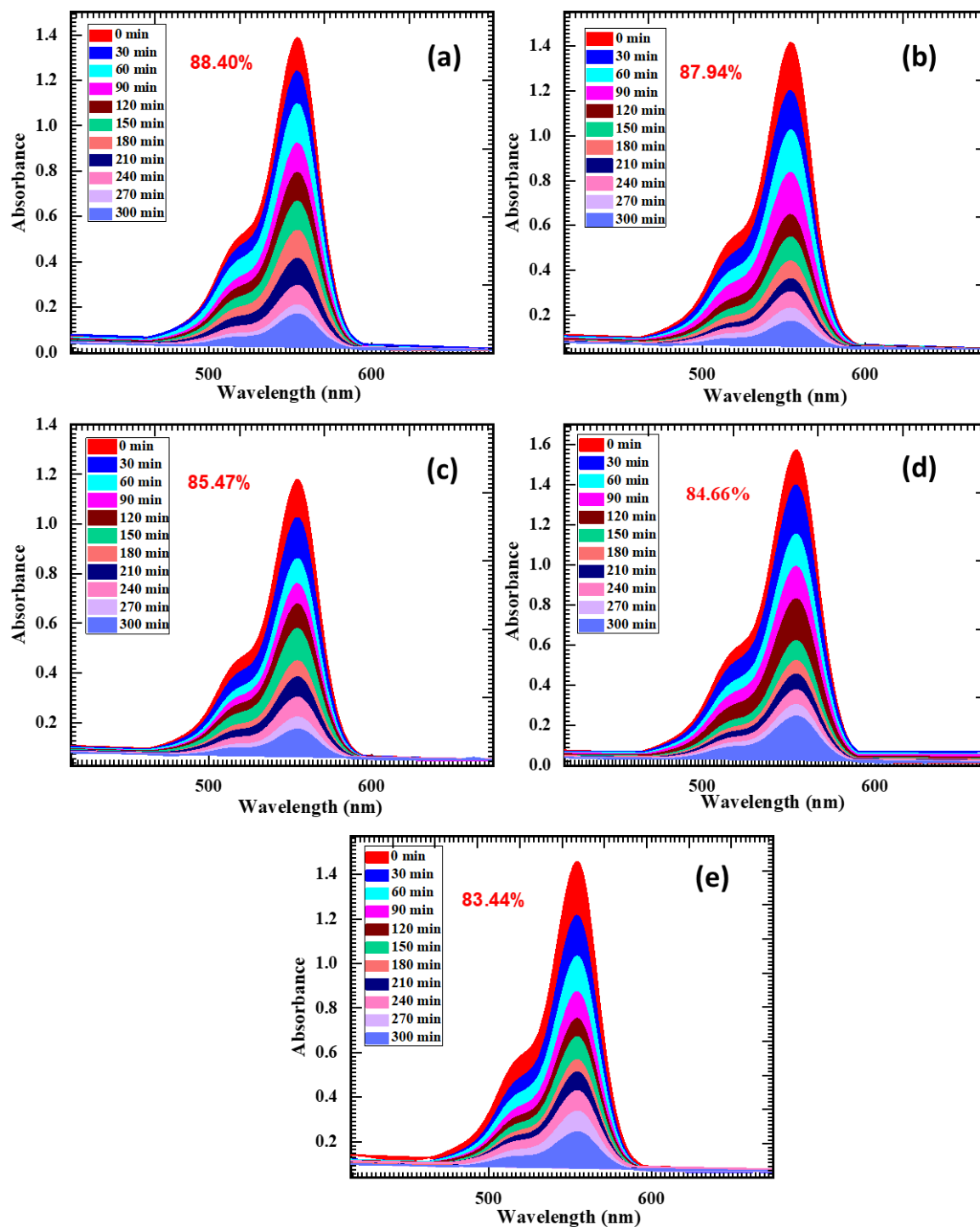


Fig. 5.4: Photocatalytic dye degradation of RhB by using different G/N ratios, (a) Z1, (b) Z2, (c) Z3, (d) Z4, and (e) Z5.

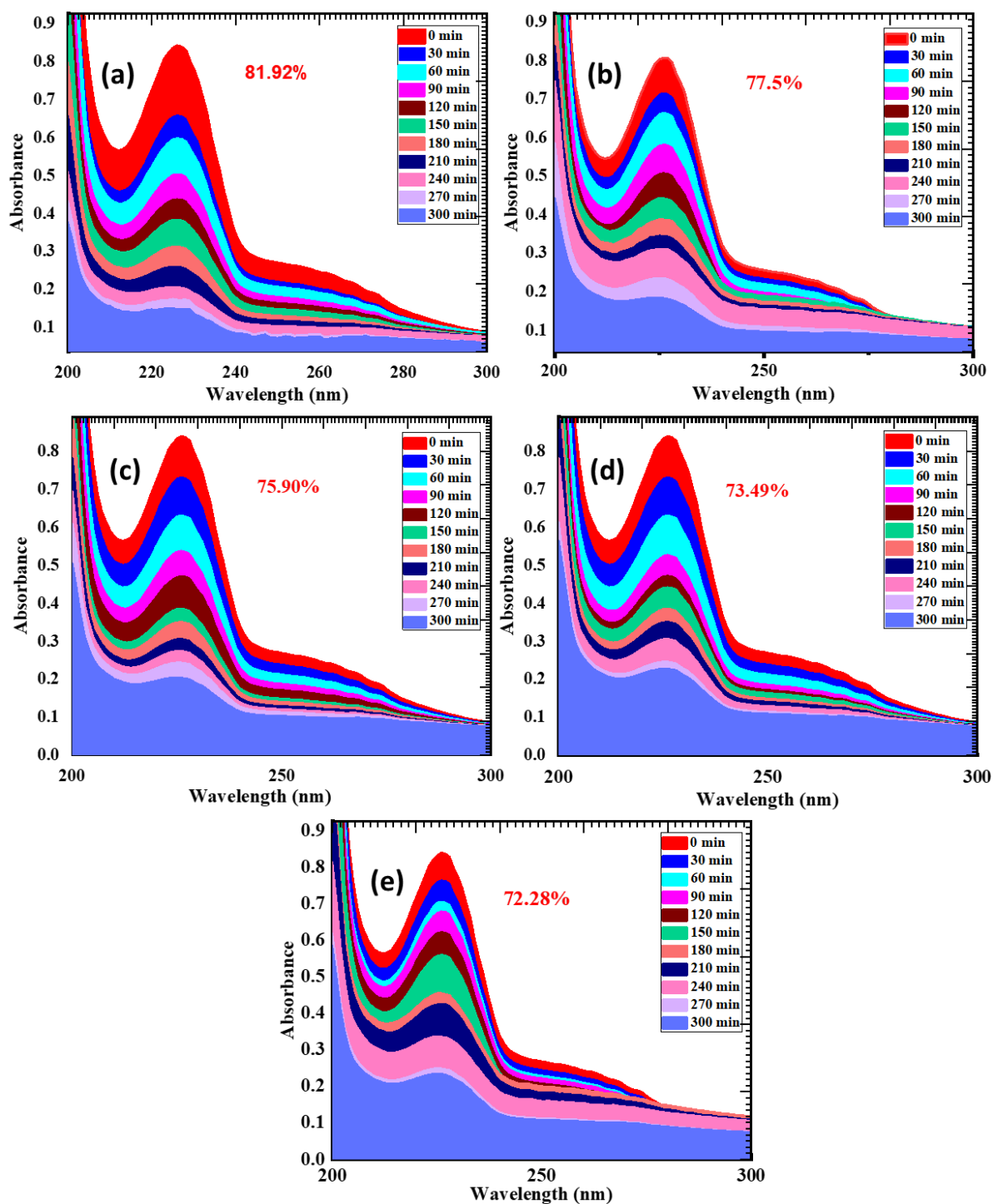


Fig. 5.5: Photocatalytic dye degradation of ChT by using different G/N ratios, (a) Z1, (b) Z2, (c) Z3, (d) Z4, and (e) Z5.

5.3.1. Catalyst dosage for MB RhB and ChT dyes:

The efficiency of photocatalytic dye degradation process is significantly influenced by the dosage of the catalyst used. Catalyst dosage plays a crucial role in determining the overall surface area available for photocatalytic reactions, the number of active sites, and the light absorption capacity of the system. Understanding the optimal catalyst dosage is essential for maximizing the degradation efficiency while maintaining cost-effectiveness and minimizing potential drawbacks such as catalyst aggregation and light shading.

At lower catalyst dosages, the available surface area and number of active sites may be insufficient to facilitate effective interactions between the catalyst and the pollutant molecules. This limitation can result in lower degradation rates and reduced overall efficiency. As the catalyst dosage increases, the surface area and number of active sites also increase, leading to improved photocatalytic activity and higher degradation rates. However, beyond a certain point, further increases in catalyst dosage can lead to adverse effects. Excessive catalyst concentrations can cause aggregation of catalyst particles, which reduces the effective surface area and blocks light from reaching all active sites. This phenomenon, known as light shading, hinders the photocatalytic process and decreases the overall efficiency.

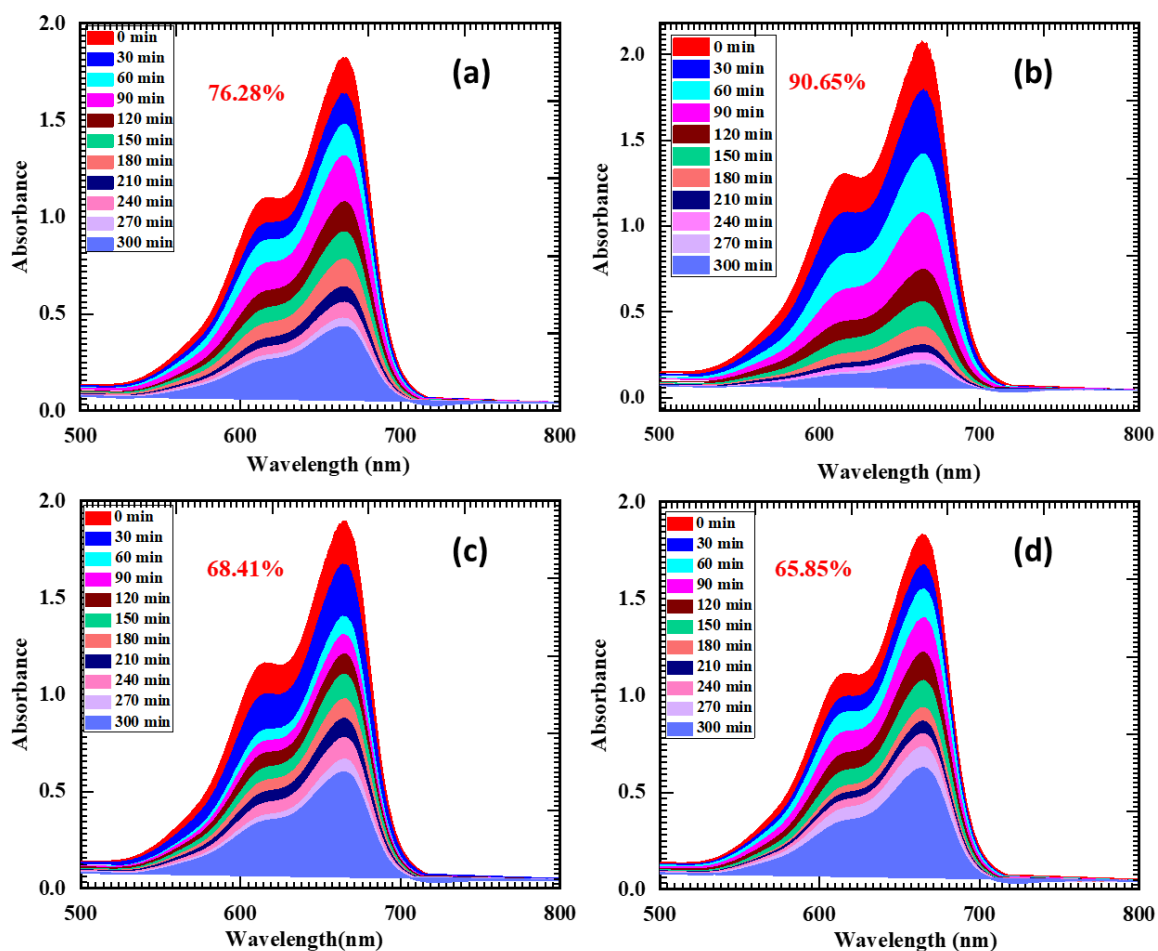


Fig. 5.6: Photocatalytic dye degradation of MB by using G/N=0.48 (Z1) Effect of catalyst loading (a) 15 mg, (b) 30 mg, (c) 45 mg, and (d) 60 mg.

Optimizing the catalyst dosage of optimized Z1 catalyst is therefore critical to achieving the best performance in photocatalytic degradation processes. It ensures that the maximum number of active sites are available for the reaction without causing significant aggregation or light shading. The following study evaluates the degradation performance of three different dyes, Methylene Blue (MB), Rhodamine B (RhB), and Chloramine T (ChT) under various catalyst dosages (15 mg, 30 mg, 45 mg, and 60 mg) to identify the optimal dosage for each dye as shown in **Fig. 5.6-5.8** respectively.

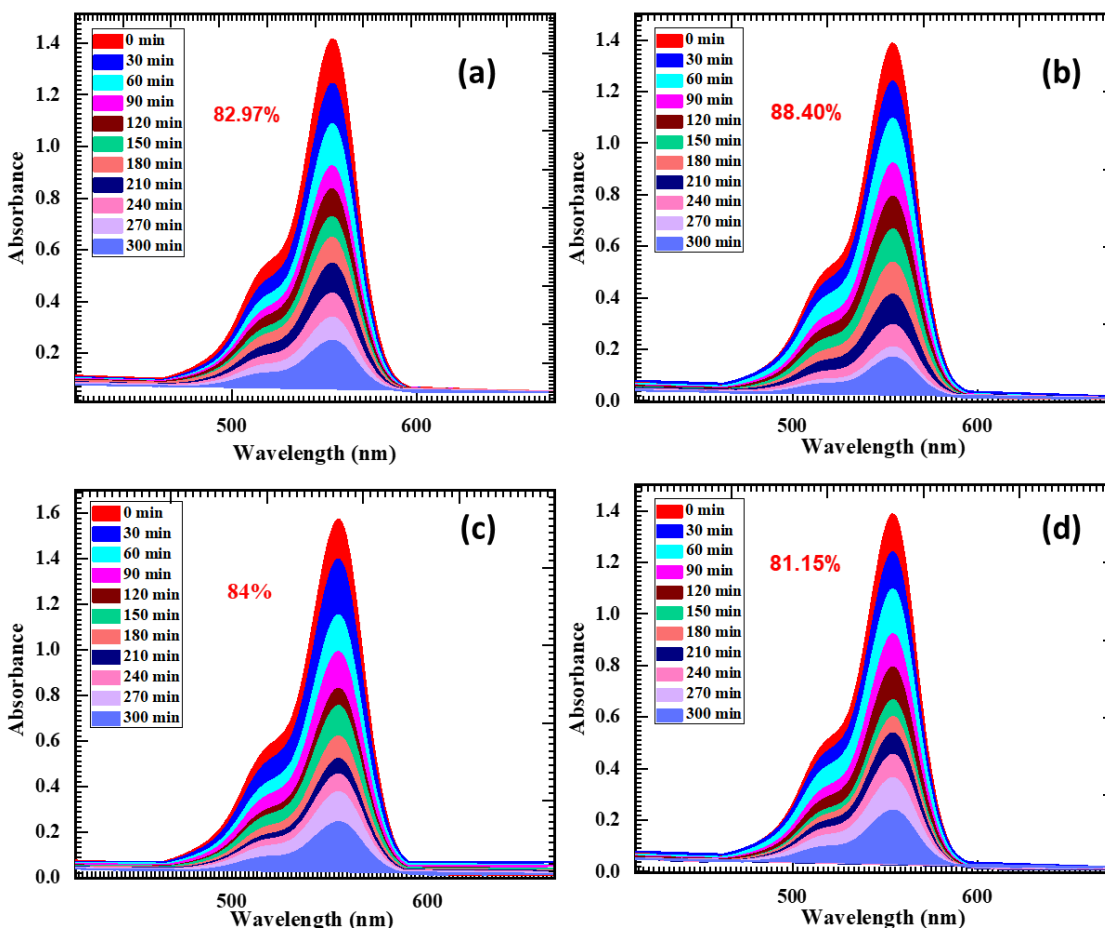


Fig. 5.7: Photocatalytic dye degradation of RhB by using G/N=0.48 (Z1) Effect of catalyst loading (a) 15 mg, (b) 30 mg, (c) 45 mg, and (d) 60 mg.

The study evaluates the photocatalytic degradation performance of MB, RhB, and ChT dyes using various catalyst dosages (15 mg, 30 mg, 45 mg, and 60 mg). At a 15 mg dosage, MB, RhB, and ChT dyes showed reduction percentages of 76%, 82.97%, and 73.80%, respectively. This lower catalyst loading resulted in suboptimal degradation due to insufficient surface area and active sites. The 30 mg dosage proved to be the most effective, with MB, RhB, and ChT dyes achieving reduction percentages of 90%, 88.40%, and 81.92%, respectively. This dosage offered an optimal balance of surface area and active sites, maximizing photocatalytic efficiency. However, increasing the catalyst dosage to 45 mg led to a decline in degradation efficiency for all dyes, with MB, RhB, and ChT achieving 68%, 84%, and 76.19% reduction, respectively. This decrease is likely due to catalyst aggregation and diminished light penetration [15-17]. At the highest dosage of 60

mg, the degradation performance further declined, with MB, RhB, and ChT reduction percentages dropping to 65%, 81.15%, and 64.70%, respectively. This reduction is attributed to excessive catalyst causing light shading and reduced active site availability. Overall, the 30 mg dosage is identified as the optimal loading for effective photocatalytic degradation of MB, RhB, and ChT dyes.

Furthermore, the pseudo-first-order kinetic model is employed to understand the kinetics of the degradation process as shown in **Fig. 5.9** The present study suggests that Z1 exhibit rate constant of 0.0086016, 0.0071613, and 0.0056924 min^{-1} for MB, RhB, and ChT dyes with R^2 value of 0.98787, 0.96945, and 0.99477 respectively. The R^2 values and kinetic constants for kinetic model are tabulated in **Table 5.2**.

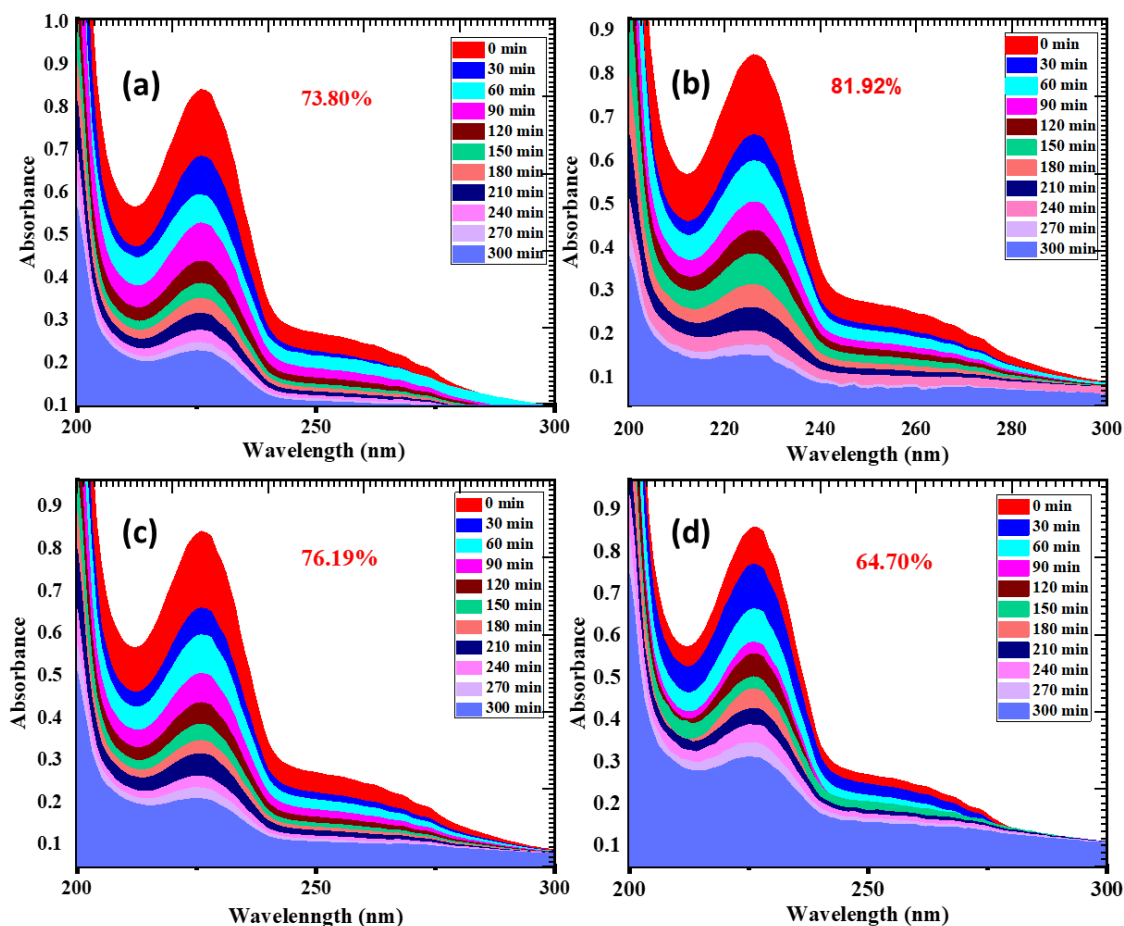
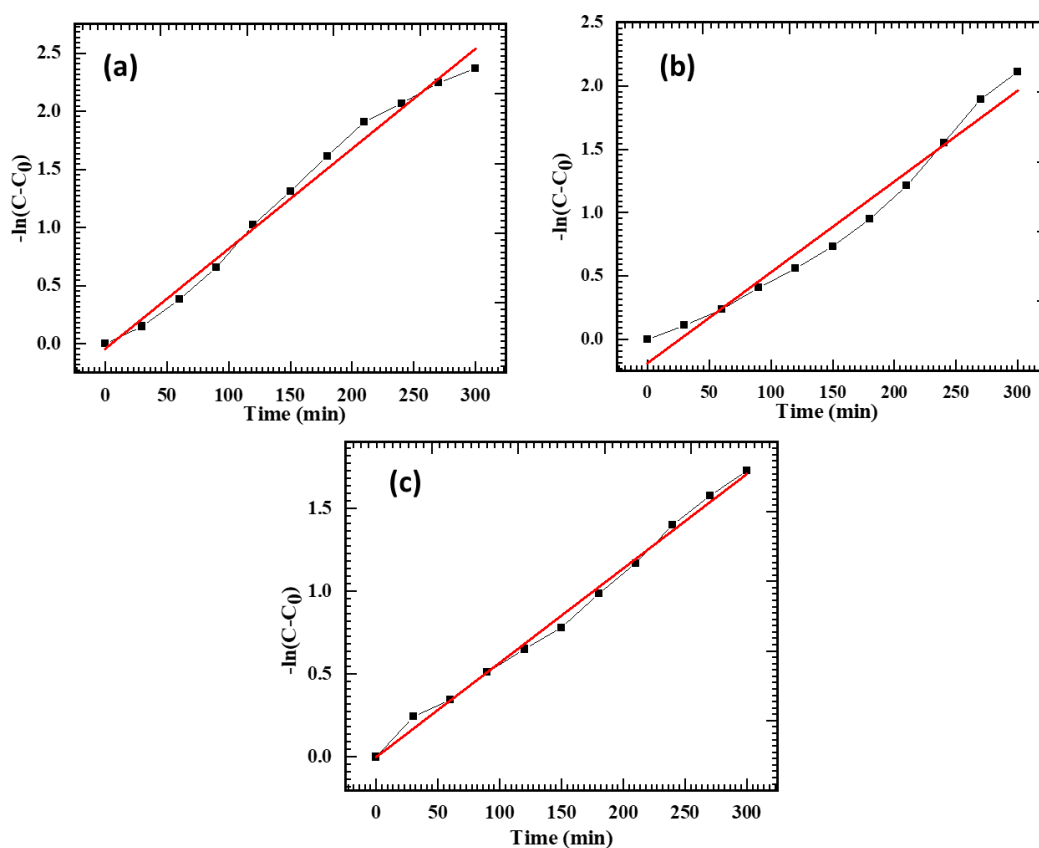


Fig. 5.8: Photocatalytic dye degradation of ChT by using G/N=0.48 (Z1) Effect of catalyst loading (a) 15 mg, (b) 30 mg, (c) 45 mg, and (d) 60 mg.

Table 5.2. Kinetic parameters of Z1 for MB, RhB, and ChT dyes.

Dyes	Degradation (%)	Rate constant (min^{-1})	R^2
MB	90.65	0.0086016	0.98787
RhB	88.40	0.0071613	0.96945
ChT	81.92	0.0056924	0.99477

**Fig. 5.9:** Pseudo first-order kinetics for (a) MB, (b) RhB, and (c) ChT dyes of Z1.

5.3.2. Scavenger studies for MB RhB and ChT dyes:

Scavenger studies are essential for elucidating the underlying mechanisms of photocatalytic degradation processes. Understanding the specific reactive species involved in the degradation of pollutants allows for the optimization of photocatalysts and reaction

conditions, thereby improving efficiency and effectiveness. In photocatalysis, reactive species such as hydroxyl radicals ($\cdot\text{OH}$), superoxide radicals ($\text{O}_2^{\cdot-}$), and photogenerated holes (h^+) play crucial roles in breaking down contaminants. Identifying which of these species are most active in the degradation process is vital for designing targeted strategies to enhance photocatalytic performance.

For this study, scavenger experiments were conducted to determine the primary reactive species responsible for the degradation of MB (blue color), RhB (pink color), and ChT (colorless) dyes using the Z1 photocatalyst. We have used same color combination as that of dyes to depict scavenger activity. By introducing specific scavengers that selectively inhibit different reactive species, the study aims to reveal the contributions of hydroxyl radicals, superoxide radicals, and holes in the photocatalytic processes. This detailed understanding is necessary to optimize the conditions for maximum degradation efficiency and to tailor the photocatalyst for diverse environmental applications.

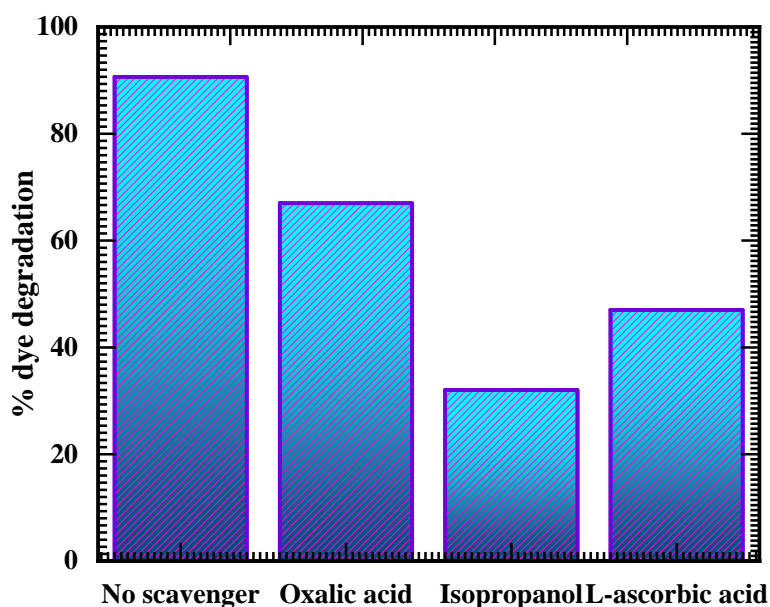


Fig. 5.10: Scavenger study of Z1 photocatalyst for MB dye.

The scavenger studies provided crucial insights into the primary reactive species involved in the photocatalytic degradation of MB, RhB, and ChT dyes using the Z1 photocatalyst. For MB, the investigation revealed that hydroxyl radicals ($\cdot\text{OH}$) play a predominant role in the degradation process. When isopropanol, a hydroxyl radical

scavenger, was introduced, the degradation efficiency dropped significantly to 32%, highlighting the critical involvement of hydroxyl radicals. The presence of L-ascorbic acid, a hole scavenger, results in a moderate reduction in efficiency to 47% as shown in **Fig. 5.10**, indicating that holes also contribute to the process, albeit to a lesser extent. Oxalic acid, a superoxide radical scavenger, led to a degradation efficiency of 67%, suggesting that superoxide radicals are involved but are not the primary reactive species.

In the case of RhB, the degradation efficiency decreased markedly to 24% when isopropanol was used, again underscoring the essential role of hydroxyl radicals in the photocatalytic degradation process. The introduction of L-ascorbic acid results in a 52% degradation efficiency as shown in **Fig. 5.11**, further demonstrating that holes play a secondary role compared to hydroxyl radicals. With oxalic acid, the degradation efficiency was 64%, indicating that superoxide radicals have a moderate impact on the degradation process.

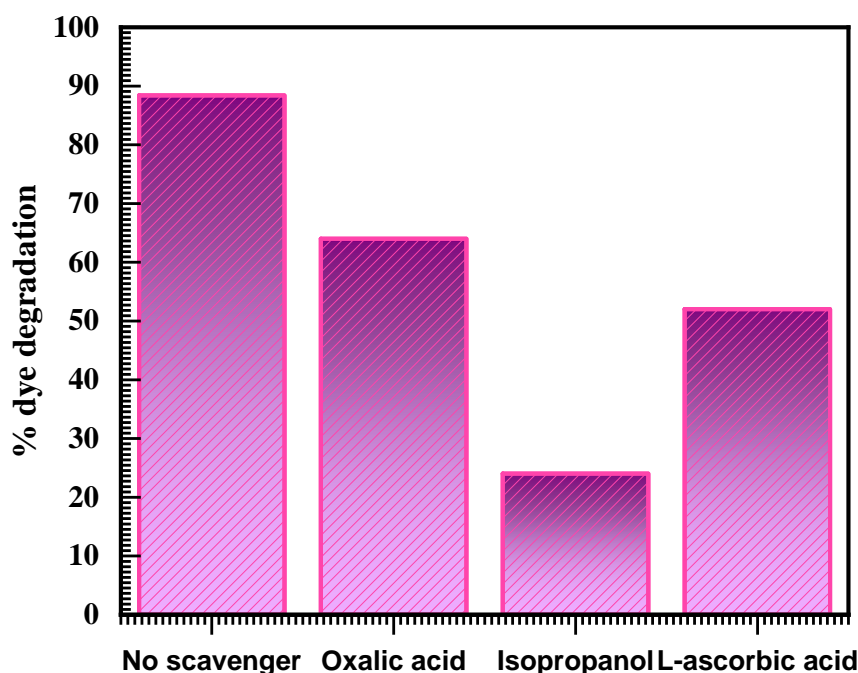


Fig. 5.11: Scavenger study of Z1 photocatalyst for RhB dye.

For ChT, the scavenger study similarly identified hydroxyl radicals as the primary reactive species. The degradation efficiency dropped significantly to 29% in the presence of isopropanol, affirming the crucial role of hydroxyl radicals. The presence of L-ascorbic

acid reduces the efficiency to 48%, while oxalic acid decreases it to 61% as shown in **Fig. 5.12**. These results suggest that while superoxide radicals and holes do contribute to the degradation process, their roles are secondary to that of hydroxyl radicals.

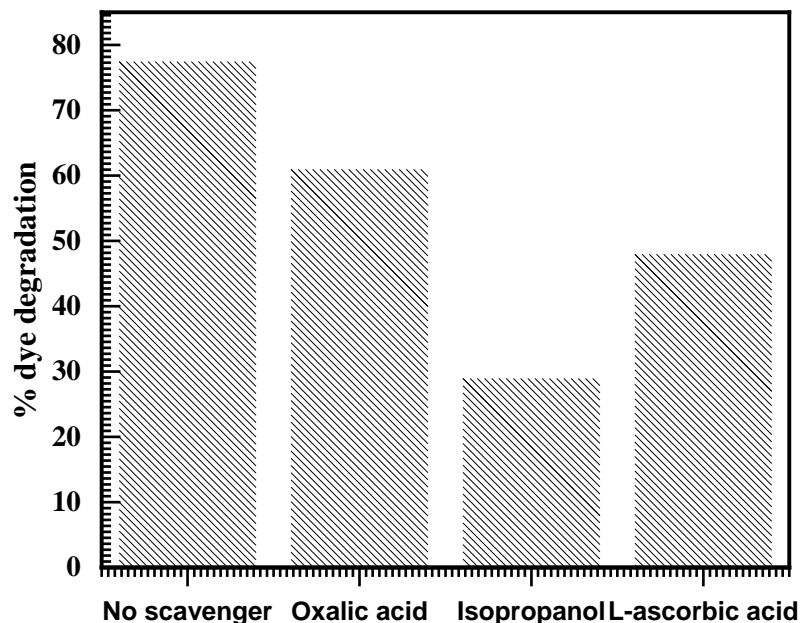


Fig. 5.12: Scavenger study of Z1 photocatalyst for ChT dye.

Overall, the scavenger studies for MB, RhB, and ChT dyes consistently demonstrated the dominant role of hydroxyl radicals in the photocatalytic degradation process facilitated by the Z1 photocatalyst. This finding is pivotal for optimizing photocatalytic processes for environmental remediation, emphasizing the need to enhance the generation and utilization of hydroxyl radicals to maximize degradation efficiency across different types of pollutants.

5.3.3. Investigation of the reusability and chemical stability of the Z1 sample:

Recyclability studies are essential for assessing the durability and long-term efficiency of photocatalysts in practical applications. These studies simulate real-world conditions where photocatalysts are subjected to repeated use, providing insights into their stability, robustness, and potential for commercial viability. Understanding how well a photocatalyst maintains its activity over multiple cycles is crucial for industrial processes, such as wastewater treatment and environmental remediation, where sustained

performance is key to cost-effectiveness and environmental sustainability. The ability to recycle and reuse photocatalysts reduces the need for frequent replacement, thereby minimizing operational costs and environmental impact. In this context, the recyclability of the Z1 photocatalyst was evaluated for its performance in degrading Methylene Blue (MB), Rhodamine B (RhB), and Chloramine T (ChT) dyes over multiple cycles.

The recyclability study demonstrated the robust performance and sustained efficiency of the Z1 photocatalyst across multiple cycles for degrading MB, RhB, and ChT dyes. We have used same color combination as that of dyes to depict recyclability activity. For MB, the Z1 photocatalyst maintain a high degradation efficiency of 74% after five consecutive cycles as shown in **Fig. 5.13**. This indicates the durability and resilience of the photocatalyst, which are essential for continuous operation in practical applications. The process involved separating the photocatalyst via an applied magnetic field and drying at room temperature to prevent thermal degradation. These steps ensured that the activity of the photocatalyst was preserved for subsequent cycles.

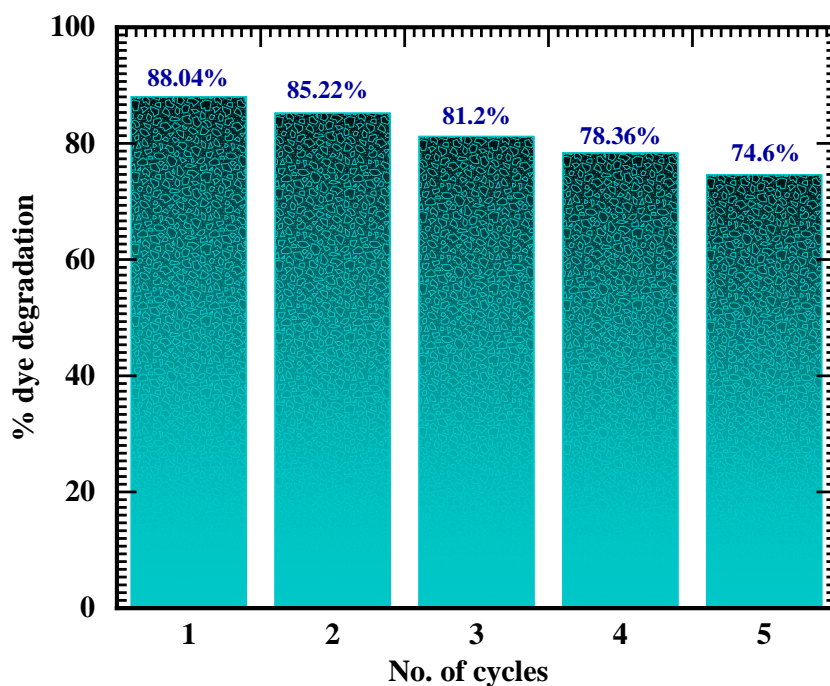


Fig. 5.13: Recyclability study of Z1 photocatalyst for MB dye.

In the case of RhB, the Z1 photocatalyst exhibits an end efficiency of 75.17% after five cycles as shown in **Fig. 5.14**, highlighting its stability and robustness. The minimal decline in performance underscores the ability of the photocatalyst to withstand repeated use without significant loss of activity. This stability is crucial for reducing operational costs in industrial applications, as it decreases the frequency of catalyst replacement.

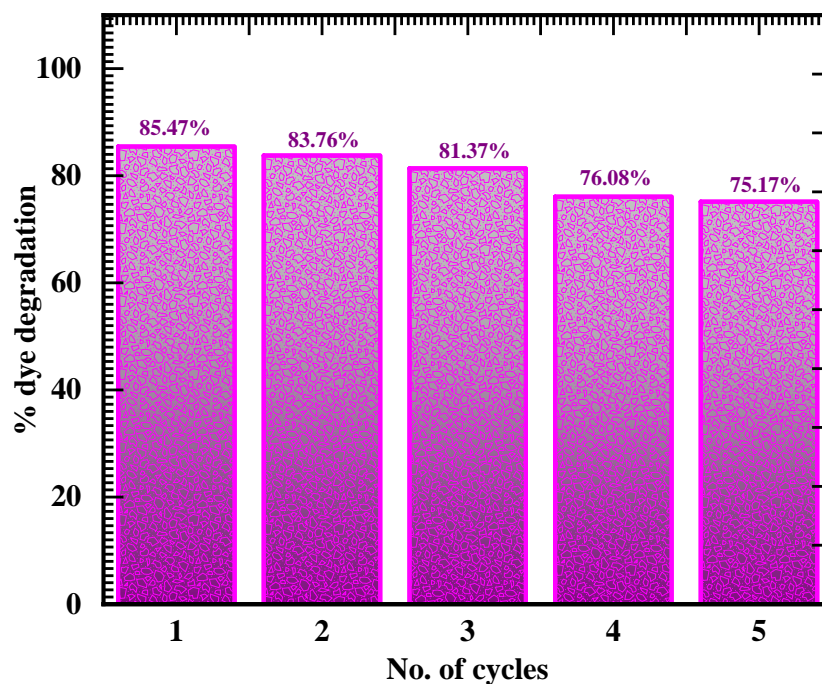


Fig. 5.14: Recyclability study of Z1 photocatalyst for RhB dye.

For ChT, the Z1 photocatalyst shows a degradation efficiency of 63.4% after five cycles as shown in **Fig. 5.15**. This sustained high performance over multiple cycles indicates the long-term stability and effectiveness of the photocatalyst. The consistent degradation efficiency across cycles demonstrates the potential of the Z1 photocatalyst for practical applications in various industrial and environmental contexts.

Overall, the recyclability study confirms the suitability of the Z1 photocatalyst for commercial applications, as it maintains high degradation efficiencies for MB, RhB, and ChT dyes over multiple cycles. This capability enhances its attractiveness for use in sustainable and cost-effective water treatment and pollutant remediation processes, aligning with environmental and economic goals.

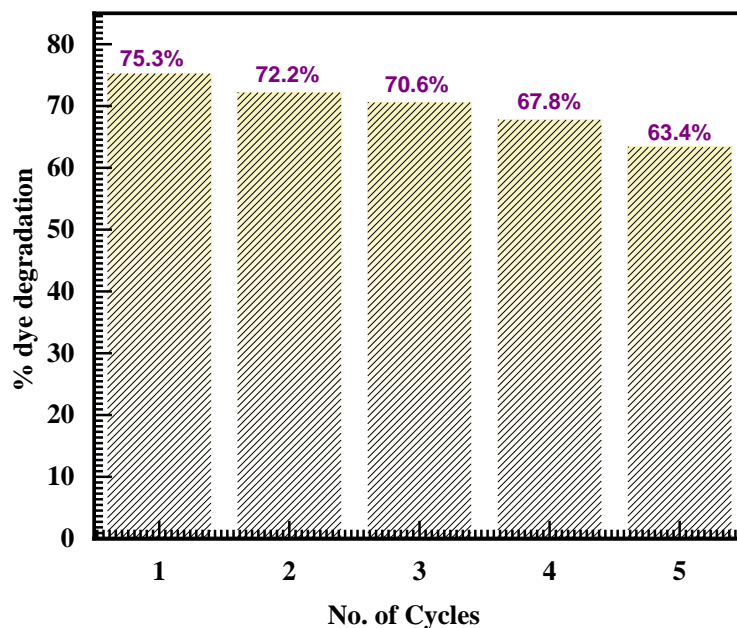


Fig. 5.15: Recyclability study of Z1 photocatalyst for ChT dye.

Fig. 5.16 shows XRD patterns of Z1 before and after the degradation process. It is evident from the literature that a stable photocatalyst sustain its structural stability even after degrading a specific dye. Nevertheless, the continuous reaction in the dye solution has the potential to reduce the crystallinity of the catalyst [18, 19]. In present case, the catalyst shows a similar XRD pattern after degradation, with slightly decreased crystallinity.

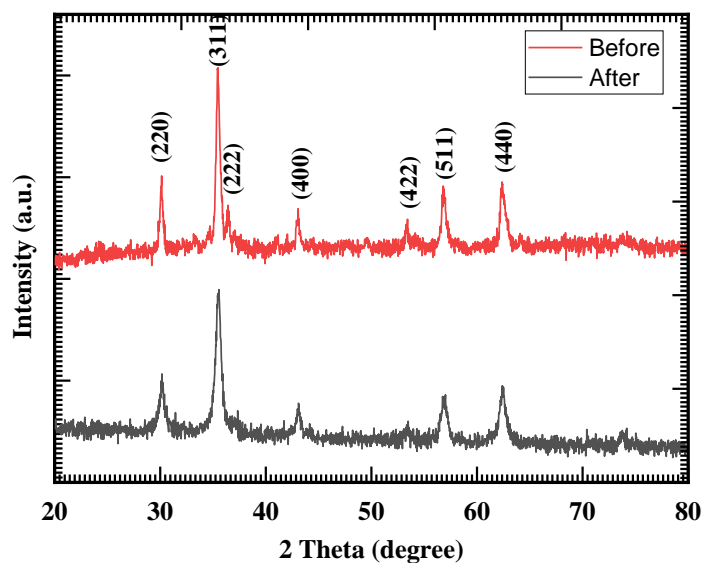
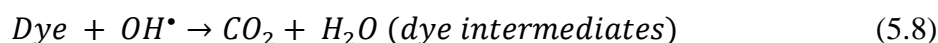
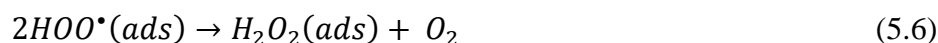
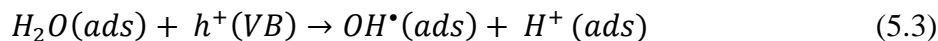
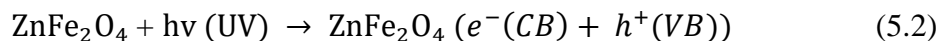
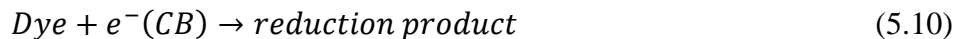
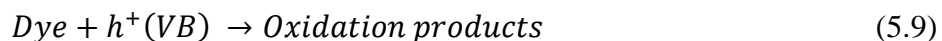


Fig. 5.16: Stability study of Z1 before and after irradiation using XRD.

5.4. Plausible dye degradation mechanism:

In photocatalysis, when a photocatalyst is exposure to solar radiation, resulting electrons transfer from valence band to the conduction band and holes generate in the valence band [eqⁿ 5.2]. The surface hydroxyl group on the catalyst's surface combines with the photogenerated hole to form the hydroxyl radical [eqⁿ 5.3]. Contrarily, the photogenerated electron in the conduction band reacts with the dissolved oxygen to form superoxide radical [eqⁿ 5.4], then the superoxide produced gets protonated forming hydroperoxyl radical and then subsequently H₂O₂ which further dissociates into highly reactive hydroxyl radicals [eqⁿ 5.5-5.7]. Both oxidation and reduction processes commonly take place on the surface of the photoexcited semiconductor photocatalyst [eqⁿ 5.8-5.10s] [20-22]. Several variables have been explored in order to explain Z1 sample's greater catalytic activity. Among all samples, Z1 demonstrated remarkable photocatalytic activity in the photocatalytic reduction of MB. In general, a larger surface area is better for photocatalytic reactions. The surface area of the photocatalysts synthesized at the Z1 ratio was higher, at 41.861 m²/g. As a result, there are more active sites available for photocatalytic reactions, increasing the activity of the overall structure. In comparison to Z3 (1.6 eV) and Z5 (1.87 eV), Z1 has a lower electron hole recombination energy and a higher absorptive power in the visible spectrum. This improves free charge carrier separation. As a result, the main cause of strong photocatalytic activity is the huge number of free electrons and holes [23].





5.5. Conclusions:

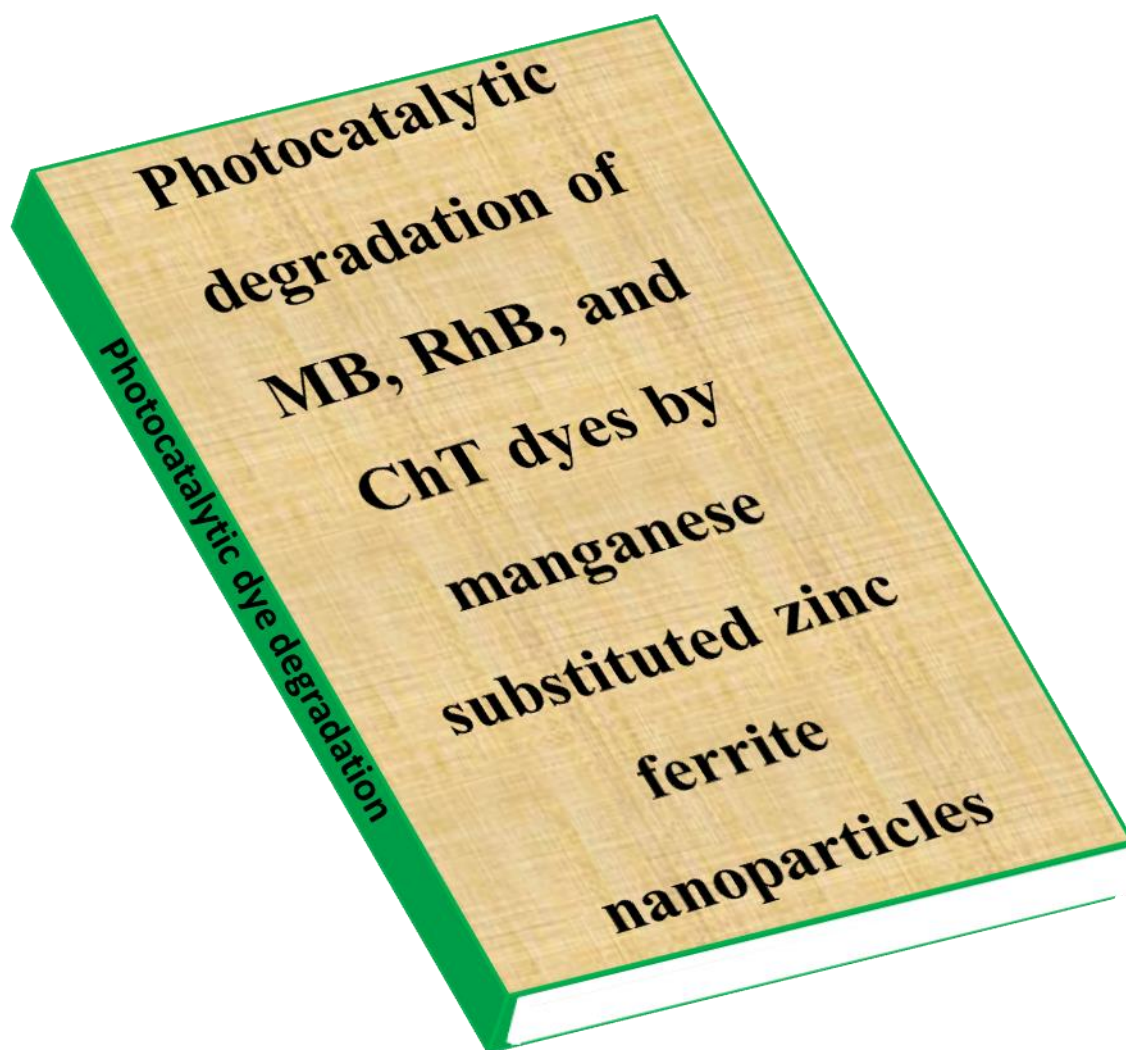
In conclusion, this chapter comprehensively investigates the photocatalytic degradation of Methylene Blue, Rhodamine B, and Chloramine T dyes using zinc ferrite nanoparticles under visible light irradiation. The study demonstrates the superior catalytic performance of ZnFe₂O₄ (Z1) 30 mg catalyst, achieving 90.65% for MB dye, 88.40% for RhB dye, and 81.92% for ChT dye, emphasizing the importance of glycine and nitrate content, catalyst dosage, and the presence of scavengers in the degradation process. Hydroxyl radicals are identified as the primary reactive species driving the degradation mechanism. The findings underscore the significant impact of catalyst composition, surface area, and charge carrier separation on the photocatalytic efficiency, providing valuable insights for optimizing photocatalytic processes for environmental remediation.

5.6. References:

1. Pavel M, Anastasescu C, State R, Vasile A, Papa F, Balint I. *Catalysts.*, 13, (2023), 380 (1-45).
2. Sharma S, Dutta V, Raizada P, Hosseini-Bandegharai A, Thakur V, Nguyen V, VanLe Q, Singh P. *Journal of Environmental Chemical Engineering.*, 9, (2021), 105812 (1-20).
3. Khan I, Saeed K, Zekker I, Zhang B, Hendi A, Ahmad A, Ahmad S, Zada N, Ahmad H, Shah L, Shah T. *Water.*, 4, (2022), 242 (1-30).
4. Ashfaq M, Imran M, Haider A, Shahzadi A, Mustajab M, Ul-Hamid A, Nabgan W, Medina F, Ikram M. *Scientific Reports.*, 13, (2023), 17847 (1-16).
5. Sharma P, Ganguly M, Sahu M. *RSC Advances.*, 14, (2024), 11411-11428.
6. Xu W, Vebrosky E, Armbrust K. *Journal of Hazardous Materials.*, 394, (2020), 122575 (1-11).
7. Huo J, Yu D, Li H, Luo B, Arulsamy N. *RSC Advances.*, 9, (2019), 39323-39331.
8. Liu H, Hao H, Xing J, Dong J, Zhang Z, Zheng Z, Zhao K. *Journal of Materials Science.*, 51, (2016), 5872-5879.
9. Jaafar S, Faeq R, Naji A, Nief O, Mohammed M. *RSC Advances.*, 14, (2024), 26066-26076.
10. Yadav N, Chaudhary L, Sakhare P, Dongale T, Patil P, Sheikh A. *Journal of Colloid and Interface Science.*, 527, (2018), 289-297.
11. Chahar D, Taneja S, Bisht S, Kesarwani S, Thakur P, Thakur A, Sharma P. *Journal of Alloys and Compounds.*, 851, (2021), 156878 (1-9).
12. Janani B, Syed A, Sruthi L, Sivaranjani P, Elgorban A, Bahkali A, Zaghloul N, Badawy M, Das A, Khan S. *Colloids and Surfaces A: Physicochemical and Engineering Aspects.*, 628, (2021), 127307 (1-11).
13. Pius M, Joseph S, *IOP Conference Series: Materials Science and Engineering.*, 1233, (2022), 012001 (1-9).
14. Anchieta C, Severo E, Rigo C, Mazutti M, Kuhn R, Muller E, Flores E, Moreira R, Foletto E. *Materials Chemistry and Physics.*, 160, (2015), 141-147.
15. Nguyen T, Huang C, Doong R. *Science of the Total Environment.*, 646, (2019), 745-756.

16. Wang M, Shen S, Li L, Tang Z, Yang J. *Journal of Materials Science.*, 52, (2017), 5155-5164.
17. Nikam D, Jadhav S, Khot V, Phadatare M, Pawar S. *Journal of Magnetism and Magnetic Materials.*, 349, (2014), 208-213.
18. Tateishi I, Katsumata H, Suzuki T, Kaneco S. *Catalysis Letters.*, 147, (2017), 1503-1509.
19. Bagwade P, Magdum V, Malavekar D, Chitare Y, Gunjekar J, Patil U, Lokhande C. *Journal of Materials Science: Materials in Electronics.*, 33, (2022), 24646-24662.
20. Pradhan G, Parida K. *International Journal of Engineering, Science and Technology.*, 2, (2010), 53-65.
21. Gokulakrishnan N, Pandurangan A, Sinha P. *Industrial & Engineering Chemistry Research.*, 48, (2009), 1556-1561.
22. Niu M, Huang F, Cui L, Huang P, Yu Y, Wang Y. *ACS Nano.*, 4, (2010), 681-688.
23. Kumar S, Rao K., *Applied Surface Science.*, 391, (2017), 124-48.

CHAPTER VI



6.1 Introduction:

In recent years, the degradation of organic pollutants in water has become a critical environmental challenge [1]. Among these pollutants, synthetic dyes pose a significant threat due to their persistence, toxicity, and potential to cause environmental pollution [2]. Rhodamine B, Methylene Blue, Chloramine T dye, a commonly used fluorescent dye in various industrial applications such as textiles, printing, and cosmetics, is known for its resistance to degradation and adverse effects on aquatic ecosystems [3-6]. As discussed in the previous chapter, zinc ferrite (ZnFe_2O_4) has been studied for its structural and photocatalytic properties. Building on this, the following sections will examine the effect of manganese substitution, specifically exploring how Mn doping influences the structural and functional behavior of ZnFe_2O_4 in photocatalytic activity.

To address this issue, substitution with Mn^{2+} ions was selected to tailor the structural, and optical properties of Zn ferrite due to the difference in ionic radii and electronic configuration between Mn^{2+} and Zn^{2+} ions. This substitution allows for controlled tuning of the bandgap and charge carrier dynamics, leading to improved photocatalytic efficiency. Additionally, Mn^{2+} doping is known to influence the spinel structure of ferrites, which further contributes to enhanced magnetic and photocatalytic properties. This investigation introduces the utilization of the combustion method for the fabrication of manganese-doped zinc ferrite nanoparticles (MZNPs), with a focus on illustrating the influence of Mn ion concentration on the photocatalytic degradation efficiencies against RhB, MB, and ChT dyes. By spotlighting the combustion synthesis approach, this study endeavors to reveal novel insights of investigating the effect of manganese substitution on the structural and optical properties of zinc ferrite nanoparticles, an area not extensively explored. Furthermore, we evaluate the visible-light-mediated photocatalytic dye degradation efficiency of manganese-substituted zinc ferrite nanoparticles against various dyes, providing new insights into tailoring the photocatalytic properties of spinel ferrites for environmental applications. The combustion synthesis method used in this work is shown to be proficient for fabricating these nanoparticles, revealing novel insights into optimizing spinel ferrites for environmental remediation, elucidating the contribution of a wider array of reactive

species in photocatalysis, including but not limited to hydroxyl radicals (OH^\bullet), superoxide anions ($\text{O}_2^{\bullet-}$), and singlet oxygen (O_2), which are instrumental in the photocatalytic degradation mechanism [7- 11].

This chapter aims to investigate the photocatalytic degradation of Rhodamine B dye using various compositions of metal ferrite nanoparticles as catalysts. Specifically, we focus on metal ferrite compositions including ZnFe_2O_4 , MZ1, MZ2, MZ3, MZ4, and M1. By systematically varying the composition of metal ions in the ferrite structure, we aim to elucidate the influence of composition on the photocatalytic activity and degradation efficiency towards Rhodamine B, Methylene Blue, Chloramine T dye.

Through a comprehensive investigation and analysis of the experimental results, this study seeks to contribute to the understanding of the photocatalytic degradation mechanisms of Rhodamine B dye and provide insights into the design and development of efficient metal ferrite-based photocatalysts for environmental remediation applications.

Improvements in Dye Degradation:

Given the theoretical enhancements discussed, the substitution of Mn in zinc ferrite is predicted to result in significant improvements in the photocatalytic degradation of dyes. Enhanced charge carrier separation, shifted absorption edges into the visible light range, and increased generation of reactive oxygen species contribute to a more efficient and effective photocatalytic process. Consequently, Mn-substituted zinc ferrite is expected to exhibit higher degradation rates and improved efficiencies in less irradiation time compared to bare zinc ferrite.

In terms of specific dyes, Mn- substituted zinc ferrite should be particularly effective against a wide range of organic dyes, including methylene blue, rhodamine B, chloramine T dyes. These dyes are commonly used in industries and are known for their stubborn persistence in the environment due to complex molecular structures that resist breakdown. The enhanced photocatalytic activity of Mn- substituted zinc ferrite could lead to more complete degradation of these dyes, breaking them down into less harmful or inert compounds.

6.2. Photocatalytic dye degradation study Experimental Setup:

The experimental setup for photocatalytic dye degradation followed the same procedure as for zinc ferrite, described in Chapter V, Section 5.2, **Fig.5.1**.

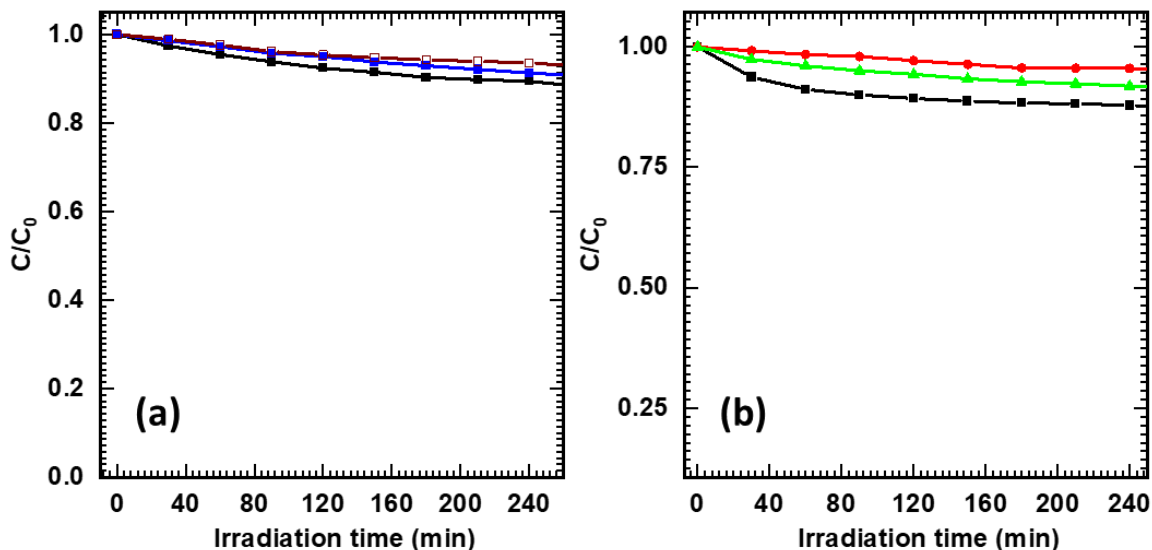


Fig. 6.1: (a) Control experiment (without light) for MB (black) and RhB (red) dyes and ChT (Blue). (b) Control experiment (without catalyst) for MB (black) and RhB (red) dyes and ChT (green).

Further, to verify that the degradation is not taking place by photolysis, blank experiments were performed in presence of light for MB, RhB and ChT dyes without using a catalyst. As shown in **Fig. 6.1a** and **b**, the photolysis of MB, RhB and ChT is very less as compared to the degradation performance in the presence of a catalyst. In addition, the photoactivity of MZ4 was checked in the absence of light for all three dyes. The results show a significant difference in the degradation performance of MZ4 in the presence and absence of light confirming the excellent visible light activity of MZ4 material.

Photocatalytic activity:

In order to assess the applicability of synthesized MZ catalyst, photocatalytic degradation of MB, RhB, and ChT were carried out under visible light irradiation. **Fig. 6.2-6.4** shows absorbance spectra for MB, RhB, and ChT dye using MZ photocatalyst.

6.3. Photocatalytic degradation of MB, RhB, and ChT dyes:

In this study, the photocatalytic activity of various metal ferrite nanoparticles was tested for the degradation of Rhodamine B dye under identical experimental conditions to enable a fair comparison of their efficiencies. The results are as follows:

ZnFe₂O₄ (Z1) catalyst achieved a degradation efficiency of 79.13%. While it was the least efficient among the tested catalysts, it still showed a substantial capability to degrade Rhodamine B. The lower efficiency of ZnFe₂O₄ compared to its manganese-substituted counterparts may be attributed to its relatively lower surface area and lesser generation of reactive species essential for the degradation process. (MZ1) manganese-substituted zinc ferrite catalyst showed a significant increase in degradation efficiency, achieving 84.66%. The incorporation of Mn into the zinc ferrite structure likely enhances the charge separation efficiency and provides more active sites for the photocatalytic reaction.

Fig 6.2 explains photocatalytic dye degradation of RhB using Z1, MZ1, MZ2, MZ3, MZ4, and M1. From **Fig. 6.2**, MZ2 Slightly outperforming the MZ1, this composition achieved a degradation efficiency of 84.71%. The slight increase in manganese concentration may contribute to better electron-hole pair generation, thus slightly enhancing the photocatalytic activity. MZ3 with a degradation efficiency of 87.82%, this composition indicates further improvement in photocatalytic activity with increased manganese content. The higher content of Mn seems to favor the photocatalytic process possibly by modifying the band gap and improving the redox potential of the material. MZ4 composition achieved the highest degradation efficiency of 90%. The substantial manganese content could have optimized the structural and electronic properties of the ferrite nanoparticles, thus maximizing the photocatalytic degradation of Rhodamine B dye. This suggests a favorable balance between zinc and manganese for effective dye degradation. M1 pure manganese ferrite achieved a degradation efficiency of 85%. Despite being highly efficient, it did not outperform the MZ4, which might suggest that a small amount of zinc presence could be critical in achieving the optimal photocatalytic activity within this series of ferrite nanoparticles.

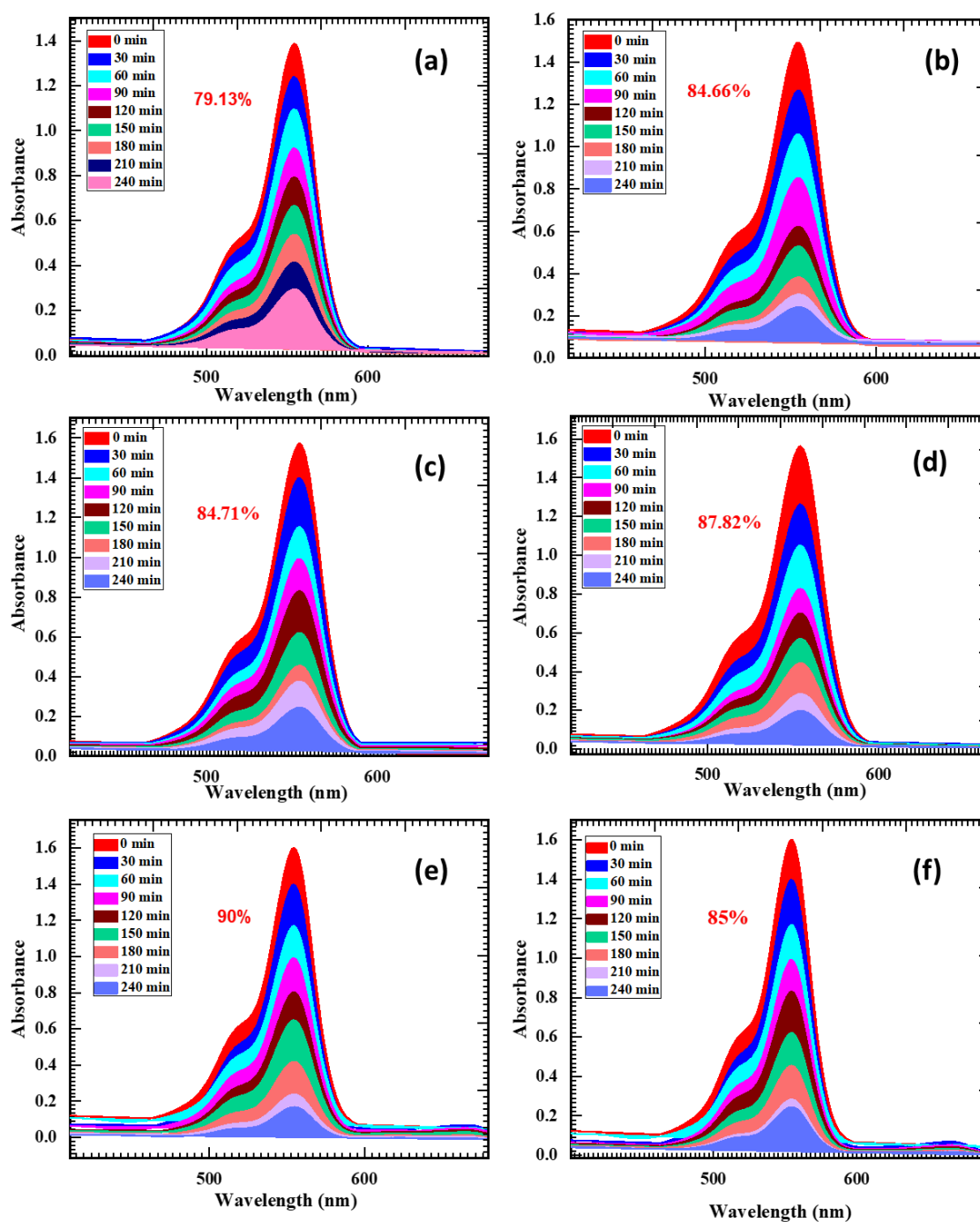


Fig. 6.2: Photocatalytic dye degradation of RhB using (a) Z1, (b) MZ1, (c) MZ2, (d) MZ3, (e) MZ4, and (f) M1.

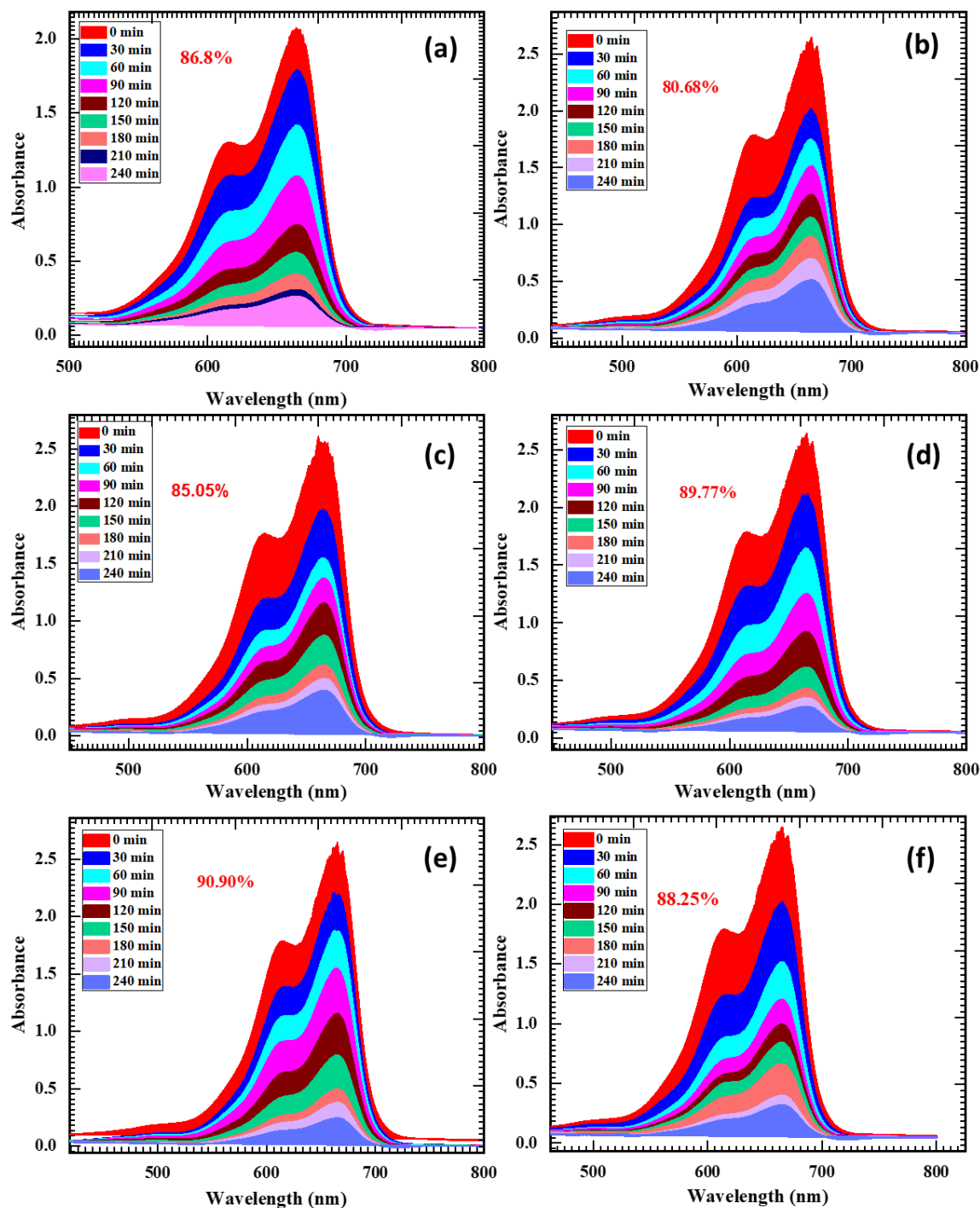


Fig. 6.3: Photocatalytic dye degradation of MB using (a) Z1, (b) MZ1, (c) MZ2, (d) MZ3, (e) MZ4, and (f) M1.

The varying efficiencies of these catalysts illustrate the impact of metal ion substitution in the ferrite structure on photocatalytic performance. Each composition

offers unique benefits that influence the rate of dye degradation, attributed to differences in electronic properties, surface chemistry, and interaction with the dye molecules. Further exploration into the physical and chemical properties of these nanoparticles can provide deeper insights into their photocatalytic mechanisms.

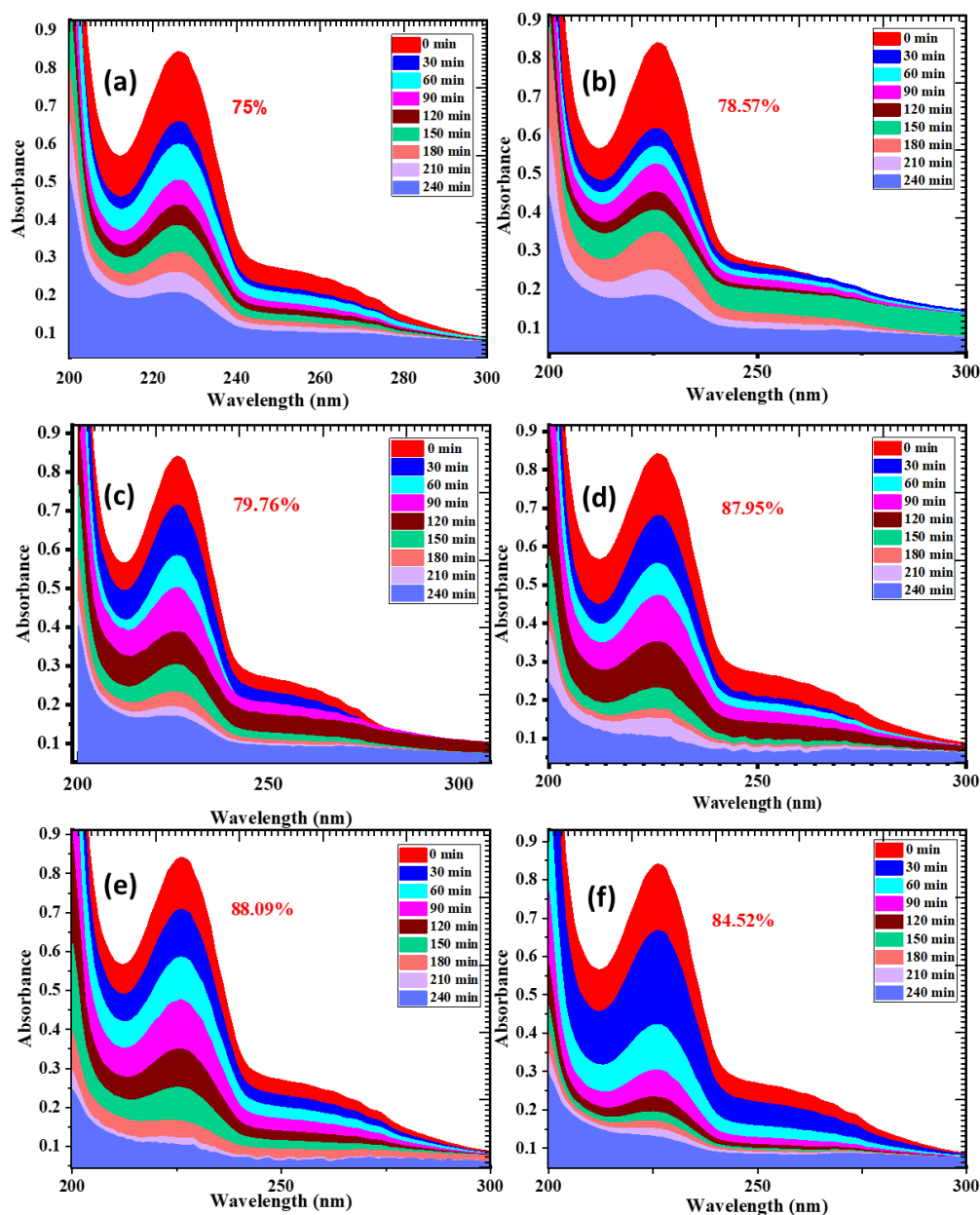


Fig. 6.4: Photocatalytic dye degradation of ChT using (a) Z1, (b) MZ1, (c) MZ2, (d) MZ3, (e) MZ4, and (f) M1.

Fig 6.3 shows photocatalytic dye degradation of MB using Z1, MZ1, MZ2, MZ3, MZ4, and M1. It is observed that MZ4 shows 90.90% of efficiency for MB dye degradation in 240 min. **Fig 6.4** shows photocatalytic dye degradation of ChT using Z1, MZ1, MZ2, MZ3, MZ4, and M1. It is observed that MZ4 shows 88.09% of efficiency for ChT dye degradation in 240 min.

The superior performance of MZ4 is attributed to its mesoporous structure. Mesoporous materials have a network of pores with diameters between 2 and 50 nanometers, which is crucial for creating more active sites for photocatalytic reactions. These active sites provide locations where chemical reactions can occur, thus enhancing the catalyst's efficiency in degrading dyes. The mesoporous structure not only provides more active sites but also facilitates the diffusion of dye molecules within the catalyst. This means that dye molecules can more easily access the active sites where the photocatalytic reactions occur, further enhancing the catalyst's performance. The findings are consistent with prior research on ferrites, which emphasizes the importance of specific surface area in enhancing photocatalytic efficiency. A higher specific surface area means there is more surface area available for interactions with dye molecules, leading to increased degradation efficiency.

The MZ4 sample has a narrow optical bandgap of 1.46 electron volts (eV). The bandgap refers to the energy difference between the valence band and the conduction band in a material. A narrow bandgap means that the material can absorb a wider range of wavelengths of light, including visible light, which is important for photocatalytic reactions since visible light constitutes a significant portion of sunlight. Another advantage of the spinel samples, including MZ4, exhibit magnetic properties that allow them to be rapidly separated from the solution under the influence of an applied magnetic field following the photocatalytic reaction. This means that the catalyst can be easily recovered and reused multiple times, reducing the need for fresh catalyst material and improving the overall sustainability of the process. The degradation performance of other photocatalysts is tabulated in **Table 6.1**.

Table 6.1: Degradation percentages of all the samples for MB, RhB, and ChT dyes.

Sample ID	MB Dye Degradation (%)	RhB Dye Degradation (%)	ChT Dye Degradation (%)
Z1	86.8	79.13	75
MZ1	80.68	84.66	78.57
MZ2	85.05	84.71	79.76
MZ3	89.77	87.82	87.95
MZ4	90.90	90	88.09
M1	88.25	85	84.52

The experimental findings underscore a significant variation in the photocatalytic degradation efficiency of MB, RhB, and ChT dyes contingent upon the specific composition of the metal ferrite nanoparticles utilized. Here, this study presents a detailed analysis of the critical factors influencing the photocatalytic activity of these nanoparticles, focusing on the effects of compositional composition.

The degradation efficiencies observed reveal a clear pattern as the concentration of manganese in the zinc ferrite structure increases, there is generally an enhancement in photocatalytic activity, up to a point. MZ4, with the highest manganese content among the mixed compositions, exhibits the most elevated degradation efficiency at 90.90%, 90%, and 88.09% for MB, RhB, and ChT dyes. This high efficiency can be attributed to the unique electronic structure imparted by manganese, which may facilitate more effective separation of charge carriers and extend their lifespan, thereby increasing the likelihood of interacting with and degrading the dye molecules.

In contrast, ZnFe_2O_4 , lacking in manganese substituting, shows the lowest degradation efficiency. Zinc ferrite typically has a higher bandgap compared to manganese- substituted variants, which can result in less efficient utilization of visible light for the generation of electron-hole pairs, a key aspect of photocatalytic activity under sunlight.

The surface area of the photocatalysts is crucial as it directly influences the adsorption of dye molecules onto the catalyst's surface, an essential step before photocatalytic degradation can occur. Nanoparticles with higher surface areas provide

more active sites for photocatalytic reactions. Substituting ferrites with manganese can alter the physical properties, including changes to surface area and pore structure, which can enhance the adsorption capacity and consequently, the photocatalytic efficiency.

The generation and subsequent dynamics of electron-hole pairs play a pivotal role in the efficiency of photocatalytic processes. The separation of these charge carriers is crucial; recombination leads to loss of efficiency as the energy is dissipated as heat rather than being used for photocatalytic reactions. The composition of the nanoparticles significantly affects these dynamics. Manganese in the ferrite structure enhances the magnetic properties, which can influence the electronic properties by reducing the recombination rate of electron-hole pairs through spin-related effects. In summary, the analysis suggests that the interplay between manganese and zinc within the ferrite structure critically influences the photocatalytic properties through modifications in electronic band structure, surface properties, and magnetic effects.

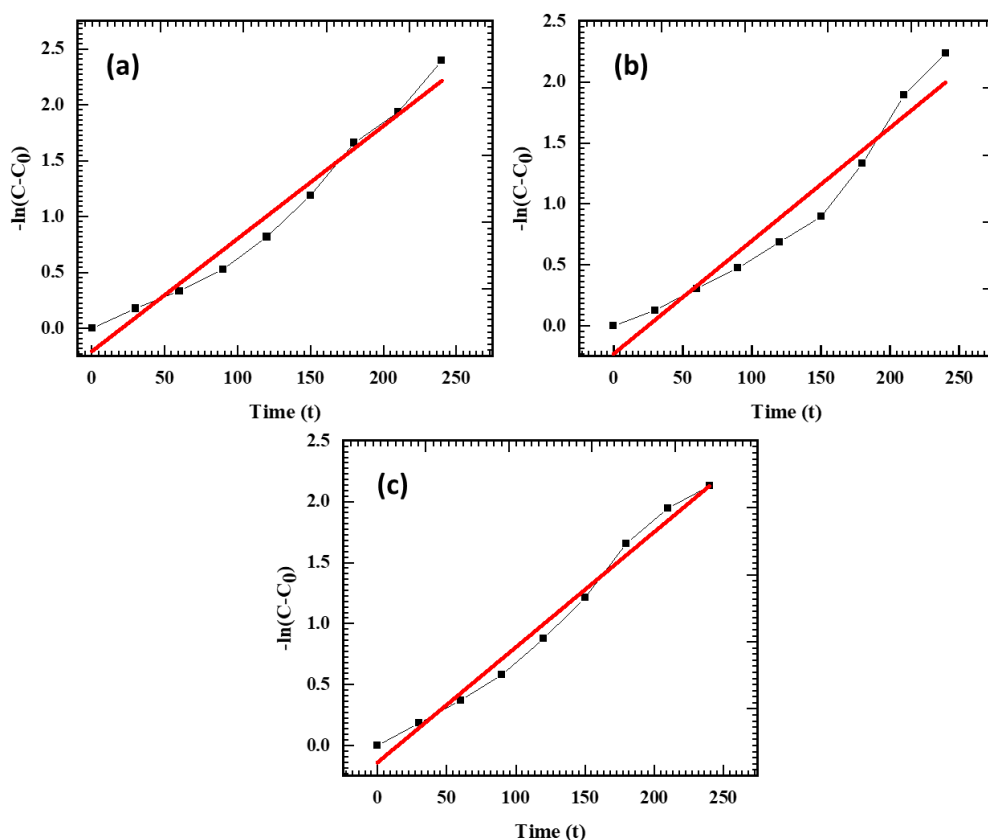


Fig. 6.5: Pseudo first-order kinetics for (a) MB, (b) RhB, (c) ChT dyes of MZ4.

To understand the degradation process, kinetic graphs are plotted as shown in **Fig. 6.5**. The present study suggests that MZ4 exhibit rate constant of 0.010086, 0.00928, and 0.00945 min^{-1} for MB, RhB, and ChT dyes with R^2 value of 0.9705, 0.9421, and 0.9838 respectively. The R^2 values and kinetic constants for kinetic model are tabulated in **Table 6.2**. From the values of R^2 can be considered as a pseudo first order kinetic reaction involved in a dye degradation.

Table 6.2. Kinetic parameters of optimized MZ4 for MB, RhB, and ChT dyes.

Dyes	Degradation (%)	Rate constant (min^{-1})	R^2
MB	90.90%	0.010086	0.97058
RhB	90%	0.00928	0.94217
ChT	88.09%	0.00945	0.98383

6.3.1. Catalyst dosage for MB RhB and ChT dyes:

To investigate the influence of MZ4 photocatalyst dose on the degradation of RhB (**Fig. 6.6**), MB (**Fig. 6.7**), and ChT (**Fig. 6.8**) under visible light, the impact of varying photocatalyst amounts (15 mg, 30 mg, 45 mg, and 60 mg) on the degradation performance is observed. For this study, optimized MZ4 samples were used. The results demonstrated a clear correlation between the photocatalyst dose and RhB degradation efficiency. As shown in fig. 10, 30 mg photocatalyst shows higher degradation performance than that of 15, 45, and 60 mg under scoring significance of use of optimum amount of photocatalyst during photocatalytic reaction. The observed enhancement in photodegradation efficiency using 30 mg photocatalyst can be attributed to the increased number of photons absorbed by the catalyst and the availability of additional surface-active sites for photocatalytic reactions. The decrease in performance for 45 and 60 mg is attributed to the aggregation of catalyst which blocks the visible light [12]. This aligns with previous studies [13], which emphasize the positive impact of catalyst dosage on photocatalytic performance.

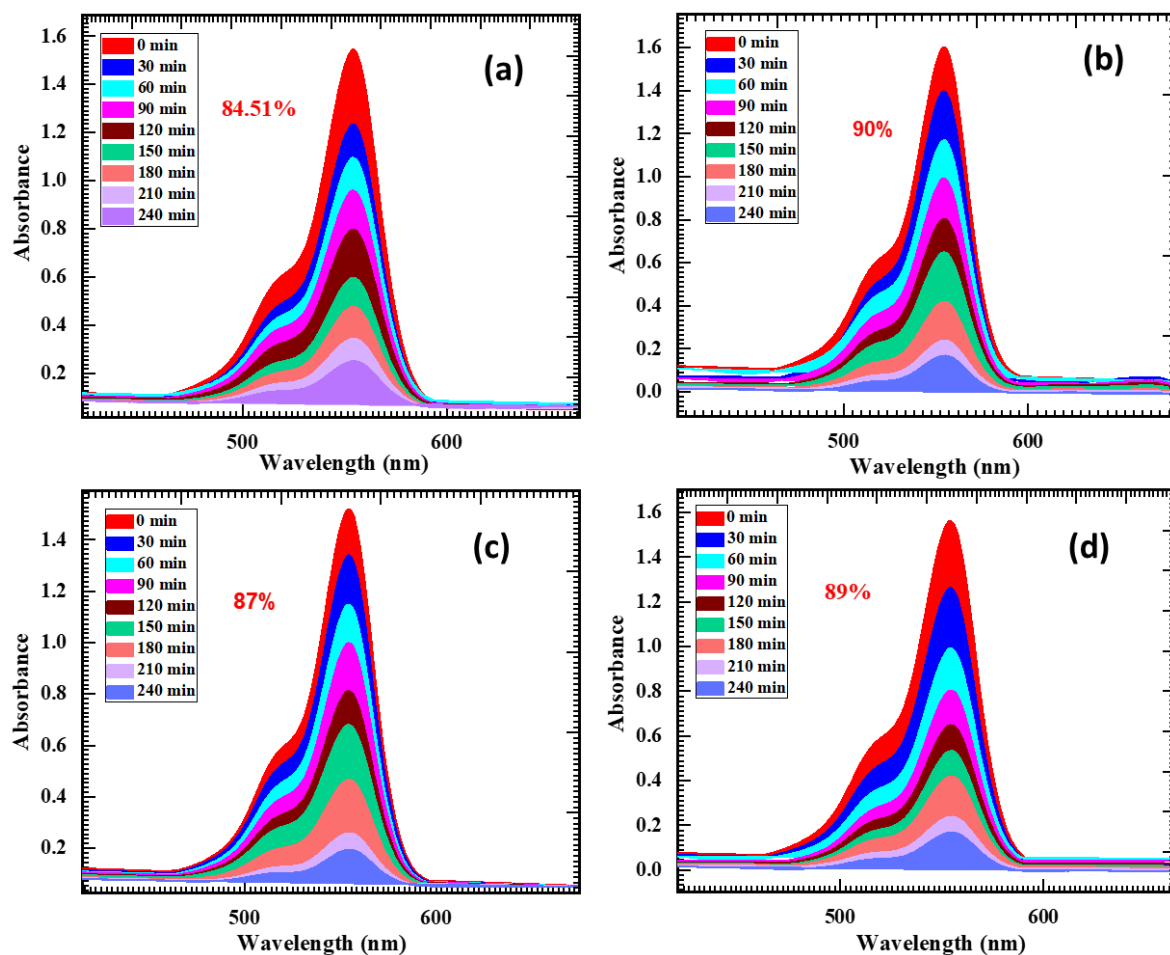


Fig. 6.6: Photocatalytic dye degradation of RhB using MZ4 catalyst loading (a) 15 mg, (b) 30 mg, (c) 45 mg, and (d) 60 mg.

The effect of catalyst loading on the photocatalytic activity, as observed in the degradation of RhB, MB, and ChT with varying amounts of the MZ4 photocatalyst, reflects an interplay between several factors. At lower doses, such as 15 mg, there might not be enough photocatalyst surface area to effectively absorb a significant amount of visible light or provide sufficient active sites for the photocatalytic reactions to occur. When the catalyst amount is increased to an optimal level, in this case, 30 mg, the available surface area for light absorption and the number of active sites both increase, enhancing the degradation efficiency of the dyes.

At higher catalyst loadings, such as 45 mg and 60 mg, the photocatalyst particles can aggregate, reducing the effective surface area that comes in contact with the dye

molecules. This aggregation can also hinder light penetration, as the packed particles create a shadowing effect, blocking light from reaching the inner layers of the catalyst mass. Furthermore, aggregation reduces the dispersion of catalyst in the solution, limiting the interaction between the catalyst active sites and dye molecules.

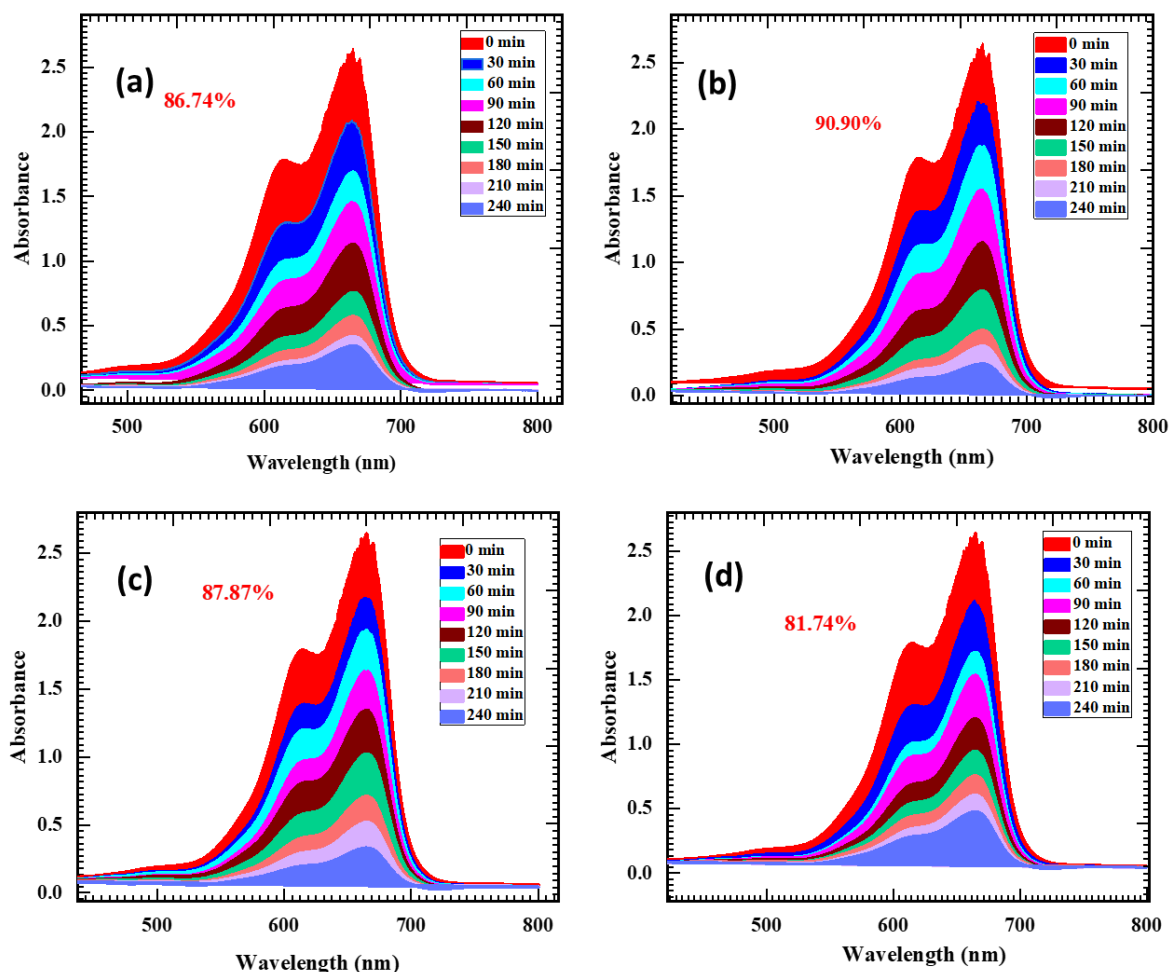


Fig. 6.7: Photocatalytic dye degradation of MB by using MZ4 Effect of catalyst loading (a) 15 mg, (b) 30 mg, (c) 45 mg, and (d) 60 mg.

The increase in photocatalytic activity up to a certain catalyst dose and the subsequent decrease beyond this optimal point can be attributed to the balance between the increased availability of active sites (up to the optimal dose) and the limitations posed by aggregation and reduced light penetration at higher doses. The optimal catalyst loading maximizes the interactions between the dye molecules and the photocatalyst

under the given light intensity, balancing effective light absorption, minimization of aggregation effects, and efficient mass transport.

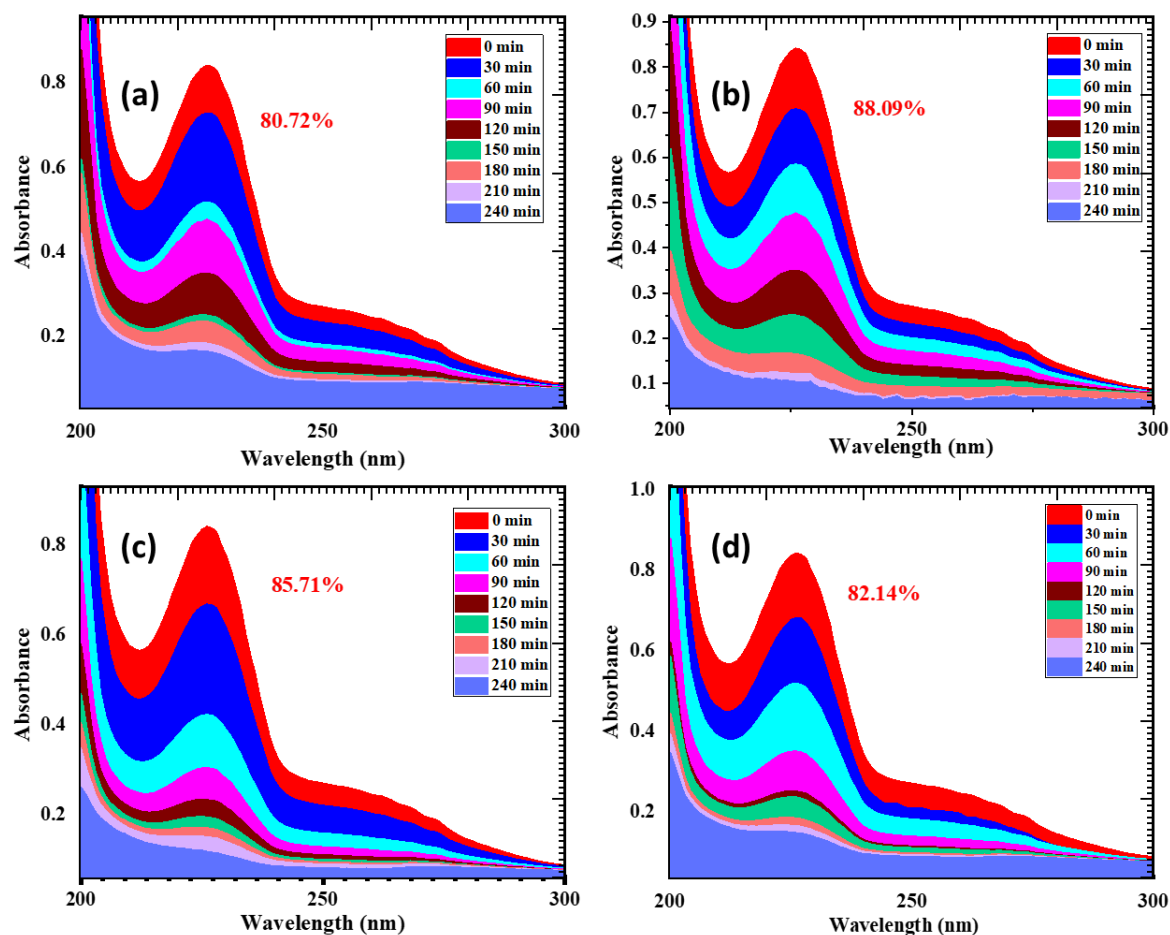


Fig. 6.8: Photocatalytic dye degradation of ChT by using MZ4 Effect of catalyst loading (a) 15 mg, (b) 30 mg, (c) 45 mg, and (d) 60 mg.

In summary, the influence of catalyst dose on photocatalytic activity is a result of the interplay between the increased availability of active sites and light absorption at optimal doses and the negative effects of aggregation and diffusion limitations at higher doses. Identifying the optimal catalyst dose is crucial for maximizing photocatalytic degradation efficiency.

This highlights the importance of finding a balance in catalyst dosage for optimal photocatalytic performance. In summary, the study underscores the significance of MZ4 photocatalyst dosage in influencing RhB, MB, ChT degradation efficiency. The results

emphasize the need for careful consideration and optimization of catalyst dosage to achieve the highest photocatalytic performance.

6.3.2 Scavenger studies of MB, RhB, ChT dyes:

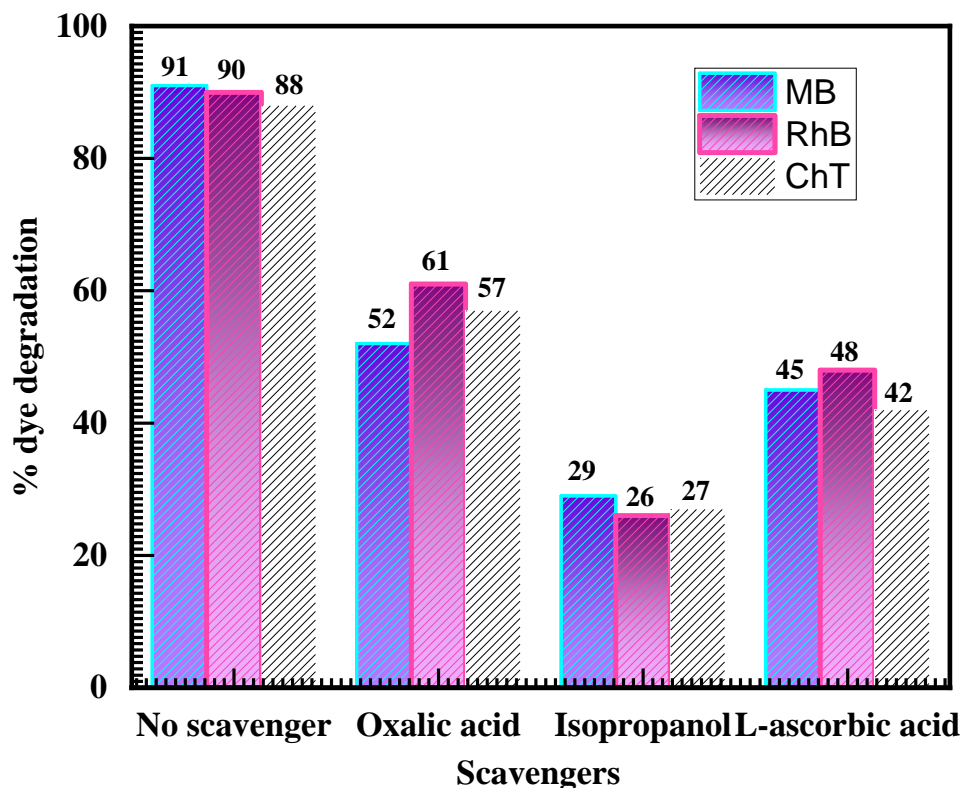


Fig. 6.9: Scavenger study of MZ4 photocatalyst for MB, RhB and ChT dyes.

The scavenger study conducted in the research aimed to identify the primary reactive species involved in the photodegradation process of MB (blue color), RhB (pink color), and ChT (colorless) using MZ4 photocatalyst. We have used same color combination as that of dyes to depict scavenger activity. Three scavengers viz. L-ascorbic acid, isopropanol (IPA), and oxalic acid were employed to capture superoxide radicals, hydroxyl radicals, and holes, respectively and to determine the dominant reactive species influencing the photocatalytic performance. As shown in **Fig. 6.9**, the results demonstrate distinct responses to the scavengers, highlighting the crucial role of hydroxyl radicals in the degradation process. For MZ4 photocatalysts, the presence of IPA as a hydroxyl radicals scavenger led to significantly less photocatalytic performance compared to solutions containing L-ascorbic acid and oxalic acid. Specifically, the

degradation efficiency for IPA-containing solutions was 29% for MB, 26% for RhB and 27% for ChT. On the contrary, solutions containing L-ascorbic acid and oxalic acid demonstrated significantly higher degradation efficiencies. Specifically, observed efficiencies reached 45%, 48%, 42% for the L-ascorbic acid, and 52%, 61%, and 57% for the oxalic acid. These findings strongly suggest that the predominant reactive species responsible for the enhanced photocatalytic activity of MZ4 photocatalysts are hydroxyl radicals. In summary, the scavenger study provides crucial insights into the photocatalytic degradation mechanism, emphasizing the pivotal role of hydroxyl radicals in the enhanced performance of MZ4 photocatalyst for MB, RhB, and ChT degradation.

6.3.3. Investigation of the reusability and chemical stability of the MZ4 sample:

The investigation into the reusability of the optimum photocatalyst MZ4 for RhB, MB, and ChT photodegradation revealed valuable insights into its practical application. We have used same color combination as that of dyes to depict recyclability activity Which is helpful for the implementation of photocatalysts in real-world scenarios.

In this study, the recycled MZ4 photocatalyst was subjected to multiple cycles, and its photoactivity was assessed for RhB, MB, and ChT degradation. After degradation process, the catalyst was collected, separated via an applied magnetic field, washed with water, and dried after each cycle. **Fig. 6.10** illustrates the recyclability of MZ4 photocatalyst over five experimental cycles.

The results showed a consistent photodegradation efficiency for RhB, and steady stability. In the fifth cycle, a ~17% loss in photocatalyst activity compared to the first cycle for MB, and 10% loss in photocatalyst activity compared to the first cycle for RhB, and a 20% loss in photocatalyst activity compared to the first cycle for ChT dye was noted, potentially due to the slight solubility of MZ4 sample in the aqueous solution and the loss during washing. Additionally, the reduction in photocatalytic efficiency over cycles could be linked to the reduction in surface area due to annealing treatment after each cycle, leading to the aggregation of the photocatalyst. The study emphasized the importance of catalyst stability and recyclability, crucial for long-term applications in wastewater treatment. The magnetic characteristics of MZ4 photocatalyst facilitated easy

separation from the reaction medium, making it a promising candidate for practical use [14].

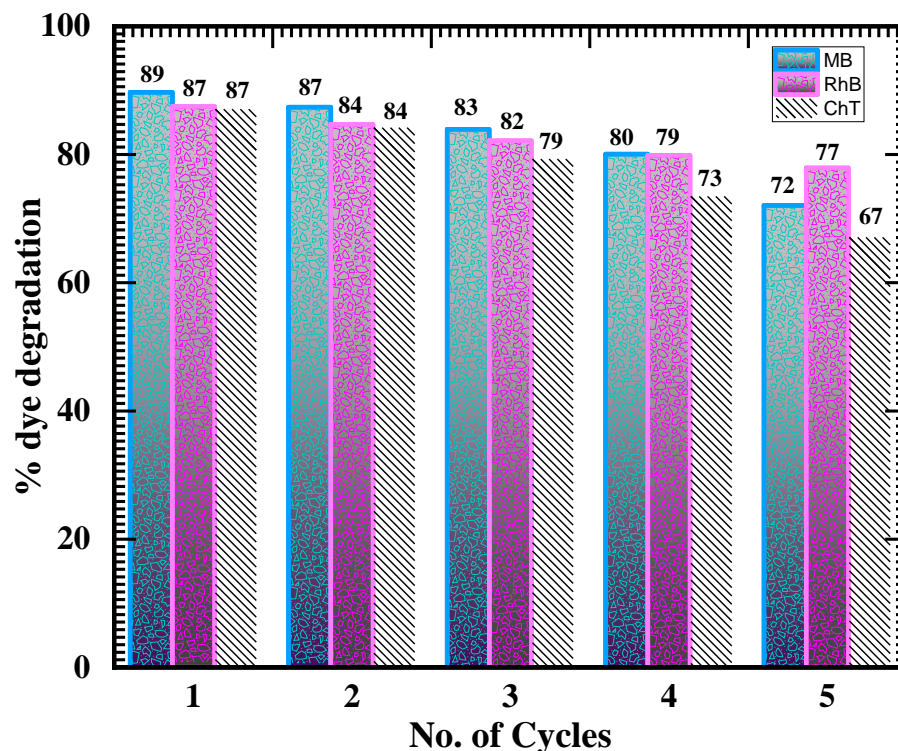


Fig. 6.10. Recyclability study of MZ4 photocatalyst.

Fig. 6.11 shows XRD patterns of MZ4 before and after the degradation process. It is evident from the literature that a stable photocatalyst sustain its structural stability even after degrading a specific dye [15, 16]. Nevertheless, the continuous reaction in the dye solution has the potential to reduce the crystallinity of the catalyst [17-19]. In present case, the catalyst shows a similar XRD pattern after degradation, with slightly decreased crystallinity.

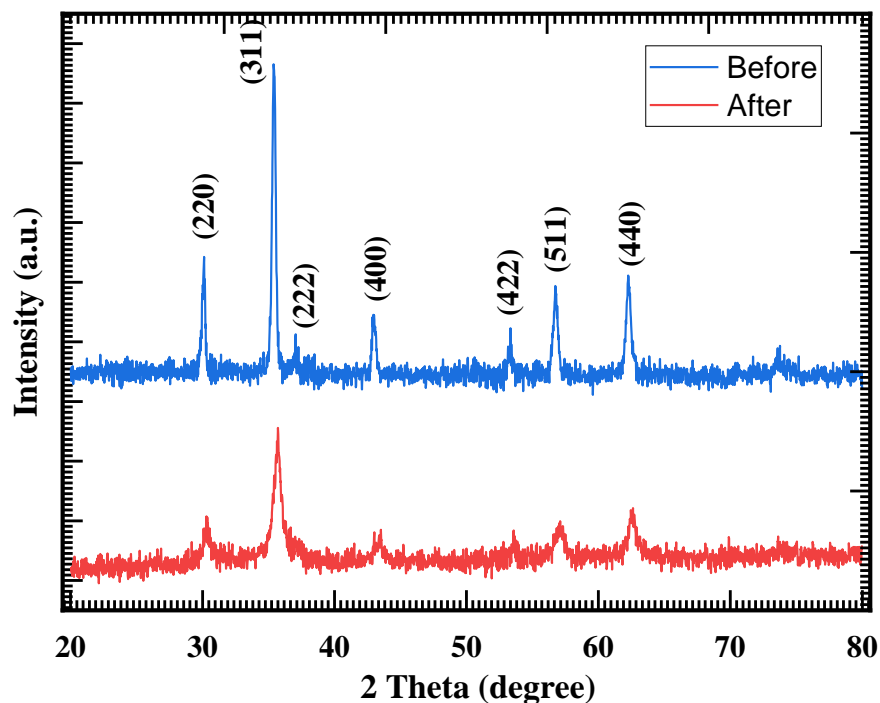


Fig. 6.11: Stability study of MZ4 before and after irradiation using an XRD.

6.4. Plausible dye degradation mechanism:

The provided information elucidates the mechanistic aspects underlying the photocatalytic degradation of all the dyes using MZ4 as the photocatalyst under visible light shown in **Fig. 1.2**. The process involves the excitation of electrons from the valence band to the conduction band upon visible light irradiation, generating electron-hole (e^- - h^+) pairs. These electrons and holes are responsible for the formation of reactive oxygen species (ROS), which further results in the degradation of organic molecules. Along with ROS, such as OH^\bullet radicals and $O_2^{\bullet-}$, the redox potentials of the radicals and the valence band and conduction band edges of the photocatalyst determines the degradation performance of a photocatalyst.

The redox potentials of OH^\bullet radicals and $O_2^{\bullet-}$ are considered, emphasizing the higher oxidation potential of OH^\bullet radicals compared to hydrogen peroxide. The introduction of Mn^{2+} , Zn^{2+} , and other metals in the spinel structure of ferrites modifies their redox properties. The holes in the valence band oxidize water, generating OH^\bullet

radicals, while electrons in the conduction band react with H_2O_2 to produce more OH^\bullet radicals. Fe^{3+} ions on the catalyst surface also capture photo-generated electrons, contributing to the formation of OH^\bullet radicals. These radicals efficiently oxidize dye molecules adsorbed on the photocatalyst surface, enhancing photocatalytic degradation efficiency.

6.5. Conclusions:

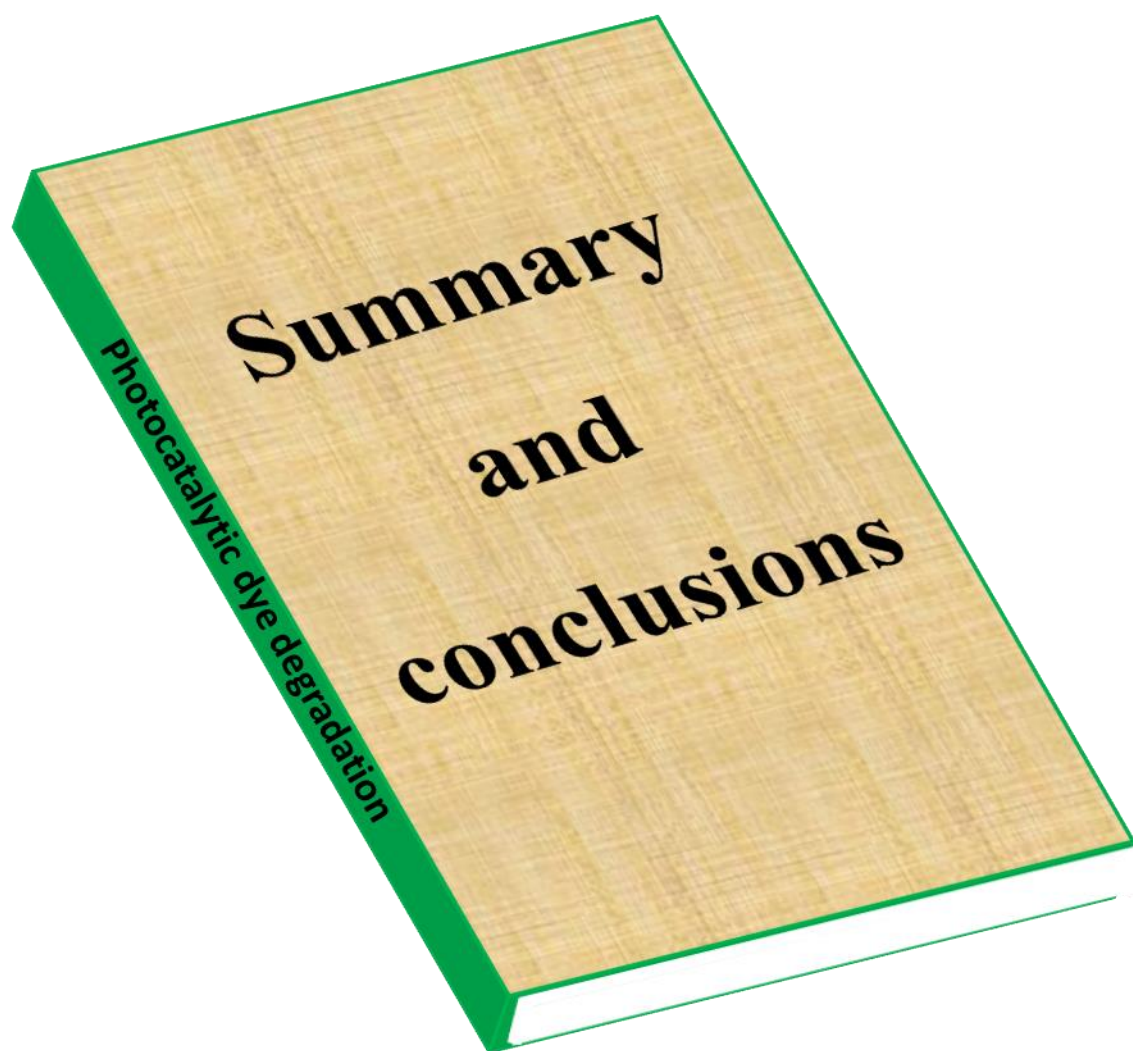
Mn substitution in zinc ferrite enhances charge carrier separation and shifts absorption into the visible range, improving photocatalytic efficiency. This makes Mn-substituted ZnFe_2O_4 more effective in degrading stubborn organic dyes like methylene blue, rhodamine B, and chloramine T. In conclusion, Chapter VI offers a thorough investigation into the photocatalytic degradation of MB, RhB, ChT dyes using various compositions of Mn-Zn ferrite nanoparticles, highlighting the environmental challenge posed by synthetic dyes and the potential of these catalysts for remediation. The study demonstrates that MZ4 exhibits the highest photocatalytic degradation efficiency, with manganese substituting significantly enhancing charge carrier separation and overall activity. The MZ4 catalyst achieved 90% degradation for both Methylene Blue (MB) and Rhodamine B (RhB), and 88.09% for Chloramine T (ChT), showcasing its superior performance across all dyes. The kinetics of the degradation process, optimal catalyst dosage, and the reusability and chemical stability of the catalysts are explored, with hydroxyl radicals identified as key reactive species. This chapter provides valuable insights for designing efficient Mn-Zn ferrite-based photocatalysts for effective environmental remediation.

6.6. References:

1. Mohod A, Teixeira A, Bagal M, Gogate P, Giudici R. Journal of Environmental Chemical Engineering., (2023), 109773 (1-24).
2. Yusuf M. Textiles and Clothing., (2019), ISBN:9781119526599.
3. Al-Buriahi A, Al-Gheethi A, Kumar P, Mohamed R, Yusof H, Alshalif A, Khalifa N. Chemosphere., 287, (2022), 132162 (1-14).
4. Rápó E, Tonk S. Molecules., 26, (2021), 5419 (1-31).
5. Rani M, Shanker U. InHandbook of Green and Sustainable Nanotechnology: Fundamentals, Developments and Applications, Cham: Springer International Publishing., (2023), 1267-1298.
6. Dassanayake R, Acharya S, Abidi N. Molecules. 26, (2021), 4697 (1-20).
7. Khan S, Noor T, Iqbal N, Yaqoob L. ACS Omega., 9, (2024), 21751-21767.
8. Ibhaddon A, Fitzpatrick P. Catalysts., 3, (2013), 189-218.
9. Tejashwini D, Harini H, Nagaswarupa H, Naik R, Harlapur S, Basavaraju N. Results in Chemistry., 7, (2023), 101247 (1-34).
10. Chahar D, Taneja S, Bisht S, Kesarwani S, Thakur P, Thakur A, Sharma PB., J. Alloys and Compounds, 851, (2021), 156878 (1-9).
11. Nekvapil F, Bortnic RA, Leostean C, Barbu-Tudoran L, Bunge A., Analytical Letters., 56, (2022), 42-52.
12. Bagwade P, Magdum V, Malavekar D, Chitare Y, Gunjekar J, Patil U, Lokhande C. Journal of Materials Science: Materials in Electronics., 33, (2022), 24646-24662.
13. Groeneveld I, Kanelli M, Ariese F, van Bommel M. Dyes and Pigments., 210, (2023), 110999 (1-14).
14. Tony M, Lin L. Environmental Technology., 43, (2022), 718-727.

15. Xu L, Wang S, Jin Y, Liu N, Wu X, Wang X. Separation and Purification Technology., 276, (2021), 119405 (1-14).
16. Diao Z, Liu J, Hu Y, Kong L, Jiang D, Xu X. Separation and Purification Technology., 184, (2017), 374-383.
17. Troncoso F, Tonetto G. Sustainable Environment Research., 31, (2021), 1-14.
18. Lops C, Ancona A, Di Cesare K, Dumontel B, Garino N, Canavese G, Hernández S, Cauda V. Applied Catalysis B: Environmental., 243, (2019), 629-640.
19. Kadam K, Phalake S, Lad M, Parale V, Gunjekar J, Khot V. Emergent Materials., 7, (2024), 1489-1501. `

CHAPTER VII



Summary and Conclusion of the Research Work:

This comprehensive research work focuses on developing and optimizing photocatalytic materials for environmental remediation, particularly for degrading synthetic dyes in wastewater. The study highlights the growing environmental threat posed by contaminants like dyes and evaluates modern water purification techniques, with a focus on Advanced Oxidation Processes (AOPs) like photocatalysis due to its simplicity, eco-friendliness, and effectiveness. Traditionally, TiO_2 and ZnO semiconductors are explored for visible-light photocatalysis. However, their limitations such as wide band gap can be overcome by introducing metal ferrites, as promising visible-light-active photocatalysts. In all metal ferrites, Zinc ferrite (ZnFe_2O_4) nanoparticles have been selected and synthesized using solution combustion synthesis (SCS). An effort has been taken to tune the physico-chemical properties of ZnFe_2O_4 Nps by varying Fuel to oxidizer ratio (glycine-to-nitrate). It is found to influence structural, morphological, and optical properties, enhancing photocatalytic efficiency. The composition for which the material shows highest efficiency is fuel lean composition and the same has been used for further study. The research further examines manganese-doped zinc ferrite nanoparticles, where increased Mn^{2+} concentration reduces the band gap and enhances visible-light absorption, optimizing their photocatalytic properties. The work further explores the photocatalytic degradation of Methylene Blue (MB), Rhodamine B (RhB), and Chloramine T (ChT) dyes using both ZnFe_2O_4 and MZNPs under visible light irradiation. The said work is presented in six chapters systematically correlating the obtained results with characteristic properties of material. The study concludes with insights into the design and optimization of metal ferrite-based photocatalysts for effective environmental remediation applications.

In conclusion, this research successfully demonstrates the development and optimization of zinc ferrite (ZnFe_2O_4) and manganese-doped zinc ferrite (MZNP) nanoparticles as efficient photocatalysts for the degradation of synthetic dyes in wastewater. Through solution combustion synthesis (SCS), the study highlights varying the glycine-to-nitrate (G/N) ratio and substitution with manganese significantly influence the structural, optical, and photocatalytic properties of these materials. The reduced band

gap and enhanced visible-light absorption of MZNPs, particularly the MZ4 catalyst, these findings underscore the potential of Mn-substituted zinc ferrite nanoparticles in addressing environmental challenges by providing a sustainable and effective solution for water purification. The research offers valuable insights into the design of advanced photocatalysts, paving the way for future innovations in environmental remediation technologies.

The **chapter I** delves into the significance of water purification techniques in combating pollution and environmental degradation. It emphasizes the increasing challenges posed by contaminants, particularly dyes, to aquatic systems. Traditional and conventional purification methods, dating back to ancient times, are discussed alongside modern approaches like AOPs. photocatalysis, are highlighted for their efficacy, simplicity, and eco-friendliness in degrading organic pollutants into harmless byproducts using atmospheric oxygen.

The chapter explores the limitations of current photocatalysts, such as their reliance on UV light and difficulties in catalyst separation and recycling, are acknowledged. The introduction of metal ferrites as visible-light-active photocatalysts, their synthesis methods, and efforts to enhance their efficiency through modifications are discussed. Furthermore, the chapter outlines factors influencing photocatalytic activity, such as catalyst loading and light intensity. It concludes by highlighting the urgency of addressing water contamination issues and the potential of photocatalysis, especially using manganese-substituted zinc ferrite nanoparticles, in achieving efficient water treatment. The next step involves studying the photocatalytic performance of these nanoparticles in degrading various dyes like methylene blue, chloramine T, and rhodamine B, to advance water purification efforts.

The **chapter II** explores the synthesis of nanostructured metal oxides, focusing on the solution combustion synthesis (SCS) technique. It highlights the advantages of bottom-up methods like SCS, which stands out for its simplicity, cost-effectiveness, and ability to produce high-purity products and scalability.

The chapter presents the chemistry of SCS, discussing key parameters like the fuel-to-oxidizer ratio, choice of fuel, and their impact on the combustion process and

resulting material properties. The combustion synthesis process is elucidated, emphasizing the role of fuel in complexing metal ions and providing energy for synthesis reactions. The use of fuel to oxidizer ratio is explored for their ability to create porosity and unique microstructures in the final product.

Zinc ferrite (ZnFe_2O_4) nanoparticles are highlighted as a target material synthesized via SCS due to their tunable physico-chemical properties. The synthesis process for ZnFe_2O_4 nanoparticles using glycine as a fuel is outlined, with variations in the fuel-to-oxidizer ratio. The combustion reaction mechanism and synthesis steps are discussed.

Furthermore, the chapter discusses characterization techniques crucial for analyzing the morphology, composition, and physio-chemical properties of materials synthesized via SCS. Common techniques such as scanning electron microscopy (SEM), energy dispersive spectroscopy (EDS), X-ray diffraction (XRD), Fourier Transform Infrared Spectroscopy, (FT-IR), UV–Vis Diffuse Reflectance Spectroscopy (UV-DRS), Transmission electron microscopy (TEM), X-ray photoelectron spectroscopy (XPS), and Brunauer-Emmett-Teller (BET) analysis are outlined.

Overall, the chapter provides a comprehensive overview of SCS as a versatile method for synthesizing metal oxides, with a focus on its application in producing zinc ferrite nanoparticles. It offers insights into optimizing synthesis conditions and characterizing the resulting materials

Chapter III correlates structural, morphological, and optical properties of ZnFe_2O_4 NPs with varied G/N ratio. The study provides valuable insights into the impact of G/N ratio variations on the characteristics of ZnFe_2O_4 nanoparticles, which is crucial for optimizing their performance in photocatalytic applications, particularly in wastewater treatment for dye removal. It includes the thermodynamic analysis, structural characterization, and surface properties of ZnFe_2O_4 nanoparticles synthesized using different glycine-to-nitrate (G/N) ratios.

Theoretical calculations using thermodynamic factors such as reaction and flame temperatures aid in predicting ignition and combustion. As the G/N ratio increases, both

the reaction temperature and adiabatic flame temperature was found to be increased. The cubic spinel structure of ZnFe_2O_4 is confirmed, with diffraction peaks corresponding to specific crystallographic planes. The lattice parameters shift with changes in the G/N ratio, indicating variations in lattice strain. Absorption bands in FTIR corresponding to metal-oxygen bond stretching confirm the spinel cubic structure formation. The M-O stretching band intensity varies with G/N ratio, indicating changes in cation distribution. Morphological analysis from SEM reveals nanoparticle with varying degrees of porosity and agglomeration, influenced by the G/N ratio. Particle size distribution from TEM confirms nanometer-sized particles with a polycrystalline structure consistent with XRD findings. Chemical states of ZnFe_2O_4 nanoparticles are examined by XPS confirming the presence of Zn, Fe, and O ions with specific binding energies indicative of their oxidation states. Surface area measured from BET decreases with increasing G/N ratio due to changes in the porous structure, impacting catalytic activity. Higher surface area in fuel-lean samples supports enhanced catalysis. ZnFe_2O_4 nanoparticles exhibit visible light absorption, with band gap energy ranging from 1.6 to 1.87 eV, which decreases as the crystallite size increases from 9.74 to 22.85 nm. These results highlight potential of Zn-Fe and SCS for photocatalytic degradation of contaminants.

Chapter IV presents the experimental process and results of synthesizing manganese-substituted zinc ferrite nanoparticles (MZNPs) with the formula $\text{Mn}_x\text{Zn}_{1-x}\text{Fe}_2\text{O}_4$ (where $x = 0, 0.2, 0.4, 0.6, 0.8, 1$) using the combustion method to enhance photocatalytic dye degradation. MZNPs were synthesized using metal nitrates as oxidizers and glycine as the fuel, with the manganese concentration varied to investigate its influence on the structural, morphological, and optical properties of the nanoparticles. Building upon the optimized glycine-to-nitrate (G/N) ratio for zinc ferrite (Z1), as discussed in the previous chapter, this ratio was maintained while substituting zinc with manganese. This approach allowed for precise tuning of the nanoparticle properties to enhance photocatalytic performance.

XRD confirmed the spinel structure of MZNPs, with lattice parameter increasing with Mn^{2+} concentration. FT-IR revealed changes in molecular structure with Mn^{2+} addition. Raman spectroscopy confirmed the spinel structure and suggested a normal to inverse spinel transition. SEM showed porous morphology, with increasing porosity with

higher Mn concentration, while EDS confirmed elemental composition. XPS indicated the presence of Mn^{2+} , Zn^{2+} , Fe^{3+} , and O^{2-} . BET analysis revealed mesoporous structures with increased surface area, beneficial for catalytic reactions. UV-DRS demonstrated a decreasing trend in band gap energy from 1.56 to 1.43 eV with increasing Mn^{2+} concentration, thereby enhancing visible light absorption. In summary, the experimental results demonstrate the successful synthesis of Mn^{2+} -doped zinc ferrite nanoparticles with tailored properties suitable for efficient photocatalytic degradation of dyes, offering insights into their structural, morphological, and optical characteristics.

Chapter V delves into the experimental setup and results of a photocatalytic dye degradation study, primarily focusing on the degradation of Methylene Blue (MB), Rhodamine B (RhB), and Chloramine T (ChT) dyes using zinc ferrite nanoparticles (MZNPs) under visible light irradiation. This chapter introduces the experimental setup, including the light source, filters, and measurement techniques. The % dye degradation equation is provided, serving as a basis for evaluating the catalyst's effectiveness over time.

This chapter explores the photocatalytic degradation of MB, highlighting the superior activity of ZnFe_2O_4 (Z1) catalyst and its dependence on glycine and nitrate content. Catalyst dosage and scavenger studies further elucidate the degradation mechanism, with hydroxyl radicals identified as primary reactive species.

The study to RhB and ChT dyes, respectively, emphasizing the impact of catalyst dosage and scavenger presence on degradation efficiency. Z1 consistently outperforms other catalysts, with hydroxyl radicals playing a crucial role in all three dye degradation processes. The mechanism of photocatalytic degradation, explaining the generation and role of reactive species in the process is discussed. Factors contributing to the superior catalytic activity of Z1, such as surface area and charge carrier separation, are discussed and tabulated in **Table 7.1**. In summary, Chapter V provides comprehensive insights into the photocatalytic degradation of various dyes using zinc ferrite nanoparticles, elucidating the role of catalyst composition, dosage, and reactive species in the degradation mechanism. These findings offer valuable contributions to understanding and optimizing photocatalytic processes for environmental remediation applications.

In **Chapter VI**, the focus is on investigating the photocatalytic degradation of MB, RhB, ChT dyes using various compositions of Mn-Zn ferrite nanoparticles as catalysts. This chapter aims to contribute to understanding the photocatalytic mechanisms involved and provide insights into the design of efficient metal ferrite-based photocatalysts for environmental remediation applications. The chapter begins with an introduction highlighting the environmental challenge posed by synthetic dyes in water and the potential of photocatalysis using Mn-Zn ferrite nanoparticles as a solution. It outlines the objectives of the study and discusses the theoretical enhancements expected through manganese substitution in zinc ferrite. The experimental results present the photocatalytic degradation efficiencies of various metal ferrite compositions, including Z1, MZ1, MZ2, MZ3, MZ4, and M1, for the degradation of Methylene Blue (MB), Rhodamine B (RhB), and Chloramine T (ChT) dyes. Among these, MZ4 demonstrated the highest degradation efficiencies, achieving 90% for both MB and RhB, and 88.09% for ChT.

The discussion delves into the factors influencing photocatalytic activity, such as composition, surface area, and electron-hole pair dynamics, highlighting the role of manganese substitution in enhancing charge carrier separation and overall efficiency. The chapter also explores the kinetics of the degradation process using a pseudo-first-order kinetic model, providing insights into the rate constants for different dyes. Furthermore, the impact of catalyst dosage on photocatalytic activity is investigated, emphasizing the importance of finding the optimal balance to maximize efficiency while avoiding aggregation effects. The study evaluates the reusability and chemical stability of the optimized MZ4 photocatalyst, demonstrating its potential for practical applications in wastewater treatment. XRD patterns before and after degradation indicate the structural stability of the catalyst, while a scavenger study confirms the crucial role of hydroxyl radicals in the degradation process. Finally, mechanistic aspects underlying the photocatalytic degradation process are discussed, detailing the generation of reactive oxygen species and their role in dye degradation. Overall, Chapter VI provides a comprehensive analysis of the photocatalytic degradation of MB, RhB and ChT dyes using Mn-Zn ferrite nanoparticles, offering valuable insights for the design and

development of efficient photocatalysts for environmental remediation is presented in **Table 7.2**.

Table 7.1: Photocatalytic Degradation of MB, RhB, ChT dyes using Various G/N Ratios for Different Pollutants.

Photocatalyst	Dye degradation efficiency (%)			Time (min)
	MB	RhB	ChT	
Z1	90.65	88.40	81.92	300
Z2	85.10	87.94	77.5	300
Z3	81.95	85.47	75.90	300
Z4	83.58	84.66	73.49	300
Z5	65.64	83.44	72.28	300

Table 7.2: Photocatalytic Degradation of MB, RhB, ChT dyes using Manganese Substituted Zinc Ferrite.

Photocatalyst	Dye degradation efficiency (%)			Time (min)
	MB	RhB	ChT	
MZ1	80.68	84.66	78.57	240
MZ2	85.05	84.71	79.76	240
MZ3	89.7	87.82	87.95	240
MZ4	90.9	90	88.09	240
M1	88.25	85	84.52	240

MZ4 is the top performer across all dyes (MB, RhB, ChT), showcasing high degradation efficiency. Increasing manganese in ZnFe_2O_4 (up to MZ4) boosts photocatalytic activity, attributed to factors like enhanced surface area and visible light absorption. This catalyst efficiently generates hydroxyl radicals crucial for dye degradation. Its stability and performance make it promising for wastewater treatment. MZ4 emerges as the optimal choice for efficient dye degradation, underlining the significance of manganese optimization for superior photocatalytic outcomes in environmental applications.

***“MANGANESE SUBSTITUTED ZINC FERRITE NANOSTRUCTURES FOR
PHOTOCATALYTIC DYE DEGRADATION”***

CHAPTER VIII
80-Recommendations



8.1 Recommendations:

Based on the findings of this study, it is recommended to further explore the optimization of manganese doping concentrations in zinc ferrite nanoparticles to maximize photocatalytic efficiency for the degradation of various organic dyes. Additionally, future research should investigate the effects of different synthesis parameters, such as temperature and precursor ratios, on the structural and optical properties of the nanoparticles. It would also be beneficial to evaluate the long-term stability and reusability of Mn-doped zinc ferrite in practical applications. Lastly, expanding the scope of photocatalytic tests to include a wider range of pollutants could provide valuable insights into the versatility and effectiveness of these materials in environmental remediation.

8.2 Conclusions of the Research Work:

In conclusion, this research has demonstrated the successful synthesis of zinc ferrite nanoparticles via the combustion method, showcasing their performance in degrading dyes as Methylene blue (MB), Rhodamine B (RhB), and Chloramine T (ChT), through photocatalysis. Additionally, the incorporation of manganese into the zinc ferrite lattice further enhanced the photocatalytic activity of the nanoparticles. The characterization of the synthesized materials confirmed their structural integrity, morphology, and optical properties, elucidating the mechanisms behind their enhanced performance.

These findings underscore the potential of zinc ferrite nanoparticles, both pristine and manganese-substituted, as promising candidates for wastewater treatment applications, particularly in the degradation of organic dyes under visible light irradiation. The scalability and recyclability of these photocatalysts warrant further investigation to assess their practical feasibility for large-scale environmental remediation. Scalability of manganese-substituted zinc ferrite nanoparticles involves adapting the combustion synthesis method for large-scale production while maintaining high performance. This includes optimizing reaction conditions, scaling up equipment, and ensuring consistent quality across batches. Economic feasibility is crucial, requiring

an assessment of raw material costs, energy consumption, and operational expenses. Pilot-scale studies are essential to test the photocatalysts in real-world scenarios, such as treating industrial wastewater or natural water bodies, to confirm their effectiveness on a larger scale.

Recyclability is critical for practical applications, as it determines the ability of the photocatalysts to be reused without significant performance loss. This involves evaluating the long-term stability of the photocatalysts over multiple cycles and developing efficient regeneration methods, such as physical cleaning or chemical treatments. Additionally, the environmental impact of the recycling process and the associated costs must be assessed to ensure that the economic benefits of recycling outweigh the costs. A thorough investigation into both scalability and recyclability will determine the practical feasibility of these photocatalysts for large-scale environmental remediation.

Overall, the insights gained from this research pave the way for the development of advanced photocatalytic materials with improved efficiency, addressing the pressing challenges associated with dye pollution in wastewater streams.

8.3 Summary:

- Zinc ferrite nanoparticles, synthesized via the combustion method with controlled fuel-to-oxidizer ratios, displayed optimized photocatalytic properties, effectively degrading methylene blue (MB), rhodamine B (RhB), and chloramine T (ChT) dyes.
- Manganese substitution in zinc ferrite nanoparticles further enhanced their photocatalytic performance, with the optimal composition (MZ4) demonstrating exceptional dye degradation efficiency for MB, RhB, and ChT.

8.4 Future Findings:

- To Optimize of fuel-to-oxidizer ratios for other metal ferrites such as Manganese Ferrite.

- To substitute cobalt (Co), nickel (Ni), and copper (Cu) as substitution elements, as these metals may influence the structural, magnetic, and catalytic properties of the material. Their varied ionic radii and electronic configurations could enhance performance characteristics, leading to improved efficiency in applications such as catalysis or magnetic materials. Understanding their effects may help tailor the properties of the material for environmental remediation.
- Studying the effects on band gap modification is crucial because the band gap determines a material's ability to absorb and utilize visible light for photocatalytic processes. Modifications to the band gap can enhance light absorption, increase charge carrier mobility, and ultimately improve photocatalytic efficiency. By understanding how changes in crystal structure influence band gap properties, we can optimize materials for better performance in applications such as solar energy conversion and environmental remediation.
- Testing photocatalysts in pilot-scale studies. Testing practical viability over multiple cycles in larger-scale tests.
- Assessing effectiveness in real-world conditions (e.g., natural water bodies, industrial wastewater systems).
- To explore possibility of ZnFe_2O_4 based composites with other semiconductors or support materials (e.g., graphene, carbon nanotubes, TiO_2).
- To Investigating synergistic effects on photocatalytic activity, stability, and pollutant degradation range.
- Analyzing by-products formed during the photocatalytic degradation process.
- Evaluating economic feasibility considering synthesis, operation, and disposal phases of the photocatalyst lifecycle.



Low temperature glycine nitrate combustion synthesis of nanostructured zinc ferrites for enhanced visible light-driven methylene blue degradation

K. V. Kadam¹ · S. S. Phalake¹ · M. S. Lad¹ · V. G. Parale² · J. L. Gunjekar¹ · V. M. Khot¹

Received: 17 December 2023 / Accepted: 3 March 2024
© Qatar University and Springer Nature Switzerland AG 2024

Abstract

In this study, we present the efficient degradation of methylene blue (MB) under visible light using nanostructured zinc ferrite (ZnFe_2O_4) photocatalysts. The ratio of glycine and nitrate as a fuel and oxidant, respectively employed for the preparation of ZnFe_2O_4 nanoparticles by using the combustion method. The ratio variation of glycine and nitrate shows an effect on crystal structure, texture, and pores formation which is supported for photodegradation. The X-ray diffraction and scanning electron microscopy study exhibited cubic spinel structure and highly porous morphology respectively. X-ray photoelectron spectroscopy, and ultra-violet diffuse reflectance spectroscopy techniques utilized for the confirmation of ZnFe_2O_4 material and band gap energy measurement. Furthermore, the adiabatic flame temperature (T_{ad}) and the properties of the resulting product were studied in various combinations of nitrates and glycine. Thermodynamic analyses reveal that both the number of gases produced, and adiabatic flame temperature increase with a rising fuel-to-oxidant ratio. The synthesized photocatalysts are evaluated for their efficacy in the MB dye degradation under visible light ($\lambda \geq 400$ nm). The ZnFe_2O_4 nanoparticles (GN⁻¹ ratio of 0.48 (Z1)) showed efficient photocatalytic activity up to 90.65% degradation of MB dye in 5 h (h). These results played a crucial role due to the formation of hydroxyl radicals ($\bullet\text{OH}$) reactive species, leading to the efficient degradation of MB under visible light irradiation. ZnFe_2O_4 (Z1) nanoparticles demonstrated excellent recyclability and stability study. The highly porous morphology as well as the reduced band gap enabled the photodegradation of MB dye. Also, this work highlights the influence of the fuel-to-oxidizer ratio for MB dye degradation under visible light.

Keywords Combustion method · Nanoparticles · Photocatalysis · Porous morphology · Zinc-iron-oxide

1 Introduction

Water pollution is a critical environmental issue primarily caused by the release of harmful substances, including organic dyes and heavy metals, in industrial wastewater [1]. These pollutants pose a serious threat to humans, animals, plants, and aquatic ecosystems [2]. Various types of dyes, such as synthetic, azo, acidic, basic, reactive, diazo, and anthraquinone, further contribute to water pollution

[3]. Cationic dyes like methylene blue (MB) are challenging to remove from wastewater due to their harmful effects, and they are commonly used in industries for applications like coloring paper, clothing dye, photosensitizers, and redox indicators [4–6]. Several wastewater treatment methods exist, including physical–chemical processes like coagulation, irradiation, ozonation, chemical oxidation, ion exchange, adsorption, and reverse osmosis [7]. Photocatalysis, particularly visible light-driven photocatalysis, has emerged as a promising technology for wastewater cleanup, effectively breaking down dyes by absorbing a broad spectrum of light and promoting the formation of hydroxyl groups [8]. Nanoparticles responding to visible light, such as zinc ferrite (ZnFe_2O_4), have shown effectiveness in photocatalytic degradation of MB and other dyes, making them promising for wastewater treatment [9–13]. Their choice is driven by affordability, non-toxicity, and magnetic properties, especially under visible light exposure [14, 15].

✉ V. M. Khot
wish.khot@gmail.com

¹ Centre for Interdisciplinary Research, D. Y. Patil Education Society (Deemed to Be University), Kolhapur 416 006, India

² Department of Materials Science and Engineering, Yonsei University, 50 Yonsei-Ro, Seodaemun-Gu, Seoul 03722, Korea



Application of $\text{Mn}_x\text{Fe}_{1-x}\text{Fe}_2\text{O}_4$ ($x = 0-1$) Nanoparticles in Magnetic Fluid Hyperthermia: Correlation with Cation Distribution and Magnetostructural Properties

Satish S. Phalake, Manohar S. Lad, Ketaki V. Kadam, Syed A. M. Tofail, Nanasaheb D. Thorat,* and Vishwajeet M. Khot*



Cite This: <https://doi.org/10.1021/acsomega.2c05651>



Read Online

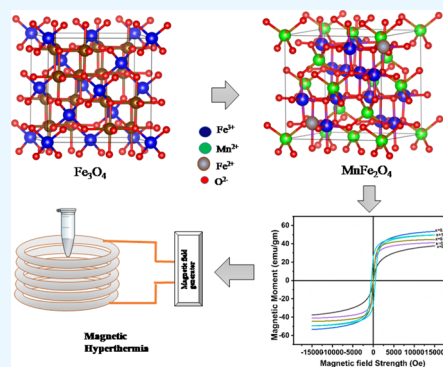
ACCESS |

Metrics & More

Article Recommendations

Supporting Information

ABSTRACT: Optimization of manganese-substituted iron oxide nanoferrites having the composition $\text{Mn}_x\text{Fe}_{1-x}\text{Fe}_2\text{O}_4$ ($x = 0-1$) has been achieved by the chemical coprecipitation method. The crystallite size and phase purity were analyzed from X-ray diffraction. With increases in Mn^{2+} concentration, the crystallite size varies from 5.78 to 9.94 nm. Transmission electron microscopy (TEM) analysis depicted particle sizes ranging from 10 ± 0.2 to 13 ± 0.2 nm with increasing Mn^{2+} substitution. The magnetization (M_s) value varies significantly with increasing Mn^{2+} substitution. The variation in the magnetic properties may be attributed to the substitution of Fe^{2+} ions by Mn^{2+} ions inducing a change in the superexchange interaction between the A and B sublattices. The self-heating characteristics of $\text{Mn}_x\text{Fe}_{1-x}\text{Fe}_2\text{O}_4$ ($x = 0-1$) nanoparticles (NPs) in an AC magnetic field are evaluated by specific absorption rate (SAR) and intrinsic loss power, both of which are presented with varying NP composition, NP concentration, and field amplitudes. $\text{Mn}_{0.75}\text{Fe}_{0.25}\text{Fe}_2\text{O}_4$ exhibited superior induction heating properties in terms of a SAR of 153.76 W/g. This superior value of SAR with an optimized Mn^{2+} content is presented in correlation with the cation distribution of Mn^{2+} in the A or B position in the Fe_3O_4 structure and enhancement in magnetic saturation. These optimized $\text{Mn}_{0.75}\text{Fe}_{0.25}\text{Fe}_2\text{O}_4$ NPs can be used as a promising candidate for hyperthermia applications.



INTRODUCTION

Due to their unique physical features, known biocompatibility, ease of production, and highly adjustable nature at the nanoscale, maghemite ($\gamma\text{-Fe}_2\text{O}_3$) and magnetite (Fe_3O_4) nanoparticles (NPs) are especially well suited for various biomedical applications.^{1,2} Magnetization in Fe_3O_4 can be tuned by replacing iron ions with transition metal cations, especially manganese ions, which have higher magnetic moments.³ It is explored for many applications which include catalysts, humidity sensors, biomedicine, MRI, microwave technologies, drug delivery, and magnetic fluid hyperthermia.² The properties of manganese ferrites such as their high electrical resistance, high Curie temperature (bulk MnFe_2O_4 is T_c 577 K), low coercivity value, and a low eddy current loss allow them to serve a wide range of applications.^{4,5} The integration of secondary cations Mn^{2+} in Fe_3O_4 and synthesis reproducibility have been studied.⁶ In the past decade, the general term MFe_2O_4 ($M = \text{Co}, \text{Mg}, \text{Ni}$, etc.) of spinel ferrites has been widely used for a variety of technological and biomedical applications.^{7,8} The magnetic and electrical properties of these compounds strongly depend on the synthesis process, chemical content, annealing temperature, and cation distribution. The cation distribution in spinel ferrite materials among two interstitial sites of the structure is one of the most challenging aspects of studying these materials due to its effect on the properties of ferrites.⁹ Shahane *et al.* reported the

MnFe_2O_4 magnetic NPs (MNPs) showing the antiparallel spin moments among Fe^{3+} , Mn^{2+} , and Fe^{2+} ions at A-sites and inverse spinel structures.¹⁰ The polycrystalline spinel ferrite $\text{Co}_x\text{Ni}_{1-x}\text{Fe}_2\text{O}_4$ ($x = 0-1$) was obtained by the sol-gel autocombustion method with the Co substitution. In Co^{2+} -substituted nickel ferrite, the density is higher than Ni^{2+} ions, owing to the higher magnetocrystalline anisotropy and the smaller particle size. The saturation magnetization (M_s) was increased to $x = 0.8$, at which point there was a small reduction in M_s for CoFe_2O_4 .¹¹ There have been several proposals for substituted magnetite NPs, $\text{M}_x\text{Fe}_{3-x}\text{O}_4$ ($M = \text{Ni}, \text{Zn}, \text{Mn}$, and Co , $0 < x \leq 1$) for various bio-applications since their magnetic properties can be easily controlled by replacing divalent or trivalent metal ions without modifying the crystal structure by either replacing them completely or partially.

$\text{Mn}_x\text{Fe}_{3-x}\text{O}_4$ NPs among these ferrites show stronger magnetization (M_s), low coercivity (H_c), and low inherent

Received: September 1, 2022

Accepted: November 8, 2022



D. Y. PATIL EDUCATION SOCIETY
(Deemed to be University), KOLHAPUR
NAAC 'A' Grade in 3rd Cycle

Certificate

This is to certify that **Mr. /Ms. Kadam Ketaki Vasantrao** of Centre for Interdisciplinary Research, DYPES, Kolhapur has delivered invited talk/ chaired the session/ presented oral/ presented poster/ participated in the **International Conference on Nanotechnology Addressing the Convergence of Materials Science, Biotechnology and Medical Science (IC-NACMBM-2024)** held at the Centre for Interdisciplinary Research, D. Y. Patil Education Society (Deemed to be University), Kolhapur, Maharashtra, India during 12th to 14th February 2024. His/ Her contribution to the conference is highly appreciated.

Dr. Jayavant L. Gunjekar

Convener

Prof. Meghnad G. Joshi

Convener

Prof. Chandrakant D. Lokhande

Chairman



A⁺⁺ Accredited by NAAC (2021)
with CGPA 3.52



National Conference

on

Physics of Materials & Materials based Device Fabrication 2023

(NCPM-MDF-2023)

November 25-26, 2023

Organized by

Department of Physics

(UGC-DRS- I & II, ASIST, DSA- I & II, DST FIST- I & II, PURSE, RUSA Sponsored Department)

Shivaji University, Kolhapur-416004, (M.S.), India

Certificate

This is to certify that Prof. / Mr. / Ms. Ketaki Kadam

of Centre for Interdisciplinary Research

has ☐ worked as resource person

☐ chaired the session ☐ worked as examiner ☒ participated ☐ presented the research paper entitled Zinc Ferrite

Nanostructures for Photocatalytic MB Dye Degradation

in the

National Conference on Physics of Materials & Materials based Device Fabrication 2023 (NCPM-MDF-2023) held at

Department of Physics, Shivaji University, Kolhapur-416004, (M.S.), India during November 25-26, 2023. His/her contribution to the conference is highly appreciated.



K. Kadam
Director
NCPM-MDF-2023

N. Kadam
Convener
NCPM-MDF-2023

Rayat Shikshan Sanstha's

D. P. Bhosale College, Koregaon, District- Satara
International Conference on
Emerging Trends in Material Science

e-Certificate

This is to certify that **Miss Ketaki Vasantrao Kadam** of **D. Y. Patil Education Society (Institution Deemed to be University)** has presented an Poster on **Induction Heating Studies of Combustion Synthesized ZnFe₂O₄ Nanoparticles for Hyperthermia Application** in **International Conference on “Emerging Trends in Material Science”** dated 9th & 10th November, 2022 jointly organized by Department of Physics & Chemistry in association with IQAC, D. P. Bhosale College, Koregaon, District- Satara, Maharashtra, India. **She awarded as the First Poster presentation research scholar. Certificate ID: ETMS_OPA_01**



Prof. Dr. S. D. Jadhav

Convener



Dr. V. S. Jamdade

Co-Convener



Dr. B. S. Lokde

IQAC Coordinator



Dr. V. S. Sawant

Principal



Hands-on Training Program on Advanced Research Characterization Techniques

विज्ञान एवं प्रौद्योगिकी विभाग
DEPARTMENT OF
SCIENCE & TECHNOLOGY

17-23 December, 2022

Organized by

FACULTY OF LIFE SCIENCES, BANASTHALI VIDYAPIETH, RAJASTHAN

Under the Scheme

Synergistic Training program Utilizing the scientific and Technological Infrastructure (STUTI)

Sponsored by : DST, Govt. of India

Certificate of Participation

This is to certify that Prof./Dr./Mr./Ms. Ketaki Vasantrao Kadam
from Centre for Interdisciplinary Research, D.Y. Patil Education Society,
has participated/delivered lecture on
Kolhapur (MH)
in the Hands-on Training Program organized by Faculty of Life Sciences, Banasthali
Vidyapeeth.

Prof. Jaya Dwivedi
Dean, Faculty of Life Sciences

Prof. Sarvesh Paliwal
Head, Dept. of Pharmacy

Prof. Dipjyoti Chakraborty
Head, Dept. of Biotechnology

Dr. Anshuman Shastri
Convenor

Dr. Saral K. Gupta
Coordinator

Dr. C. M. S. Negi
Coordinator

Dr. Parvej A. Alvi
Head, Dept. of Physical Sciences
& PMU Coordinator



SHIVAJI UNIVERSITY, KOLHAPUR

SOPHISTICATED ANALYTICAL INSTRUMENT FACILITY (SAIF) – COMMON FACILITY CENTRE (CFC)

WORKSHOP & HANDS-ON TRAINING ON XRD ORGANISED

BY SAIF-CFC UNDER STRIDE PROGRAMME

Certificate of Participation

This is certify that Miss Kadam Ketaki Vasantrao has successfully participated in the workshop & hands-on training on XRD organised by SAIF (CFC), Shivaji University, Kolhapur held during 11-12 Nov, 2021 under the STRIDE (Scheme for Trans-disciplinary Research for India's Developing Economy) programme.

Prof. R. G. Sonkawade
Co-ordinator : SAIF, Head (i/c) : CFC
Shivaji University, Kolhapur.
Chairman



SCHEME FOR TRANS-DISCIPLINARY RESEARCH
FOR INDIA'S DEVELOPING ECONOMY

CERTIFICATE OF COMPLETION

Awarded to

To build a global community of outstanding young people committed to improving the state of the world. With its motto we award

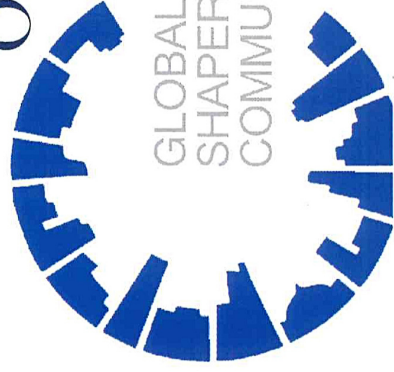
Mr./ Miss/ Ms.

Ketaki V. Kadam

College.

CIR, DYPS, Kolhapur.

On topic of "Introduction to the basics of Medical coding and application" Phase-I



SOUTH ASIA • INDIA

Kolhapur Hub

Gaurav Ghewade

Mr. Gaurav Ghewade

World Economic Forum



BIOCYTE

Institute of Research & Development

Sandeep Patil

Dr. Sandeep Patil

Biocyte Lab